Semiconductors, Vol. 38, No. 8, 2004, pp. 861–898. Translated from Fizika i Tekhnika Poluprovodnikov, Vol. 38, No. 8, 2004, pp. 897–936.

REVIEW

Electronic and Vibrational States in InN and $In_xGa_{1-x}N$ Solid Solutions

V. Yu. Davydov[1] and A. A. Klochikhin[1, 2]

[1]*Ioffe Physicotechnical Institute, Russian Academy of Sciences, St. Petersburg, 194021 Russia*
[2]*Institute of Nuclear Physics, Russian Academy of Sciences, St. Petersburg, 188350 Russia*

Submitted January 19, 2004; accepted for publication February 2, 2004

Abstract—The review presents the results of optical studies of the fundamental physical characteristics of InN, the material which remains the least studied among nitrides of Group-III elements. The results of early optical studies of InN are analyzed and compared with recent data. New experimental facts reported in the review refer to hexagonal single-crystal epitaxial InN layers with an electron concentration of $(1–2) \times 10^{18}$ to 6×10^{20} cm^{-3}, which are grown by molecular beam epitaxy (MBE) and metal-organic vapor-phase epitaxy (MOVPE) on Al_2O_3 substrates. The aim of this review is to make a joint analysis of optical spectra (absorption, photoluminescence (PL), PL excitation, and photomodulated reflection) near the fundamental band gap. Furthermore, basic structural and electrical characteristics that have been obtained by a whole range of techniques are given for epitaxial layers of hexagonal InN. The principal result of recent studies is that the hexagonal InN crystal is a narrow-gap semiconductor with a band gap of 0.65–0.7 eV. Previously, the band gap of this material was considered to be 1.89 eV. It is shown that the Burstein–Moss effect accounts for the strong difference between the band gap and the optical absorption threshold in InN samples with a high concentration of electrons. The small value of the band gap of hexagonal InN is confirmed by optical studies of $In_xGa_{1-x}N$ solid solutions at high concentrations of In. Theoretical calculations of the band structure of hexagonal InN crystals are briefly reviewed. © *2004 MAIK "Nauka/Interperiodica".*

TABLE OF CONTENTS

1063-7826/04/3808-0861$26.00 © 2004 MAIK "Nauka/Interperiodica"

1. INTRODUCTION

Recently, indium nitride has attracted considerable attention both in view of its use in heterostructures based on GaN in the system of AlN–GaN-InN solid solutions and by itself, as a material for various semiconductor devices [1–3].

1.1. History of the Problem

Synthesis conditions of InN layers are very unfavorable because of the low dissociation temperature of the material [4]. The pronounced lattice mismatch between InN and single crystals of sapphire, which are the most appropriate substrates, also causes imperfection of the epitaxial layers obtained. As a result, it has long been possible to grow only defective layers, in which the concentration of free electrons exceeded 10^{20} cm^{-3}. As is now clear, optical studies of such InN crystals require careful analysis of experimental data in a wide range of energies, since the threshold of interband optical transitions, derived from the absorption coefficient, does not coincide with the band gap. In early studies, this circumstance was almost completely ignored. Mainly for this reason, overestimated (by nearly a factor of 3) widths of the band gap E_g were obtained (1.9–2.05 eV [5–8]) and then appeared in reference books.

Analysis of previously published data in terms of modern knowledge reveals facts that cast doubt on the correctness of the above value of the band gap of InN. Some of these facts are presented below.

Until recently, there were no published data on photoluminescence (PL) from InN; however, absorption and PL spectra of $In_xAl_{1-x}N$ solid solutions at $x \approx 0.47$ were used in [9] to estimate the band gap of such a solid solution to be $E_g \approx 1.7$ eV, which is considerably lower than the known reference values for InN.

In addition, PL bands at 1.7–2.2 eV have been observed in $In_xGa_{1-x}N$ solid solutions at $x = 0.35$–0.4 [10–12]. Such a position of the interband PL bands can hardly be accounted for if the band gap of InN is taken from reference data.

Finally, mention should be made of a study [13] in which the absorption edge of single-crystal InN films grown by plasma-assisted molecular beam epitaxy (PAMBE) was observed in the range 1.1–1.5 eV.

Nevertheless, the above facts have not been critically comprehended. The only study [14] in which it was assumed, on the basis of an analysis of absorption spectra of $In_xGa_{1-x}N$ solid solutions with $0 < x < 0.42$, that InN may have an optical absorption threshold considerably below 2 eV remains unknown to a wide circle of readers, because it was published only in conference proceedings.

As crystalline InN still remains the least studied among nitrides of Group-III elements, it seems of interest to describe in brief the history of the synthesis and studies of this material. A detailed description of InN synthesis by PAMBE, MOMBE, MOVPE, and RF-MBE techniques can be found in reviews [15–17]. We refer the reader to these publications and only schematically outline here the main stages of the development of the synthesis technology.

The modern technology of the synthesis of InN crystals originates from the first half of the 1970s; at the same time a more detailed study of their physical properties was begun. In the first stage of the investigations, the main method used to obtain InN films was reactive sputtering of an indium anode (target) heated by an electron beam. The chemical reaction proceeded in a flow of nitrogen activated with an electric discharge in a hollow cathode. Quartz, sapphire, or glass served as substrates for the films that were formed [5, 18, 19]. The resulting polycrystalline films of a wurtzite modification of InN were characterized by a high concentration of electrons (>10^{20} cm^{-3}), which probably resulted from a slow growth rate, low (room) substrate temperature, and insufficiently good vacuum.

The most complete study of the optical properties of films of this kind was performed in [5]. We will now discuss the results of this study in more detail. The threshold of interband absorption in such films with an electron concentration of 3×10^{20} cm^{-3} was found to be 2.05 eV. Noteworthy is the unusual energy dependence of the absorption coefficient. The corresponding curve is V-shaped: the transparency of the film is the highest at $\hbar\omega \approx 1.2$–1.3 eV and steeply decreases when the photon energy decreases or increases. Such a behavior of the absorption coefficient was accounted for in [5] in terms of two different mechanisms: absorption by free carriers in the low-energy part of the spectrum and interband transitions at high energies.

The increase in the absorption coefficient from the minimum value of 6×10^3 cm^{-1} at $\hbar\omega \approx 1.2$–1.3 eV to 2×10^4 cm^{-1} in the range of low energies at $\hbar\omega \approx 0.8$ eV was attributed in [5] to a rise in the absorption by free carriers. The plasma resonance revealed in the reflectance spectrum at $\hbar\omega \approx 0.6$ eV confirmed this interpretation and indicated that the transmission of a film is indeed strongly modified by plasma reflectance. Using data on plasma reflectance and on the interference pattern in the range of transparency, the authors of [5] found the effective electron mass for InN to be $m_e = 0.11m_0$. Their further conclusions were drawn on the assumption that the shift of the optical absorption edge by the Burstein–Moss effect [20] does not exceed 0.1 eV. Such a small Burstein–Moss shift apparently conflicts with the high carrier concentration established on the basis of the plasma reflection observed. Therefore, to bring to agreement the observed position of the absorption threshold at about 2 eV, the high electron concentration of 3×10^{20} cm^{-3}, and the effective mass $m_e = 0.11m_0$, the authors of [5] assumed that there are side minima in the conduction band that lie below the minima at the $\mathbf{\Gamma}$ point.

However, if we assume that there are no side minima below that at the $\mathbf{\Gamma}$ point, then the shift of the edge of

interband optical transitions by the Burstein–Moss effect at a carrier concentration of 3×10^{20} cm^{-3} and effective mass $m_e = 0.11m_0$ should be no less than 1.4 eV. As a consequence, such an estimate would give a considerably narrower "true" band gap at room temperature, specifically, 0.55–0.60 eV. However, this possibility was not even considered at that time as a possible interpretation of the experimental results.

Later, our understanding of the electronic structure of InN was also determined by the results obtained in studies of the optical absorption edge [6, 7]. It is the widely cited results of [7] that served as a basis for the conclusion that the band gap is within the range 1.9–2 eV. The first of these two papers reported that InN films with an electron concentration of 2×10^{16}–1×10^{17} cm^{-3} were obtained by RF sputtering of indium targets preliminarily enriched with nitrogen [6]. In [7], a room-temperature electron mobility of 2700 cm^2/(V s) and a band gap of about 1.89 eV were reported for these samples. It is noteworthy that such electron concentrations and mobilities in InN were not be achieved in any later studies. The fact that such record characteristics for a film with an electron concentration of 10^{17} cm^{-3} [7] contradict the observed absorption spectrum remained unnoticed. This spectrum practically coincided with the spectrum [5] for a material with an electron concentration of 3.3×10^{20} cm^{-3}. This coincidence primarily refers to the plasma reflection edge in both spectra in the same spectral range, which indicates that the carrier concentration was determined in [7] with an error of at least three orders of magnitude. However, the authors disregarded this inconsistency in the experimental data.

1.2. Advances in Synthesis Techniques

Success in studies of InN has primarily been achieved through improvement of the synthesis technology, which, however, has not been as a fast as desired because of a number of fundamental difficulties. Among them are the following:

(i) the low dissociation temperature of InN (500°C [21], 550°C [22], and 630°C [23]), which is determined by the relatively low In–N bonding energy and depends on the external pressure of the N vapor on the InN surface;

(ii) the fast rise in the equilibrium pressure of N_2 when the growth temperature T_S is raised, which begins at 470°C according to theoretical predictions [24] or at 450°C, as recently established experimentally in a study of the evaporation of InN in a vacuum [25], and results in the fact that the film surface is rapidly depleted of nitrogen; and, finally,

(iii) the low pyrolitic efficiency of ammonium NH_3 at low growth temperatures, which is a critical factor for metal-organic vapor-phase epitaxy (MOVPE). Moreover, the surface mobility of atoms decreases at low temperatures, which makes the growth of high-quality films problematic.

Like films of other nitrides of Group-III elements, InN films are grown on substrates made of foreign materials. In this case, it is impossible to find a material that is well lattice-matched with InN and has about the same thermal expansion coefficient. Under these conditions, the nitridation of the substrate, the formation of a buffer layer, and the initial stage of the growth process have a very strong effect on the perfection of a heteroepitaxial InN film, as do such parameters as the growth temperature T_S, the In/N flux ratio, and the growth rate. Compared with other materials, (0001) sapphire (Al_2O_3) substrates are more frequently used for heteroepitaxy of InN because they have a hexagonal symmetry and are readily available. In addition, (111) and (100) Si substrates are used, but the quality of the resulting material is low because of the mixing of cubic and hexagonal phases of InN [26]. Attempts have also been made to grow cubic InN on (100) GaAs substrates with an InAs buffer layer [27]. However, even with a well-formed GaN layer as a buffer, the lattice mismatch is rather strong (~12%), which leads to the formation of structural defects because of the relaxation of elastic stresses.

Metal-organic vapor-phase epitaxy was not used to grow InN before 1989, when it was first employed in combination with RF activation of the gas N_2 to deposit InN films onto sapphire at growth temperature $T_S \approx$ 500°C [28].

Later, this technique was modified [29–31] both by using postgrowth annealing at 450–550°C and by improving the technology of substrate nitridation, which yielded InN films with better structural properties. However, the electrical and optical parameters of these films, such as the electron concentration (5×10^{19} cm^{-3}) and optical absorption threshold (~1.97 eV), remained at the level of characteristics observed for films obtained by means of plasma sputtering.

Information about single-crystal InN films grown by the conventional MOVPE technique appeared only in 1989 [14]. The use of a high partial pressure of NH_3 in MOVPE reactors at low or atmospheric pressure made it possible to raise the growth temperature T_S to 550°C and thereby improve the efficiency of ammonia pyrolysis [32, 33]. As a result, it became possible to deposit onto sapphire, without any additional excitation of nitrogen, InN films with a somewhat reduced concentration (~5×10^{19} cm^{-3}) and a higher mobility (up to 270 cm^2/(V s) at room temperature) of electrons.

A further increase in the T_S resulted in an improved uniformity of epitaxial InN layers [34], and the use of intermediate GaN layers grown at high temperature on sapphire yielded a higher room-temperature electron mobility (700 cm^2/(V s)) with a comparatively good quality of the films and an electron concentration not exceeding ~5×10^{19} cm^{-3}.

Considerable progress in synthesis was made when molecular beam epitaxy with plasma activation of nitrogen (plasma-assisted molecular beam epitaxy, PAMBE) was employed [36]. Several research groups used various methods for the activation of nitrogen, including electron-cyclotron resonance [13, 37], inductively coupled high-frequency discharge [38, 39], and even a combination of a metal-organic source of In and high-frequency activation of N_2 [40], to obtain epitaxial InN layers with an electron concentration of (3–9) $\times$ 10^{18} cm^{-3}. In this case, the room-temperature electron mobility was comparable with, or even exceeded, that in samples grown by MOVPE: 500 $cm^2/(V\ s)$ [40], 800 $cm^2/(V\ s)$ [38], 820 $cm^2/(V\ s)$ [39], and 1700 $cm^2/(V\ s)$ [13]. With various buffer layers (AlN [38] and InN [13, 37, 39]) and different nitridation procedures used, it was found that the PAMBE technique applied at growth temperatures within the range 470–550°C shows great promise. The improvement of the electrical characteristics of the samples was accompanied by an increase in their structural perfection, as indicated by X-ray diffraction analysis [41].

Modern technologies [38, 42, 43] made it possible to obtain *n*-InN crystals with an electron concentration of about (1.0–1.5) $\times$ 10^{18} cm^{-3}. Progress in the synthesis of comparatively high-quality single-crystal InN films also made it possible to obtain new information about the band gap in InN [44–47].

In samples of the new generation, interband PL was observed for the first time in these crystals [44, 45, 48]. The interband origin of this PL is confirmed by the variation of the band shape with the electron concentration and the sample temperature. A comparison of the parameters of PL obtained for InN crystals with data for doped GaAs and GaN crystals demonstrated that the PL observed is due to interband recombination of free electrons and photoexcited holes [15, 44, 45, 48]. A joint analysis of interband PL and absorption spectra established that InN is a narrow-gap semiconductor with a band gap of about 0.65–0.7 eV. This result was also confirmed in studies of $In_xGa_{1-x}N$ solid solutions at high indium concentrations [15, 45, 48, 49].

1.3. Plan of the Review

In Section 2 of the review we consider experimental and theoretical data on the dynamics of the crystal lattice of hexagonal InN. Experimental data on Raman scattering and IR absorption and reflection in the spectral range of lattice vibrations form a basis for model calculations of phonon dispersion curves over the entire Brillouin zone and of the phonon density-of-states function. We demonstrate that Raman spectroscopy is a useful tool for determining the quality of InN samples.

Section 3 of the review is devoted to electronic states in crystalline InN. It summarizes the principal results of theoretical calculations of the electronic spectra of InN and data obtained in studying the dielectric function in a wide range of energies. In addition, we describe in this section a new approach to the problem of determining the band gap from optical data. The approach developed includes, together with an analysis of transmission and reflectance spectra, a study of PL and its excitation spectra. We analyze the shape of the interband PL band in relation to temperature and carrier concentration and discuss the dependence of the band gap on the free-carrier concentration. Analysis of the shape of the interband PL band for samples of varied quality shows that InN crystals show a significant spatial nonuniformity of electron concentration distribution, which should also be taken into account in determining their parameters.

Section 4 of the review is devoted to studies of $In_xGa_{1-x}N$ solid solutions with a high and intermediate content of In ($0.40 < x < 1$). This section discusses the principal results of optical studies of the band gap of solid solutions and its dependence on composition. Vibrational spectra of solid solutions with widely varying compositions are also presented.

2. VIBRATIONAL SPECTROSCOPY OF HEXAGONAL InN

The phonon spectrum is a fundamental characteristic of a crystal, which determines the thermodynamic properties of a material, kinetic properties of carriers, and optical properties in the IR spectral range. Such parameters of a phonon spectrum as the phonon density-of-states function and phonon dispersion curves reflect specific features of the crystal structure and interatomic interactions and provide important information about the dynamics of the crystal lattice. As a rule, information about the phonon dispersion curves and the phonon density-of-states function is obtained from neutron scattering experiments. However, InN single crystals with the dimensions necessary for these experiments have not been synthesized until now.

Another valuable source of information about the dynamics of the crystal lattice is Raman spectroscopy. Studies of first- and second-order Raman spectra yield information about phonon energies both at the center of the Brillouin zone and at its boundaries. In addition, controlled introduction of defects into the samples studied in turn provides an opportunity to reconstruct on the basis of Raman spectra another important characteristic of the phonon spectrum, the phonon density-of-states function. A major advantage of Raman spectroscopy over neutron experiments is the possibility of obtaining information for objects only several tens of micrometers in size. Together with Raman spectroscopy, IR spectroscopy is also one of the techniques most frequently used to study long-wavelength optical phonons.

2.1. Phonons in Hexagonal InN

2.1.1. Selection rules. Like other Group-III nitrides, InN can crystallize to give a structure of wurtzite or

sphalerite type (zinc blende). Hexagonal InN crystallizes into a structure of wurtzite with four atoms in the unit cell and belongs to the C_{6v}^4 ($C6_3mc$) space group. According to group-theory analysis at the Γ point, the phonon modes in hexagonal InN are characterized by the following irreducible representations:

$$\Gamma_{ac} + \Gamma_{opt} = (A_1 + E_1) + (A_1 + 2B_1 + E_1 + 2E_2).$$

Among optical phonons, the modes of symmetry A_1 and E_1 are Raman- and IR-active, modes of symmetry E_2 are only Raman-active, and modes of symmetry B_1 are the so-called silent modes; i.e., they are observed neither in Raman nor in IR spectra [50].

Thus, six optical modes may be observed in a first-order Raman spectrum: A_1(TO), A_1(LO), E_1(TO), E_1(LO), E_2(high), and E_2(low).

Table 1 describes the scattering geometries in which optical phonon modes of various symmetries can be observed. The Porto notation system is used in the table and below to describe the scattering geometry, e.g., $z(xy)\bar{z}$. The symbol z before the parenthesis indicates the direction of propagation of the exciting light, and the symbol $\bar{z}$ after the parentheses, the direction in which scattered light is observed. In the parentheses, the polarization of the exciting (x) and scattered (y) light is indicated. The direction z is chosen parallel to the hexagonal axis, and x and y are mutually orthogonal and oriented in an arbitrary way in the plane perpendicular to the direction z.

2.1.2. Principal experimental results. The phonon spectrum of InN was first studied using Raman and IR spectroscopies on hexagonal films grown on (0001) sapphire [51–53]. In these studies, frequencies of some of the six long-wavelength optical phonons in hexagonal InN, which can be observed experimentally, were determined. However, these first studies already demonstrated discrepancies in the measured phonon frequencies and contradictions in determining the symmetry of the phonons. The frequencies of the phonon modes, determined in [51–53], and the distribution of the modes over types of symmetry are presented in Table 2.

To obtain as full information as possible from Raman and IR measurements, InN samples with different orientations of the optical axis relative to the substrate plane were studied in [54, 55]. Undoped and Mg-doped InN layers of thickness 0.1–0.7 μm were grown by MBE on (0001) and $(1\bar{1}02)$ α-Al_2O_3 substrates [61, 62]. According to the results of X-ray diffraction analysis, all the InN layers grown contained only the hexagonal phase. When a (0001) sapphire substrate was used, the optical axis of the InN layer was perpendicular to the substrate surface, whereas in deposition of InN onto a $(1\bar{1}02)$ sapphire substrate, the hexagonal axis of the layer was parallel to the substrate plane and had a fixed direction for each sample. Thus, with a set of samples composed of InN layers with different orientations of the hexagonal axis relative to the substrate plane, it was possible to observe all the six optical phonons allowed in Raman spectra and to classify them by types of symmetry.

Table 1. Selection rules for optical phonons in a wurtzite crystal lattice

Scattering geometry	Allowed modes
$z(yy)\bar{z}$	E_2, A_1(LO)
$z(xy)\bar{z}$	E_2
$y(zz)\bar{y}$	A_1(TO)
$y(xz)\bar{y}$	E_1(TO)
$y(xx)\bar{y}$	E_2, A_1(TO)

Table 2. Frequencies of optical phonons (cm^{-1}) in hexagonal InN at 300 K

Symmetry of a vibration	E_2(low)	A_1(TO)	E_1(TO)	E_2(high)	A_1(LO)	E_1(LO)	B_1(low)	B_1(high)
Experiment								
[51]				495	596			
[52]				491	590			
[53]	87	480	476	488	580	570	200	540
[54, 55]	87	447	475	488	586	593	220	565
[56]		443	477	491	590			
[57]		445	472	488	588			
[58]	88	440		490	590			
Calculation								
[57]	104	440	472	483			270	530
[58]	93	443	470	492	589	605	202	568
[59]	83	443	467	483	586	595	225	576
[60]	85	449	457	485	587	596	217	566

The Raman spectra were measured at room and low temperatures in a backscattering geometry with excitation energies in the range 1.83–2.54 eV.

The undoped samples were of n type with an electron concentration of ~10^{20} cm^{-3}. The introduction of Mg during growth made it possible to lower the carrier concentration in n-InN to ~10^{19} cm^{-3}.

Figures 1 and 2 show as an example Raman spectra of undoped n-InN samples grown on sapphire substrates of two orientations, which were measured at an excitation energy of 2.54 eV. A thorough analysis of the first-order Raman spectra obtained at room and cryogenic temperatures revealed that the polarized Raman spectra conform well to the selection rules for the wurtzite structure (see Table 1). The only exception is

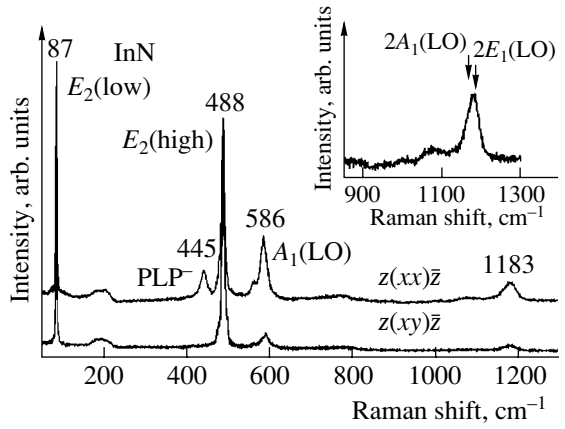

Fig. 1. Polarized room-temperature first-order Raman spectra of a nominally undoped InN sample grown on a (0001) sapphire substrate. Excitation energy E_{exc} = 2.54 eV; inset: second-order spectrum. Taken from [54].

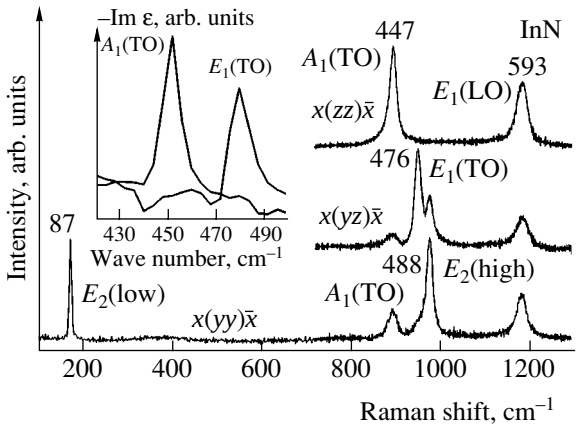

Fig. 2. Polarized room-temperature first-order Raman spectra of a nominally undoped InN sample grown on a $(1\bar{1}02)$ sapphire substrate. Excitation energy E_{exc} = 2.54 eV; inset: the imaginary part of the contribution of A_1(TO) and E_1(TO) phonons to the dielectric constant of the lattice; the result was obtained by a Kramers–Kronig transformation of experimental data on reflectance at different orientations of the electric field vector **E** of the electromagnetic wave with respect to the **c** axis: **E** ∥ **c**, A_1(TO); **E** ⊥ **c**, E_1(TO). Taken from [54].

the line at 593 cm^{-1}, which was only observed in the forbidden-scattering geometry $x(zz)\bar{x}$ (Fig. 2); this line was attributed to the phonon of symmetry E_1(LO). As an indication that the above mode was correctly attributed to the phonon of symmetry E_1(LO), it was noted that the value of its energy doubled coincides with the high-frequency boundary of the two-phonon spectrum (Fig. 1, inset). The frequencies of all the six Raman-active modes in InN [54, 55] and their distribution over types of symmetry are listed in Table 2.

According to the selection rules in Table 1, the high-intensity lines in the Raman spectra, with wave numbers in the range 580–596 cm^{-1}, were attributed to unscreened A_1(LO)- and E_1(LO)-phonon modes of hexagonal InN. At the same time, it should be noted that, as a rule, the nominally undoped InN films used in this and other studies had a free-electron concentration exceeding 10^{19} cm^{-3}. In this case, the interpretation of a spectrum in the range of longitudinal optical vibrations and identification of the absolute spectral position of LO phonons require that the interaction of the LO phonons with collective excitations of free carriers be taken into account.

2.1.3. Phonon–plasmon modes. The spectrum of phonon–plasmon excitations is generally given by the solution to the equation [63]

$$1 + \chi_{\mathbf{q}}^{inter}(\omega) + \chi_{\mathbf{q}}^{intra}(\omega) + \frac{\omega_{LO}^2 - \omega_{TO}^2}{\omega_{TO}^2 - \omega^2} = 0, \qquad (1)$$

where $\chi_{\mathbf{q}}^{inter}(\omega)$ and $\chi_{\mathbf{q}}^{intra}(\omega)$ are the contribution of interband transitions and that of free carriers to the dielectric susceptibility of a crystal, respectively, and ω_{LO} and ω_{TO} are the frequencies of longitudinal and transverse optical vibrations. The dielectric susceptibility of the crystal lattice $\chi_L(\omega)$ is related to other parameters of the crystal by

$$\frac{\chi_L(\omega)}{1 + \chi_{\mathbf{q}}^{inter}(\omega)} = \frac{\omega_{LO}^2 - \omega_{TO}^2}{\omega_{TO}^2 - (\omega)^2}. \qquad (2)$$

For wide-gap crystals in which the energy range of interest is substantially narrower than the band gap, $\hbar\omega \ll E_g$, the frequency dependence of the interband contribution to the dielectric susceptibility can be disregarded and it can be assumed that $[1 + \chi_{\mathbf{q}}^{inter}(\omega)] = \varepsilon_\infty$. In the case of crystalline InN, several factors must be taken into account. A specific feature of crystalline InN is that the free-electron concentration in this material reaches high values (which are characteristic of semimetals) and may vary widely between different samples. As a consequence, the plasmon energy may reach values comparable with the band gap.

In the energy range limited, on one side, by the energy of an optical phonon and, on the other, by the optical absorption threshold, the interband contribution to the dielectric susceptibility $[1 + \chi_{\mathbf{q}}^{inter}(\omega)]$ varies considerably. In this case, the threshold of optical transitions may shift significantly to higher energies, as shown in the next section of the review, which, in turn, results in the fact that the interband contribution to the dielectric susceptibility depends on the free-carrier concentration. Therefore, in order to accurately calculate the spectrum of phonon–plasmon modes, it is necessary to take into account the dependences of both the electronic contributions to the dielectric susceptibility on the free-

electron concentration. Simplified formulas that disregard the frequency dependence of $[1 + \chi_{\mathbf{q}}^{inter}(\omega)]$ can only give a rough estimate.

In the case of doped crystals, the LO phonon and a plasmon give way to two mixed plasmon–LO-phonon excitations (PLP) designated as $PLP^{+}(q)$ and $PLP^{-}(q)$ [64], whose frequencies strongly depend on the free-carrier concentration. When the plasmon frequency is low compared with the LO-phonon frequency (not very high free-carrier concentration), PLP^{-} modes show a behavior typical of a plasmon, while the PLP^{+} modes behave typically like a phonon. In the opposite case (high free-carrier concentration), the PLP^{-} modes exhibit a phonon-like behavior and their frequencies approach the frequency of the TO phonon, which means that the electric field of the LO phonon is nearly completely screened by free carriers. In turn, the PLP^{+} mode shifts to higher frequencies and becomes plasmon-like. Both branches have been observed, for example, in GaN crystals [65–67].

At the same time, there are examples where a band appears in the Raman spectra of samples with high carrier concentration, e.g., *n*-GaAs [64], at the frequency of an unscreened LO phonon. As a rule, two mechanisms are suggested to account for such an unusual behavior of the phonon modes in Raman spectra: (i) the existence of a thin carrier-depleted surface layer as a result of band bending near the surface and (ii) nonconservation of the wave vector in scattering and the resulting appearance of mixed modes with large wave vectors in the Raman spectra.

In [56], the existence of a carrier-depleted surface layer in InN was ruled out on the basis of an analysis of ellipsometric data. Thus, the band at the frequency of an unscreened LO phonon in InN with a high free-electron concentration can be understood if we take into account the scattering of virtual electron–hole pairs on structural defects of the crystal lattice, which, in the end, leads to violation of the wave-vector conservation law. In this case, LO phonons with wave vectors that exceed the Landau damping threshold appear in the spectrum, and the cross section of the Raman spectra is proportional to the defect concentration [68]. Figure 3 shows the example of spectra of nominally undoped *n*-InN films with various electron concentrations, which are associated with structural defects of the lattice. It is clearly seen that the intensity of the LO band grows as the electron concentration increases.

For large wave vectors, the PLP^{-} mode shifts at a given free-carrier concentration to frequencies higher than that of the TO phonon and approaches the frequency of an unscreened LO phonon from below [64]. Thus, we may consider that the spectral position of the phonon modes in the range 580–596 cm^{-1} does correspond to unscreened phonons of symmetry $A_1(LO)$ and $E_1(LO)$.

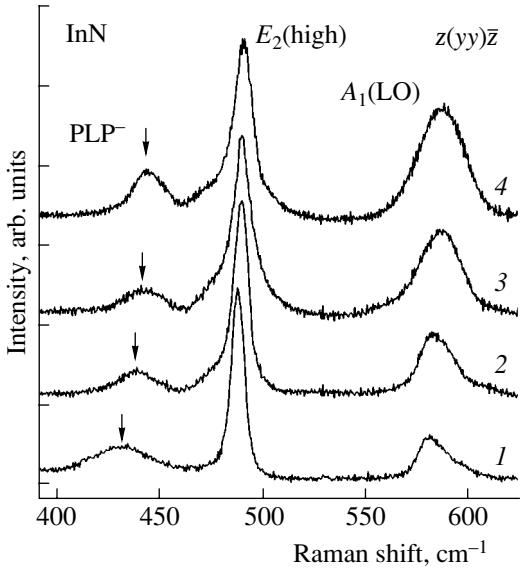

Fig. 3. Raman spectra of undoped InN samples with different electron concentrations (according to Hall measurements) *n*: (*1*) 1×10^{19}, (*2*) 5×10^{19}, (*3*) 1×10^{20}, and (*4*) 2×10^{20} cm^{-3}.

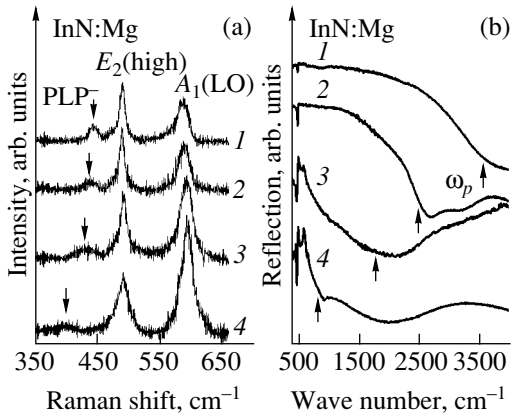

Fig. 4. (a) Raman and (b) IR reflectance spectra of InN:Mg epitaxial layers with different free carrier concentrations *n*: (*1*) 2×10^{20}, (*2*) 1×10^{20}, (*3*) 5×10^{19}, and (*4*) 1×10^{19} cm^{-3}. Taken from [54].

In addition to the two modes E_2 and $A_1(LO)$ allowed by the selection rules for the configuration $z(xx)\bar{z}$ (Fig. 1), one more band is observed in the Raman spectrum at a frequency of 445 cm^{-1}. A study of the temperature dependence of the intensity of this band made it possible to rule out assigning it to a second-order spectrum. At the same time, a study of InN samples with different carrier concentrations revealed that this band is shifted to lower frequencies when the free-electron concentration decreases (Figs. 3, 4a). This observation was the reason why this band was attributed to excitations that belong to the lower branch of mixed plasmon–LO-phonon modes with small wave vectors. This interpretation is confirmed by the fact that the line asso-

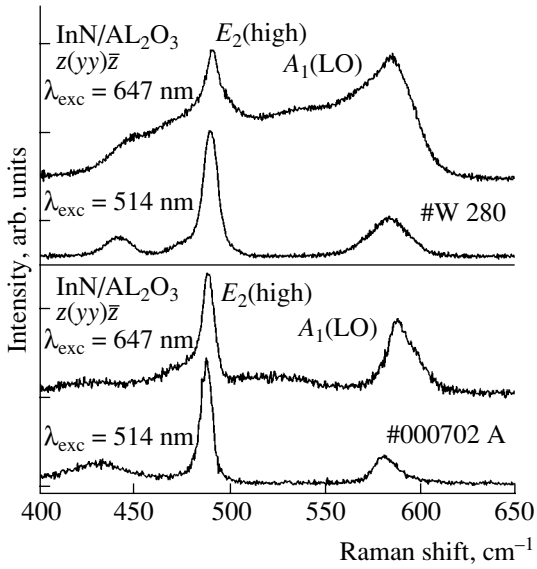

Fig. 5. Raman spectra of two undoped InN samples of unequal quality at two excitation energies.

ciated with plasma oscillations in the IR reflection spectrum shifts from 3500 to 800 cm^{-1} as the acceptor concentration increases (Fig. 4b).

One more band has been observed in the Raman spectra of some InN samples on the low-frequency wing of the phonon line A_1(LO) at 561 cm^{-1} (Fig. 1). At present, there is no definitive interpretation of this band in the literature. However, its position in the region of high density of phonon states (see below) indicates that phonons with wave vectors $q \neq 0$ are involved in this case.

In [54, 55], IR reflectance spectra were measured in the spectral range 200–4000 cm^{-1} on InN samples grown on (0001) and $(1\bar{1}02)$ α-Al_2O_3 substrates at a beam incidence angle of 20°. The phonon frequencies of 448 cm^{-1} for A_1(TO) and 476 cm^{-1} for E_1(TO), which were obtained by means of a Kramers–Kronig analysis, agree well with the results of Raman measurements (see inset in Fig. 2 and Table 1). Thus, all six Raman-active modes in InN, $1A_1(TO) + 1A_1(LO) + 1E_1(TO) + 1E_1(LO) + 2E_2$, were recorded for the first time in these studies, and their symmetry was determined. The fact that five of these were measured on the same InN sample grown on a $(1\bar{1}02)$ α-Al_2O_3 substrate makes it possible to obtain a self-consistent pattern of the behavior of optical phonons in InN under various effects (deformation, temperature, etc.).

The vibrational properties of hexagonal InN were also studied in [57, 58] by means of Raman spectroscopy and IR-spectroscopic ellipsometry [56]. The frequencies of optical phonons of varied symmetry obtained in these studies are also listed in Table 2. The difference in the frequencies for phonons of the same symmetry can, in all probability, be attributed to different residual strains in InN layers, since all the films were grown on foreign substrates (sapphire, silicon, etc.). It may be assumed that the effect of residual strain on the phonon frequencies is negligible in [57], where Raman spectroscopy was applied to a study of thick oriented InN wafers. The coincidence of the frequencies of phonons with E_2(high) symmetry, which are the most sensitive to strain, in [54, 55, 57] indicates that the data presented in [54, 55] for the six optical phonons were also obtained on InN layers with an insignificant residual strain. Apart from the experimentally recorded frequencies of optical phonons, Table 2 also lists data for zone-center optical phonons in hexagonal InN, which were calculated from first principles [59] in terms of the modified valence-force model [58] and in terms of the perturbation theory with the use of an artificial density functional [60]. It can be seen that the theoretically calculated phonon frequencies agree satisfactorily with the experimental data.

In order to study the structural homogeneity of InN layers across their thickness, different energies of exciting photons are used in Raman scattering measurements [40]. According to the estimates of [56], the depth of the layer probed when Raman spectra are excited with photons of energy 2.54 eV (514-nm wavelength) does not exceed 0.2 μm. The use of exciting light with a photon energy of 1.9 eV (647 nm), instead of 2.54 eV, provides a deeper penetration of light into InN. Figure 5 shows an example of Raman spectra of two samples, which were measured using the above two energies of exciting photons. It can be seen that the two spectra shown in the lower panel differ only slightly, which indicates that the InN layer under study is homogeneous across its thickness. At the same time, the strong difference between the spectra in the upper panel indicates that the number of structural defects increases away from the surface into the sample. It is noteworthy that, when the exciting photons have an energy of 1.9 eV, the intensity of the Raman spectrum of InN increases by more than a factor of 10. As the band gap of the InN samples studied is close to 0.7 eV, this effect cannot be attributed to a resonance enhancement of the Raman scattering at excitation energies close to the band gap. This effect has yet not been explained and requires further research. However, the strong increase in the intensity of Raman scattering undoubtedly makes it possible to study very thin InN layers, e.g., quantum wells.

Raman spectroscopy can also yield information about the interface between the InN layer and the sapphire substrate. For this purpose, it is necessary to analyze the Raman scattering on an InN layer in the backscattering geometry, with observation through a transparent sapphire substrate. Figure 6 shows spectra obtained under backscattering conditions from the upper part of the InN layer and from that adjacent to the substrate. It can be seen that the InN layer adjacent to the substrate is more defective, which is indicated by the higher intensity of the band lying at the frequency

of an unscreened LO phonon. As already mentioned, the appearance of this band is due to the violation of the wave-vector conservation law as a result of the scattering of virtual electron–hole pairs on structural defects of the crystal lattice. The intensity of this band grows as the number of structural defects increases.

The good conformity of the polarized Raman spectra of InN with the selection rules for the wurtzite structure is an indication of the satisfactory quality of the samples examined. In [54, 55], the anisotropy of the static dielectric constant was estimated for InN on the basis of the Liddan–Sax–Teller relation ($\varepsilon_0/\varepsilon_\infty = \omega_{LO}^2/\omega_{TO}^2$) and on the assumption that, at frequencies substantially exceeding the frequency of lattice vibrations, the dielectric constant is isotropic and equal to $\varepsilon_\infty = 8.4$ [69]. The anisotropy of the static dielectric constant of InN was also estimated in [69]. For the ordinary and extraordinary directions these dielectric constants were found to be $\varepsilon_{\perp 0} = 13.4$ and $\varepsilon_{\parallel 0} = 14.4$, respectively. It should be noted, however, that other values of ε_∞, 5.8 [53] and 6.7 [56], are also available in the literature. That is why the values of $\varepsilon_{\perp 0}$ and $\varepsilon_{\parallel 0}$ cannot be considered definitively established. However, the ratio of the static dielectric constants is independent of ε_∞. The anisotropy of the static dielectric constant for InN was estimated to be $\varepsilon_{\perp 0}/\varepsilon_{\parallel 0} = 0.91$.

2.1.4. Principal characteristics of the vibrational spectrum of the crystal lattice of InN. In first-order Raman spectra, only phonons with $q \approx 0$ are allowed. The selection rules that follow from the momentum conservation law for second-order Raman scattering require that the sum of the wave vectors q of two phonons involved in scattering be approximately zero. Thus, the restrictions on the wave vectors of phonons involved in two-phonon scattering are less stringent then those for the single-phonon process, and phonons from the entire Brillouin zone can be involved. Consequently, two-phonon spectra may contain information about the density-of-vibrational-states function and about the behavior of phonon dispersion curves. It can be seen in the inset in Fig. 1 that mainly longitudinal phonons predominate in the second-order spectrum of InN. The band centered near the high-energy edge of the second-order spectrum is very close in energy to doubled frequencies of the zone-center phonons with symmetry A_1(LO) or E_1(LO). Hence, the conclusion may be drawn that, at the boundary of the Brillouin zone, longitudinal phonons should have a lower energy than that at the **Γ** point. The contribution of phonons of symmetry E_2 and A_1(TO) to the second-order spectrum is poorly pronounced; however, it is obvious that the lower boundary of the second-order spectrum coincides with the doubled frequency of the zone-center A_1(TO) phonon. This, in turn, means that transverse phonons should have higher energies at the boundary of the Brillouin zone than those at the **Γ** point.

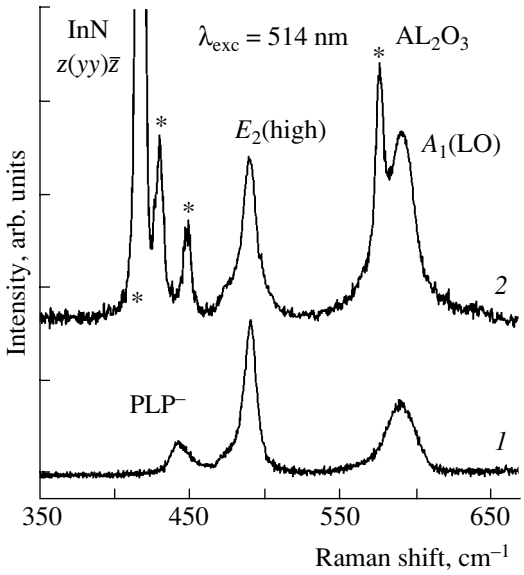

Fig. 6. Raman spectra of InN measured (*1*) from the side of the epitaxial film and (*2*) from the side of the substrate. The asterisks denote the vibrational lines of sapphire.

Important information about the width of the band gap between the regions of optical and acoustic phonons and also about the energies of silent modes of symmetry B_1 can be obtained by studying structurally imperfect InN samples. In these samples, the wave-vector conservation law is violated and, therefore, the Raman spectrum reproduces the density of vibrational states. Studies with samples of this kind made it possible to estimate the frequencies of phonons of symmetry B_1 to be 220 cm^{-1} for the lower mode and 565 cm^{-1} for the upper mode [54, 55].

The whole body of experimental data obtained made it possible to carry out model calculations of the lattice dynamics for hexagonal InN and to derive dispersion curves for acoustic and optical phonons as well as the density-of-states function. The dynamics of the InN lattice was modeled in terms of a phenomenological model based on paired interatomic potentials and the Coulomb potential in the rigid-ion approximation. The ion charges were chosen in accordance with the LO–TO splitting observed. The short-range potentials also accounted for the contributions from neighboring atoms of the second coordination sphere. The following parameters were used: the frequencies of optical phonons at the **Γ** point, which were found from first-order Raman spectra; the frequencies of silent modes, which were evaluated from spectra of structurally imperfect samples; the ion charge, whose value was determined on the basis of the experimentally observed LO–TO splitting; and published values of elastic constants.

The calculated phonon dispersion curves along the principal directions in the first Brillouin zone and the density-of-states function are shown in Fig. 7. It can be seen that the phonon spectrum of InN consists of two

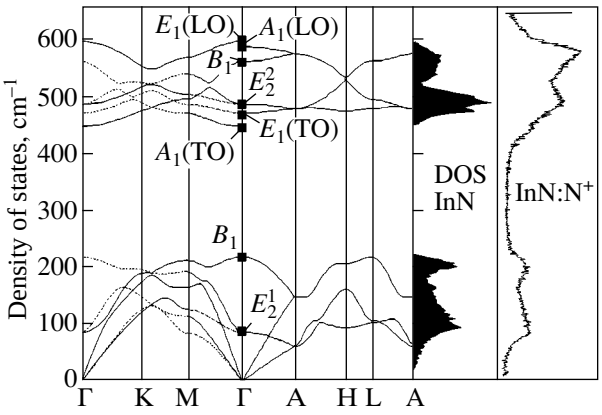

Fig. 7. Calculated dispersion curves for phonons and the density of states for hexagonal InN. For comparison, a Raman spectrum at $T = 7$ K of an InN crystal irradiated with N^+ ions is shown. Taken from [54].

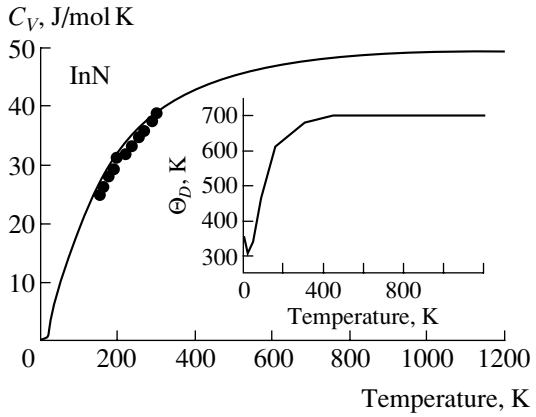

Fig. 8. Calculated (solid line) and measured (points) lattice heat capacity of InN; inset: calculated temperature dependence of the Debye temperature. Taken from [54].

regions separated by a wide gap. The low-energy region (0–230 cm^{-1}) includes three acoustic branches, a low-frequency branch B_1, and an optical branch E_2(low), while the upper region (450–600 cm^{-1}) is associated with high-frequency optical modes.

It was shown in [70] that the density of states can be reconstructed for GaN and AlN on the basis of experimental Raman spectra of single crystals with a strongly distorted crystal lattice. The same approach has been used for InN [54, 55]. MBE-grown InN samples irradiated with nitrogen ions N^+ (energy 30 keV, dose 5×10^{14} cm^{-2}) were studied. In order to exclude the temperature factor, the Raman spectra were recorded at $T =$ 7 K. As can be seen from Fig. 7, the main features of the calculated function and that obtained from the Raman spectra of the samples irradiated with N^+ are agree well in the ranges of both acoustic and optical vibrations, which suggests that the calculations of the crystal lattice dynamics for InN are correct. In later studies, first-principles calculations and those based on the modified valence-force model and perturbation theory for the artificial density functional were used to evaluate the dispersion of phonon frequencies over the entire Brillouin zone and the phonon density of states [58–60]. The data obtained agree well with the calculations [54, 55] in terms of the rigid-ion model. In contrast to AlN, the phonon spectrum of InN is on the whole similar to that of GaN [59, 70, 71]. This is not surprising as the dynamics of both the lattices is mainly determined by the motion of nitrogen atoms because of the substantial difference between the masses of the constituent cations and anions.

Analysis of the dispersion relations for acoustic and optical phonons allows important conclusions to be drawn concerning the possible anharmonic decay channels of optical phonons in InN. It was noted in [59] that three-phonon decay of the zone-center LO phonon into two LA or TA phonons with equal frequencies and opposite wave vectors is impossible for InN. This is so because $\omega_{LO} > 2\omega_{LA,\,TA}$ over the entire spectral range. Note that it is three-phonon processes of this kind that are the main decay channel of LO phonons in other III–V semiconductors. In accordance with the results obtained, it may be assumed that LO phonons in InN may decay mainly into TO phonons with large wave vectors and LA or TA phonons with large wave vectors, rather than into two acoustic phonons. Such a decay channel can affect the lifetime of LO phonons and can thereby govern the effects associated with hot phonons, which determine the transport properties of hot carriers; this is important in designing high-speed devices [59].

The calculated density of states was used to evaluate the lattice heat capacity at constant volume C_V for InN. Figure 8 shows a calculated temperature dependence of C_V, together with the experimental data on heat capacity at constant pressure C_P taken from [72]. Note that, according to [72], the difference $C_P - C_V$ can be disregarded under the atmospheric pressure. It can be seen that the results of the calculation agree well with the experimental data over the entire range of measurement temperatures. Furthermore, the Debye temperature was determined for InN as a function of temperature (Fig. 8, inset), as was done for AlN and GaN [73, 74]. The calculated estimate $\Theta_D = 580$ K at 150 K agrees well with the value $\Theta_D = 610$ K, which was obtained in experimental heat capacity measurements [72]. The calculations performed demonstrated that the Debye temperature for InN at 0 K is 370 K (note: $\Theta_D = 800$ K for AlN and 570 K for GaN [59]).

3. ELECTRONIC STATES IN InN

Until recently, there have been no experimental data that can be used to gain insight into the band structure of InN, and the available information was limited to the results of calculations. The band structure of hexagonal InN has been calculated in numerous studies [75–79]. The most difficult task in theoretical calculations of the band structure was to come to a definite conclusion

about the band gap, whose theoretically calculated width strongly depends on the choice of model. This circumstance gave no way of using the results of theoretical calculations as a criterion of correctness for experimental band gap widths.

New experimental data, which demonstrate that indium nitride should be considered a narrow-gap semiconductor, posed an additional problem associated with the violation of the so-called band-gap-common-cation (anion) rule. This rule states that the energy of the lowest-energy direct transition at the **Γ** point should decrease in a series of isomorphic crystals as the atomic number of an anion or cation increases. This rule is observed for a number of semiconductors: InAs, GaAs, and AlAs (E_g = 0.42, 1.52, and 3.13 eV, respectively), as well as the series GaSb, GaAs, GaP, and GaN (E_g = 0.81, 1.52, 2.86, and 3.3 eV). In the case of InN, the band gap, which is 0.65–0.7 eV according to new data, is narrower than the band gap of isomorphic InP (1.46 eV), and this contradicts the common-cation rule. This problem was theoretically solved only recently in [78, 79], where band gap widths of 0.8 and 0.85 eV, respectively, were obtained.

3.1. Band Structure of InN: Theory

AlN, GaN, and InN crystals are distinguished from other nitrides of Group-III elements by quite a number of physical characteristics: high ionicity, small interatomic spacings, low compressibility, high heat conductivity, and a high melting point. The band gap widths of this subgroup of nitrides also vary widely. A theoretical description of the electronic properties of nitrides of Group-III elements encounters severe difficulties because of the pronounced difference in electronic structure between their constituent atoms and those in more conventional semiconductors. Nitrogen, which is an element from the first row of the periodic table of elements, has no *p* electrons, with the result that its electron shell is small in size. As a consequence, special care should be taken to describe accurately the wave functions of electrons in the vicinity of the atomic nucleus [78]. Additional difficulties arise because of the need to take into account the hybridization of 4*d* electrons of In and 2*s* electrons of nitrogen. Moreover, the striking difference between the sizes of anions and cations and the difference between their electronegativities lead to the transfer of a considerable amount of charge from the cation to the anion and to strong ionicity of the chemical bonds that are formed.

Figure 9 shows spectra of valence bands and the lowest conduction bands of InN, which were derived in [78]. The spectra are presented in two variants: for single-electron excitations proper and for single-electron excitations taking into account self-energy corrections. The differences between these spectra approximately correspond to the still existing ambiguity of the results of calculations.

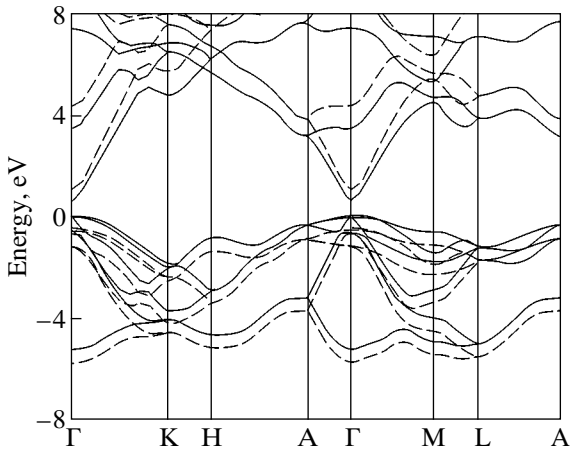

Fig. 9. Calculated band structure of InN. Taken from [78].

Taking into account the fact that the dispersion of electronic bands in crystals is, as a rule, less dependent on the details of a calculation procedure, the results of model calculations of the dielectric constant of InN obtained in [78] are of considerable interest.

The electric field of the electromagnetic wave of frequency ω, whose wave vector **k** is directed along the *z* axis, varies in the isotropic absorbing medium by the following law (see, e.g., [80]):

$$\exp i(kz - \omega t) = \exp\left\{ i\omega\left(\frac{\eta z}{c} - t\right) - \frac{\omega\kappa z}{c}\right\}, \qquad (3)$$

where *c* is the speed of light in free space. If the spatial dispersion is disregarded, the functions η and κ are functions of only the frequency $\varepsilon = 1 + \chi$, which are related to the complex dielectric constant and, accordingly, to the real and imaginary parts of the dielectric susceptibility χ of a crystal by

$$\eta^2 - \kappa^2 = 1 + \chi' \qquad (4)$$

and

$$2\eta\kappa = \chi''. \qquad (5)$$

For a hexagonal crystal, there are two different components of the dielectric-susceptibility and dielectric-constant tensors. The imaginary and real parts of the corresponding components of the dielectric-constant tensor ε are shown in Figs. 10 and 11 in a wide energy range. A characteristic feature of the imaginary part of the dielectric constant is its relatively weak energy dependence in the range from the absorption threshold to about 4 eV. As can be seen from the spectrum of electronic bands in Fig. 9, this energy range corresponds to interband transitions from the valence bands to the lowest conduction band.

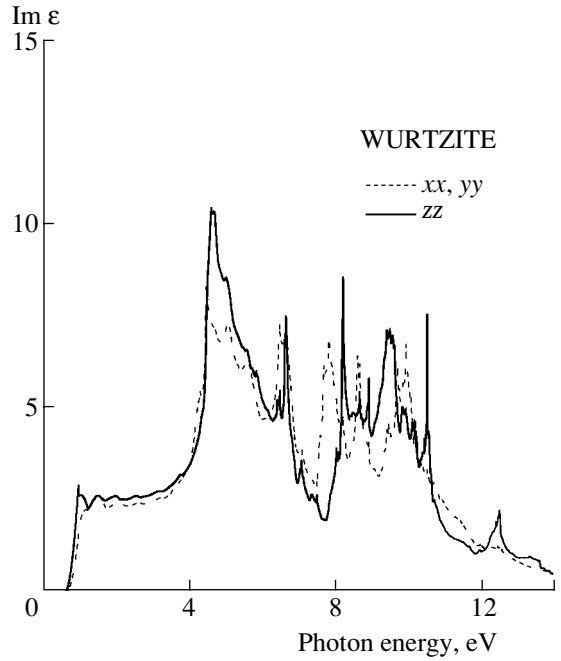

Fig. 10. Imaginary part of the dielectric constant of InN. Taken from [78].

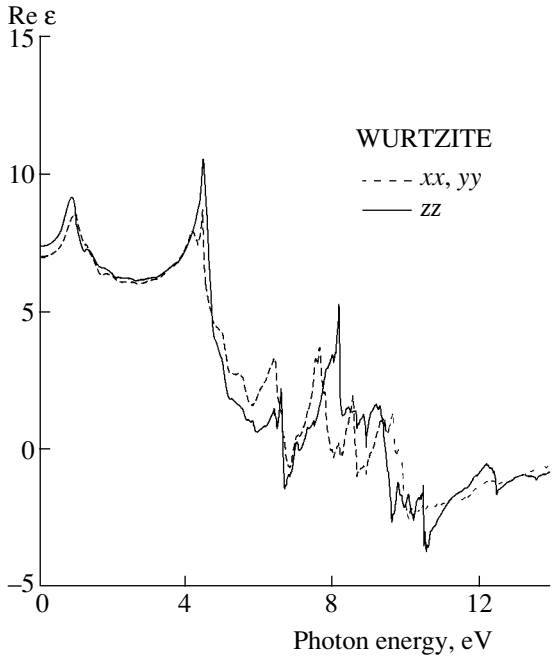

Fig. 11. Real part of the dielectric constant of InN. Taken from [78].

The decrease in the intensity $I(z)$ of the light wave because of the absorption is described by the expression

$$I(z) = I_0 \exp(-\alpha z), \quad (6)$$

where

$$\alpha(\omega) = 2\omega\kappa(\omega)/c, \quad (7)$$

and $\kappa(\omega)$ is related to the imaginary part of the dielectric susceptibility by expression (5). For comparison of the calculated results with experimental data on interband absorption, the behavior of the absorption coefficient near the threshold E_g is of interest. As follows from the last formula, the frequency dependence of the absorption coefficient mostly coincides with that for the imaginary part of the dielectric constant. The results of a calculation of the absorption coefficients in [78] in this approximation are shown in Fig. 12. This calculation disregarded the presence of free carriers in real crystals or the formation of excitonic states in crystals in the absence of free carriers.

3.2. Band Structure of InN: Experiment

Recently, the dielectric function of the nitrides GaN, AlN, and InN was analyzed systematically in a wide energy range [81]. This study confirmed both the main results of theoretical calculations [78] and the fact that indium nitride is undoubtedly a narrow-gap material.

Two types of InN samples, grown by MBE and magnetron sputtering, were studied in [81]. A single-crystal InN epitaxial film of thickness 960 nm was synthesized by MBE on a (0001) sapphire substrate. Preliminarily, a 10-nm-thick layer of AlN and a 310-nm-thick buffer layer of GaN were deposited onto the sapphire substrate. The lattice constants were determined from the symmetric (002) and asymmetric (20.5) Bragg reflections as $a = 3.552$ Å and $c = 5.686$ Å. Hall measurements at room temperature demonstrated that the con-

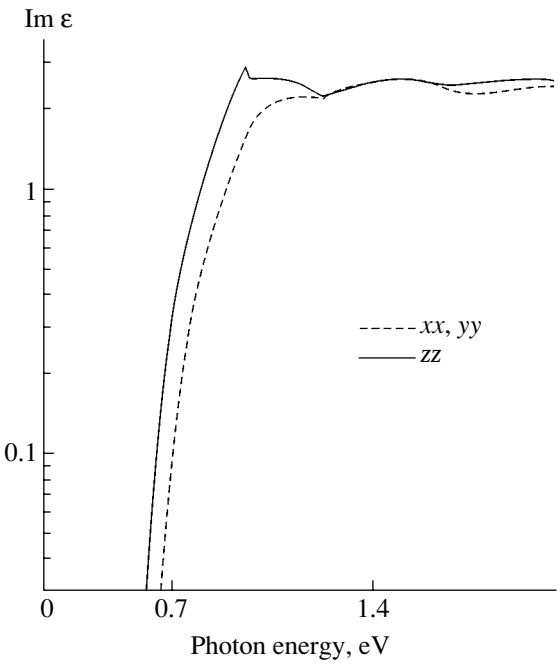

Fig. 12. Imaginary part of the dielectric constant (of the absorption coefficient) vs. the photon energy for an InN crystal. Taken from [78].

centration of electrons were $n = 8 \times 10^{17}$ cm^{-3}, and their mobility was 1500 cm^2/(V s).

Polycrystalline films deposited by magnetron sputtering onto a silicon substrate were 1210 nm thick. Their lattice constants were $c = 5.786$ Å and $a = 3.58$ Å.

The results of the calculation [78] of the real and imaginary parts of the dielectric function are compared with experimental data [81] for a film deposited by MBE and a sample synthesized by magnetron sputtering in Figs. 13a and 13b. Primarily noteworthy is the fact that the experimental results for the two types of samples are markedly different. These differences, as well as the differences in the lattice constants, are so great that it is more likely that these samples represent two crystals of different nature. Particularly characteristic in this regard is the discrepancy in the range 3.5–5 eV. In its nature, this discrepancy resembles the difference between the electronic spectra of amorphous and crystalline samples. The data for the film synthesized by MBE agree significantly better with the theoretical results.

The absorption coefficients of both types of film are compared in Fig. 13c. The behavior of the absorption coefficient of the sample synthesized by magnetron sputtering is indicative of a high electron concentration and the corresponding shift of the absorption threshold. Based on the data on absorption in an MBE-grown film, the band gap of InN was estimated in [81] to be 0.75 eV. In our opinion, it should be remembered here that (i) at a carrier concentration of $n = 8 \times 10^{17}$ cm^{-3} the real band gap will be 30 meV below the absorption threshold and (ii) the exponential decrease in the absorption, which is observed as the energy decreases, is to be taken into account in evaluating the position of the absorption threshold.

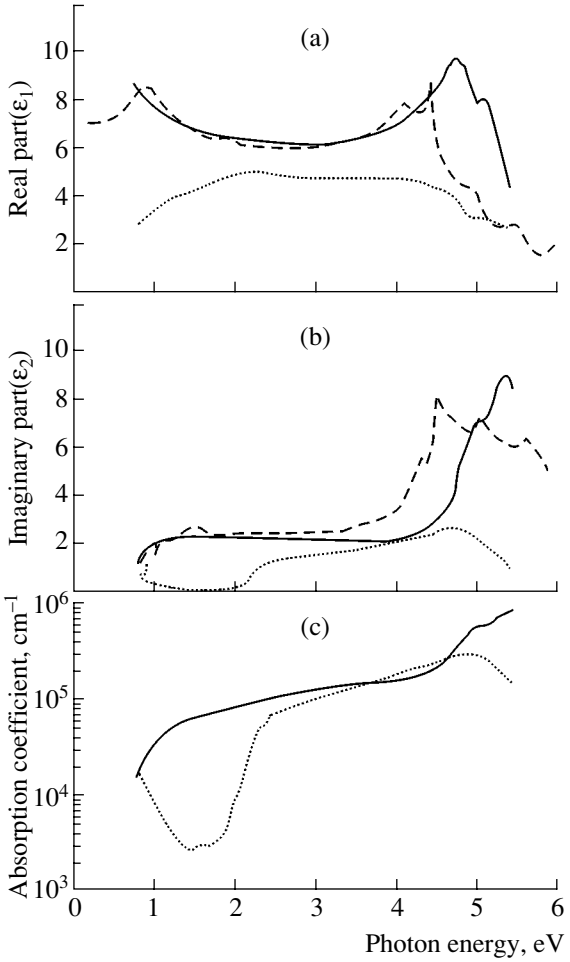

Fig. 13. (a) Real and (b) imaginary parts of the dielectric function of InN and (c) absorption coefficient. Solid lines: sample grown by MBE; dotted lines: sample obtained by magnetron sputtering; data of [81]. Dashed lines: theory [78].

3.3. Optical Properties of InN at the Fundamental Absorption Edge

The data presented indicate that determining the band gap in samples with high free-carrier concentration requires that the influence exerted by free carriers on the absorption at the threshold be taken into account in ample detail. Important additional data on the band gap and on the free-carrier concentration can be obtained from PL spectra. Below, we discuss the results of studies in which single-crystal epitaxial InN films were used to determine the band gap, and spectra of interband transitions in the vicinity of the absorption threshold and PL and PL excitation spectra, as well as spectra of photomodulated photoreflectance, were analyzed.

As all the samples had quite a high free-carrier concentration, neither absorption nor PL spectra could directly yield the band gap E_g. To evaluate E_g, a joint analysis of such spectra obtained for a set of InN samples with different free-carrier concentrations was carried out.

3.3.1. Characteristics of the samples studied. The first results that clearly indicated that the band gap of InN is narrow [44–48] were obtained on samples grown by PAMBE [37], MOMBE [40], and MOVPE [34, 82] on (0001) sapphire substrates. The samples were nominally undoped.

Taking into account the problem of the quality of the sample, all the films studied in [44, 45, 48] were preliminarily selected with respect to their structural characteristics.

The crystal structure of the samples was analyzed using a number of techniques. As indicated by X-ray spectra, all the samples had a hexagonal structure, without any traces of polymorphism. The lattice constants were determined from the symmetric and asymmetric (0002) Bragg reflections to be close to $c = 5.7039$ Å and $a = 3.5365$ Å. Special emphasis was placed on measuring the lattice constants, because it was known that the lattice parameters of samples used in [7] markedly differed from the values known for InN. For the best quality samples, the width of the rocking curves was

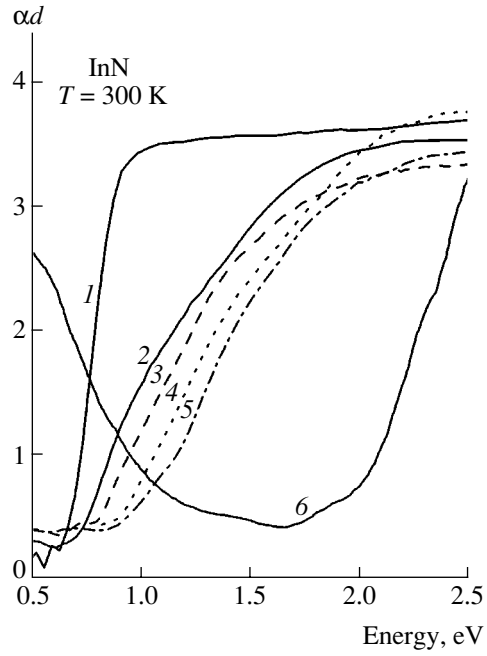

Fig. 14. Optical density spectra of *n*-InN samples with different free carrier concentrations *n*: (*1*) 1×10^{18}, (*2*) 6×10^{18}, (*3*) 9×10^{18}, (*4*) 1.1×10^{19}, (*5*) 2.1×10^{19}, and (*6*) 3×10^{21} cm^{-3}.

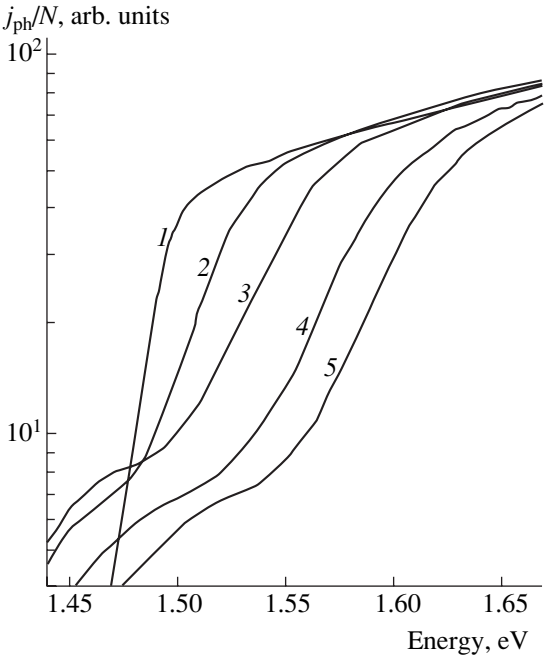

Fig. 15. Shift of the photosensitivity spectra of *n*-GaAs–Au rectifying contacts with increasing free-carrier concentration *n*: (*1*) 6×10^{16}, (*2*) 6×10^{17}, (*3*) 2×10^{18}, (*4*) 2.6×10^{18}, and (*5*) 4.4×10^{18} cm^{-3}. According to data of [83].

250–300 seconds of arc. The full widths at half-maximum (FWHM) of the (0002) reflections for θ–2θ scanning were within 50–60 seconds of arc.

Raman spectra were excited by laser lines with wavelengths of 641, 514, and 488 nm, which made it possible to obtain spectra from InN samples at different depths. The polarization of the Raman spectra conformed well with the selection rules for InN crystals of a hexagonal symmetry. The FWHM of Raman lines of InN were within the range typical of a well-ordered lattice.

Atomic-force microscopy failed to reveal in the samples any pronounced columnar structure characteristic of the samples used in [7]. According to the data furnished by Auger spectroscopy and the Rutherford backscattering technique, the content of oxygen in the samples did not exceed 1 at %. The electron concentration in most of the samples was in the range from 1×10^{18} to 4×10^{19} cm^{-3}. The highest mobility of 1900 cm^2/(V s) was recorded for an MOMBE-grown sample with carrier concentration $n = 8 \times 10^{18}$ cm^{-3}. In addition, samples with a very high carrier concentration of up to 3×10^{21} cm^{-3}, which were prepared by MOVPE and magnetron sputtering, were studied.

The absorption coefficient α(ω) was calculated from absorption spectra, with a correction made for multiple reflections. The film thicknesses were measured with a scanning electron microscope.

The measurements were performed in a wide energy range that included the near-IR region. PbS and InGaAs diodes served as IR detectors.

3.3.2. Interband absorption in heavily doped semiconductors (Burstein–Moss effect). Figure 14 shows optical density spectra of epitaxial InN films with a free-carrier concentration in the range from 1×10^{18} to 3×10^{21} cm^{-3}. It can be seen that, as the free-carrier concentration in the samples increases, the absorption threshold steadily shifts from an energy of ~0.7 eV for a sample with the lowest electron concentration to ~1.9 eV for that with the highest electron concentration. It was established that the absorption coefficient α(ω) rapidly reaches values of ~10^4 cm^{-1}, which are characteristic of interband transitions in direct-gap crystals.

These results demonstrated that a nontrivial specific feature of InN crystals is the strong dependence of the absorption threshold on the free-carrier concentration. Generally speaking, such a behavior is characteristic not only of InN crystals. Significant shifts of the absorption threshold, which are accounted for by the Burstein–Moss effect [20], can also be found in other heavily doped semiconductors, for example, gallium arsenide. As demonstrated in [83], the magnitude of the Burstein–Moss effect can be judged from the shift of the photosensitivity threshold of the rectifying contacts *n*-GaAs–Au, which is a parameter directly related to the absorption coefficient. Figure 15 shows photosensitivity spectra for a doped *n*-type GaAs crystal, in which the free-electron concentration is widely varied. Figures 14 and 15 show a similar behavior of the absorption edge with the carrier concentration. A noticeable difference between the spectra of *n*-InN and *n*-GaAs

arises only for InN crystals with an electron concentration of 3×10^{21} cm^{-3} because of the appearance of the plasma reflection edge in the low-energy part of the spectrum.

Taking into account this analogy, it seems appropriate to relate the difference in the positions of the absorption edge in InN crystals with different electron concentrations to the Burstein–Moss effect [20], i.e., to the fact that transitions from the valence band to the conduction band are impossible when the final states are occupied by electrons.

3.3.2.1. Burstein–Moss effect in a direct-gap crystal. Let us consider in more detail the Burstein–Moss effect in a direct-gap crystal. In general, the contribution of vertical interband transitions to the dielectric susceptibility tensor has the form

$$\chi_{\beta\beta}(\omega) = \frac{4\pi e^2}{\hbar\omega^2 V_0}\sum_{\mathbf{p},\sigma,\sigma',v,c}\left\{\left|\mathbf{j}^{\beta}_{c,\sigma',v,\sigma}\right|^2 n^{v}_{\mathbf{p},\sigma}(1-n^{c}_{\mathbf{p},\sigma})\right.$$
$$\left.\times\left[\frac{1}{\omega-\epsilon^{c}_{\sigma'}(\mathbf{p})+\epsilon^{v}_{\sigma}(\mathbf{p})+i0}-\frac{1}{\omega+\epsilon^{c}_{\sigma'}(\mathbf{p})-\epsilon^{v}_{\sigma}(\mathbf{p})+i0}\right]\right\}. \quad (8)$$

Here, $\mathbf{j}^{\beta}_{c,\sigma',v,\sigma}$ is the matrix element of the flux operator between the electron state with a spin σ in the valence band v and that in the conduction band c with a spin σ'; $\epsilon^{c,v}_{\sigma'}(\mathbf{p})$, the energy of an electron in the conduction or valence band; and V_0, the volume of the unit cell of the lattice. In the case of vertical transitions, both the states have the same quasi-momentum $\mathbf{p}$, and the summation is done over the first Brillouin zone. The Fermi distribution function

$$n^{v}_{\mathbf{p},\sigma} = n^{v}_{\mathbf{p},\sigma}(\epsilon^{v}_{\sigma}(\mathbf{p})) = \frac{1}{\exp\{[\epsilon^{v}_{\sigma}(\mathbf{p})-E_F]/T\}+1} \quad (9)$$

for the valence bands can be replaced with unity in the case of an *n*-type crystal because the Fermi energy for a heavily doped (degenerate) semiconductor lies above the bottom of the conduction band and all states of the valence bands are occupied. The filling of the conduction band, which depends on the carrier concentration and temperature, is given by the Fermi function

$$n^{c}_{\mathbf{p},\sigma} = n^{c}_{\mathbf{p},\sigma}(\epsilon^{c}_{\sigma}(\mathbf{p})) = \frac{1}{\exp\{[\epsilon^{c}_{\sigma}(\mathbf{p})-E_F]/T\}+1}, \quad (10)$$

and, therefore, summation over $\mathbf{p}$ is limited to those states which remain free at a given doping level, i.e., to those states for which $(1 - n^{c}_{\mathbf{p},\sigma}) \neq 0$.

In further analysis in this section, we take the photon momentum to be zero, use the effective-mass approximation, and restrict our consideration to the contribution from two bands without regard for the possible nonparabolicity on the assumption that the dispersion laws are isotropic. Substituting for the energies of the hole and electron

$$\epsilon^{v}_{\sigma}(\mathbf{p}) = -\frac{p^2}{2m_h} \quad (11)$$

and

$$\epsilon^{c}_{\sigma}(\mathbf{p}) = E_g + \frac{p^2}{2m_e}, \quad (12)$$

where m_h and m_e are the effective electron and hole masses, we obtain, as a result of integration with respect to momentum for the imaginary part of the dielectric susceptibility, an expression whose frequency dependence in the vicinity of the threshold of interband transition is given by the following function:

$$\chi''(\omega) \propto \left[\frac{(2\mu)^{3/2}V_0}{2\pi^2\hbar^3}\right]\sqrt{(\hbar\omega-E_g)}$$
$$\times\left\{1-\frac{1}{\exp\{[(\mu/m_e)(\hbar\omega-E_g)-E_F]/T\}+1}\right\}. \quad (13)$$

Here, $\mu = m_e m_h/(m_e + m_h)$ is the reduced mass of particles; $E_F = p_F^2/2m_e$, the Fermi energy of electrons; T, the temperature in energy units; $p_F/\hbar = (3\pi^2 n)^{1/3}$; and n, the free-electron concentration.

At a zero temperature, the absorption threshold has the form of a step at an energy $\hbar\omega = E_g + E_F(m_e + m_h)/m_h$. Thus, with a large difference between the electron and hole masses, $m_e \ll m_h$, the threshold is shifted away from E_g by an amount that only slightly exceeds the Fermi energy. At finite temperatures, expression (13) leads to an exponential rise in absorption at the threshold.

In real crystals, it is necessary to take into account additional factors, which considerably complicate the situation.

3.3.2.2. Violation of the momentum conservation law in interband absorption. We note first of all that the presence of dopants, which are randomly or regularly distributed over the crystal, and various defects of the crystal lattice affects the motion of electrons and holes. As a result of particle scattering from a random potential created by impurities and defects, the momentum of electrons, $\mathbf{p}_e$, may differ from that of holes, $\mathbf{p}_h$. This means that it is necessary to take into account not only vertical interband transitions. The energy of a pair created upon absorption of a photon can then be represented as

$$E_g + \frac{p^2}{2\mu} + \frac{Q^2}{2M}. \quad (14)$$

Here, $\mathbf{Q} = (\mathbf{p}_e - \mathbf{p}_h)$, $\mathbf{p} = (\mathbf{p}_e\mu/m_e + \mathbf{p}_h\mu/m_h)$, and $M = (m_e + m_h)$ is the translational mass of the pair.

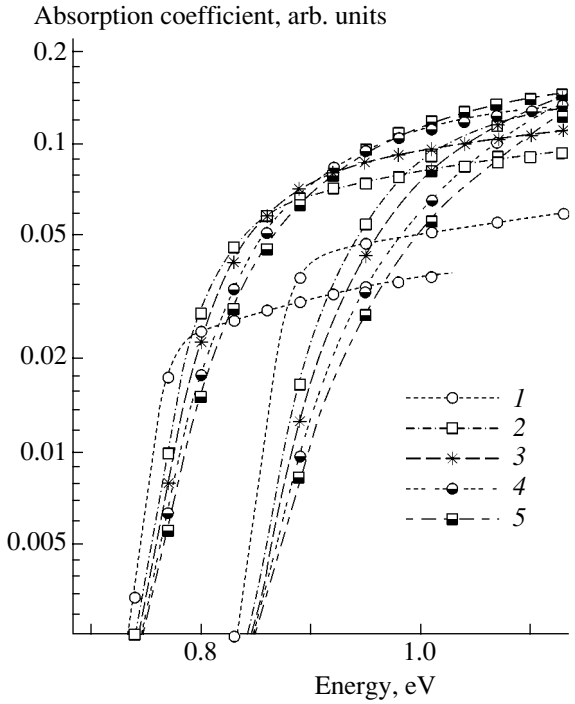

Fig. 16. Shift of the optical absorption edge due to the Burstein–Moss effect. Two sets of five curves each correspond to the Fermi energies E_F = 0.100 and 0.200 eV. Curves *1–5* were obtained at $[\Delta(Q^2/2M)/E_F]^2$ = 0.01, 0.25, 0.5, 1.0, and 1.50. T = 80 K and $E_g(n)$ = 0.7 eV.

The quantity Q may take quite a number of values, depending on the mechanism of scattering on the random potential, and it is necessary to perform summation over these values. In this case, the dependence of the interband contribution to the dielectric susceptibility, which determines the behavior of the absorption coefficient, can be represented as

$$\chi''(\omega) \propto \frac{v_0}{(2\pi\hbar)^3}\int d^3p\,d^3Q\,\Delta(\mathbf{Q}) \times \delta\left(\hbar\omega - E_g - \frac{p^2}{2\mu} - \frac{Q^2}{2M}\right)\left\{1 - n^c_{\mathbf{p},\sigma}\left(\frac{(\mathbf{p} + \mathbf{Q}\mu/m_h)^2}{2m_e}\right)\right\}, \quad (15)$$

where $\Delta(\mathbf{Q})$ is the distribution function of the allowed values of Q. This function is a squared overlapping integral between the wave functions of the electron and hole, which are created at the same point of space upon absorption of a photon and whose momentum of the center of mass is equal to Q. The function $\Delta(\mathbf{Q})$ can be found if the electron and hole wave functions for motion in a random potential are known. In the case of free motion,

$$\Delta(\mathbf{Q}) \longrightarrow \delta(\mathbf{Q}); \quad (16)$$

i.e., the function reduces to a 3D delta function that expresses the momentum conservation law. In this case, it follows from (15) that only vertical transitions are allowed and the frequency dependence of the interband absorption coefficient is transformed into (13). If $\Delta(\mathbf{Q})$ in no way restricts the possible values of Q, the integration with respect to d^3Q extends over the entire volume of the first Brillouin zone.

Both these limiting cases can be represented as the expression

$$\chi''(\omega) \propto \left[\frac{(\hbar\omega - E_g)}{E_g}\right]^{\gamma/2} \times \left\{1 - \frac{1}{\exp\{[(\mu/m_e)(\hbar\omega - E_g) - E_F]/T\} + 1}\right\}. \quad (17)$$

In the case when the conservation law is obeyed, $\gamma = 1$, which leads to (13), whereas in the absence of limitations on the momenta, $\gamma = 4$.

As the properties of $\Delta(\mathbf{Q})$ generally remain unknown, expression (15) is convenient for an approximate description of the behavior of the imaginary part of the dielectric susceptibility between the two limiting cases of $\gamma = 1$ and $\gamma = 4$, as well as for an estimate of the degree of smearing of the function $\Delta(\mathbf{Q})$.

Figure 16 shows the results of calculation of the dependence $\chi''(\omega)$ (interband absorption coefficient) for different extents of departure from the momentum conservation law. In these calculations, the function $\Delta(\mathbf{Q})$ was used in the form of a 3D Gaussian function and the ratio of effective electron and hole masses was considered to be 1 : 10. It can be seen in the figure how the shape of the curve varies as the half-width of the distribution increases.

It follows from the figure that, as before [in (13)], the absorption at the threshold grows exponentially, and then as the energy increases, expression (15) leads, depending on the uncertainty in Q, to a behavior of the type

$$\chi''(\omega) \propto \left[\frac{(\hbar\omega - E_g)}{E_g}\right]^{\gamma/2},$$

where γ can take values in the range from unity for an extremely low uncertainty in Q to four for large uncertainties.

3.3.2.3. Charge density fluctuations. The character of the frequency dependence of the absorption coefficient can be noticeably affected by large-scale fluctuations of the dopant distribution. Such fluctuations, irrespective of their origin, create a potential profile both for electrons in the conduction band and holes in the valence band. This effect was briefly analyzed for InN in [48]. We present here some substantiation of the conclusions made in that study and restrict our consideration to take account of fluctuations with sizes greater than the reciprocal of the Thomas–Fermi wave vector $q_{TF} = \sqrt{3}\,\omega_p/v_F$, where ω_p is the plasma frequency of electrons and v_F is the velocity of an electron at the Fermi surface.

The electron–hole pair created upon absorption of a photon is electrically neutral. The changes in the potential energies of the electron and hole in the field of a fluctuation have opposite signs and do not alter the band gap but modify the electron density distribution, which becomes nonuniform: $n^c_{\mathbf{p},\sigma} \longrightarrow n^c_{\mathbf{p},\sigma}(\epsilon^c_\sigma(\mathbf{p}) - \phi(\mathbf{r}))$; i.e., the distribution becomes dependent on the potential energy $\phi(\mathbf{r})$ [84]:

$$n^c_{\mathbf{p},\sigma}(\epsilon^c_\sigma(\mathbf{p}) - \phi(\mathbf{r})) = \frac{1}{\exp\{[\epsilon^c_\sigma(\mathbf{p}) - \phi(\mathbf{r}) - E_F]/T\} + 1}. \quad (18)$$

Then the absorption coefficient can be written in terms of the averaged contribution of interband transitions to the dielectric susceptibility

$$\langle \chi''(\omega)\rangle \propto \left\langle \frac{V_0}{(2\pi\hbar)^3}\int d^3p d^3Q \Delta(\mathbf{Q}) \times \delta\left(\hbar\omega - E_g - \frac{p^2}{2\mu} - \frac{Q^2}{2M}\right) \times \left\{1 - n^c_{\mathbf{p},\sigma}\left(\frac{(\mathbf{p} + \mathbf{Q}\mu/m_h)^2}{2m_e} - \phi(\mathbf{r})\right)\right\}\right\rangle, \quad (19)$$

where the angle brackets denote averaging over the distribution of values of ϕ.

The nonuniform distribution of the charge of electrons is experimentally manifested as a kind of inhomogeneous smearing of the optical absorption threshold and broadening of the PL bands. The available data [48] indicate that these effects are greater for samples in which the carrier concentration is higher. The inhomogeneous smearing and broadening result in a considerable weakening of the temperature dependences of both the absorption coefficient and the shape of PL bands. The fluctuations of ϕ usually do not exceed $0.1E_F$ in order of magnitude. Specifically, the result of this is that the slopes of the short-wavelength wing of the PL band and the long-wavelength absorption edge are not determined by the temperature of the experiment. However, they can be described by introducing an effective temperature that has been found to be considerably higher than the sample temperature [48]. In this case, the slope of the long-wavelength absorption edge or that of the short-wavelength wing of the PL band may correspond to an effective temperature of about several hundred degrees.

3.3.2.4. Dependence of the band gap on the carrier concentration. As shown in [48], the value of E_g, which appears in all expressions for χ, depends on the carrier concentration. According to the Gell-Mann–Bruckner theory, such a dependence occurs in a Fermi liquid because of the Hartree–Fock exchange interaction of Fermi particles [63, 85]. This dependence is to be taken into account when analyzing the optical properties of degenerate semiconductors. The correction to the self-energy of an electron, $\Delta E_{ex}(n)$, which is associated with the electron–electron exchange interaction, depends on the electron concentration n. To calculate this correction in the general case, it is necessary to know the wave functions of the electron. Using the average value of the correction for the exchange interaction to estimate this energy, we obtain

$$\Delta E_{ex}(n) = -\frac{e^2}{2}\sum_{\mathbf{p},\mathbf{p}'<p_F}\int d^3r d^3r' \times \Psi^*_{\sigma,\mathbf{p}}(\mathbf{r})\Psi^*_{\sigma,\mathbf{p}'}(\mathbf{r})\Psi_{\sigma,\mathbf{p}}(\mathbf{r}')\Psi_{\sigma,\mathbf{p}'}(\mathbf{r}')/|\mathbf{r} - \mathbf{r}'|. \quad (20)$$

Note that, in contrast to Coulomb interaction, the exchange interaction is not screened and, in the effective-mass approximation for an isotropic conduction band, this expression reduces to the known function for the ideal Fermi liquid [63] and gives the following shift in energy per particle:

$$\Delta E_{ex}(n) = -\left[\frac{81}{8\pi}\right]^{1/3}\frac{e^2 n^{1/3}}{2}. \quad (21)$$

For clarity, this quantity can be conveniently expressed in millielectronvolts, with $n_0 = 1\times10^{18}$ cm^{-3} used as the concentration unit. As a result, we have

$$\Delta E_{ex}(n) = -106[n/n_0]^{1/3}. \quad (22)$$

In this approximation, the function of the relative concentration n/n_0 is universal and independent of other parameters of the crystal. Nevertheless, the individual characteristics of the crystal may change $\Delta E_{ex}(n)$ because the wave functions of electrons in the crystal are different from those of free electrons. For example, substitution into (20) of the wave functions in the form

$$\Psi_{\sigma,\mathbf{p}'}(\mathbf{r}) = \frac{1}{\sqrt{V}}u_{\sigma,\mathbf{p}}(\mathbf{r})\exp(i\mathbf{pr}), \quad (23)$$

where $u_{\sigma,\mathbf{p}'}(\mathbf{r})$ is the Bloch factor and V is the volume of the crystal, shows that $\Delta E_{ex}(n)$ is proportional to squared overlapping integrals

$$\frac{1}{V_0}\int d^3r u_{\sigma,\mathbf{p}}(\mathbf{r})u_{\sigma,\mathbf{p}'}(\mathbf{r}) \quad (24)$$

between Bloch factors with $\mathbf{p} \neq \mathbf{p}'$. In the effective-mass approximation, $\mathbf{p} = \mathbf{p}' = 0$ and the overlapping integrals are equal to unity. However, in the case of degenerate electrons, the range within which the values of $\mathbf{p}$ fall is rather wide and the overlapping integral may be, on average, much smaller than their values in the effective-mass approximation. Therefore, expression (22) can be regarded as an estimate of the upper bound on the concentration-related shift of E_g. It follows from this estimate that the shift of the conduction band as a function of n is to be taken into account in evaluating the band

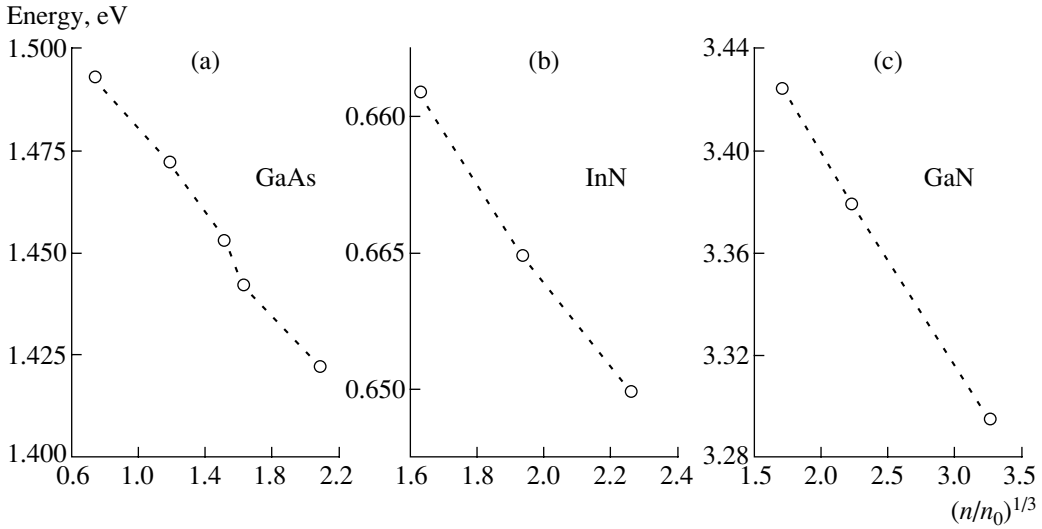

Fig. 17. E_g vs. free-carrier concentration for crystals of (a) GaAs, (b) InN, and (c) GaN; the concentration is given in units of $n_0 = 1 \times 10^{18}$ cm^{-3}. Taken from [48].

gap width. Taking this shift into account, E_g in (19) must be replaced by $E_g(n)$, i.e.,

$$\langle \chi''(\omega) \rangle \propto \left\langle \frac{V_0}{(2\pi\hbar)^3} \int d^3p d^3Q \Delta(\mathbf{Q}) \right.$$

$$\times \delta\left(\hbar\omega - E_g(n) - \frac{p^2}{2\mu} - \frac{Q^2}{2M}\right) \qquad (25)$$

$$\left. [2mm] \times \left\{1 - n^c_{\mathbf{p},\sigma}\left(\frac{(\mathbf{p} + \mathbf{Q}\mu/m_h)^2}{2m_e} - \phi(\mathbf{r})\right)\right\}\right\rangle.$$

The result obtained makes it possible to analyze data on interband absorption and PL in heavily doped GaAs, InN, and GaN crystals [48]. As shown by studies of the absorption and PL (see below), the dependence $E_g(n)$ for these three materials has a form characteristic of the Hartree–Fock exchange interaction (see Fig. 17). The shift is on the same order of magnitude as estimate (22). However, the values of the numerical factor in (22) are less than 106 meV and different for these three materials. The highest value (about 70 meV) is observed for GaAs. Extrapolation of $E_g(n)$ to a zero carrier concentration gives for this crystal E_g = 1.5 eV, i.e., a value close to the true band gap. The Bloch factor is 50 meV for the GaN crystal and about 20 meV for InN. Thus, we have a noticeable quantitative departure from estimate (22). This fact can be accounted for by the difference of overlapping integrals (24) from unity if it is assumed that, for InN and GaN, the departure from the effective-mass approximation for the conductivity bands exceeds that for GaAs. Linear extrapolation of $E_g(n)$ to zero concentration for InN gives a value E_g = 0.68 eV [48].

3.3.3. Interband PL in heavily doped semiconductors. A specific feature of heavily doped *n*-type semiconductors is that the shortest-wavelength part of their PL spectrum is formed by recombination of degenerate electrons and holes produced upon absorption of a photon. As a consequence, such characteristics of PL as the shape of the PL band and its dependence on temperature and electron concentration are now determined not only by the properties of electrons, but also by those of holes generated upon absorption of an exciting photon.

3.3.3.1. Principal characteristics of the interband PL. Typical spectra of the interband PL in InN, which was first observed in [44, 45, 48], are shown in Fig. 18. The width of the PL band and the position of its peak are determined by such characteristics of the crystal as free-carrier concentration, effective electron and hole masses, and the band gap. The dependence of the spectral density of interband transitions with emission of a photon, by analogy with (19), can be represented as

$$\frac{\{[\hbar\omega - E_g(n)]/E_g(n)\}^{\gamma/2}}{\exp\{[(2\mu/m_e)(\hbar\omega - E_g) - E_F]/T\} + 1}. \qquad (26)$$

In this case, as before, γ may take values in the range from unity for transitions with momentum conservation to four for those in which the conservation law is violated. If the dependence of the Fermi energy for a degenerate *n*-type semiconductor on the concentration *n* and the effective mass $E_F = 3.58(m_0/m_e)(n/n_0)^{2/3}$ meV (where $n_0 = 1 \times 10^{18}$ cm^{-3}) is taken into account, then expression (26) describes the most important characteristics of the PL band for various samples. At the same time, it should be noted that such a description is approximate. A more rigorous analysis of the shape of the PL band is performed below.

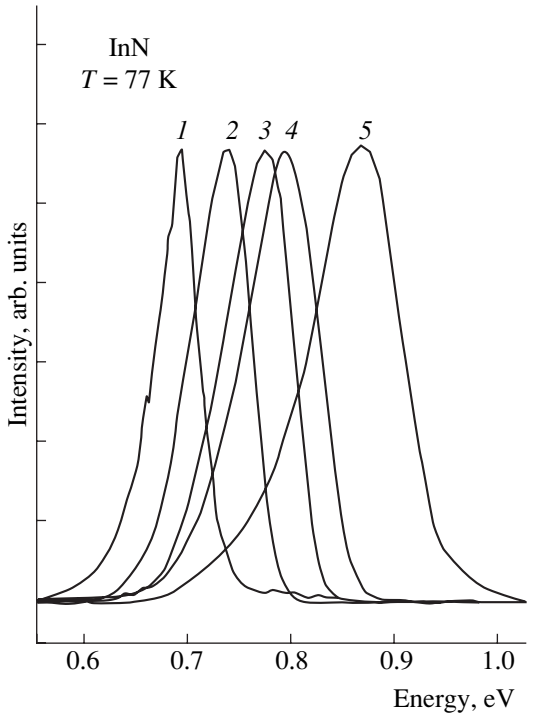

Fig. 18. PL spectra of *n*-InN samples with different free-carrier concentrations *n*: (*1*) 1×10^{18}, (*2*) 6×10^{18}, (*3*) 9×10^{18}, (*4*) 1.1×10^{19}, and (*5*) 2.1×10^{19} cm^{-3}. Taken from [15].

The general nature of such a phenomenon as interband recombination of free electrons and holes in doped semiconductors is revealed by analyzing PL spectra of various materials at comparable free-carrier concentrations.

Figure 19 compares interband PL spectra of *n*-GaAs, *n*-InN, and *n*-GaN. As follows from (26), the shape of PL bands depends on whether the recombination occurs via vertical transitions or whether the band is formed as a result of interband transitions with violation of the momentum conservation law [48]. In the case of a high electron concentration, the width of the PL band is largely determined for any variant of transitions by the energy interval into which occupied states of the conduction band fall at a given concentration. Therefore, a simple comparison of the FWHM of the bands observed in these three materials at approximately the same free-carrier concentration suggests that the effective electron mass in InN has an intermediate value between the electron masses in GaAs and GaN.

3.3.3.2. Dependence of the shape of the PL band on the carrier concentration. Figure 20 shows how the shape of the interband PL band in *n*-InN changes when the electron concentration is widely varied. The same figure presents the band shapes calculated using the model and procedure suggested in [48]. It was established that the good agreement between the calculated and observed PL band shapes is achieved on the assumption that the momentum conservation law is strongly violated in interband transitions.

The inset in the same figure shows the Fermi energy obtained for the samples studied by fitting the band shapes, with the effective mass taken to be $m_e = 0.1m_0$. Also shown are the Fermi energies for the electron concentrations obtained in Hall measurements. These values agree well with the Fermi energies found by fitting the PL band shapes, which confirms the interband origin of the bands observed.

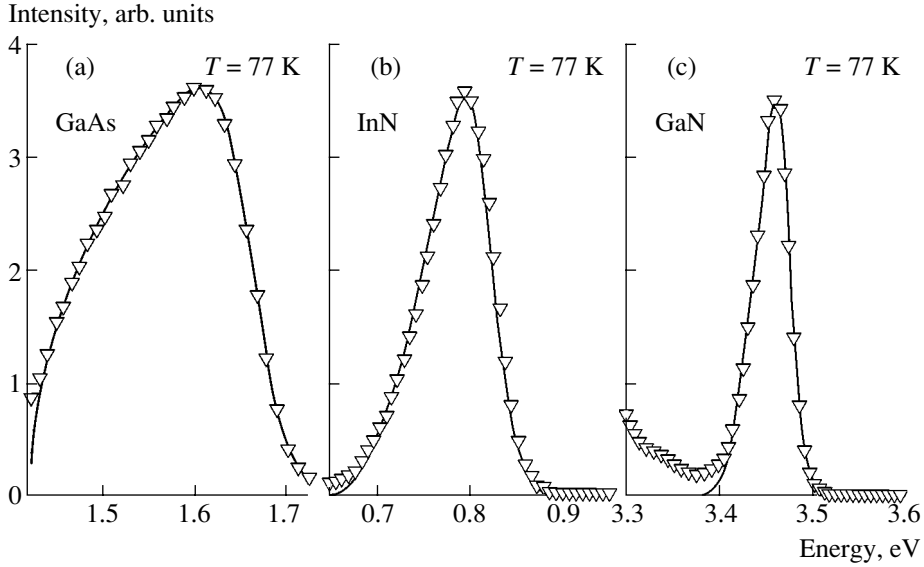

Fig. 19. Interband PL bands of heavily doped *n*-type crystals of (a) GaAs, (b) InN, and (c) GaN. The electron concentrations are 1.1×10^{19}, 0.9×10^{19}, and 0.9×10^{19} cm^{-3}, respectively. Points: experimental data; solid curves: results of calculation by formula (26) at $\gamma = 1$ for GaAs and 4 for InN and GaN. Taken from [48].

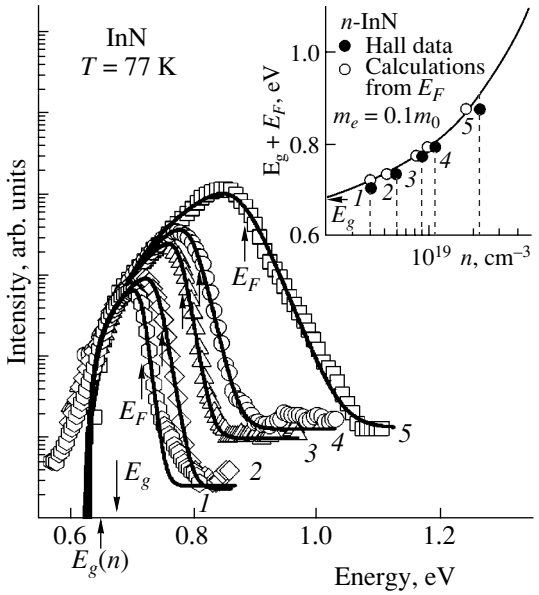

Fig. 20. Dependence of the PL bands of *n*-InN on carrier concentration, *n*: (*1*) 1×10^{18}, (*2*) 6×10^{18}, (*3*) 9×10^{18}, (*4*) 1.1×10^{19}, and (*5*) 2.2×10^{19} cm^{-3}. Points: experiment; solid lines: calculation. Inset: the Fermi energy as a function of the electron concentration for the same samples. Taken from [45].

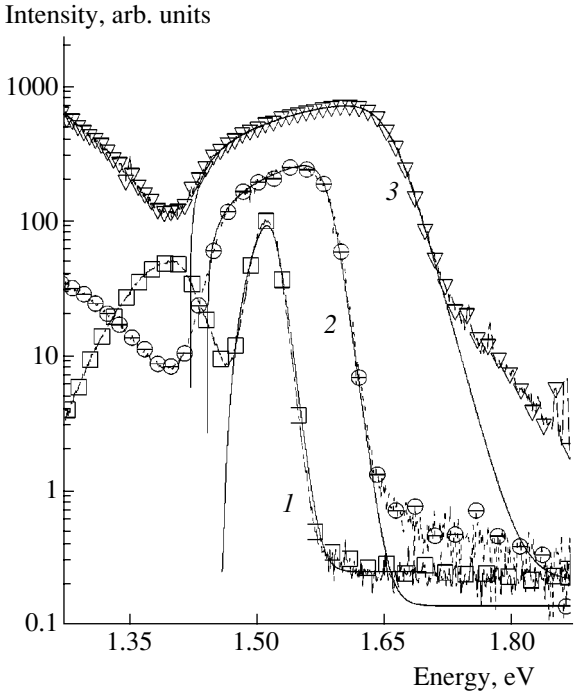

Fig. 21. Dependence of the PL bands on the doping level of *n*-GaAs; *n*: (*1*) 7.5×10^{17}, (*2*) 3.5×10^{18}, and (*3*) 1.1×10^{19} cm^{-3}.

The interband recombination in various doped semiconducting materials clearly exhibits common features. For example, Fig. 21 shows the dependence of the shape and width of the PL bands on the electron concentration for three *n*-GaAs samples. Comparison of data for InN and GaAs reveals the same behavior of the main parameters of the PL bands: as the electron concentration increases, the bands become broader and their peaks are shifted to shorter wavelengths. At the same time, noteworthy is a clearly observable shift of the long-wavelength edge of the PL band in GaAs. This shift is revealed in the fitting of the band shape and is described by the dependence $E_g(n)$. A similar shift, although considerably smaller in magnitude, is also observed in the case of InN. As shown above [see estimate (26)], the dependence $E_g(n)$ for GaAs, InN, and GaN can be attributed to an increase in the energy of the Hartree–Fock exchange interaction with the carrier concentration.

3.3.3.3. Temperature dependence of the PL band. As a rule, as the temperature increases, the PL band related to interband recombination of free carriers is shifted to longer wavelengths and broadened. The common reason for the shift of PL bands associated with recombination of free electrons is the temperature-induced narrowing of the band gap. Moreover, temperature predetermines the energy distribution of free electrons, and changing the temperature affects the band shape by primarily modifying the slope of the short-wavelength wing of the band. The presence of Urbach tails at the valence bands and the temperature dependence of the population of hole states also affect the behavior of the interband PL bands with temperature.

The temperature dependence of the intensity and shape of the PL band in InN is shown in Fig. 22. It is noteworthy that raising the temperature from 4.2 to 20 K results in the peak of the band undergoing a minor shift to shorter wavelengths. A similar anomalous shift of the absorption edge was observed in [86]. As shown below, this effect can be accounted for by the presence of the Urbach tail above the top of the valence bands. The reason is that, at extremely low temperatures, holes occupy only the deepest isolated localized states, whose number in the crystal is small compared with the total number of states in the valence bands. As a result, even a minor increase in temperature leads to a redistribution of the population of hole states and to a shift of the population maximum to the region of extended states. Thus, the magnitude of the short-wavelength shift of the peak of the interband PL band gives a reasonable estimate of the Urbach parameter for the density-of-states tail of the valence bands. If the temperature increases further, a characteristic long-wavelength shift of the band occurs, which is due to the temperature-induced shrinkage of the band gap.

Typical temperature dependences of such parameters of the PL band as intensity and FWHM are shown in Fig. 23. The intensity of PL exponentially decreases as the temperature increases, which indicates an increase in the rate of nonradiative recombination of holes. The increase in the FWHM with temperature is

accounted for by a change in the thermal distribution of both electrons and holes.

Figure 24a shows experimental data on absorption and PL at room temperature for one of the InN samples, together with the results of calculations by formulas (17) and (26) at the same fitting parameters. The good agreement between the experimental data on absorption and PL and the calculation results makes it possible to reliably identify the interband nature of these process and determine rather accurately such a parameter of the material as the band gap width.

Figures 24b and 24c compare the experimental and calculated shapes of PL bands at two temperatures for InN and GaAs. Despite the noticeable difference between the shapes of the PL bands of these two materials, the behavior is qualitatively the same in both cases. A good agreement between experiment and theory can be achieved for both semiconductors, and the results of the calculation make it possible to find the temperature-induced shrinkage of the band gap from the variation of the parameter $E_g(n)$ with temperature.

The examples considered demonstrate that it suffices to take into account the Burstein–Moss effect in order to satisfactorily interpret experimental data on interband recombination and to provide a model description of it in a wide range of electron concentrations.

Below, we consider in more detail the influence exerted by such factors as violation of the momentum conservation law, relaxation processes, inhomogeneous broadening of the PL band, and the Urbach tails of the density of states of electrons and holes on the shape of the PL band. Taking into account the above factors and their influence on the interband recombination yields valuable information that completes the evidence obtained from a simple model analysis of spectra of interband absorption and PL.

3.3.3.4. Recombination of thermalized holes. When considering recombination processes, as in the case of absorption, it is necessary to take into account the scattering of electrons and holes from impurities and crystal lattice defects that are randomly distributed over the crystal. This leads to violation of the momentum conservation law and necessitates taking into account not only vertical interband transitions. In addition to this mechanism, which is common to absorption and PL and complicates the analysis, the departure from equilibrium in the distribution of electrons over states in the conduction band and in that of holes (generated upon absorption of a photon) over states in the valence band may be important in the case of PL.

In the case of a high electron concentration, the shape of the interband PL band in crystalline *n*-type semiconductors is determined by transitions of electrons with an equilibrium energy distribution to the hole states formed upon absorption of photons and intraband relaxation. When PL is excited by photons with an

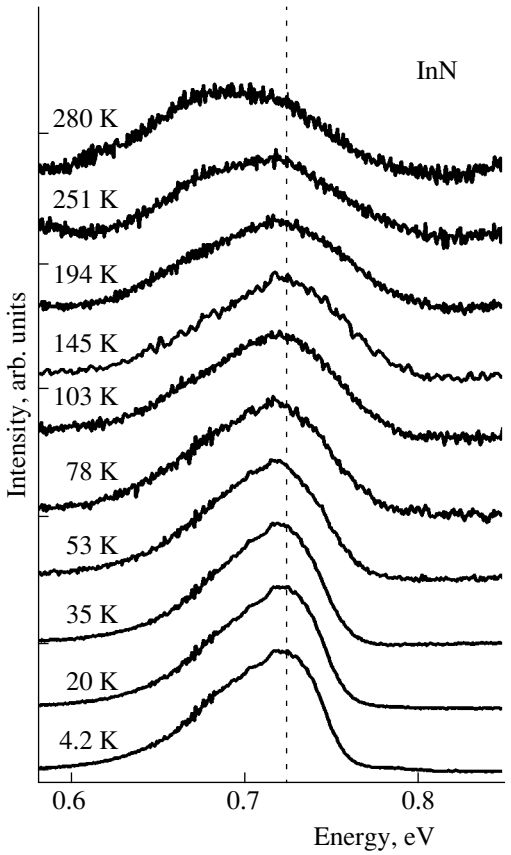

Fig. 22. Temperature dependence of the PL band of InN. Taken from [15].

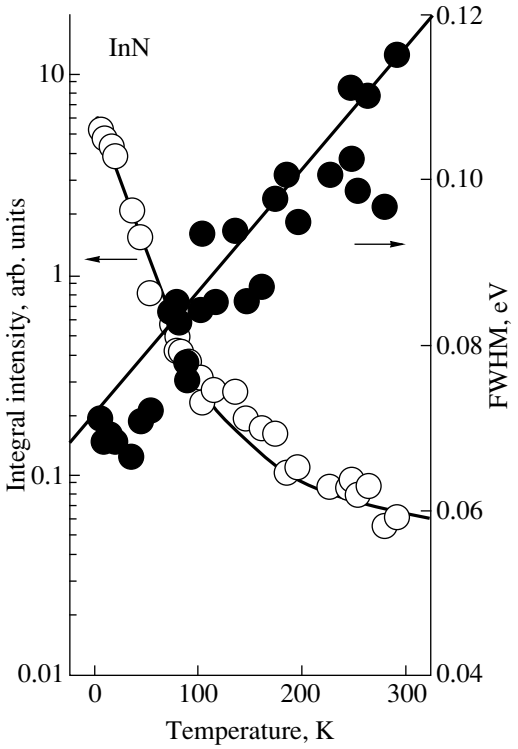

Fig. 23. Temperature dependence of the FWHM and intensity of the PL band of InN. Taken from [15].

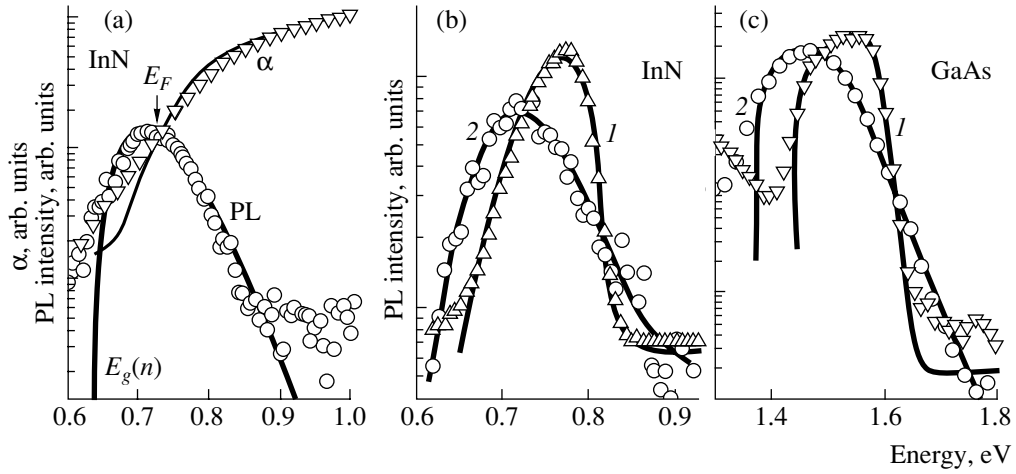

Fig. 24. (a) Absorption (α) and PL spectra of InN ($n = 6 \times 10^{18}$ cm^{-3}) at $T = 300$ K; points: experiment; solid lines: calculation. (b, c) PL bands at $T =$ (*1*) 77 and (*2*) 300 K of InN ($n = 6 \times 10^{18}$ cm^{-3}) and GaAs ($n = 4.3 \times 10^{18}$ cm^{-3}); points: experiment; solid lines: calculation. Taken from [48].

energy considerably exceeding the band gap width, the generated holes have a high kinetic energy, which is lost in the course of energy relaxation. The fastest process of energy loss is commonly associated with the emission of optical phonons. In this case, one would expect the relaxation times to be short and the fraction of hot holes that have enough time to recombine with emission of a photon to be negligible.

However, with the loss of energy, optical phonons are excluded from relaxation processes and the relaxation of holes decelerates. Nevertheless, the fraction of holes that recombine before the relaxation is complete does not exceed the ratio of the relaxation time $\tau_{rel} \approx 10^{-12}$ s to the time of radiative recombination, $\tau_{rad} \gtrsim 10^{-9}$ s. The rest of the holes occupy states that correspond to thermal energies of about T.

If the momentum conservation law is violated in recombination, the spectral density of states is proportional to E_F^2 at energies of about $[E_g(n) + E_F]$ and to T^2 at thermal energies. Therefore, the ratio of the spectral densities of states at these energies may be rather high $[\sim(E_F/T)^2]$ at high doping levels. The Fermi energy in millielectronvolts can be conveniently represented as $E_F = 3.58/m_e(n/n_0)^{2/3}$ meV, where $n_0 = 1 \times 10^{18}$ cm^{-3}. At a concentration of about 10^{19} cm^{-3}, E_F for an effective electron mass $m_e = 0.1m_0$ is 150–200 meV. The ratio $(E_F/T)^2$ has a value on the order of $\sim 10^4$ even at temperatures that are not too low. Therefore, the recombination of hot holes may be observable even at a ratio $\tau_{rel}/\tau_{rad} \approx 10^{-3}$. This process is the more probable, the higher the excitation intensity.

However, it may be considered that the main channel of recombination under weak excitation is recombination of holes that have had enough time to thermalize completely, or to a greater extent. In this case, the general expression for the PL intensity can be represented as

$$I(\omega) \propto \frac{V_0}{(2\pi\hbar)^3}\int d^3p d^3Q f\left(\frac{(\mathbf{p} + \mathbf{Q}\mu/m_e)^2}{2m_h T}\right)\Delta(\mathbf{Q}) \times \delta\left(\hbar\omega - E_g(n) - \frac{p^2}{2\mu} - \frac{Q^2}{2M}\right) n^c_{\mathbf{p},\sigma}\left(\frac{(\mathbf{p} + \mathbf{Q}\mu/m_h)^2}{2m_e}\right), \quad (27)$$

where $f((\mathbf{p} + \mathbf{Q}\mu/m_e)^2/2m_hT)$ is the function describing the thermal distribution of holes over energy.

Figure 25 shows the result of a model calculation of how the shape of the PL band changes because of the violation of the momentum conservation law for recombination of thermalized holes and electrons. The same figure shows the absorption coefficient under similar conditions in the case of the violation of the momentum conservation law. The PL band shapes and the behavior of the absorption edge, which were obtained as a result of this calculation, agree well with the approximate description (17) and (26), which was used in [44, 45, 48].

The manner in which the shape of PL bands and the absorption edge change when the extent of violation of the momentum conservation law becomes greater can be traced in going from curves *1* to curves *4* in Fig. 25; curves *1* correspond well to value $\gamma = 1$, and curves *4* are close to the corresponding curves at $\gamma = 4$.

3.3.3.5. Influence of a nonequilibrium distribution of carriers on the shape of the PL band and the inhomogeneous broadening of the PL band. Published data indicate that the experimentally observed PL band shapes vary widely at the same observation temperature. Specifically, this can be seen from the slope of the short-wavelength wing, which can markedly differ from that determined by temperature, especially in sam-

ples with a high electron concentration. Such changes in the band shapes are also characteristic of other heavily doped semiconductors, for example, gallium arsenide. Thus, it may be concluded that there are rather general reasons for the complication of the shapes of interband PL bands. One of these is the nonuniform distribution of the electron density over a sample.

Another possible reason is the recombination of hot holes and hot electrons. The hot PL in relatively lightly doped crystals was discussed in detail in [87].

Taking into account the violation of the momentum conservation law, arbitrary distribution of holes over energies, and nonuniform distribution of the electron density, the intensity of PL at a frequency ω can be represented as

$$\langle I(\omega)\rangle \propto \left\langle \frac{V_0}{(2\pi\hbar)^3}\int d^3p d^3Q f((\mathbf{p}+\mathbf{Q}\mu/m_e)^2) \right.$$
$$\times \Delta(\mathbf{Q})\delta\left(\hbar\omega - E_g(n) - \frac{p^2}{2\mu} - \frac{Q^2}{2M}\right) \qquad (28)$$
$$\left. \times n^c_{\mathbf{p},\sigma}\left(\frac{(\mathbf{p}+\mathbf{Q}\mu/m_h)^2}{2m_e} - \phi(\mathbf{r})\right)\right\rangle.$$

Here, the function $f((\mathbf{p} + \mathbf{Q}\mu/m_e)^2)$ is the distribution of holes over kinetic energies. As in the case of absorption, the nonuniform distribution of the electron density over the crystal is taken into account by averaging over the distribution of the random potential $\phi(\mathbf{r})$.

Recombination of holes with relatively high kinetic energy would give rise to a short-wavelength wing of the PL band, whose slope would be different from that determined by temperature. In this sense, one would expect the hot holes and nonuniformities in the electron density distribution to exert about the same influence on the shape of the PL band.

The effect produced by hot holes can be determined by comparing the behavior of the long-wavelength absorption edge, which is independent of the hole distribution, with that of the short-wavelength wing of the PL band. A noticeable difference between the slope of the short-wavelength wing of PL bands and that determined by temperature can be observed in many cases under conditions of weak stationary excitation. However, as already mentioned, the behavior of the absorption coefficient and the PL band are in rather good agreement, and therefore there is no reason to believe that hot holes contribute to PL.

A special situation occurs in the case of a strong excitation of samples in which the equilibrium concentration of electrons is relatively low. Then the electron concentration can be changed by exciting light [88]. Time-resolved subpicosecond measurements of differential transmission on a sample with an electron concentration $n = 1.3 \times 10^{18}$ cm^{-3}, which were carried out in [88] under a strong pulsed excitation, demonstrated that the short-wavelength wing of the PL band shape is

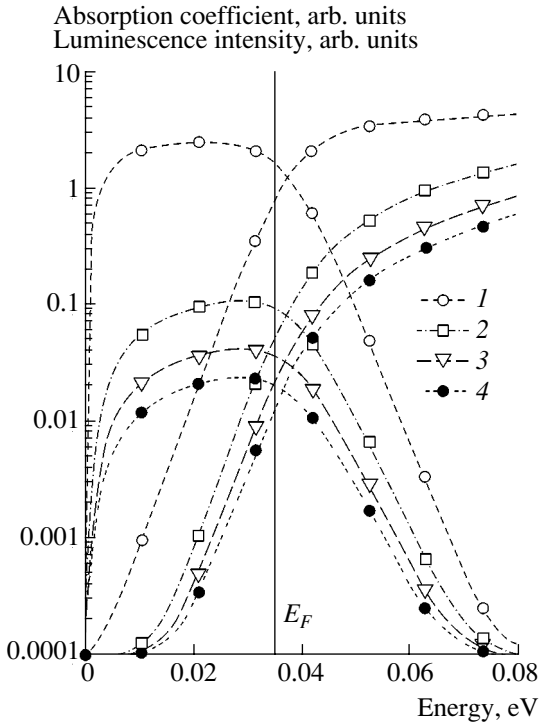

Fig. 25. Model calculation of how the absorption coefficient and the shape of the PL bands are transformed because of the violation of the momentum conservation law. Curves *1–4* were obtained at $\Delta(Q^2/2M)$ = 0.02, 0.036, 0.050, and 0.060 eV, T = 40 K, and E_F = 0.035 meV. Electron to hole mass ratio 1 : 10. Energy reckoned from $E_g(n)$.

substantially changed under strong pumping because of the recombination of hot electrons and holes. An excitation pulse resulted in an increase in the electron concentration to $(n + \Delta n) = 3.2 \times 10^{18}$ cm^{-3}, and, therefore, the PL band was significantly broadened and its peak shifted to shorter wavelengths compared with its position under weak excitation. This shift of the band peak corresponded to an increase in the electron concentration during the excitation pulse. As the time delay of PL observation increased, the electron concentration decreased and the peak shifted to longer wavelengths. The time in which a quasi-thermalized carrier distribution with an effective temperature exceeding that of the lattice was attained was estimated to be 100 fs. The distribution corresponding to the temperature of the crystal lattice is established in 20 ps. In this case, the relaxation time depends on the energy of a recombining pair and is at a minimum at the short-wavelength wing of the PL band.

The estimates of [88] demonstrated that, at the initial instant of excitation, the effective temperature of carriers is as high as 1200 K and rapidly decreases as the time delay of PL observation increases. The rate of cooling decreases dramatically after the first 20 ps, after which the relaxation time is 300–400 ps, depending on the energy of emitted photons. The radiative lifetime was estimated in [88] to be 10.4 ns, which can presumably be considered a reasonable value for the case

of recombination of free electrons and holes. As a consequence, the authors of [88] believe that the time of PL decay is determined by the faster nonradiative recombination processes.

3.3.3.6. Role of the Urbach tails of the density of states. The fact that samples with a relatively low electron concentration on the order of $n \sim 10^{18}$ cm^{-3} could be obtained necessitated taking into account shallow localized electron and hole states, which form exponentially decreasing tails of the density of states of the valence and conduction bands. Tails of this kind appear in solid solutions and amorphous semiconductors [89–92] as a result of the random distribution of atoms of the solid solution over crystal lattice sites or structural imperfections randomly scattered over the crystal. The formation of the tails of localized states leads to significant changes in the spectra of interband absorption and PL.

In the case of heavily doped semiconductors, the role of a random factor can be played by the arrangement of doping centers.

In the case of moderate doping, one would expect localized hole states related to uncontrollable acceptor-type impurities and localized states of the conduction band to play a noticeable role in the formation of interband PL. Then the PL bands associated with the recombination of electrons and deeply localized holes whose Bohr radius is smaller than q_{TF}^{-1} are markedly redshifted, as in the case of GaAs and GaN, compared with the main band of interband PL. However, tails of shallower states are commonly formed in systems of this kind, together with deep states, and the optical transitions that involve these states form the Urbach tail of the PL band.

The origin of localized states that lie below the bottom of the conduction band may be associated with, for example, spatial fluctuations in the positions of shallow donors. For example, if the Bohr radius of a Coulomb center $a_B > q_{TF}^{-1}$, then the bound state on a single center will disappear, but a pair of such centers situated within a sphere of radius q_{TF}^{-1} may lead to the formation of a shallow localized state.

Let us consider a model description of the density of states for the example of the valence bands. The behavior of the density of states in the Urbach tail is usually well described in a wide energy range by the exponential law [89–92], which can be represented for holes as

$$\rho^h(\omega) = \rho_0^h \exp(-\hbar\omega/E_U^h), \tag{29}$$

where E_U^h is the characteristic Urbach energy, which determines the typical localization energy and the radius of the bound state, $r_{loc} = \sqrt{\hbar^2/2m_hE_U^h}$.

If the PL in a heavily doped *n*-type crystal is associated with unthermalized holes, then the presence of the Urbach tail of density of states at the valence band will be manifested only in the smearing of the long-wavelength wing of the PL band. A more complicated pattern may occur in the case when recombination of thermalized holes dominates. PL of this kind is observed in spectra of disordered systems, when excitons captured in localized states of the tail recombine under permanent and weak excitation.

By analogy with the situation in spectra of disordered systems, we consider that, at low temperature under conditions of fast relaxation of holes, the PL spectrum of a doped crystal is formed by recombination of holes in isolated states of the tail [91, 92]. As a model scheme (see Fig. 26a), let us represent the tail of the density of hole states as

$$\rho^h(E) \propto \left[\frac{(2m_h)^{3/2}V_0}{4\pi^2\hbar^3}\right]\sqrt{|E|} \tag{30}$$

in the range below the top of the valence band, where E is negative and $|E| > E_U^h/2$. In the region $E > -E_U^h/2$, the density of hole states can be represented as

$$\rho^h(E) \propto \left[\frac{(2m_h)^{3/2}V_0}{4\pi^2\hbar^3}\right] \times \sqrt{E_U^h/2}\exp[-(E - E_U^h/2)/E_U^h]. \tag{31}$$

As shown in [91, 92], for localized states of the tail that are isolated from one another the classical percolation theory in terms of the model of overlapping spheres then yields

$$\rho_{\text{isol}}^h(E) = \rho^h(E)\exp[-2.8N(E)/N(E_{ME})], \tag{32}$$

where $\rho^h(E)$ is the density of states and $N(E)$ is the integral density of states at an energy E. $N(E)$ can be written as

$$N(E) = \int_{\infty}^{E} dE_1\rho^h(E_1). \tag{33}$$

The energy $E_{ME}^h > 0$ has the meaning of a boundary below which, at $E < E_{ME}^h$, extended hole states appear because of the percolation over overlapping localized states. This energy can be regarded as the energy of the top of the valence band in a disordered system.

Using the approach developed for describing exciton luminescence in disordered solid solutions [91, 92], we assume that only isolated states are occupied in the case of fast energy relaxation of holes in the low-temperature limit. The steady-state occupancy of these states is not equilibrium because they are isolated, and, at low temperature and a weak level of excitation, the number of holes at a given localization energy is simply proportional to the density of states at this energy. Further, it may be considered that the thermal equilibrium between the population of isolated states and that of other excited states of holes is attained in a time that is

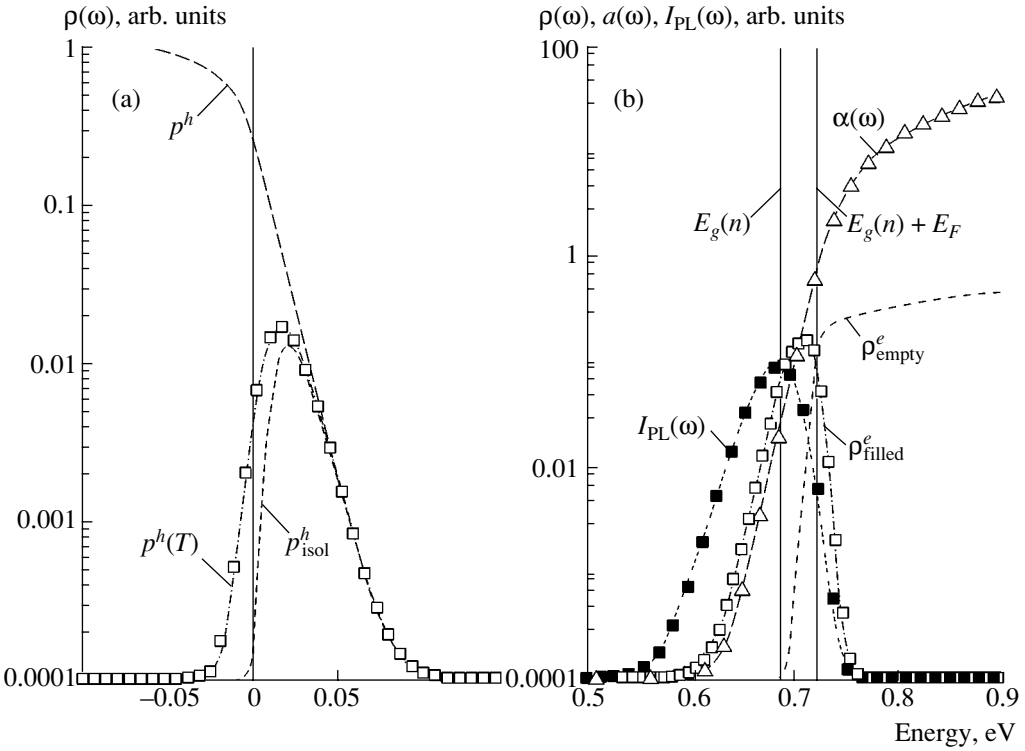

Fig. 26. (a) Scheme of states in the valence band in the presence of an Urbach density-of-states tail: ρ^h, density of states; p^h_{isol}, isolated states; $p^h(T)$, states with equilibrium population. (b) Scheme of states in the conduction band: ρ^e_{filled}, density of occupied states; ρ^e_{empty}, density of empty states; α, interband absorption coefficient; I_{PL}, PL band shape.

much shorter than the characteristic recombination time. Then, raising the temperature will result in an equilibrium population of the excited states of holes, whose density can be represented as

$$\rho^h_{excit}(E) = \rho^h(E)\{1 - \exp[-2.8N(E)/N(E_{ME})]\}, \quad (34)$$

and the equilibrium population $p^h(E)$ can be written as

$$p^h(E) = \frac{\rho^h_{isol}(E)}{Z(T)} + \int_{\infty}^{-\infty} dE_1 \left[\frac{\rho^h_{isol}(E_1)}{\overline{z_{isol}}}\right]\frac{\rho^h_{excit}(E)}{Z(T)}\exp[(E_1 - E)/T]. \quad (35)$$

Here,

$$\overline{z_{isol}} = \int_{\infty}^{-\infty} dE\rho^h_{isol}(E) \quad (36)$$

and

$$Z(T) = \overline{z_{isol}} + \int_{\infty}^{-\infty} dE \int_{\infty}^{-\infty} dE_1 \left[\frac{\rho^h_{isol}(E_1)}{\overline{z_{isol}}}\right]\rho^h_{excit}(E)\exp[(E_1 - E)/T]. \quad (37)$$

In the low-temperature limit, $T \ll E^h_U$, the statistical sum $Z(T) \longrightarrow \overline{z_{isol}}$ and the population $\rho^h_{isol}(E)$ reproduces $p^h(E)$, whereas in the high-temperature limit, $T \gg E^h_U$, it gives a Boltzmann population of the extended states.

We represent the density of states of the conduction band $\rho^e(E)$ (see Fig. 26b) in a form similar to (30) and (31):

$$\rho^e(E) \propto \left[\frac{(2m_e)^{3/2}V_0}{4\pi^2\hbar^3}\right]\sqrt{E - E_g(n)} \quad (38)$$

at $[E - E_g(n)] > E^e_U/2$ and

$$\rho^e(E) \propto \left[\frac{(2m_e)^{3/2}V_0}{4\pi^2\hbar^3}\right]\sqrt{E^e_U/2} \times \exp\{-[|E - E_g(n)| - E^e_U/2]/E^e_U\} \quad (39)$$

at $[E - E_g(n)] < E^e_U/2$, where E^e_U is the characteristic Urbach energy, which determines the typical energy of electron localization.

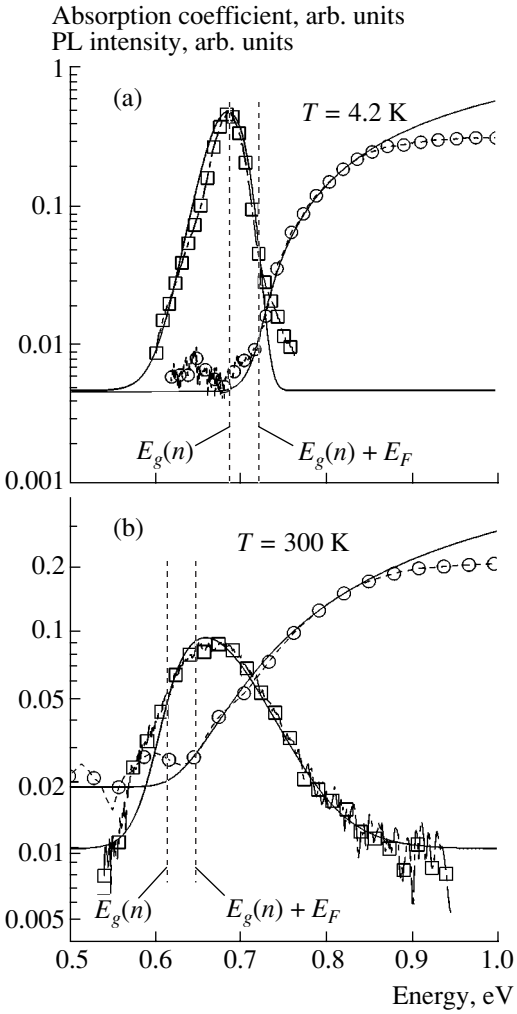

Fig. 27. PL and absorption spectra of an InN sample with an electron concentration of ~1×10^{18} cm^{-3} at T = (a) 4.2 and (b) 300 K; points: experiment; solid lines: calculation. Two vertical dashed lines show the values of the parameters $E_g(n)$ and $[E_g(n) + E_F]$.

Then the PL intensity can be represented as

$$I_{PL}(\omega) \propto \int_{E_g(n)}^{\infty} \rho^e(E)dE \times \int_{\infty}^{-\infty} dE_1 p^h(E_1)\Phi_{E,E_1} \frac{\delta[\hbar\omega - E_g(n) - E + E_1]}{\exp[(E - E_F)/T] + 1}. \quad (40)$$

Here $\Phi_{E,E_1} = \left|\int d^r \psi_E^e(r)\psi_{E_1}^h(r)\right|^2$ is the overlapping integral between the electron and hole wave functions.

The result of a model calculation of the PL band shape is shown in Fig. 26b. The same figure shows the characteristic energies in the spectrum: $E_g(n)$ and $[E_g(n) + E_F]$. It can be seen that the shape of the PL band is shifted with respect to the shape of the density of filled electron states. This shift is due to the presence of the Urbach tail of the valence bands, because the shape of the PL band is a convolution of the curves that describe the population of electron and hole states.

An example of a description of the PL band shape and of the absorption spectrum that takes account of the Urbach tails of the conduction band and valence bands is shown in Fig. 27 for an InN crystal with an electron concentration of about 1×10^{18} cm^{-3} at T = 4.2 K and room temperature. Agreement between the experimental data and the results of the calculation was achieved at Urbach energies of 10 meV for each of the bands.

3.3.4. PL excitation spectra and spectra of photomodulated reflection from heavily doped semiconductors. A study of PL excitation spectra and spectra of photomodulated reflectance provides additional insight into the nature of light-emitting states.

3.3.4.1. PL excitation spectra. At first sight, it seems that the excitation spectrum of interband recombination of free electrons and photogenerated holes should reproduce the spectrum of interband absorption. Such a situation would be expected if all the photogenerated holes recombined with emission of photons. However, only a relatively small number of holes live sufficiently long and have enough time to recombine with electrons from the conduction band. Most of the holes disappear via nonradiative recombination, as result of which the quantum yield of PL is markedly different from unity.

It may be assumed that the fraction of holes that disappear via nonradiative recombination depends on their ability to move along the crystal. If a hole is created in a localized state, its further fate depends on the concentration of traps and on whether or not the wave function of this hole overlaps with the position of the trap that provides nonradiative recombination. The quantum yield of PL depends on the probability of capture of a localized hole in a time τ_{rad}, i.e., on the product $w_{nr}(E)\tau_{rad}$, as

$$\exp[-w_{nr}(E)\tau_{rad}],$$

where the capturing probability $w_{nr}(E)$ depends on the energy of hole localization. This quantity must included as a weighting coefficient when calculating the PL intensity.

In the case when a hole is created in an extended state, we should find the probability of its capture by a trap, $w_{trap}(E)$, during the time of radiative recombination, τ_{rad}. As a result, the intensity of PL via recombination of a hole with an energy E should include a factor of the form

$$\exp[-w_{trap}(E)\tau_{rad}].$$

As the processes of capture of localized and mobile holes are different, one would expect the type of dependence on the energy $\hbar\omega$ of the exciting photon in the PL excitation spectrum to change when this energy

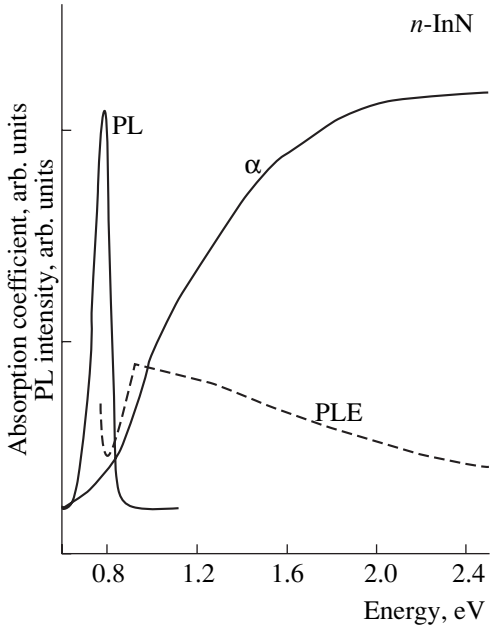

Fig. 28. Comparison of the absorption (α), photoluminescence (PL), and PL excitation (PLE) spectra. Taken from [15].

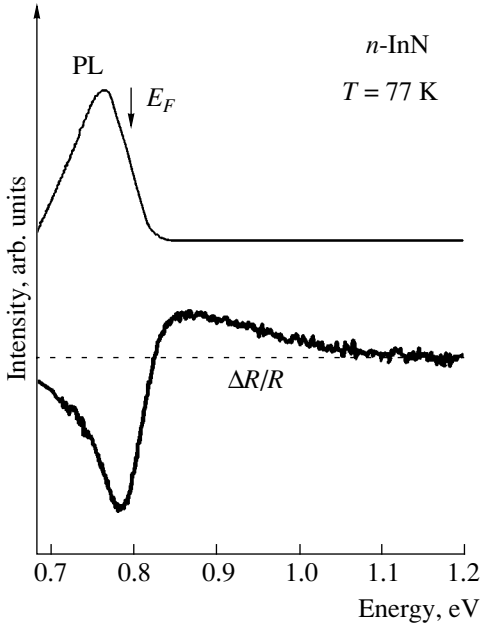

Fig. 29. Photoluminescence (PL) and photomodulated reflectance ($\Delta R/R$) spectra of an InN sample. Taken from [15].

becomes equal to the transition energy, $\hbar\omega \approx [E_{ME} + E_g(T) + E_F]$. If the photon energy exceeds this threshold value, the creation of a mobile hole with the transition of an electron to unoccupied states of the conduction band becomes possible.

Figure 28 shows the PL excitation spectrum. It can be seen that this spectrum exhibits a sharp drop at energies at which the absorption is still far from its maximum value. Thus, it seems natural to relate this drop to the attainment of the threshold energy $\hbar\omega = [E_{ME} + E_g(T) + E_F]$, when a hole is created in an extended state upon absorption of a photon.

3.3.4.2. Photomodulated reflection spectra. An interesting opportunity to study emitting interband transitions in heavily doped semiconductors is provided by photomodulated reflection spectra. A representative spectrum is shown in Fig. 29. The modulating illumination leads to an additional varying population of hole states and to a similar variation in the population of electron states near the Fermi surface. As a result, modulation $\delta\chi(\omega)$ of the dielectric susceptibility $\chi(\omega)$ of the crystal and, accordingly, of its reflectance occurs. The signal recorded in this case can be represented as

$$\frac{\Delta R}{R} = \frac{8\eta^2\kappa[\delta\chi''(\omega)]}{[(\eta-1)^2+\eta^2\kappa^2][(\eta+1)^2+\eta^2\kappa^2]}. \quad (41)$$

We assume that minor changes in the distribution of holes and electrons can be described using equilibrium distribution functions taken at an effective temperature T^*. Using the same assumptions on which expression (40) was derived, we obtain the dependence of the modulated reflectance signal on frequency and temperature in the form

$$\frac{\Delta R}{R} \propto \int_{E_g(n)}^{\infty} \rho^e(E)dE \int_{\infty}^{-\infty} dE_1 \Phi_{E,E_1} \times \delta(\hbar\omega - E_g(n) - E + E_1)\left[\frac{p^*(E_1)n^*(E) - p(E_1)n(E)}{T^* - T}\right]. \quad (42)$$

Here, $p^*(E_1)$ and $n^*(E)$ are the occupancy functions for hole and electron states in the presence of a modulating signal, i.e., at a temperature T^*, and $p(E_1)$ and $n(E)$ are the same functions in the absence of a modulating signal at a temperature T. This relation accounts for the modulation of the populations for both holes and electrons.

It can be seen in Fig. 30 how the shape of the photomodulated reflectance spectrum changes when temperature is varied in a wide range (disregarding the temperature shrinkage of the band gap).

The results of the calculations (shown in Fig. 30) demonstrate that, as the temperature of the crystal is increased, the shape of the signal becomes more symmetric because of the increasing contribution from the change in the population of electron states near the Fermi surface. Thus, photomodulated reflectance spectra make it possible to judge the relative contribution from the population modulation for electrons and holes. Comparison of the calculated curves in Fig. 30 and the experimental spectrum of photomodulated reflectance in Fig. 29 demonstrates their good qualitative agreement.

3.3.5. "Wide-gap" InN samples. Extensive data have by now appeared in the literature that convincingly demonstrate the narrow width of the band gap in

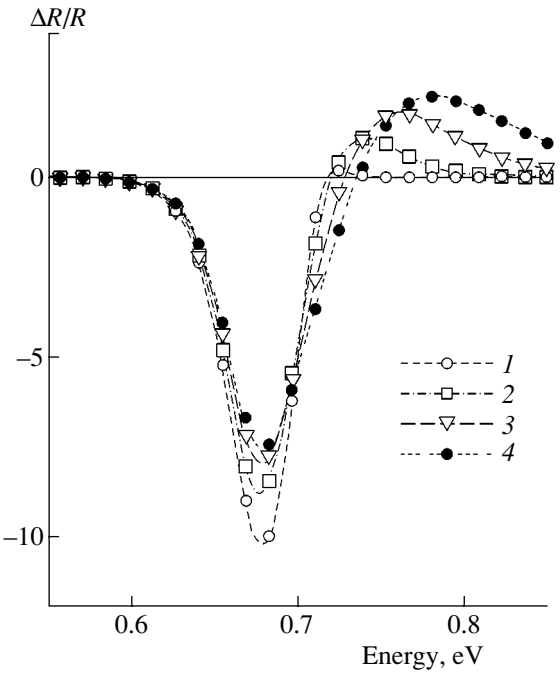

Fig. 30. Model temperature dependence of a photomodulated reflectance spectrum: curves *1–4* were obtained for T = 40, 120, 200, 280, and 360 K. The parameters of an InN sample with an electron concentration of ~1×10^{18} cm^{-3} were used in the calculation.

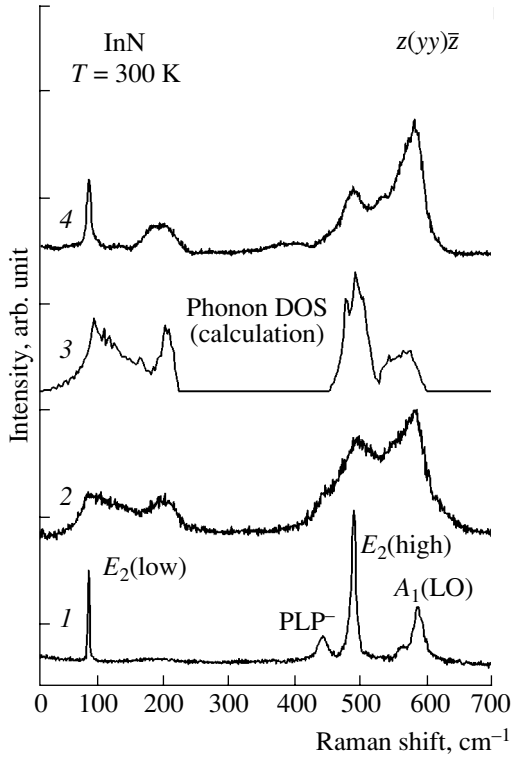

Fig. 31. Raman spectra of single-crystal InN (*1*) before and (*2*) after irradiation with N^+ ions; (*3*) Calculated phonon density of states of InN; and (*4*) Raman spectrum of an InN sample with an interband absorption threshold at about 1.9 eV (synthesized by MOVPE on an Al_2O_3 substrate). Taken from [15].

hexagonal InN. These results have been obtained on single-crystal layers that have high structural perfection, quite a low free-electron concentration (on the order of ~10^{18} cm^{-3}), and exhibit a good stoichiometry with a low oxygen content on the order of 1 at %.

At the same time, there are some publications [7, 93, 94] in which an absorption threshold of about 1.9–2.1 eV is reported for InN samples. These materials were grown by different methods on different substrates but had quite a number of coincident or close properties, which are described below.

(1) The transmission spectra demonstrated the presence of a plasma reflectance edge in the near-IR spectral range, which was indicative of a high electron concentration (up to 5×10^{20}–1×10^{21} cm^{-3}) in these films.

(2) The samples were polycrystalline, as followed from the very large width of rocking curves in X-ray measurements.

(3) First-order Raman spectra reproduced the phonon density-of-states function, in contrast to the narrow polarized lines for single-crystal samples (see, e.g., Fig. 31). Thus, the X-ray and Raman studies confirm the presence of a high concentration of crystal lattice defects in the samples in question.

(4) An elemental analysis by means of Auger spectroscopy and the Rutherford backscattering method revealed a rather high content of oxygen in materials of this kind. According to this parameter, the samples can be divided into two groups.

In the first group, the content of oxygen is higher than that in "narrow-gap" InN samples but does not exceed 3–5 at %. The crystal lattice parameters of these materials are close to those of single-crystal InN films discussed in this review. We therefore believe that the formation of indium oxide phases in the given set of samples is insignificant and the high electron concentration is determined by oxygen acting as a dopant. As a consequence, the Burstein–Moss effect is presumably the main reason why the optical absorption edge is shifted in the first group of samples.

The second group of samples is characterized by a high oxygen content (up to 20 at %). Such a high oxygen content leads to a strong modification of the crystal lattice constants (c = 5.7680 Å). Note that it is this value of the crystal lattice constant that was observed for the samples used in [7]. The considerable difference between the crystal lattice parameters of these samples, on the one hand, and their values for single-crystal InN, on the other, may indicate that InN–In_2O_3 solid solutions are formed. Taking into account the fact that the compound In_2O_3 has a band gap of 3.7 eV, it may be concluded that the shift of the optical absorption edge should be strongly affected not only by the Burstein–Moss effect, but also by the presence of oxide phases.

The above considerations were additionally confirmed by the experiments with postgrowth thermal

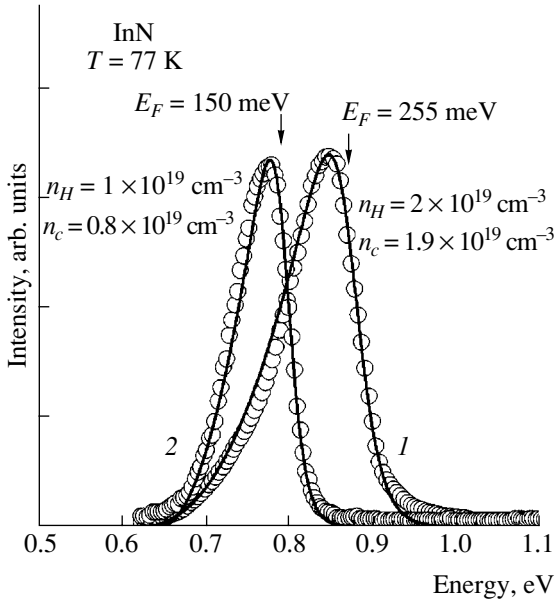

Fig. 32. PL spectra of InN samples (*1*) before and (*2*) after annealing in a vacuum. Points: experiment; solid lines: fits. Concentration: n_H, from Hall measurements; n_c, found by calculating the band shape. Taken from [48].

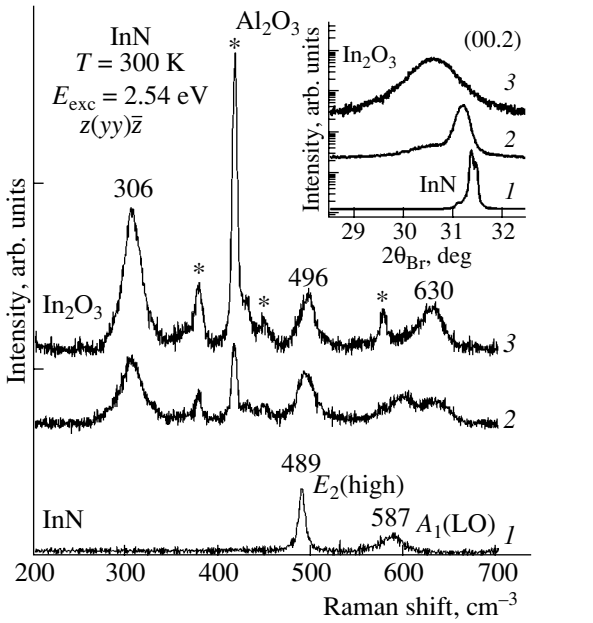

Fig. 33. Raman spectra of (*1*) an as-grown InN sample and InN samples annealed in oxygen at 400°C for (*2*) 12 and (*3*) 18 h. Inset: X-ray spectra of the same samples. Taken from [95].

treatment of single-crystal InN films, which are described below.

3.3.5.1. Results of experiments with postgrowth treatment of InN samples. To determine how the band gap of InN depends on the quality of the crystals, the influence exerted by postgrowth thermal treatment of single-crystal films on their optical properties has been studied [15, 95].

(a) Some of the InN samples were annealed in a vacuum at 490°C for 5 h. As can be seen in Fig. 32, this led to a significant decrease in the FWHM of the PL band and to a simultaneous increase in the slope of its short-wavelength wing. This result can be interpreted as a consequence of a decrease in the free-electron concentration and a leveling of the nonuniformity of charge distribution over the crystal. In this case, the Hall data actually showed a decrease in the electron concentration.

(b) In contrast to the first experiment, the result of annealing in an atmosphere of oxygen was that single-crystal InN, which is nontransparent in the visible, was transformed into an optically transparent (pinkish) material, and its optical absorption edge was shifted to 2 eV at an oxygen content of about 20 at %.

Both the absorption and the PL show that broad bands of localized states with an Urbach-like density-of-states distribution are formed upon annealing in oxygen; these bands extend as far as the optical absorption threshold.

X-ray and Raman data (see Fig. 33) indicate that InN–In_2O_3 alloys are formed. It is this fact that, in all probability, leads in this case to a strong shift of the optical absorption edge.

As suggested by the PL spectra of InN films whose absorption edge lies at about 2 eV, these samples still contain InN fragments. The PL band of such samples (see Fig. 34) is somewhat shifted to shorter wavelengths, which may be due to the confinement effect associated with the small size of these fragments. The final stage of oxidation is the formation of In_2O_3 crystals.

3.3.5.2. Irradiation with protons. It is well known that radiation experiments can yield a considerable body of information about properties of point defects in semiconductors. In [96], the effect of irradiation with 150-keV protons on crystalline InN was studied. For thin films with a thickness of about (or less than) one micrometer, such "shoot-through" irradiation makes it only possible to study point defects in a crystal (without passivation and compensation with hydrogen atoms). It was established that the irradiation leads to an effective formation of very shallow donor centers, with the result that the free-electron concentration in the irradiated material grows rapidly.

Judging by the kinetics of their accumulation, these defects can be regarded as intrinsic. They are stable at room temperature and start to be annealed out at temperatures of about 200°C. Based on theoretical considerations (see, e.g., [97]), these defects can be identified as vacancies in the nitrogen sublattice. Also of interest is the behavior of the band at 590 cm^{-1}, which appears in Raman spectra of the initial and the irradiated samples and is identified as the L_-–LO mode of Raman scattering. It was found that the intensity of this band almost linearly depends on the irradiation dose. Apparently, the irradiation generates those same defects that

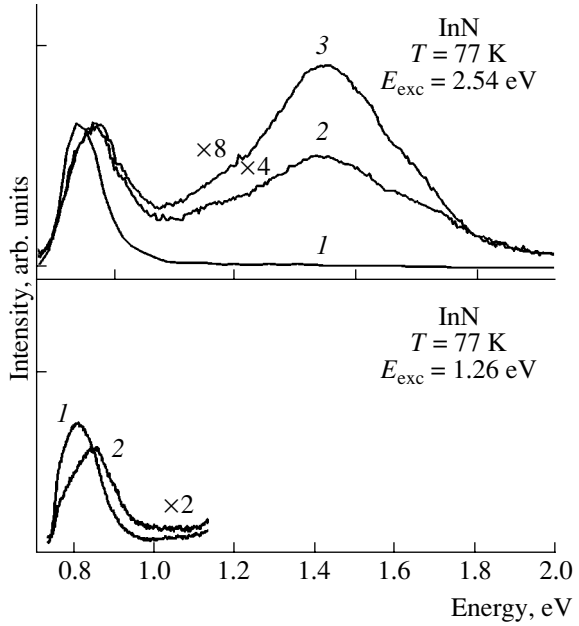

Fig. 34. Upper panel: PL spectra of (*1*) an as-grown InN sample and InN samples annealed in oxygen at 400°C for (*2*) 12 and (*3*) 18 h. Excitation energy E_{exc} = 2.54 eV. Lower panel: PL spectra of (*1*) an as-grown InN sample and (*2*) an InN sample annealed in oxygen at 400°C for 18 h. Excitation energy E_{exc} = 1.26 eV. Taken from [95].

are responsible for the same band in the starting material. Theoretical calculations show that the Raman scattering under consideration is associated with defects characterized by a short-range potential.

4. OPTICAL SPECTRA OF $In_xGa_{1-x}N$ SOLID SOLUTIONS

Isoelectronic solid solutions constitute a broad class of semiconducting materials formed by mixing compounds composed of different chemical elements from the same group. The most widely occurring solid solutions have a structure of a ternary compound characterized by a simple formula $A_xB_{1-x}C$. Here, symbols A an B stand for elements of the same group and C represents an element that can form binary compounds AC and BC. In contrast to atoms of chemically foreign elements, isoelectronic atoms can in many cases substitute one another at crystal lattice sites in arbitrary proportions, so that the content x is generally not small. The chemical affinity of isoelectronic atoms means that the perturbation introduced into the electronic structure in the isoelectronic substitution may be primarily related to the difference between the energies of the electronic levels of the substituting and substituted atoms, and the lattice vibrations are mainly affected by the change in the mass of an atom.

The simplest approximation used to describe the electronic properties of a solid solution and the dynamics of its crystal lattice is based on replacing real atoms in the "impaired" sublattice with an atom that has an averaged characteristic $\bar{Q} = xQ_A + (1 - x)Q_B$. Such a replacement eliminates the main difficulty encountered in describing a solid solution, namely, the random arrangement of atoms A and B at sublattice sites. The "virtual" crystal formed in the case of such an averaging should have a spectrum similar to that of an ordered crystal and can be calculated using the known methods. This approximation can be used with good reason only if the perturbation introduced upon isoelectronic substitution can be considered weak. In general, if the perturbation is not small, a noticeable role can be played by those deviations from the virtual-crystal approximation that are associated with composition fluctuations in solid solutions.

In the case of isoelectronic solid solutions $In_xGa_{1-x}N$, one would expect large deviations from the simple linear interpolation to occur. This primarily refers to such an important characteristic as the band gap width. Publications devoted to the dependence of this parameter on the composition of $In_xGa_{1-x}N$ solid solutions are scarce, and the reported data are rather contradictory. Moreover, these data mostly refer to solid solutions with a high gallium content. This is mainly associated with the problem of phase segregation, which hinders the growth of high-quality solid solutions with a high In content ($x > 0.3$).

4.1. Spectra of Interband Absorption and PL of $In_xGa_{1-x}N$ Solid Solutions

Spectra of interband absorption and PL of $In_xGa_{1-x}N$ solid solutions with a high and medium content of In ($0.40 < x < 1$) were first studied in [45]. The samples were synthesized by PAMBE and MOMBE on sapphire substrates.

To determine how the band gap width of solid solutions depends on the content of In, samples with the best structural characteristics were selected.

Figure 35 shows X-ray diffraction spectra of the $In_xGa_{1-x}N$ samples studied. It can be seen that the X-ray spectra of the solid solutions are distinguished by their substantial broadening compared with the spectrum obtained for InN. This means that the $In_xGa_{1-x}N$ samples are even less perfect than InN crystals. However, no traces of phase separation or polymorphism were revealed in the X-ray data for the $In_xGa_{1-x}N$ samples studied; in this context, the Raman spectra of these samples were also studied (see below).

The band gap width of the solid solutions was estimated using data on interband optical absorption and PL. Figure 36 shows absorption and PL spectra of a number of $In_xGa_{1-x}N$ samples with an In content of $0.40 < x < 1$. In the range studied, the composition of the solid solution was initially determined using the Wegard rule on the basis of the lattice constant c obtained from X-ray measurements. The composition was refined by the method of Rutherford backscattering

for the same samples. In the case in question, this technique is more accurate as the data it provides does not depend whether or not the samples are strained. As can be seen from the figure, the optical absorption threshold steadily shifts to higher energies as the indium content decreases.

The interband PL bands of $In_xGa_{1-x}N$ are redshifted, like those of InN, with respect to the absorption threshold by an energy of about the FWHM of the PL band. Estimates of the free-carrier concentrations in the samples of solid solutions, which are based on optical spectral data, give values in the range $(4–7) \times 10^{19}$ cm^{-3}, which agrees well with the results of Hall measurements. Comparison of the relative positions of the PL bands and the absorption thresholds suggests that the behavior observed is a manifestation of the Burstein–Moss effect.

An analysis of the PL band shape similar to that made for InN [45] made it possible to determine the dependence of the parameter $E_g(n)$ on the composition of the solid solution (Fig. 37). In constructing the dependence of the band gap width in the entire range of compositions, published data on the position of the PL band for solid solutions with a high Ga content were also used [10–12].

As expected, the experimental dependence of the band gap width on the composition of the solid solution strongly deviates from a simple linear interpolation and is characterized by a high value of parameter b, which determines the extent of this deviation. The resulting dependence is well described by the equation

$$E_g = 3.493 - 2.843x - bx(1-x) \qquad (43)$$

with $b = 2.5$ eV. If one takes into account the fact that b is found in solid solutions only approximately, it may be considered that the previous estimate $b = 2.8$ eV [98], as well as the value $b \approx 2.3$ eV recently obtained in [49], are in good agreement.

The behavior of the dielectric function in a wide range of energies for $In_xGa_{1-x}N$ solid solutions with a high content of indium was recently analyzed in [81]. It was shown that, in the range of composition studied, the dielectric function retains features characteristic of indium nitride, and its structural singularities are shifted to energies higher than 0.7 eV as the gallium content increases (Fig. 38).

The results obtained for the dependence of the band gap width on the composition of the $In_xGa_{1-x}N$ solid solution are a good confirmation of the narrow band gap of InN.

4.2. Phonons in Hexagonal $In_xGa_{1-x}N$

The dynamics of the crystal lattice of hexagonal $In_xGa_{1-x}N$ was theoretically analyzed in [99]. The calculations performed demonstrated that the selection rules characteristic of InN should be retained in the solid solution and all the Raman-active modes should exhibit a single-mode behavior in the entire range of compositions from InN to GaN. This means that the frequencies of all the modes should vary continuously with the composition of the solid solution between their values for InN and GaN.

Samples of hexagonal $In_xGa_{1-x}N$ with a high Ga content were studied experimentally by Raman spec-

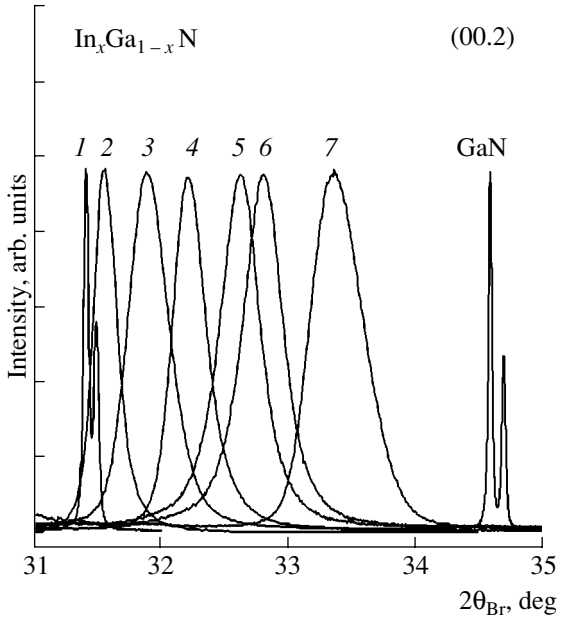

Fig. 35. X-ray spectra of $In_xGa_{1-x}N$, x: (*1*) 1, (*2*) 0.96, (*3*) 0.88, (*4*) 0.68, (*5*) 0.60, (*6*) 0.54, and (*7*) 0.40. The compositions were determined by the Rutherford backscattering method. Taken from [95].

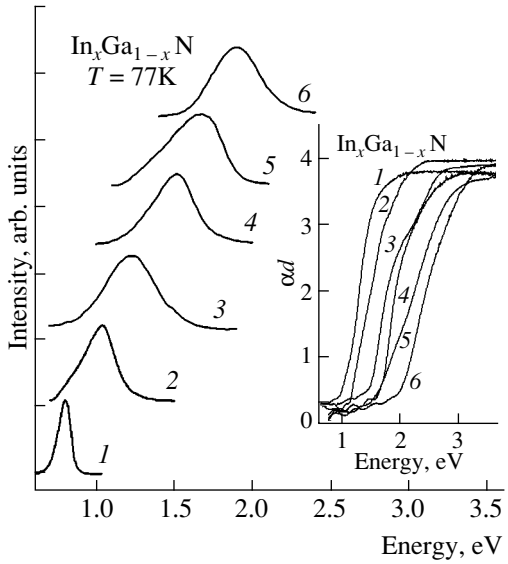

Fig. 36. PL and absorption (inset) spectra of $In_xGa_{1-x}N$ solid solutions, x: (*1*) 1, (*2*) 0.96, (*3*) 0.88, (*4*) 0.68, (*5*) 0.60, and (*6*) 0.40. The compositions were determined by the Rutherford backscattering method. Taken from [45].

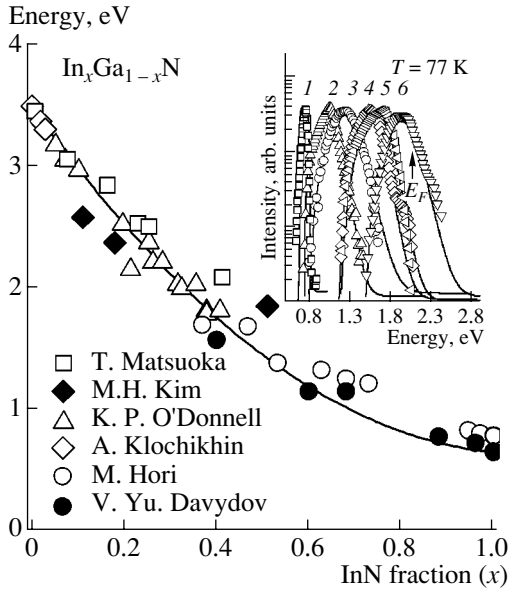

Fig. 37. Band gap width as a function of the composition of the $In_xGa_{1-x}N$ solid solution. Data for high and medium indium content were obtained by V.Yu. Davydov *et al.* [45] and M. Hori *et al.* [49]; data for low content were taken from M.H. Kim *et al.* [10], K.P. O'Donnell *et al.* [12], T. Matsuoka *et al.* [14], and A. Klochikhin *et al.* [92]. Inset: PL bands and results of fitting for InN and the most structurally perfect $In_xGa_{1-x}N$ solid solutions, x: (*1*) 1, (*2*) 0.96, (*3*) 0.88, (*4*) 0.68, (*5*) 0.60, (*6*) 0.40. Taken from [45].

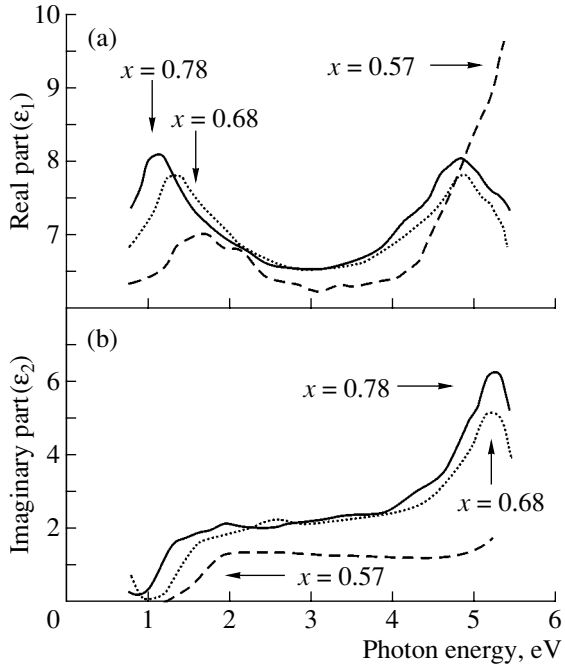

Fig. 38. (a) Imaginary and (b) real parts of the dielectric function of $In_xGa_{1-x}N$ for three values of x. Taken from [81].

troscopy in [100, 101]. As a result, data on the behavior of phonons of symmetry E_2 and A_1(LO) were obtained for the concentration ranges x = 0–0.11 [100] and x = 0–0.07 [101]. According to the data obtained, both types of phonons observed in Raman experiments show a single-mode type of behavior for the solid solution compositions studied, which agrees with the theoretical predictions [99].

Epitaxial $In_xGa_{1-x}N$ layers with a high and medium In content ($0.4 < x < 1$), grown by PAMBE and MOMBE on sapphire substrates, were studied in [95]. Figure 39 shows Raman spectra of the samples studied. The experimentally observed Raman spectra are similar to those of InN with a hexagonal structure, which indicates, as do the X-ray data, that the quality of the samples studied is rather good. It was established that the frequencies of all the modes observed in the experiment become high as the Ga content increases, while the single-mode type of behavior is preserved. Figure 40 shows the dependence of the frequencies of zone-center phonons in hexagonal $In_xGa_{1-x}N$ on the composition of the solid solution, which was calculated in [99], and also the experimental data obtained in [95]. A noteworthy feature is the nonlinearity of the experimentally observed dependence in the region with approximately the same content of In and Ga, which may be due to the scattering of phonons from composition fluctuations in the solid solution.

4.3. Broadening of Raman Lines of LO Phonons in $In_xGa_{1-x}N$

A study of the Raman spectra of $In_xGa_{1-x}N$ solid solutions with a high content of indium demonstrated that the spectrum contains a band at a frequency corresponding to the frequency of the unscreened LO phonon, despite the fact that the electron concentration in the sample studied is high. This means that, as in the case of InN, first-order scattering occurs with violation of the selection rule for the wave vector. As a result, the scattering involves excitations of the L_- branch, which have widely varying wave vectors and include LO phonons with large wave vectors, which weakly interact with free carriers.

As a study of how the FWHM of the band of LO phonons in solid solutions depends on In content has demonstrated, the Raman bands associated with LO phonons experience, in addition to a broadening that can be related to the dispersion of the L_- branch, an additional broadening dependent on the composition of the solid solution. The dependence of the broadening of this band on the composition of the solid solution is shown in Fig. 39 (inset).

A natural feature of solid solutions is composition fluctuations, which determine many aspects of their physical properties. These composition fluctuations are manifested in an inhomogeneous broadening of phonon lines in the vibrational spectrum of a solid solution, and the result is that their spectra differ considerably from those of perfect crystals. Studying this effect provides additional information about a solid solution because it answers the question of whether the distribution of

atoms over crystal lattice sites in a solid solution is random or not. Therefore, a study of how the broadening of the phonon lines depends on the composition of a solid solution makes it possible to estimate the degree of statistical disorder in a solid solution. The broadening of phonon lines in Raman spectra of solid solutions has been analyzed theoretically in terms of the perturbation theory [102–104] and with the use of a coherent-potential approximation [105, 106]. Both the approaches employed the so-called single-site approximation.

All the approaches to the problem of inhomogeneous broadening rely upon the assumption that the concept of phonons characterized in the zeroth approximation by a wave vector can be used to describe lattice vibrations, and that the elastic scattering of phonons can account for the inhomogeneous broadening observed.

The theory of phonon scattering from composition fluctuations in a solid solution involves various aspects of lattice vibrations in a disordered system.

First, note that describing the lattice dynamics in terms of phonons assumes that an averaged medium can be introduced instead of the real disordered system and the scattering of phonons that describe its motion from fluctuations placed in this medium can be considered. In this case, the type, size, and number of fluctuations, as well as the dependence of these parameters on the composition of the solid solution, are of fundamental importance for the problem under study.

Thus, two aspects of the problem should be considered: dynamical and statistical. As was shown in [107], these two aspects of the problem can be separated in the case of the simplest random (single-site) fluctuations. The assumption that the type of solution to the problem that is obtained in the simplest case remains valid for statistical fluctuations of arbitrary scale makes it possible to find the main characteristics of the fluctuations that account for the dependence of the inhomogeneous broadening of phonon lines on the composition of a solid solution in the entire range of concentrations. The statistical factors that govern the dependence of the broadening on composition can be calculated quite accurately, and the dynamical part of the problem can be reduced to two physical parameters with a transparent physical meaning.

The disorder in the arrangement of atoms in a solid solution leads to violation of the law of wave-vector conservation and makes it possible for phonons with wave vectors $\mathbf{q} \neq \mathbf{k} - \mathbf{k}'$ that are not equal to the difference of the wave vectors of the incident and scattered photons to appear in a first-order Raman spectrum. This gives rise to an additional broadening of the spectral line, which is determined by the effectiveness of the elastic scattering of phonons, by the dispersion of the phonon branch, and by the range of values of the wave vectors that become allowed in the first-order Raman spectrum as a result of the disorder.

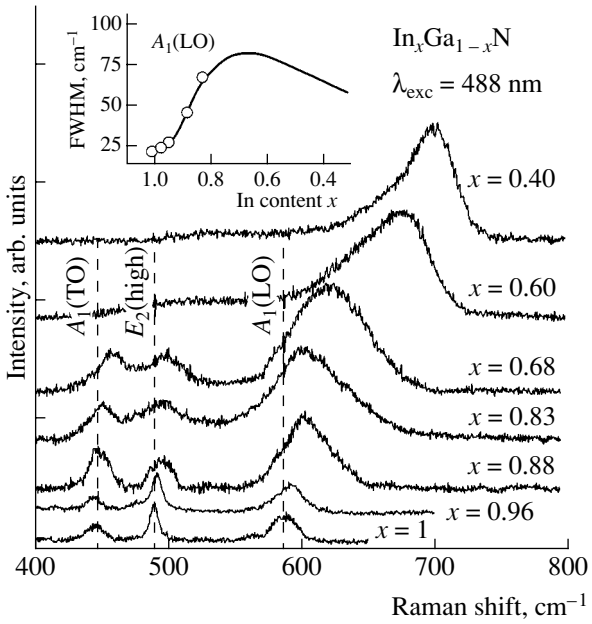

Fig. 39. Dependence of the frequencies of the bands in the Raman spectrum of an $In_xGa_{1-x}N$ solid solution on the composition of the solid solution. Inset: composition dependence of the FWHM of the band of LO phonons. Taken from [95].

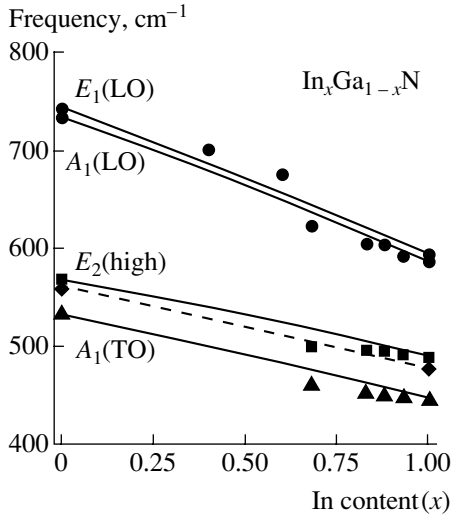

Fig. 40. Dependence of the frequencies of the optical phonons on the composition of the solid solution in the entire range of compositions. Points: data of [95]; solid lines: calculation from [99].

The shape of the phonon band, which appears because of elastic scattering of a phonon, can be written in the standard form

$$I_{ph}(\mathbf{k}-\mathbf{k}', \omega) \propto \frac{\gamma_{j\mathbf{q}}(\omega)}{[\omega^2 - \omega^2_{\mathbf{q},j} - \Delta_{j\mathbf{q}}(\omega)]^2 + \gamma^2_{j\mathbf{q}}(\omega)}, \quad (44)$$

where $\Delta_{j\mathbf{q}}(\omega)$ and $\gamma^2_{j\mathbf{q}}(\omega)$ are the real and imaginary parts of the scattering matrix, which determine the shift

of the phonon frequency and the broadening of the phonon line.

If $\gamma_{j\mathbf{q}}(\omega) \ll \omega_{\mathbf{q},j}$, then the band shape can be described using the Lorentz approximation, in which the broadening is considered to be constant,

$$\gamma_{j\mathbf{q}}(\omega) \longrightarrow \gamma_{j\mathbf{q}}(\omega_{\mathbf{q},j}). \tag{45}$$

A similar approximation is also valid in this case for the frequency shift $\Delta_{j\mathbf{q}}(\omega)$.

In general, expression (44) gives a more complex shape of the band, because $\gamma_{j\mathbf{q}}(\omega)$ depends on frequency and is the "weighted" density of one-phonon states of the jth branch.

The problem of phonon scattering from composition fluctuations in a solid solution is closely associated with the problem of the statistics of composition fluctuations. The approximation of single-site fluctuations, which is frequently used when considering the scattering problem, has a severely limited range of applicability: it is applicable only in the limiting cases of small x or $(1-x)$. As the In content x increases, the number of isolated single-site scattering centers decreases and scattering from fluctuations of larger size starts to dominate. In this case, it becomes necessary to find the number of such fluctuations, i.e., of clusters of atoms that replace the host atoms. The percolation theory is helpful in solving this problem.

As the content x of substituting atoms A in a solid solution $A_xB_{1-x}C$ increases, these atoms form clusters of steadily increasing size until the percolation threshold is reached. For simplicity, it can be considered that only a change in mass plays a significant part in scattering, and the change in the force constants can be disregarded. Then the percolation threshold over lattice sites in the disordered sublattice will mean the appearance of an infinite cluster for the substituting atoms. The number of clusters in the hexagonal sublattice can be found using the available data for a face-centered cubic lattice, with the insignificant difference between the wurtzite and sphalerite (zinc blende) crystal lattice structures ignored. The percolation over sites of the face-centered cubic sublattice appears when the content of atoms of type A $x \approx 0.2$. The same refers to atoms of type B for small $(1-x)$. The influence of clusters on the motion of phonons is the stronger, the greater the cluster size. At the same time, the number of clusters sharply decreases as the size grows. Therefore, below the percolation threshold at a content of substituting atoms that is not too high, clusters exist whose influence on the motion of phonons is the strongest. The scattering from such clusters that are not too large in size, or optimal, dominates up to $x \approx 0.10$–0.12, and when the content x increases further, it becomes necessary to consider scattering from relatively compact fragments of large clusters. It is convenient to search for the sizes of these compact regions over the entire range of contents x, both above and below the percolation threshold, with the use of data on the number of optimal clusters in order to reconcile the solution obtained at an arbitrary content with the cluster solution at $x \approx 0.10$–0.12.

Above the percolation threshold, at $x > 0.2$, nearly all atoms A belong to a percolation cluster [108–111]. A similar statement is valid for atoms B at $(1-x) > 0.2$. In the case of a chaotic distribution of atoms of two types, regions in which their concentrations differ significantly from the average over the crystal inevitably arise. The size of such regions and the deviation of the content from the average value, as well as the amplitude of a perturbation introduced by each atom, determine the effectiveness of phonon scattering from such a fluctuation and the range of wave vectors of phonons transferred in the course of scattering.

As shown in [107], it can be written for the dependence of the broadening of the phonon line on the composition x that

$$\gamma_{j\mathbf{k}-\mathbf{k}'}(\omega) \propto \{\mathcal{F}_{n,\bar{p}}[x,(1-x)]G_A + \mathcal{F}_{n,\bar{p}}[x \longleftrightarrow (1-x)]G_B\}, \tag{46}$$

where the statistical factors are given by

$$\mathcal{F}_{n,\bar{p}}[x,(1-x)] = (1-x)^2\left(\frac{x}{x+\bar{p}}\right)^{n(x+\bar{p})}\left(\frac{1-x}{1-x-\bar{p}}\right)^{n(1-x-\bar{p})}, \tag{47}$$

$$\mathcal{F}_{n,\bar{p}}[(1-x),x] = x^2\left(\frac{1-x}{1-x+\bar{p}}\right)^{n(1-x+\bar{p})}\left(\frac{x}{x-\bar{p}}\right)^{n(x-\bar{p})}. \tag{48}$$

The parameters G_A and G_B are in general frequency-dependent and have the meaning of a weighted single-phonon density of states of the jth branch. The first term in (46) describes the phonon scattering from fluctuations that contain an excess amount of atoms A compared with the average, and the second term, scattering from fluctuations with excess atoms B.

Note that the functions (47) and (48) are transformed into each other by replacing the argument x with $(1-x)$. The factor $\mathcal{F}_{n,\bar{p}}[x,(1-x)]$ is a well-defined function of the composition x of the solid solution in the range $0 \le x \le (1-\bar{p})$, which describes the probability of appearance of a scattering potential because of the deviation by $n\bar{p}$ from the average number n of atoms of the first type in a volume that contains n sublattice sites. Both the value and the type of the dependence of $\mathcal{F}_{n,\bar{p}}[x,(1-x)]$ are determined by the size n of the fluctuation and by the excess content $\bar{p}$ of atoms of the first type. The factor $\mathcal{F}_{n,\bar{p}}[(1-x),x]$ is defined in the interval $0 \le (1-x) \le (1-\bar{p})$ and has the

form of a mirror reflection with respect to the point $x = 0.5$ of the curve described by expression (47).

Similar statistical factors were determined in [107] in the range of x in which the scattering from clusters dominates, and it was shown that the factors (47) and (48) calculated at $\bar{p} = 0.2$ are well matched with these cluster factors in the range $x \le 0.10$. The value $\bar{p} = 0.2$ approximately corresponds to the percolation threshold in the fcc lattice, i.e., such an excess content makes it possible for $n\bar{p}$ excess atoms to form a percolation cluster of finite size n. The choice of n is determined in this case by that maximum size of the optimal cluster which is taken into account in calculations in the cluster region.

Because the statistical factors in the cluster region can be calculated exactly, the coincidence of the data obtained using the percolation theory and the results of calculations at high x can serve as a good criterion for the quality of the approximations employed.

The function $\mathcal{F}_{n,\bar{p}}[x, (1-x)]$ was derived via summation of contributions from all the fluctuations within the statistical-average deviation from the average fluctuation size n. Taking into account the fact that the probability of appearance of a fluctuation with $n\bar{p}$ excess atoms exponentially decreases as the size n increases, it may be stated that the function $\mathcal{F}_{n,\bar{p}}[x, (1-x)]$ gives a good estimate of the statistical factors in the probability of scattering for all fluctuations of size n or larger.

The dependence of the additional broadening of the band of the LO phonon for an $In_xGa_{1-x}N$ solid solution was calculated in accordance with expression (46) with the use of the statistical factors (47) and (48) at $n = 30$ and $\bar{p} = 0.20$. The absolute value and the asymmetry of the dependences of this broadening on the composition of the solid solution were provided by choosing one of the parameters G_A and G_B at a ratio of $G_A/G_B = 2$.

The experimental data are compared with the results of the calculation in the inset in Fig. 39. It can be seen that the theoretical curve reproduces the experimental dependence quite well, whose main distinctive feature is the clearly pronounced asymmetry of this curve with respect to the point $x = 0.5$. The agreement observed provides additional evidence that $In_xGa_{1-x}N$ solid solutions, which were studied by optical methods, can be considered disordered with good reason. Despite the fact that the solid solutions are less structurally perfect than InN, no traces of phase separation were revealed in Raman spectra of the $In_xGa_{1-x}N$ solid solutions in the range $0.40 < x < 1$.

5. CONCLUSION

The results of the studies carried out over the last three years, which are presented in this review, suggest that crystalline InN is a narrow-gap semiconductor with a band gap width of ~0.65–0.70 eV. Earlier studies were concerned with materials with an electron concentration of ~10^{20}–10^{21} cm^{-3}, whereas the best InN samples synthesized now have an electron concentration lower than 10^{18} cm^{-3}. It is this improvement of the physical parameters of InN crystals that made it possible to obtain new information about the fundamental characteristics of the electronic and vibrational spectra of this material. However, the quality of currently available InN crystals gives no way of eliminating the still existing ambiguity in estimates of the basic physical parameters. For example, only crystals in which the excitonic structure of the fundamental absorption edge can be observed will make it possible to determine such an important physical parameter as the exact band gap width.

The present interest in crystalline InN is manifested in the rapidly growing number of publications that report the results obtained in the leading laboratories of the United States, Australia, Japan, and Europe [112–140]. A number of conferences have been devoted, completely or largely, to precisely this material. This makes it virtually inevitable that this review will lag behind the present-day situation. The great interest shown in this semiconductor by the world's leading laboratories is an indication of the hope that this material will be widely used in electronics and optoelectronics in the near future.

6. ACKNOWLEDGMENTS

The authors are grateful to V. Emtsev, A. Mudryĭ, R. Seĭsyan, S. Ivanov, R. Suris, S. Permogorov, B. Novikov, F. Bechstedt, J. Furthmüller, J. Graul, J. Aderhold, H. Harima, A. Yamamoto, A. Hashimoto, E. Haller, T. Inushima, Y. Nanishi, M. Higashwaki, and A. Yoshikawa for helpful discussions and also to B. Ber, B. Vekshin, V. Kapitonov, D. Kurdyukov, V. Lebedev, V. Mamutin, A. Sakharov, A. Skvortsov, A. Smirnov, N. Shmidt, M. Shcheglov, and H. Feick for fruitful cooperation.

This study was financially supported by the Russian Foundation for Basic Research (grant nos. 03-02-17562 and 03-02-17565); the "Low-Dimensional Quantum Structures" program of the Presidium of the Russian Academy of Sciences; and the "Physics of Solid-State Nanostructures" program of the Ministry of Industry, Science, and Technology of the Russian Federation.

REFERENCES

1. S. N. Mohammad and H. Morkoc, Prog. Quantum Electron. **20**, 361 (1996).
2. S. Nakamura and G. Fasol, *The Blue Laser Diodes* (Springer, Berlin, 1997).
3. S. K. O'Leary, B. E. Foutz, M. S. Shur, *et al.*, J. Appl. Phys. **83**, 826 (1998).
4. J. B. McChesney, P. M. Bridenbaugh, and P. B. O'Connor, Mater. Res. Bull. **5**, 783 (1970).
5. V. A. Tyagaĭ, A. M. Evstigneev, A. N. Krasiko, *et al.*, Fiz. Tekh. Poluprovodn. (Leningrad) **11**, 2142 (1977) [Sov. Phys. Semicond. **11**, 1257 (1977)].

6. T. L. Tansley and C. P. Foley, Electron. Lett. **20**, 1066 (1984).
7. T. L. Tansley and C. P. Foley, J. Appl. Phys. **59**, 3941 (1986).
8. Q. Guo and A. Yoshida, Jpn. J. Appl. Phys., Part 1 **33**, 2454 (1994).
9. S. Yamaguchi, M. Kariya, S. Nitta, *et al.*, Appl. Phys. Lett. **76**, 876 (2000).
10. M. H. Kim, J. K. Cho, I. H. Lee, and S. J. Park, Phys. Status Solidi A **176**, 269 (1999).
11. C. C. Chuo, C. M. Lee, T. E. Nee, and J. I. Chyi, Appl. Phys. Lett. **76**, 3902 (2000).
12. K. P. O'Donnell, Phys. Status Solidi A **183**, 117 (2001).
13. T. Inushima, V. V. Mamutin, V. A. Vekshin, *et al.*, J. Cryst. Growth **227–228**, 481 (2001).
14. T. Matsuoka, H. Tanaka, T. Sasaki, and A. Katsui, in *Proceedings of 16th International Symposium on Gallium Arsenide and Related Compound* (1989), p. 141.
15. V. Davydov, A. Klochikhin, S. Ivanov, *et al.*, in *Nitride Semiconductors: Handbook on Materials and Devices*, Ed. by P. Ruterana, M. Albrecht, and J. Neugebauer (Wiley–VCH, Weinheim, 2003), p. 241.
16. Y. Nanishi, Y. Saito, and T. Yamaguchi, Jpn. J. Appl. Phys., Part 1 **42**, 2549 (2003).
17. A. G. Bhuiyan, A. Hashimoto, and A. Yamamoto, J. Appl. Phys. **94**, 2779 (2003).
18. H. J. Hovel and J. J. Cuomo, Appl. Phys. Lett. **20**, 71 (1972).
19. K. L. Westra, R. P. W. Lawson, and M. J. Brett, J. Vac. Sci. Technol. A **6**, 1730 (1988).
20. E. Burstein, Phys. Rev. **93**, 632 (1954).
21. J. W. Trainor and K. Rose, J. Electron. Mater. **3**, 821 (1974).
22. Q. Guo, O. Kato, and A. Yoshida, J. Appl. Phys. **73**, 7969 (1993).
23. O. Ambacher, M. S. Brandt, R. Dimitrov, *et al.*, J. Vac. Sci. Technol. B **14**, 3532 (1996).
24. S. Y. Karpov, Y. N. Makarov, and M. S. Ramm, MRS Internet J. Nitride Semicond. Res. **2** (Art. 45) (1997).
25. J. Ambacher, J. Phys. D: Appl. Phys. **31**, 2653 (1998).
26. T. Yodo, H. Ando, D. Nosei, and Y. Harada, Phys. Status Solidi B **288**, 21 (2001).
27. A. P. Lima, A. Tabata, J. R. Leite, *et al.*, J. Cryst. Growth **201–202**, 396 (1999).
28. A. Wakahara and A. Yoshida, J. Appl. Phys. **54**, 709 (1989).
29. Q. Guo, N. Yamamura, and A. Yoshida, J. Appl. Phys. **75**, 4927 (1994).
30. A. Yamamoto, M. Tsujino, M. Ohkubo, and A. Hashimoto, J. Cryst. Growth **137**, 415 (1994).
31. T. Tsuchiya, H. Yamano, O. Miki, *et al.*, Jpn. J. Appl. Phys. **38**, 1884 (1999).
32. A. Yamamoto, M. Tsujino, M. Chkubo, and A. Hasimoto, Sol. Energy Mater. **53**, 53 (1994).
33. Y.-C. Pan, W.-H. Lee, C.-K. Chu, *et al.*, Jpn. J. Appl. Phys. **38**, 645 (1999).
34. A. Yamamoto, Y. Murakami, K. Koide, *et al.*, Phys. Status Solidi B **228**, 5 (2001).
35. S. Yamaguchi, M. Kariya, S. Nitta, *et al.*, J. Appl. Phys. **85**, 7682 (1999).
36. W. E. Hoke, P. J. Lemonias, and D. G. Weir, J. Cryst. Growth **111**, 1024 (1991).
37. V. V. Mamutin, V. A. Vekshin, V. Yu. Davydov, *et al.*, Phys. Status Solidi B **176**, 247 (1999).
38. H. Lu, W. J. Schaff, J. Hwang, *et al.*, Appl. Phys. Lett. **79**, 1489 (2001).
39. Y. Saito, T. Yamaguchi, H. Kanazawa, *et al.*, J. Cryst. Growth **237**, 1017 (2002).
40. J. Aderhold, V. Yu. Davydov, F. Fedler, *et al.*, J. Cryst. Growth **222**, 701 (2001).
41. V. V. Ratnikov, V. V. Mamutin, V. A. Vekshin, and S. V. Ivanov, Fiz. Tverd. Tela (St. Petersburg) **43**, 913 (2001) [Phys. Solid State **43**, 949 (2001)].
42. M. Higashiwaki and T. Matsui, Jpn. J. Appl. Phys., Part 2 **41**, L540 (2002).
43. K. Xu and A. Yoshikawa, Appl. Phys. Lett. **83**, 251 (2003).
44. V. Yu. Davydov, A. A. Klochikhin, R. P. Seisyan, *et al.*, Phys. Status Solidi B **229**, R1 (2002).
45. V. Yu. Davydov, A. A. Klochikhin, V. V. Emtsev, *et al.*, Phys. Status Solidi B **230**, R4 (2002).
46. J. Wu, W. Walukiewicz, K. M. Yu, *et al.*, Appl. Phys. Lett. **80**, 3967 (2002).
47. T. Matsuoka, H. Okamoto, M. Nakao, *et al.*, Appl. Phys. Lett. **81**, 1246 (2002).
48. V. Yu. Davydov, A. A. Klochikhin, V. V. Emtsev, *et al.*, Phys. Status Solidi B **234**, 787 (2002).
49. M. Hori, K. Kano, T. Yamaguchi, *et al.*, Phys. Status Solidi B **234**, 750 (2002).
50. C. A. Arguello, D. L. Rousseau, and S. P. S. Porto, Phys. Rev. **181**, 1351 (1969).
51. H. J. Kwon, Y. H. Lee, O. Miki, *et al.*, Appl. Phys. Lett. **69**, 937 (1996).
52. M. C. Lee, H. C. Lin, Y. C. Pan, *et al.*, Appl. Phys. Lett. **73**, 2606 (1998).
53. T. Inushima, T. Shiraishi, and V. Yu. Davydov, Solid State Commun. **110**, 491 (1999).
54. V. Yu. Davydov, V. V. Emtsev, I. N. Goncharuk, *et al.*, Appl. Phys. Lett. **75**, 3297 (1999).
55. V. Yu. Davydov, A. A. Klochikhin, M. B. Smirnov, *et al.*, Phys. Status Solidi B **216**, 779 (1999).
56. A. Kasic, M. Schubert, Y. Saito, *et al.*, Phys. Rev. B **65**, 115206 (2002).
57. J. S. Dyck, K. Kim, S. Limpijumnong, *et al.*, Solid State Commun. **114**, 355 (2000).
58. G. Kaczmarczyk, A. Kaschner, S. Reich, *et al.*, Appl. Phys. Lett. **76**, 2122 (2000).
59. C. Bungaro, K. Rapcewicz, and J. Bernholc, Phys. Rev. B **61**, 6720 (2000).
60. H. M. Tutuncu, G. P. Srivastava, and S. Duman, Physica B (Amsterdam) **316–317**, 190 (2002).
61. V. V. Mamutin, V. A. Vekshin, V. Yu. Davydov, *et al.*, Phys. Status Solidi A **176**, 247 (1999).
62. V. V. Mamutin, V. A. Vekshin, V. Yu. Davydov, *et al.*, Phys. Status Solidi A **176**, 373 (1999).
63. D. Pines and P. Nozieres, *The Theory of Quantum Liquids* (Benjamin, New York, 1966; Mir, Moscow, 1967).

64. G. Abstreiter, M. Cardona, and A. Pinczuk, in *Light Scattering in Solids*, Ed. by M. Cardona and G. Guntherodt, 2nd ed. (Springer, Berlin, 1984; Mir, Moscow, 1986), Vol. 4, p. 12.
65. T. Kozawa, T. Kachi, H. Kano, *et al.*, J. Appl. Phys. **75**, 1098 (1994).
66. P. Perlin, J. Camassel, W. Knap, *et al.*, Appl. Phys. Lett. **67**, 2524 (1995).
67. H. Harima, H. Sakashita, and S. Nakashima, Mater. Sci. Forum **264–268**, 1363 (1998).
68. J. Menendez and M. Cardona, Phys. Rev. B **31**, 3696 (1985).
69. T. L. Tansley, in *Properties of Group III Nitrides*, Ed. by J. H. Edgar (INSPEC, London, 1994), p. 39.
70. V. Yu. Davydov, Yu. E. Kitaev, I. N. Goncharuk, *et al.*, Phys. Rev. B **58**, 12899 (1998).
71. K. Karch and F. Bechstedt, Phys. Rev. B **56**, 7404 (1997).
72. S. Krukowski, A. Witek, J. Adamczyk, *et al.*, J. Phys. Chem. Solids **59**, 289 (1998).
73. J. C. Nipko and C.-K. Loong, Phys. Rev. B **57**, 10550 (1998).
74. J. C. Nipko, C.-K. Loong, C. M. Balkas, and R. F. Davis, Appl. Phys. Lett. **73**, 34 (1998).
75. B. Wenzien, G. Cappelini, and F. Bechstedt, Phys. Rev. B **51**, 14701 (1995).
76. U. Grossner, J. Furthmüller, and F. Bechstedt, Phys. Rev. B **58**, R1722 (1998).
77. C. Stampfl and C. G. Van der Walle, Phys. Rev. B **59**, 5521 (1999).
78. F. Bechstedt, J. Furthmüller, M. Ferhat, *et al.*, Phys. Status Solidi A **195**, 628 (2003).
79. S.-H. Wei, X. Nie, I. G. Batyrev, and S. B. Zhang, Phys. Rev. B **67**, 165209 (2003).
80. R. Loudon, *The Quantum Theory of Light* (Clarendon Press, Oxford, 1973; Mir, Moscow, 1976).
81. R. Goldhahn, Acta Phys. Pol. A **104**, 123 (2003).
82. E. Kurimoto, H. Harima, A. Hashimoto, and A. Yamamoto, Phys. Status Solidi B **228**, 1 (2001).
83. A. A. Gutkin and A. Stano, Fiz. Tekh. Poluprovodn. (Leningrad) **5**, 96 (1971) [Sov. Phys. Semicond. **5**, 79 (1971)].
84. G. E. Pikus, *Fundamentals of the Theory of Semiconductor Devices* (Nauka, Moscow, 1965) [in Russian].
85. M. Gell-Mann and K. A. Brueckner, Phys. Rev. **106**, 364 (1957).
86. Y. Ishitani, K. Xu, W. Terashima, *et al.*, Phys. Status Solidi C **0**, 2838 (2003).
87. B. P. Zakharchenya, D. N. Mirlin, V. I. Perel', and I. I. Reshina, Usp. Fiz. Nauk **136**, 459 (1982) [Sov. Phys. Usp. **25**, 143 (1982)].
88. F. Chen, A. N. Cartwright, H. Lu, and W. J. Schaff, Appl. Phys. Lett. **83**, 4984 (2003).
89. A. A. Klochikhin and S. G. Ogloblin, Phys. Rev. B **48**, 3100 (1993).
90. A. A. Klochikhin, Phys. Rev. B **52**, 10979 (1995).
91. A. A. Klochikhin, S. A. Permogorov, and A. N. Reznitskiĭ, Fiz. Tverd. Tela (St. Petersburg) **39**, 1170 (1997) [Phys. Solid State **39**, 1035 (1997)].
92. A. Klochikhin, A. Reznitsky, S. Permogorov, *et al.*, Phys. Rev. B **59**, 12947 (1999).
93. M. Yoshimoto, H. Yamamoto, W. Huang, *et al.*, Appl. Phys. Lett. **83**, 3480 (2003).
94. A. G. Bhuiyan, K. Sugita, K. Kasashima, *et al.*, Appl. Phys. Lett. **83**, 4788 (2003).
95. V. Yu. Davydov, A. A. Klochikhin, V. V. Emtsev, *et al.*, Phys. Status Solidi B **240**, 425 (2003).
96. V. V. Emtsev, V. Yu. Davydov, E. E. Haller, *et al.*, Physica B (Amsterdam) **308**, 58 (2001).
97. C. Stampfl, C. G. Van de Walle, D. Vogel, *et al.*, Phys. Rev. B **61**, R7846 (2000).
98. A. Reznitsky, A. Klochikhin, S. Permogorov, *et al.*, Phys. Status Solidi C **0**, 280 (2002).
99. H. Grille, Ch. Schnittler, and F. Bechstedt, Phys. Rev. B **61**, 6091 (2000).
100. D. Behr, R. Niebuhr, H. Obloh, *et al.*, Mater. Res. Soc. Symp. Proc. **468**, 213 (1997).
101. H. Harima, E. Kurimoto, Y. Sone, *et al.*, Phys. Status Solidi A **216**, 785 (1999).
102. A. A. Maradudin, E. W. Montroll, and G. H. Weiss, in *Solid State Physics* (Academic, New York, 1963), Suppl. 3 [*Theory of Lattice Dynamics in the Harmonic Approximation* (Mir, Moscow, 1965)].
103. A. A. Maradudin, Rep. Prog. Phys. **28**, 331 (1965).
104. A. A. Maradudin, Solid State Phys. **18**, 273 (1966); Solid State Phys. **19**, 1 (1966).
105. B. Velicky, S. Kirkpatrick, and H. Ehrenreich, Phys. Rev. **175**, 745 (1968).
106. R. J. Elliott, J. A. Krumhansl, and P. L. Leath, Rev. Mod. Phys. **46**, 465 (1974).
107. V. Yu. Davydov, I. N. Goncharuk, A. N. Smirnov, *et al.*, Phys. Rev. B **65**, 125203 (2002).
108. J. W. Essam, in *Phase Transitions and Critical Phenomena*, Ed. by C. Domb and M. S. Green (Academic, London, 1972), Vol. 2, p. 197.
109. J. W. Essam, Rep. Prog. Phys. **43**, 833 (1980).
110. A. Bunde and S. Havlin, in *Fractals and Disordered Systems*, Ed. by A. Bunde and S. Havlin (Springer, Berlin, 1994), p. 51.
111. M. F. Sykes, D. S. Gaunt, and M. Glen, J. Phys. A: Math. Gen. **9**, 1705 (1976).
112. J. Wu, W. Walukiewicz, K. M. Yu, *et al.*, Appl. Phys. Lett. **80**, 4741 (2002).
113. J. Wu, W. Walukiewicz, W. Shan, *et al.*, Phys. Rev. B **66**, 201403 (2002).
114. J. Wu, W. Walukiewicz, K. M. Yu, *et al.*, Solid State Commun. **127**, 411 (2003).
115. J. Wu, W. Walukiewicz, W. Shan, *et al.*, J. Appl. Phys. **94**, 4457 (2002).
116. J. Wu, W. Walukiewicz, K. M. Yu, *et al.*, J. Appl. Phys. **94**, 6477 (2003).
117. S. X. Li, J. Wu, E. E. Haller, *et al.*, Appl. Phys. Lett. **83**, 4963 (2003).
118. T. Inushima, M. Higashiwaki, and T. Matsui, Phys. Rev. B **68**, 235204 (2003).
119. D. B. Haddad, J. S. Thakur, V. M. Naik, *et al.*, Mater. Res. Soc. Symp. Proc. **743**, L11.22.1 (2003).

120. K. S. A. Butcher, M. Wintrebert-Fouquet, Motlan, *et al.*, Mater. Res. Soc. Symp. Proc. **743**, L11.23.1 (2003).
121. K. S. A. Butcher, H. Dou, E. M. Goldis, *et al.*, Phys. Status Solidi C **0**, 373 (2002).
122. Z. Dridi, B. Bouhafs, and P. Ruterana, Phys. Status Solidi C **0**, 315 (2002).
123. F. Demangeot, J. Frandon, C. Pinquier, *et al.*, Phys. Rev. B **68**, 245308 (2003).
124. Y. Nanishi, Y. Saito, T. Yamaguchi, *et al.*, Phys. Status Solidi A **200**, 202 (2003).
125. M. Higashiwaki, T. Inushima, and T. Matsui, Phys. Status Solidi B **240**, 417 (2003).
126. K. Sugita, T. Takatsuka, A. Hashimoto, and A. Yamamoto, Phys. Status Solidi B **240**, 421 (2003).
127. T. Yamaguchi, Y. Saito, C. Morioka, *et al.*, Phys. Status Solidi B **240**, 429 (2003).
128. M. Wintrebert-Fouquet, K. S. A. Butcher, and Motlan, Phys. Status Solidi C **0**, 2785 (2003).
129. K. Xu, N. Hashimoto, B. Cao, *et al.*, Phys. Status Solidi C **0**, 2790 (2003).
130. T. Araki, S. Ueta, K. Mizuo, *et al.*, Phys. Status Solidi C **0**, 2798 (2003).
131. T. Yodo, H. Yona, Y. Harada, *et al.*, Phys. Status Solidi C **0**, 2802 (2003).
132. T. Matsuoka, H. Okamoto, and M. Nakao, Phys. Status Solidi C **0**, 2806 (2003).
133. F. Matsuda, Y. Saito, T. Muramatsu, *et al.*, Phys. Status Solidi C **0**, 2810 (2003).
134. K. Xu, W. Terashima, T. Hata, *et al.*, Phys. Status Solidi C **0**, 2814 (2003).
135. V. Cimalla, Ch. Forster, G. Kittler, *et al.*, Phys. Status Solidi C **0**, 2818 (2003).
136. T. Inushima, M. Higashiwaki, T. Matsui, *et al.*, Phys. Status Solidi C **0**, 2822 (2003).
137. M. Drago, T. Schmidtling, U. W. Pohl, *et al.*, Phys. Status Solidi C **0**, 2842 (2003).
138. V. N. Jmerik, V. A. Vekshin, T. V. Shubina, *et al.*, Phys. Status Solidi C **0**, 2846 (2003).
139. O. Briot, B. Maleyre, S. Ruffenach, *et al.*, Phys. Status Solidi C **0**, 2851 (2003).
140. E. Kurimoto, M. Hangyo, H. Harima, *et al.*, Appl. Phys. Lett. **84**, 212 (2004).

Translated by M. Tagirdzhanov

Semiconductors, Vol. 38, No. 8, 2004, pp. 899–908. Translated from Fizika i Tekhnika Poluprovodnikov, Vol. 38, No. 8, 2004, pp. 937–948.

SYMPOSIUM ON THE EFFICIENT USE OF SOLAR RADIATION IN PHOTOVOLTAIC POWER ENGINEERING (St. Petersburg, November 3–4, 2003)

Solar Photovoltaics: Trends and Prospects

Zh. I. Alferov, V. M. Andreev*, and V. D. Rumyantsev

Ioffe Physicotechnical Institute, Russian Academy of Sciences, St. Petersburg, 194021 Russia

**e-mail: vmandreev@mail.ioffe.ru*

Submitted February 9, 2004; accepted for publication February 11, 2004

Abstract—Key areas in the development of photovoltaic methods of solar energy conversion, which open up wide prospects for semiconductor solar energy conversion, are discussed. The article focuses mainly on photovoltaic cells based on III–V heterostructures, primarily on cascade solar cells, which provide the highest efficiency of solar energy conversion and are produced by high-tech methods such as MBE or MOCVD. It is shown that the use of intermediate sunlight concentration makes the area of solar cells smaller and, hence, lowers their cost proportionally to the sunlight concentration ratio. © *2004 MAIK "Nauka/Interperiodica".*

1. INTRODUCTION

In modern public opinion, there is a growing conviction that power engineering in the future must be based on the large-scale use of solar energy in all its diverse forms. The Sun is a vast, inexhaustible, and absolutely safe energy source, which belongs and is equally accessible to everyone. Counting on solar energy should be regarded not only as risk-free, but also as the only possible choice for humanity in the long run. We discuss the past and future prospects of possible ways of converting solar energy into electrical energy with the use of modern semiconductor photovoltaic cells. These devices have now matured scientifically and technologically to such an extent that they may be regarded as a technical basis for large-scale solar power engineering in the future.

2. THE EARLY STAGE OF SOLAR PHOTOVOLTAICS

The photovoltaic effect was first observed in an electrolytic cell by Edmond Becquerel in 1839. The first experiments with solid-state photocells based on selenium were performed by Adams and Day in London in 1876 [1]. It took more than half a century to develop the first solar photocells with an efficiency slightly exceeding 1%. These were sulfur–thallium photocells with a barrier layer that were developed at the Physicotechnical Institute [2]. The studies were performed under the direction of the founder of the institute, Academician A.F. Ioffe, who submitted a proposal to the Soviet government concerning the use of solar photovoltaic roofs as power sources. However, the real start of solar photovoltaics (even disregarding the economic considerations) demanded much higher efficiency. The decisive step in this direction was the development of silicon photocells with a *p–n* junction, which had an efficiency of about 6% [3]. The first practical application of silicon solar arrays as power sources was not on the Earth, but in near-Earth space. In 1958, satellites equipped with such arrays were launched: the Soviet *Sputnik-3* and American *Vanguard-1*.

It is worth noting that the scientific basis for first solar arrays was the development of the theory and technology of semiconductor materials and device structures with *p–n* junctions. At that time, it was foreseen that the main fields of application of semiconductor devices would be in the area of electric power conversion (ac-to-dc conversion, high-frequency generation, switching, etc.) and electronic devices for information transfer and processing (radio, communication, etc.). In addition to the "classical" semiconductor materials Ge and Si, the synthesis of III–V materials began in 1950 [4]. The first GaAs solar cells with a *p–n* junction were produced in the early 1960s. Their efficiency was lower than that of Si photocells, but they were capable of operating even when heated considerably. The first practical application of improved GaAs solar arrays as a power source was even more exotic than in the case of silicon ones. They provided the power supply for the Soviet space probes operating in the vicinity of Venus (1965) and the lunar surface rovers *Lunokhod-1* and *Lunokhod-2* (1970 and 1972).

3. HETEROSTRUCTURE SOLAR CELLS

The design of AlGaAs–GaAs heterostructure solar cells opened up new fields in solar power conversion [5]. Once again, an important contribution was made by the Ioffe Physicotechnical Institute. In the second half of the 1960s, pioneering studies were performed here in the fabrication and investigation of "ideal" heterojunctions in the AlAs–GaAs system, which were aimed at improving solar cells, among other things.

One of the results of these studies of heterojunctions was the technical implementation of the idea of a wide-gap window for solar photocells. This idea was suggested earlier, and its aim was to protect the photoactive

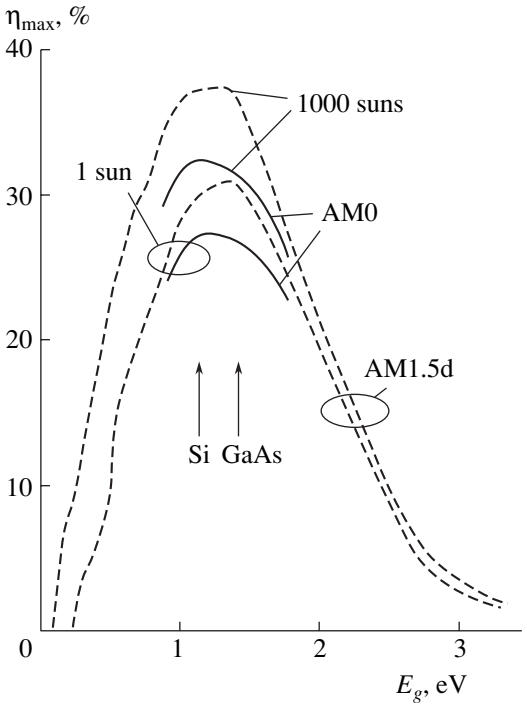

Fig. 1. Maximum accessible conversion efficiency (η_{max}) of a solar cell with a single *p–n* junction as a function of the material band gap width E_g. Solid lines, AM0 solar spectrum; dashed lines, AM1.5d spectrum for unconcentrated (1 sun) sunlight and for 1000-fold concentration.

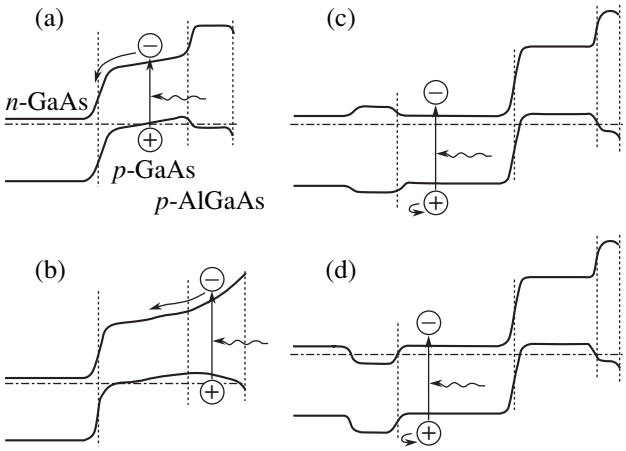

Fig. 2. Band diagrams of *p*-AlGaAs–*p–n*-GaAs heterojunction solar cells: (a) a structure in which a *p*-GaAs layer with a built-in electric field is produced by Zn diffusion into an *n*-GaAs base during the growth of a wide-gap *p*-AlGaAs layer; (b) a structure with a high built-in electric field; (c) a structure with a back wide-gap layer, which gives rise to the potential barrier; (d) a structure with a back potential barrier formed by a heavily-doped n^+-GaAs layer.

region of a cell against the influence of surface states. Defect-free heterojunctions between AlGaAs (wide-gap window) and *p–n* GaAs (photoactive region) were successfully formed, which provided ideal conditions for the photogeneration of electron–hole pairs and their collection by the *p–n* junction. Since photocells with a GaAs photoactive region turned out to be even more radiation-resistant, they quickly found an application in space technologies, despite their significantly higher cost compared to silicon cells. An example of a large-scale application of AlGaAs/GaAs solar cells was the solar array installed on the Soviet space station *Mir* (1986).

Silicon and GaAs largely meet the requirements for "ideal" semiconductor materials. If these materials are compared in terms of their suitability for fabricating solar cells with a single *p–n* junction, the maximum possible efficiencies of photovoltaic conversion are nearly the same and are close to the absolute maximum for a single-junction photocell (Fig. 1). Clearly, the undoubted advantages of silicon are its wide natural abundance, nontoxicity, and relatively low price. All these factors and the intensive development of the industry of semiconductor electronic devices have determined the extremely important role of silicon photocells in the formation of solar photovoltaics. Despite the considerable efforts applied to the development of various types of thin-film solar arrays, crystalline silicon (both in single- and polycrystalline modifications) still makes the greatest contribution to the world's production of solar arrays for terrestrial applications.

Until the mid-1980s, the development of solar photocells, both silicon and GaAs, was based on relatively simple structures and technologies. A planar structure with a shallow *p–n* junction produced by diffusion was used in silicon photocells. Epitaxial technologies were necessary for the formation of an AlGaAs wide-gap window on GaAs photocells. The relatively simple liquid-phase epitaxy (LPE) technique was applied, which was derived earlier for the fabrication of the first generation of heterostructure lasers. In the case of photocells, only one wide-gap *p*-AlGaAs layer had to be grown, whereas the *p–n* junction was formed by the diffusion of a *p*-type impurity from the melt into the base material of *n*-GaAs (Fig. 2a).

From the middle of the 1980s, high-tech methods began to penetrate the sphere of semiconductor solar photovoltaics. Complicated silicon photocell structures were proposed that allowed one to decrease both optical and recombination losses. Efforts were also made to improve the quality of the base material itself. The fabrication of these structures became possible owing to the application of multistage technological procedures, which by that time became a routine practice in the production of silicon-based integrated circuits. These efforts resulted in a steep rise in the photovoltaic conversion efficiency of silicon photocells [6]. The efficiency exhibited by the laboratory samples was close to the theoretical limit (Fig. 1). Unfortunately, the cost of these highly efficient silicon photocells was many times higher than that of conventional photocells.

At the same time, progress in the field of GaAs-based photocells was stimulated by the application of

new epitaxial techniques for heterostructure growth. The main achievement here was metal-organic chemical vapor deposition (MOCVD). This method was derived in the course of the development and improvement of injection lasers and second-generation photocells based on III–V compounds.

So what improvements were introduced into the structure of solar heterophotocells owing to the new technologies? First, the wide-gap AlGaAs window was optimized, and its thickness became comparable with that of the nanosized active regions in heterolasers. The AlGaAs layer also served as the third component in the triple-layered interference antireflection coating of a photocell (ARC, Fig. 3a). A heavily doped narrow-gap contact layer was grown on top of the wide-gap AlGaAs window, and it was removed during the post-growth treatment in the areas between the contact stripes. Second, a back (behind the *p–n* junction) wide-gap layer was introduced, which ensured, along with the front wide-gap layer, a double-sided confinement of photogenerated carriers within the region of light absorption (Fig. 2c). The recombination losses of carriers before their collection by the *p–n* junction were reduced. At this stage of the optimization of single-junction AlGaAs/GaAs photocell heterostructures, the newly developed MOCVD technique was still competing with the modified low-temperature LPE technique. So for these structures the record efficiency of 27.6% for illumination with concentrated AM1.5 sunlight was obtained in MOCVD-grown photocells (this value is an absolute record for photocells with a single *p–n* junction) [6]. At the same time, the record efficiency of 24.6% for illumination with a 100-fold concentration of AM0 sunlight still belongs to LPE-grown photocells [7].

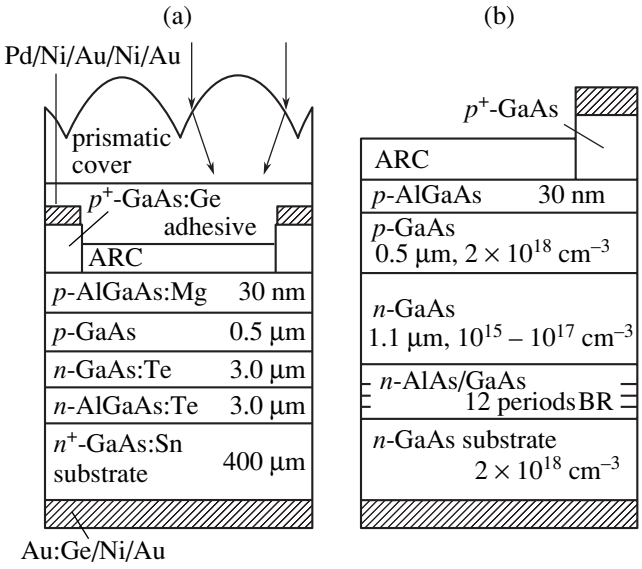

Fig. 3. Schematic diagrams of AlGaAs/GaAs single-junction multilayer solar cells for space applications. (a) Solar cell structure with a back potential barrier and thin wide-gap *p*-AlGaAs window. These elements demonstrated an efficiency of 24.6% for "space" sunlight (AM0) with a concentration ratio of 100, the highest among the single-junction solar cells. (b) MOCVD-grown solar cell structure with an embedded Bragg mirror. The Bragg mirror comprises 12 pairs of ⟨AlAs (72 nm)⟩/⟨GaAs (59 nm)⟩ layers; it is tuned to wavelength $\lambda = 850$ nm with a reflectance of 96%. As a result, a double pass of the long-wavelength light through the structure is attained, which allows the base *n*-layer thickness to be reduced to 1–1.5 μm. These cells demonstrated a high radiation resistance; the "residual power" was 84–86% after irradiation with 1-MeV electrons with a flux density of 10^{15} cm^{-2}.

In MOCVD-grown AlGaAs/GaAs photocell structures, a wide-gap AlGaAs layer, which forms the back potential barrier, could be replaced by a system of alternating pairs of AlAs/GaAs layers making up a Bragg mirror (Fig. 3b). The wavelength of the reflection peak for such a mirror was chosen in the vicinity of the absorption edge of the photoactive region, so that the long-wavelength light that was not absorbed in this region in one pass could be absorbed during the second pass after reflection from the mirror [8]. At the same time, the wide-gap mirror layers continued to serve as the back barrier for photogenerated carriers. In these conditions, the thickness of the photoactive region could be reduced by half without loss of current as compared to the thickness of structures without a mirror. This factor led to a significant increase in the radiation resistance of photocells, because the amount of lattice defects generated under irradiation by high-energy particles, which lead to degradation of the diffusion length of carriers, decreased proportionally to the thickness of the photoactive region [8].

Apart from implementing the scientific and technological achievements in the development of heterolaser structures in the structures of solar photocells, the application of new epitaxial techniques made it possible to resolve several strictly "photoelectric" problems. The use of nonequilibrium epitaxy conditions and/or the insertion of intermediate superlattices made it possible to grow perfect AlGaAs/GaAs heterostructures on germanium substrates. From this point onwards, heterophotocells on germanium became the main candidates for applications on the majority of spacecraft. The decisive factor here was the mechanical strength of germanium, which is higher than that of GaAs previously used for substrates. Therefore the arrays composed of AlGaAs/GaAs photocells on germanium were comparable in weight and strength with silicon ones but outperformed them in efficiency and radiation resistance. The second "photoelectric" problem was of fundamental importance for solar photovoltaics: the creation of cascade multijunction solar cells.

4. CASCADE SOLAR CELLS

The idea of cascade photocells has been discussed since the early 1960s and was considered then an obvious but remote prospective way of increasing efficiency. The situation began to change in the late 1980s,

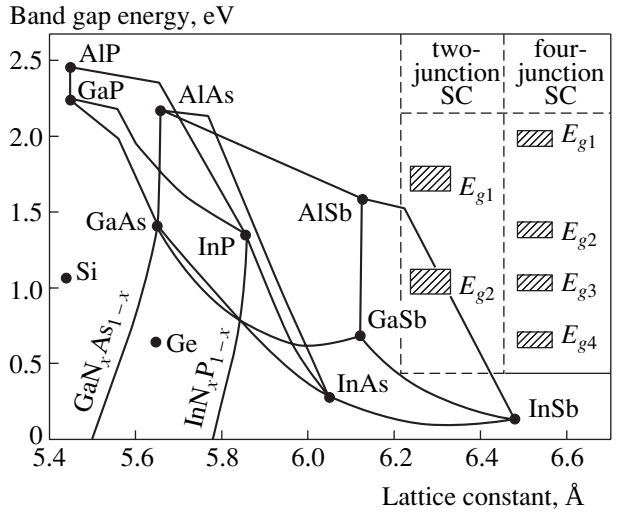

Fig. 4. Band gap E_g as a function of the lattice constant for Si, Ge, and III–V compounds and their solid solutions. Hatched rectangles correspond to E_g ranges for various materials that provide the highest efficiency of solar cells with two and four *p–n* junctions.

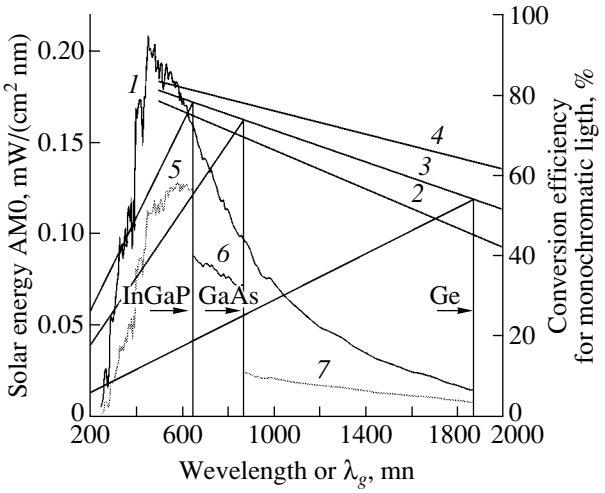

Fig. 5. Curve *1*, the AM0 energy spectrum for unconcentrated sunlight. Straight lines *2*, *3*, and *4* are the maximum "monochromatic" efficiency of an ideal solar cell for photocurrent densities j_{ph} = 0.1, 1.0, and 10 A/cm^2, respectively; they depend on the cutoff wavelength λ_g of the semiconductor material. Slanting lines on the left represent the dependences of the conversion efficiency in ideal solar cells based on $In_{0.5}Ga_{0.5}P$, GaAs, and Ge at j_{ph} = 1.0 A/cm^2. Curves *5*, *6*, and *7* show the fraction of solar energy converted to electric power in the corresponding cascades that make up a solar cell with three *p–n* junctions.

when several research groups concentrated their efforts on the development of various types of double-junction solar cells (Figs. 4, 5). At the first stage, the highest efficiency was obtained in mechanically stacked photocells, although everyone understood that the really promising cells were those with a monolithic structure. Researchers from NREL (National Renewable Energy Laboratory, USA) were the first to develop these structures. Using germanium substrates, they grew by MOCVD lattice-matched multilayer structures in which the upper photocell had a *p–n* junction in $In_{0.5}Ga_{0.5}P$ solid solution and a lower photocell in GaAs. In order to connect the cells in series, a tunnel *p–n* junction was specially formed between the cascades. Later, a third cascade with a *p–n* junction in the germanium substrate was included in the photovoltaic conversion (Fig. 6). Nowadays, triple-junction photocells (see table) are already in practical use in spacecraft.

It may seem that we have concentrated too much on describing photocells based on III–V compounds, which are rather complicated in structure and expensive. As they were developed for a relatively narrow and specific field of power engineering application, space technology, are there prospects for their use in the large-scale photovoltaics of the future? We believe that the answer to that question is positive, and there are numerous reasons to support this view.

Theoretical, expected, and obtained efficiencies of cascade solar cells

Sunlight spectrum	Value	Efficiency, %				
		Number of *p–n* junctions in a cascade				
		1	2	3	4	5
Near-Earth space conditions (AM0)	Theoretical	28	33	38	42	45
	Expected	23	28	33	36	38
	Obtained	21.8 [10]	27.2 [11]	29.3 [11]	–	–
Terrestrial conditions (AM1.5)	Theoretical	30	36	42	47	49
	Expected	27	33	38	42	44
	Obtained [6]	25.1	30.3	31.0	–	–
Terrestrial conditions with concentration (AM1.5)	Theoretical	35	42	48	52	54
	Expected	31	38	43	47	49
	Obtained [6]	27.6	31.1	34.0	–	–

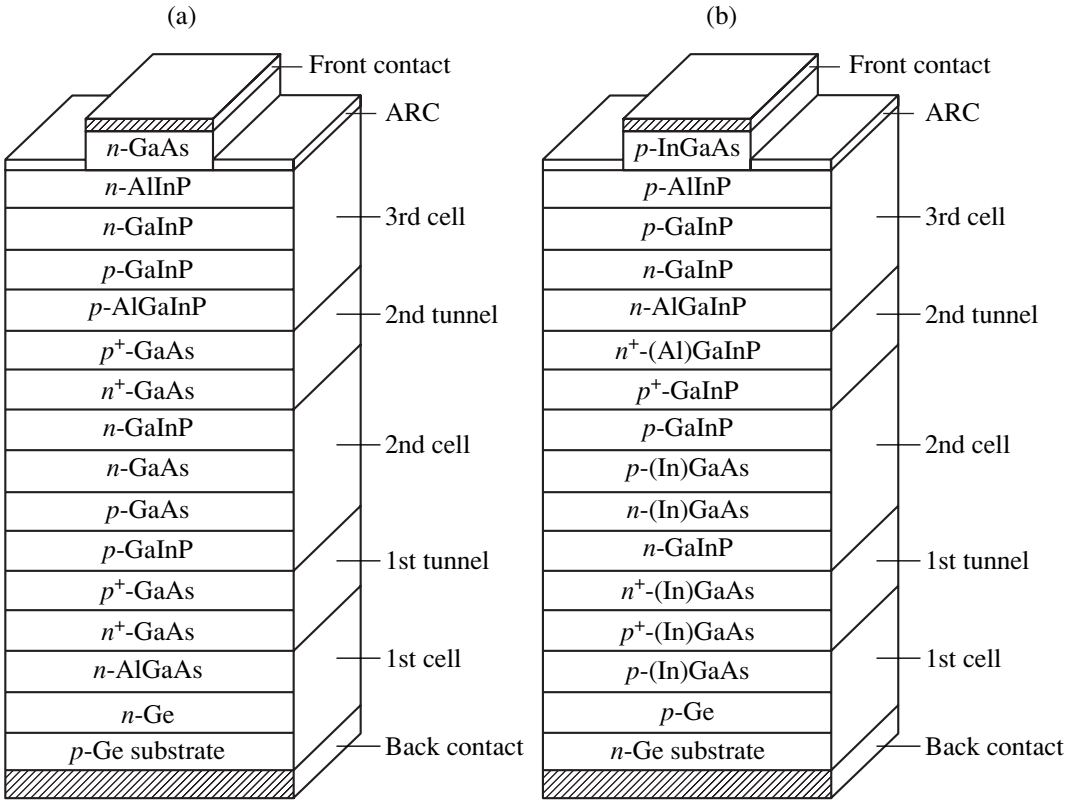

Fig. 6. Cross sections of solar cells with three *p–n* junctions: (a) (Al)GaInP/GaAs/Ge heterostructure in which the second element, as well as the first and second tunnel junctions are made of GaAs; (b) (Al)GaInP/(In)GaAs/Ge heterostructure in which the first tunnel junction is made of InGaAs, while the second element and the second tunnel junction are made of (Al)GaInP.

The structure of a triple-junction heterophotocell is complex, and it will become even more complicated after the development of, say, four- and even five-junction photocells. However, the epitaxial growth of such structures is a completely automated single-stage process the success of which is totally dependent on the progress made in the base technology. The consumption of the initial materials (gases in the MOCVD technique) depends only slightly on the number of cascades. Since all photoactive regions are, as a rule, made of direct-band materials, the total thickness of the epitaxial structure grown is only a few micrometers.

The cost of an epitaxial structure is largely determined by its substrate. As mentioned above, the use of a germanium substrate, which was foreign to III–V materials, enabled us to improve the operational parameters of space solar arrays. In fact, this has resulted in the "second birth" of the technology of germanium, which was the first classical material in semiconductor electronics but was later superseded by silicon. The cost of germanium as a substrate material is lower than that of GaAs used for this purpose, to say nothing of its technological merits (mechanical stability in post-growth treatment) and the fact that it can be included in the process of photovoltaic conversion in a cascade structure. However, looking back at the successes achieved in nanoheterostructure technologies, one may suppose that germanium, now a substrate material, will probably be superseded again by silicon, which is an even cheaper and technologically more convenient material. Research in this area is already under way. Thus, the application of high-tech methods in the production of photocells based on III–V compounds may result not only in a radical increase in efficiency (in multijunction structures), but also a radical decrease in the cost of heterostructure photocells.

We will now consider the prospects for increasing efficiency in multijunction photocells (see table). An experience to date in the development of triple-junction photocells gives reason to hope for achieving higher efficiency in four-, five-, and maybe even more multiple-junction structures. There are no scientific or theoretical doubts that these hopes will be justified when suitable materials for intermediate cascades are found and grown to the appropriate quality. The search for these materials is under way, and here several areas may be singled out.

The traditional area is "simply" the synthesis of new materials. Among III–V materials, these are semiconductor nitrides and borides, which have yet found little or no commercial application. We already have considerable technological experience of wide-gap nitrides (grown by the MOCVD technique mentioned above),

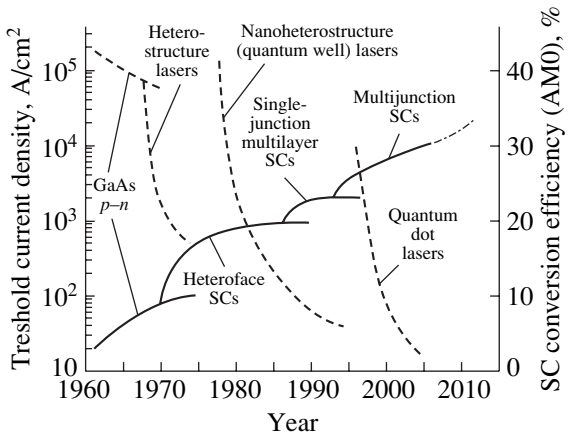

Fig. 7. Evolution of parameters of injection lasers and solar cells based on III–V materials. Dashed lines (left axis), the evolution of threshold current for three generations of injection lasers. Solid lines (right axis), the evolution of photoconversion efficiency in solar cells based on different structures (AM0 solar spectrum without concentration of light).

motivated by the bright prospects of revolution in lighting technology. It is quite likely that we will witness the general replacement of hot mercury and incandescent tungsten in lighting devices by "cold" structures based on III–V materials of micrometer thickness. However, more favorable for cascade photocells are narrow-gap materials, which are better lattice-matched (in lattice type and lattice constant) with the materials currently used in triple-junction structures. These may be, for example, GaInNAs solid solutions (Fig. 4), which are currently being intensively studied. It is noteworthy that complication of the photocell structure, namely, the transition to multijunction structures, reduces the requirements for the bulk properties of the materials used. Indeed, the larger the number of junctions, the thinner the photoactive region in each junction and the weaker the effect of such parameters as the minority carrier diffusion length on the efficiency of the device. The method of compensating insufficiently good bulk properties of a material by technologically perfecting the cascade structure has also begun to be used in the development of new types of thin-film solar arrays.

We will now discuss some other possible ways of improving cascade solar cells. We will refer to earlier experience in the development of semiconductor electronics, in particular, III–V lasers (Fig. 7). Until now, two stages could be distinguished in this development. The first is associated with the creation of heterostructures; the second, with the creation of nanoheterostructures. In both cases, the main initial ideas were directed toward improving injection lasers and developing technologies for their fabrication. In the 1970s, a tradition was even established according to which the parameters of injection heterolasers produced by a particular technique always served as a criterion of perfection for this technique. The definition a "laser-quality material" implied that, owing to high crystal perfection, a given heterostructure would be capable of operating at the super-high excitation densities necessary for lasing. Analyzing current trends in the design of third-generation injection lasers, we find primarily a transition to quantum dot (QD) structures [9].

As for solar photovoltaic converters, new approaches involving the use of materials with QDs have been proposed to develop them: the creation of a photoactive medium with an "intermediate band" [12]. In multicascade photocell structures, in addition to using newly created materials with the desired absorption spectrum, it might be possible to improve the characteristics of commutating tunnel diodes (to increase the peak current) by introducing superlattices of vertically coupled QDs between the n^+ and p^+ layers. It should be added that there are other suggestions, some of which are quite old, for increasing photovoltaic converter efficiency, the implementation of which would require the use of some "newly constructed" materials. Among these is the idea of using graded heterostructures in which a very large variation in the energy gap must be achieved with the provision of very high carrier mobility. All these proposals are related to the quest to increase (first theoretically and then in practice) the efficiency of solar photovoltaic conversion to the thermodynamic limit of 93%, which is determined by the Carnot cycle.

Previous experience shows that all achievements in increasing solar cell efficiency will be applied first of all in space technology [10, 11]. The same conclusion may be drawn from an estimation of the scale of the tasks to be accomplished by modern space technology. A large number of high-power telecommunication satellites are required, the demands for the energy supply of orbital stations are growing, and there is now a need to produce specialized power-producing satellites that could serve as power sources for space vehicles. Specifically, power-producing satellites would convert solar energy into electrical energy, and this would be converted into radiative energy to be transferred by laser or microwave beam. In the distant future, large amounts of energy could be transferred to the Earth for electric power generation. In order to implement the most large-scale projects, solar cell structures should be MBE-grown directly in orbit in the vacuum of space. In any case, the significant expansion of solar cell production for space applications will allow the "incidental" creation of a technological base for even larger-scale production of solar cells for terrestrial application.

5. PHOTOVOLTAIC CONVERSION OF CONCENTRATED SUNLIGHT

Until now, we have not considered one more possibility for increasing the efficiency of photovoltaic conversion: the conversion of preliminarily concentrated sunlight. The maximum calculated concentration ratio at the distance from the Sun corresponding to the Earth's orbit is 46200. This concentration ratio is usu-

ally set in the estimations of thermodynamically limited efficiency for different types of solar cells. Specifically, for multijunction cells comprising several tens of cascades, the limiting efficiency is almost 87%, which is very close to the Carnot cycle efficiency. Thus, multijunction photocells, apart from demonstrating the highest efficiencies and prospects for increasing them in the near future, also have the best "fundamental" prospects.

However, can one talk of prospects for large-scale applications of these photocells in terrestrial devices, where the economic factor is decisive? Multijunction photocells have an extremely complicated structure indeed. Moreover, they have perhaps the most complicated structure of all semiconductor devices. The largest variation of the band gap must be achieved here for several photoactive regions with p–n junctions. The doping level in the layers varies rather widely, and there are sharp changes in the type of conduction during the formation of several (as the structure is grown) tunnel p–n junctions connecting the cascades. The prescribed thickness of photoactive layers must be maintained with high precision, thus providing the calculated absorption of specific portions of the solar spectrum to generate the same photocurrent in the layers. The layers that form the tunnel p^+–n^+ junctions must be extremely thin (in the nanometer range) to minimize the absorption of light, whereas the photoactive layers must be about two orders of magnitude thicker. The whole set of III–V materials (in the form of solid solutions) is involved in forming the structure of multijunction photocells (in future, nitrides also), which are, apart from everything else, grown on the foreign substrates (Ge and, in future, Si). However, as stated above, the economic factor is not so dramatically important here. Growing a structure is a one-stage automatic process, the total thickness is only several micrometers, and the cost of a nonphotoactive substrate can be quite low. The decisive factor for an economically justified application of multijunction photocells is the fact that they can operate with high efficiency under highly concentrated sunlight.

The fact that GaAs-based heterojunction solar cells can operate efficiently at a significant (several hundred or even several thousand times) concentration of sunlight, and in this respect differ favorably from silicon cells, was pointed out as early as the late 1970s and early 1980s. The first experiments on the design of concentrator-based photovoltaic modules with high-current heterophotocells belong to that period [13]. The generated photocurrent increases linearly as the light intensity increases, and the output voltage in turn increases with current by the logarithmic law. Thus, the generated power increases superlinearly as sunlight is concentrated, so the photovoltaic conversion efficiency increases. This situation can be used in practice if a higher current does not produce a noticeable voltage drop across the internal resistance of a photocell. So radically reducing internal ohmic loss became the key problem in the development of concentrator photocells. The prospect of increasing efficiency in working with

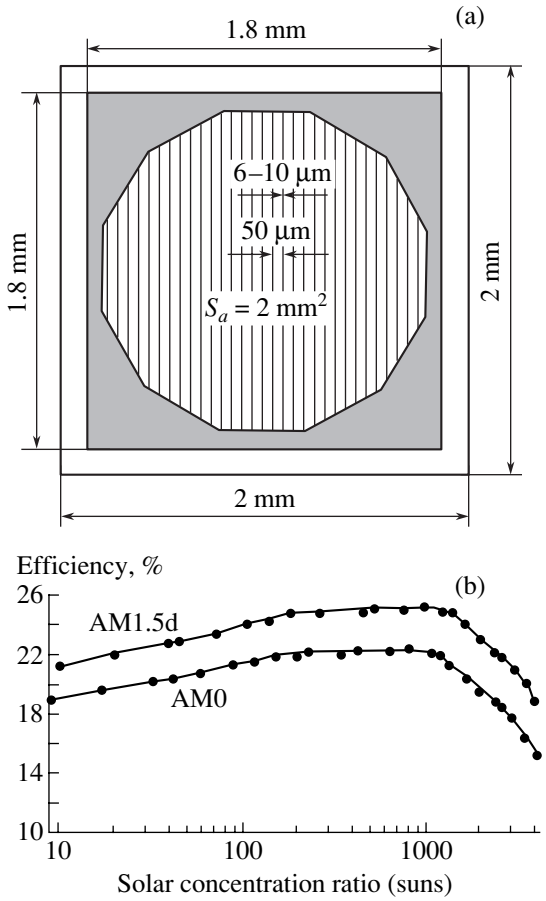

Fig. 8. (a) Schematic of a concentrator solar cell; (b) conversion efficiency as a function of the sunlight concentration ratio for a single-junction AlGaAs/GaAs cell for AM0 and AM1.5 irradiation conditions.

concentrators seemed highly tempting. However, the main motive force in creating concentrator modules was the possibility of reducing the consumption of semiconductor materials in proportion to the sunlight concentration ratio in the generation of the required electric power. In this case, mirrors or lenses fabricated from relatively inexpensive materials concentrated sunlight onto semiconductor photocells of relatively small area, located in the focal plane of the concentrators. The contribution of the cost of the photocell to that of the solar module became insignificant, while the efficiency of the module depended directly on the efficiency of the photocells employed. This is an essential prerequisite for an economically justified application of the most effective, though expensive, photocells based on III–V compounds [14, 15].

In the early 1990s, a new approach appeared in the design of concentrator systems; it is based on the concept of small-aperture modules that have all the prerequisites for highly efficient and economically justified solar energy conversion [14–19]. When the linear dimensions of a concentrator decrease and the predetermined ratio between the aperture and the focal distance

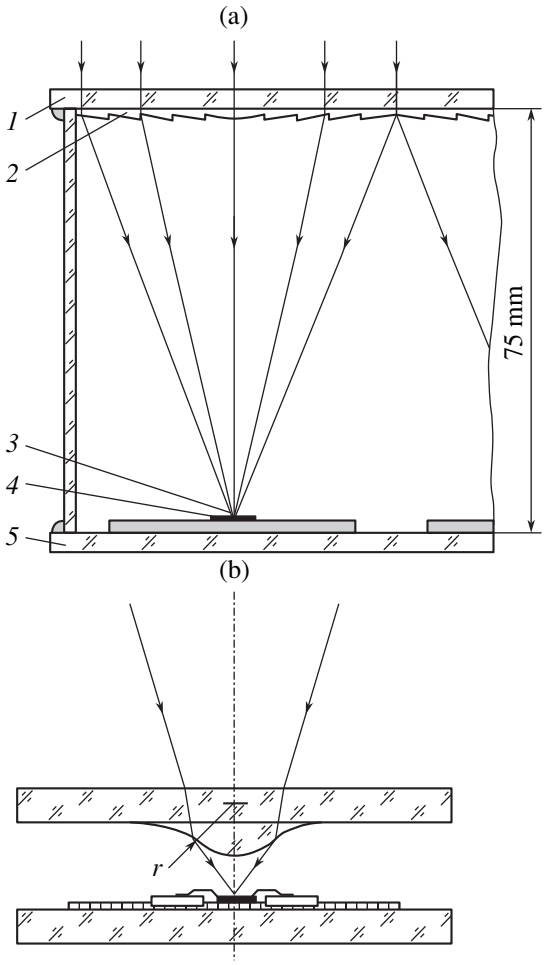

Fig. 9. (a) Cross section of a concentrator module: (*1*) the glass base of the lens panel; (*2*) silicone microprisms of the Fresnel lenses; (*3*) focused sunlight beams; (*4*) solar cell mounted on a metal base; (*5*) glass base of the solar cell panel. (b) System with secondary minilenses that increase the sunlight concentration ratio.

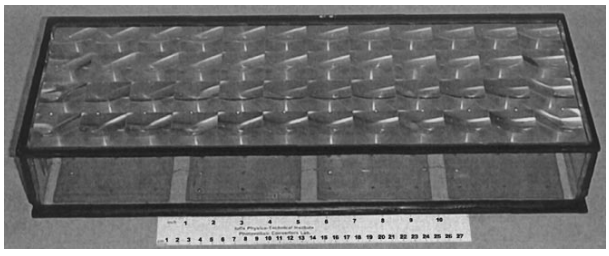

Fig. 10. Experimental photovoltaic module for the conversion of concentrated sunlight with a panel of 48 Fresnel lenses.

is maintained, the concentration ratio remains the same. However, in this case the structural height of a module is reduced owing to the shorter focal distance of lenses. The linear dimensions of photocells are reduced to 1–2 mm (Fig. 8), so they can be assembled with automatic equipment used for assembling discrete devices in mass production in the electronic industry. With small linear dimensions of photocells, thinner substrates can be used to grow the structure, and the useful fraction of the wafer area can be increased, which results in a further saving of semiconductor materials (in addition to that provided by the sunlight concentration). The assembly can be carried out without a complicated compensation of the thermal expansion coefficients of the cell material and the metallic heatsink base. Of particular importance is the fact that the heatsink thickness also decreases proportionally to the decrease in concentrator linear dimensions, which results in a considerable reduction in metal consumption in the fabrication of such a module. Thus, in the concept of small-aperture concentrator modules the advantages of concentrator systems (increase in efficiency, saving on semiconductor materials) can be used while retaining a distributed character of sunlight conversion and heat dissipation as a whole (as in systems without concentration).

Note that, from the point of view of prospects for large-scale solar power engineering, the consumption of any, even the most conventional, structural materials is economically justified only when there is high efficiency of conversion per total area of the solar cell. This is determined by the need to cover considerable areas of the Earth's surface to intercept sunlight in the generation of high power.

Naturally, solar power installations should be protected from the effects of weather to ensure long-term (20–30 years) serviceability. In this respect, the construction of "all-glass" concentrator modules (Figs. 9, 10) developed in recent years at the Ioffe Physicotechnical Institute in cooperation with the Fraunhofer Institute for Solar Energy Systems (Freiburg, Germany) [16, 17] looks very promising. Small-aperture Fresnel lenses are combined in an integrated panel. Concentrator photocells mounted on thin (~0.5 mm) metallic heatsinks are also combined in a panel. Both panels are fastened by glass sidewalls, so that the inner volume of the module is hermetically sealed. The lens panel has a composite structure. A sheet of conventional silicate glass, which protects the front side of the module, serves as a superstrate for a thin transparent silicone Fresnel profile, which focuses the sunlight. The base for the panel of photocells is also a silicate glass sheet, which serves as a heatsink. Thus, low-cost glass with stable properties is the main structural material for the concentrator module. The consumption of optical-quality silicone is reduced to the minimum necessary to form refractive microprisms (with an average thickness of about 0.2 mm). A standard structural silicone is used to fix and hermetically seal the glass parts of the module (Fig. 9). Owing to the use of materials that are most resistant to the influence of irradiation and weather (glass and silicone), these concentrator modules seem to be the most promising for long-term operation. In the experimental "all-glass" modules, the optical efficiency of Fresnel lenses

reached 89%. When double-junction InGaP/InGaAs photocells with an efficiency of ≃30% (AM1.5d) were used, the module efficiency measured under natural sunlight illumination conditions was 24.8%, calculated relative to sunlight incident onto the surface of the lenses [17].

Further development of module designs is aimed at increasing the sunlight concentration ratio. For example, if the size of a unit lens in a submodule is 4×4 cm^2, high optical efficiency is obtained when photocells of 2 mm in diameter are used (Fig. 8), which corresponds to a concentration ratio of about 500. A further reduction in the size of photocells and a transition to concentration ratios of 1000 or higher are possible if secondary minilenses with a smooth profile are placed directly in front of the photocells (Fig. 9). In this case, the secondary lenses can also be combined into a panel (Fig. 10) [18, 19]. With highly concentrated sunlight, the use of multijunction photocells offers additional advantages. When the number of junctions increases, the output voltage increases and the generated photocurrent decreases. Therefore, the internal ohmic loss in current collection decreases, so a high conversion efficiency is maintained at higher sunlight concentration ratios.

There are certain misgivings regarding the practical use of concentrator cells related to the need to ensure that the concentrator modules track the Sun. Indeed, this situation requires the construction of special supporting–turning mechanisms for the installation of the modules, equipped with sun-position sensors and electric drives. Compared with conventional modules without concentrators, this leads to an additional consumption of structural materials and power consumption for tracking. However, the power generated even in a conventional module with continuous sun tracking during a light day is 30–40% greater than that in a module without sun tracking. Taking into account this gain and the higher efficiency of a concentrator module, we may say that this compensates for the additional expenses of materials. As for the consumption of electric power for tracking, it is only 0.2–0.3% of the power generated by concentrator modules with tracking devices [18, 19].

Concentrator modules should not be contrasted with conventional ones in estimating the prospects for the development of solar photovoltaics. Both types should be used in the power-generation systems of the future. It seems that conventional modules with crystalline silicon cells or thin film structures will form the basis of a decentralized electric power generation system. As private or public property belonging to a broad circle of owners, they will be installed on the roofs and walls of houses and buildings and integrated into a network. Thus, they will embody new "democratic principles" of solar power engineering compared with the current "dictatorship" of power giants. However, the demands of power-consuming industries, municipal communities, etc., will require the construction of large-scale solar stations providing a minimum cost for generated electric power. Such stations located on specially assigned territories and attended by special personnel will form part of the decentralized power system. The use of concentrator photovoltaic modules seems to be a quite reasonable solution in the development of these stations. Numerous economic estimates (see, e.g., [20–22]) indicate that, within the coming decade, concentrator photovoltaics may become not only economically effective compared to other types of installations for photovoltaic conversion, but also compete with the existing traditional power sources in terms of the cost of generated electric power. It is important also that solar power stations of substantial output can be built without the deployment of new large semiconductor plants. In this case, the main efforts will be directed toward fabricating the mechanical parts of the concentrator modules and supporting structures, and the basis for producing these already exists.

Meanwhile new production capacities in the semiconductor industry may be required in the near future because of the need to supply space technology with high-efficiency photocells based on III–V compounds. Here the concentration approach is considered as one possible way of solving the problem. In the conditions of space, the most promising solution seems to be the application of linear Fresnel lenses as sunlight concentrators. This allows one to use relatively accurate Sun tracking around one axis only, the axis parallel to the microprisms of the lenses, while the tracking around the second axis can be much rougher. In this case, the typical concentration ratio is about 6–10. The refractive profile in lenses is produced from transparent silicone. Lenses for application in space may have a very thin (~0.1 mm) glass base [23] or even have no base at all [24]. In the first case, a sheet of glass doped with cerium dioxide acts as a lens protector from ultraviolet light and the impact of high-energy particles. In the second case, a multilayer coating is deposited onto the front surface of a silicone lens. In both cases, the photocells are protected against unfavorable effects better than in solar arrays without concentrators. Furthermore, the radiation resistance of an array increases due to operation at higher photocurrent densities under concentrated sunlight. A high current density becomes especially important when space probes are launched in a direction away from the Sun. In this case, the concentration of light compensates for the effect of the decrease in efficiency as the density of sunlight power decreases. In concentrator solar arrays for conditions of near-Earth space, a specific power per unit weight of about 180 W kg^{-1} and a specific power per unit area of about 300 W m^{-2} can be obtained [24]. These parameters are expected in InGaP/GaAs/Ge triple-junction photocells and cannot be achieved in any other type of space solar arrays. Space modules with short-focus (23 mm) Fresnel lenses devised at the Ioffe Physicotechnical Institute can be used instead of conventional flat arrays without any modification of the transport containers.

6. CONCLUSION

We are witnesses to and participants in many interesting and important processes in modern science and technology. Semiconductors, whose history of technical development spans little more than 50 years, have resoundingly conquered all the fields of electric power conversion techniques and electronics, have prepared and are carrying out "the information revolution," and are ready to produce a revolution in lighting techniques. The scientific and technological successes of the last decade give grounds to hope that a revolution with the participation of semiconductors may also take place in the field of electric power generation.

In a broad sense, the development of a new power base has never come cheaply. It is even hard to imagine how many efforts and resources were spent on the development and creation of systems for electric power generation, distribution, and consumption when the electric power industry was only beginning to enter everyday life. The further development of this industry required the involvement of new forms of fuel. Nuclear power stations were built, which, it seemed, would resolve all our power problems. But could these power stations have been built were it not for the national programs to create nuclear weapons? It is well known that tremendous resources were initially invested in precisely these programs and that electric power stations were only one of the results of realizing them. The seemingly low cost of this ready-to-use engineering resulted in a situation where, even for rejecting the use of nuclear power stations, one had to pay a huge price.

Solar photovoltaics has not been born out of nowhere. Largely as a result of the development of electronics, laser techniques, and electric power engineering for spacecraft, a scientific and technological basis has been created that may serve as the starting point for the expansion of a terrestrial solar electric power industry based on semiconductors. The time is coming when it will be necessary to provide much wider investment of resources in this field, corresponding to the significance solar electric power will have in the future.

ACKNOWLEDGMENTS

This study was supported by the European Commission through the funding of the project FULLSPECTRUM (ref. no. SES6-CT-2003-502620).

REFERENCES

1. W. G. Adams and R. E. Day, Philos. Trans. R. Soc. London **167**, 313 (1877).
2. A. F. Ioffe and A. V. Ioffe, Phys. Z. Sowjetunion **7**, 343 (1935).
3. D. M. Chapin, C. S. Fueller, and G. L. Pearson, J. Appl. Phys. **25**, 676 (1954).
4. N. A. Goryunova, Dissertation (Leningrad State Univ.–Physicotechnical Inst., Leningrad, 1951).
5. Zh. I. Alferov, V. M. Andreev, M. B. Kagan, *et al.*, Fiz. Tekh. Poluprovodn. (Leningrad) **4**, 17 (1970) [Sov. Phys. Semicond. **4**, 12 (1970)].
6. M. E. Green, K. Emery, D. L. King, *et al.*, Prog. Photovoltaics: Res. Appl. **10**, 355 (2002).
7. V. M. Andreev, A. B. Kazantsev, V. P. Khvostikov, *et al.*, in *Proceedings of 1st World Conference on Photovoltaic Energy Conversion* (Hawaii, 1994), p. 2096.
8. V. M. Andreev, I. V. Kochnev, V. M. Lantratov, and M. Z. Shvarts, in *Proceedings of 2nd World Conference on Photovoltaic Solar Energy Conversion* (Vienna, 1998), p. 3757.
9. N. N. Ledentsov, M. Grundmann, F. Heinrichsdorff, *et al.*, IEEE J. Sel. Top. Quantum Electron. **6**, 439 (2000).
10. S. G. Bailey and D. F. Flood, Prog. Photovoltaics **6**, 1 (1999).
11. R. R. King *et al.*, in *Proceedings of 28th IEEE Photovoltaic Specialists Conference, Anchorage, Alaska* (IEEE, New York, 2000), p. 998.
12. A. Luque, A. Marti, P. Wahnon, *et al.*, in *Proceedings of Workshop on the Path to Ultra-High Efficient Photovoltaics* (Ispra, Italy, 2002), p. 40.
13. Zh. I. Alferov, V. M. Andreev, Kh. K. Aripov, *et al.*, Geliotekhnika **6**, 3 (1981).
14. V. M. Andreev, V. A. Grilikhes, and V. D. Rumyantsev, *Photovoltaic Conversion of Concentrated Sunlight* (Nauka, Leningrad, 1989; Wiley, Chichester, 1997).
15. V. M. Andreev, V. P. Khvostikov, V. D. Rumyantsev, *et al.*, in *Technical Digest of the International PVSEC-11* (Sapporo, Japan, 1999), p. 147.
16. V. D. Rumyantsev, M. Hein, V. M. Andreev, *et al.*, in *Proceedings of 16th European Photovoltaic Solar Energy Conference* (Glasgow, 2000), p. 2312.
17. M. Hein, M. Meusel, C. Baur, *et al.*, in *Proceedings of 17th European Photovoltaic Solar Energy Conference* (Munich, Germany, 2001), p. 496.
18. V. D. Rumyantsev, O. I. Chosta, V. A. Grilikhes, *et al.*, in *Proceedings of 29th IEEE Photovoltaic Specialists Conference, New Orleans, 2002* (IEEE, New York, 2002), p. 1596.
19. V. D. Rumyantsev, V. M. Andreev, N. A. Sadchikov, *et al.*, in *Proceedings of Conference on PV in Europe* (Rome, 2002).
20. H. L. Cotal *et al.*, in *Proceedings of 28th IEEE Photovoltaic Specialists Conference, Anchorage, Alaska, 2000* (IEEE, New York, 2000), p. 955.
21. M. Yamaguchi, in *Proceedings of Workshop on the Path to Ultra-High Efficient Photovoltaics* (Ispra, Italy, 2002), p. 15.
22. M. Yamaguchi and A. Luque, IEEE Trans. Electron Devices **46**, 41 (1999).
23. V. M. Andreev, V. R. Larionov, V. M. Lantratov, *et al.*, in *Proceedings of 28th IEEE Photovoltaic Specialists Conference, Anchorage, Alaska, 2000* (IEEE, New York, 2000), p. 1157.
24. M. J. O'Neill, M. F. Piszczor, M. I. Eskenazi, *et al.*, in *Proceedings of 29th IEEE Photovoltaic Specialists Conference, New Orleans, 2002* (IEEE, New York, 2002), p. 916.

Translated by D. Mashovets

Semiconductors, Vol. 38, No. 8, 2004, pp. 909–917. From Fizika i Tekhnika Poluprovodnikov, Vol. 38, No. 8, 2004, pp. 949–957.

SYMPOSIUM ON THE EFFICIENT USE OF SOLAR RADIATION IN PHOTOVOLTAIC POWER ENGINEERING (St. Petersburg, November 3–4, 2003)

Quantum Dot Solar Concentrators[1]

A. J. Chatten[1]*, K. W. J. Barnham[1], B. F. Buxton[2], N. J. Ekins-Daukes[3], and M. A. Malik[4]

[1]*Physics Department, Imperial College, London, SW7 2BW, UK*

**e-mail: a.chatten@imperial.ac.uk*

[2]*Computer Science Department, U.C.L., London, WC1E 6BT, UK*

[3]*Toyota Technological Institute, Nagoya, 468-8511, Japan*

[4]*Chemistry Department, University of Manchester, Manchester, M13 9PL, UK*

Submitted February 9, 2004; accepted for publication February 11, 2004

Abstract—The luminescent properties of core-shell quantum dots are being exploited in an unconventional solar concentrator, which promises to reduce the cost of photovoltaic electricity. Luminescent solar collectors have advantages over geometric concentrators in that tracking is unnecessary and both direct and diffuse radiation can be collected. However, development has been limited by the performance of luminescent dyes. We present experimental and theoretical results with a novel concentrator in which the dyes are replaced by quantum dots. We have developed a self-consistent thermodynamic model for planar concentrators and find that this three-dimensional flux model shows excellent agreement with experiment. © *2004 MAIK "Nauka/Interperiodica".*

1. INTRODUCTION

The luminescent planar solar concentrator [1] was originally proposed in the late 1970s. It consisted of a transparent sheet doped with appropriate organic dyes. Sunlight is absorbed by the dye and then reradiated isotropically, ideally with high quantum efficiency (QE) and trapped in the sheet by internal reflection. A stack of sheets doped with different dyes [1] can separate the light, as in Fig. 1, and solar cells can be chosen to match the different luminescent wavelengths to convert the trapped light at the edge of the sheet.

Advantages over geometric concentrators include the fact that expensive solar tracking is unnecessary and that both direct and diffuse radiation can be collected. However, the development of this promising concentrator was limited by the stringent requirements on the luminescent dyes, namely high QE, suitable absorption spectra and redshifts, and stability under illumination [2].

2. THE QUANTUM DOT CONCENTRATOR (QDC)

We have recently proposed a novel concentrator [3] in which the dyes are replaced by quantum dots (QDs). The first advantage of the QDs over dyes is the ability to tune the absorption threshold simply by choice of dot diameter. Secondly, high luminescence quantum efficiency has been observed. CdSe/CdS heterostructure dots have demonstrated luminescence quantum yields above 80% at room temperature [4]. Thirdly, since they are composed of crystalline semiconductor, the dots should be inherently more stable than dyes.

The disappointing results obtained with dye concentrators were probably mainly because of reabsorption, which was considered but not modeled at the time of the original calculations [1]. Therefore, in [3], we have argued that a further advantage in the redshift between absorption and luminescence is *quantitatively* related by the thermodynamic model to the *spread* of quantum dot sizes, which can be determined during the growth process [5]. The ability to limit the overlap between the luminescence and absorption by the choice of QD size distribution is a significant improvement compared to dye concentrators, allowing reabsorption losses to be minimized [6, 7].

3. THERMODYNAMIC MODELING OF THE QDC

Yablonovitch [8] applied a detailed balance argument to the original dye-concentrator to relate the absorbed light and self-absorbed concentrated light to the spontaneous emission. The paper considers a uni-

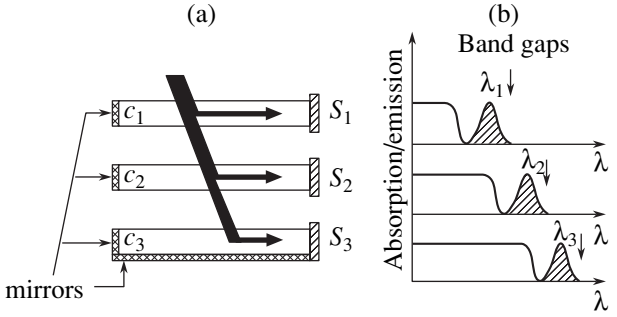

Fig. 1. (a) Schematic of a three-stack luminescent concentrator. Each layer in the stack absorbs and reemits light of longer wavelength with ideal absorption coefficient and luminescence spectra as in (b).

[1]This article was submitted by the authors in English.

formly illuminated thin slab, for which the variation of the incident light with depth is negligible. In a practical device, however, a significant fraction of the incident flux is absorbed. Yablonovitch applies the boundary condition to the trapped flux that it is zero at the edge of the sheet and derives an expression for the flux propagating towards the cell. It is not possible using Yablonovitch's boundary condition to derive an expression for the flux propagating backwards that is consistent with that propagating forwards. The form of the detailed balance expression in [8] is again limited to thin sheets for which a negligible fraction of the radiation emitted into the escape cone may be reabsorbed by the sheet. This model does not consider losses owing to absorption by the "transparent" sheet material, and we find that this is one of the most important factors limiting the efficiency of planar luminescent solar concentrators. Yablonovitch's one-dimensional model is also limited to the case where there is no spectral overlap of the incident radiation and the luminescence. To overcome these difficulties, we have developed a self-consistent three-dimensional (3D) flux model in which we apply reflection boundary conditions to the radiation depending on whether it falls within the escape cone, Ω_c, or within the solid angle of total internal reflection in each coordinate direction *x*, *y*, *z*.

Our 3D flux model allows for (1) a significant fraction of the incident flux to be absorbed by the sheet; (2) spectral overlap of the incident radiation with the luminescence; (3) reabsorption of radiation emitted into the escape cone; (4) reflection at the surfaces; and (5) losses due to absorption in the host material. Including (1) to (5) can make an order of magnitude difference to the calculated luminescence escaping the right surface (see Fig. 1a) compared to the predictions of [8], even for a small $42 \times 10 \times 5$ mm test slab. The model provides equations from which the photon chemical potential as a function of position within a finite slab of material may be determined by iteration.

4. 3D FLUX MODEL

To obtain the differential equations describing the propagation of the trapped and escaping photon intensities, we start with Chandrasekhar's general three-dimensional radiative transfer equation [9]. We consider a finite slab of material of thickness *D* in the *z* direction, length *L* in the *x* direction, and width *W* in the *y* direction, uniformly illuminated on (say) the top surface.

We apply the method of Schwarzschild and Milne [10], in which the detailed angular dependence of the radiative intensity described by the transfer equation is ignored and the radiation is considered as consisting simply of forward (+) and backward (–) streams. However, in addition, we also distinguish between what happens when the angle of propagation, θ, is greater or less than the critical angle θ_c. Escaping photons with $\theta < \theta_c$ and trapped photons with $\theta > \theta_c$ are treated as separate streams. We then integrate over the appropriate angular ranges to obtain the intensities of the photon streams and ignore other details of the angular dependence. Integrating over the escape cones in each coordinate direction produces two differential equations [6] for the luminescent escaping fluxes propagating in the positive and negative directions:

$$\mp\frac{\partial I^{(\pm)}_{x,y,z}}{\partial x, y, z} = \lambda_a I^{(\pm)}_{x,y,z} - \frac{\Omega_c}{4\pi}\lambda_e B. \qquad (1)$$

In Eq. (1), $I^{(\pm)}_x$, $I^{(\pm)}_y$, and $I^{(\pm)}_z$ are the escaping luminescent fluxes propagating within the slab in the positive and negative *x*, *y*, and *z* directions, respectively, and λ_a and λ_e are defined by

$$\lambda_a = \frac{N\sigma_a(\nu)}{\cos^2(\theta_c/2)}, \quad \lambda_e = \frac{N\sigma_e(\nu)}{\cos^2(\theta_c/2)}. \qquad (2)$$

Here, *N* is the density of luminescent centers, and $\sigma_a(\nu)$ is the absorption cross section of the slab material comprising a transparent medium with absorption cross section $\sigma_b(\nu)$ within which the luminescent species with absorption cross section $\sigma_e(\nu) = \sigma_a(\nu) - \sigma_b(\nu)$ is uniformly dispersed. The luminescent brightness, *B*, of a radiation field in equilibrium with the electronic degrees of freedom of the absorbing species is given by

$$B(\nu) = \frac{8\pi n^2\nu^2}{c^2}\frac{1}{\exp[(h\nu-\mu)\beta]-1}, \qquad (3)$$

where *n* is the refractive index, ν is the frequency, μ is the photon chemical potential, $\beta = 1/kT$, and the other quantities have their usual meaning. The incident radiation, I_1, is not distributed over the same angular range as the escaping luminescence and, thus, must be treated separately. If I_1 is incident at θ_i, it generates escaping fluxes $I^{(\pm)}_d$ within the slab which depend on *z* and the transmission angle θ_t:

$$\mp\frac{\partial I^{(\pm)}_d}{\partial z} = \frac{N\sigma_a}{\cos\theta_t} I^{(\pm)}_d. \qquad (4)$$

4.1. Trapped Intensity

Suitable transparent media generally have refractive indices close to 1.5. Thus, the totally trapped solid angle $\Omega_6 = 4\pi - 6\Omega_c$ is small. The trapped intensity also equilibrates within the slab by multiple reflections, and, hence, we may integrate the radiative transfer equation over this solid angle to obtain an average trapped intensity:

$$I^{(\cdot)}_t = \frac{N\sigma_e}{N\sigma_a}\frac{\Omega_6 B}{4\pi}. \qquad (5)$$

4.2. Detailed Balance

Application of the principle of detailed balance within the slab of material leads to the equation

$$F(\mu) = \int d\nu \sigma_e(\nu) I_C(\nu) - \int d\nu \frac{\sigma_e(\nu)}{Q_e} B(\nu) = 0, \quad (6)$$

where Q_e is the quantum efficiency of the luminescent species and $F(\mu)$ is minimized to determine μ. I_C is the concentrated photon field within the slab which is obtained by adding the total trapped and escaping intensities in the *x*, *y*, and *z* directions:

$$I_C = I_t^{(\cdot)} + I_x + I_y + I_z + I_d. \quad (7)$$

The escaping intensities are themselves given by adding the appropriate photon streams as

$$I_{x,y,z,d} = I_{x,y,z,d}^{(+)} + I_{x,y,z,d}^{(-)}. \quad (8)$$

Equation (6) shows that the variation of I_C with position in the slab is dependent on the variation of μ with position.

For thin films, the differential equations (1) may be solved analytically [7]. For thick slabs, we can only solve the differential equations up to integration over the slab of the luminescent brightness *B* multiplied by the appropriate forward and backward Green's functions [6].

4.3. Boundary Conditions

For the luminescent escaping fluxes, $I_{x,y,z}^{(\pm)}$, we have to consider reflection and transmission at the surfaces. For example, at the left surface $x = 0$, the far surface $y = 0$, and the top surface $z = 0$, these are

$$I_{x,y,z}^{(+)}(0) = B_{L,F,T} I_{x,y,z}^{(-)}(0), \quad (9)$$

where $R_{L,F,T}$ are the reflection coefficients averaged over the escape cone for the luminescent escaping fluxes at the left, far, and top surfaces, respectively. Similar boundary conditions on $I_{x,y,z}^{(\pm)}$ apply at the right surface $x = L$, the near surface $y = W$, and bottom surface $z = D$, with appropriate reflection coefficients $R_{R,N,B}$ at the right, near, and bottom surfaces, respectively. At the top and bottom, we also have boundary conditions on the fluxes $I_d^{(\pm)}$:

$$I_d^{(+)}(0) = (1 - R_{Td}) I_1 + R_{Td} I_d^{(-)}(0), \quad (10)$$

$$I_d^{(-)}(D) = R_{Bd} I_d^{(+)}(D) \quad (11)$$

with reflection coefficients R_{Td} and R_{Bd} as required for the angle of incidence of the direct incident light.

In the *x* and *y* directions at the left (L) and far (F) surfaces, the boundary conditions for the luminescent escaping fluxes outside the slab are

$$I_{L,F} = (1 - R_{L,F}) I_{x,y}^{(-)}(0) \quad (12)$$

with similar equations at the right (R), near (N), top (T), and bottom (B) surfaces. By integrating the differential equations for the escaping fluxes, evaluating the resulting expressions at the surfaces and applying the boundary conditions, we derive the escaping intensities. In carrying out these calculations, it is convenient, since the reflection coefficients lie in the range [0, 1], to rewrite the reflectivities as

$$R_P = e^{-\alpha_P}, \quad \alpha_{PQ} = \frac{\alpha_P + \alpha_Q}{2}, \quad (13)$$

where P, Q = L, R, F, N, T, B, Td, Bd.

4.4. Escaping Intensities

The expressions for the luminescent escaping intensities within the slab in the *x*, *y*, and *z* directions are related by symmetry. For example, I_x is given by

$$I_x(x, y, z) = \frac{\Omega_c \lambda_e \cosh(\lambda_a x + \alpha_L/2)}{2\pi \sinh(\lambda_a L + \alpha_{LR})} \times \int_0^L dx' \cosh[\lambda_a(L - x') + \alpha_R/2] B(x', y, z) - \frac{\Omega_c \lambda_e}{2\pi} \int_0^x dx' \sinh[\lambda_a(x - x')] B(x', y, z), \quad (14)$$

and the expressions for I_y and I_z are generated by replacing the coordinate, the slab dimension, and the α subscripts in Eq. (14) with those appropriate for the direction of interest. The intensity, I_d, within the slab owing to unabsorbed incident radiation is given by

$$I_d(z) = \frac{2 I_1 \sinh(\alpha_{Td}/2) \cosh[N\sigma_a(D - z)/\cos\theta_t + \alpha_{Bd}/2]}{\sinh(N\sigma_a D/\cos\theta_t + \alpha_{TdBd})}. \quad (15)$$

The expressions for the luminescent fluxes outside the slab escaping the surfaces in the *x*, *y*, and *z* directions are again related by symmetry. For example, the fluxes I_R and I_L escaping the right and left surfaces in the *x* direction, respectively, are

$$I_R(y, z) = \frac{\Omega_c \lambda_e}{2\pi} \frac{\exp(-\alpha_{LR}) \exp(-\lambda_a L) \sinh(\alpha_R/2)}{\sinh(\lambda_a L + \alpha_{LR})} \times \int_0^L dx' \cosh[\lambda_a(L - x') + \alpha_R/2] B(x', y, z) + \frac{\Omega_c \lambda_e \exp(-\alpha_R/2) \sinh(\alpha_R/2)}{2\pi} \times \int_0^L dx' \exp[-\lambda_a(L - x')] B(x', y, z), \quad (16)$$

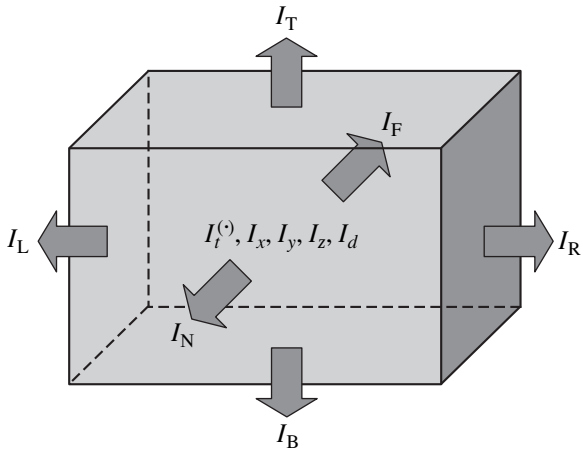

Fig. 2. Schematic diagram illustrating the intensities within the slab comprising the concentrated intensity, I_C, and the fluxes escaping the surfaces.

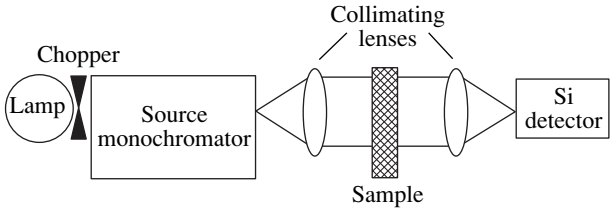

Fig. 3. Apparatus used to measure the absorption properties of test slabs.

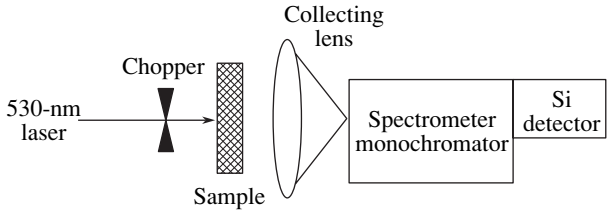

Fig. 4. Apparatus used to measure the luminescence properties of test slabs.

$$I_L(y,z) = \frac{\Omega_c \lambda_e}{2\pi}\frac{\sinh(\alpha_L/2)}{\sinh(\lambda_a L + \alpha_{LR})} \times \int_0^L dx' \cosh[\lambda_a(L-x') + \alpha_R/2] B(x', y, z). \quad (17)$$

The expressions for I_N and I_F and the luminescent components of I_B and I_T are generated by appropriate substitution as for Eq. (14). The latter, I_B and I_T, are similar but contain additional terms arising from the incident flux:

$$I_B(\text{incident}) = I_1 \frac{2\sinh(\alpha_{Bd}/2)\sinh(\alpha_{Td}/2)}{\sinh(N\sigma_a D/\cos\theta_t + \alpha_{TdBd})}, \quad (18)$$

$$I_T(\text{incident}) = I_1 \times \frac{\left[\exp(-\alpha_{Td}/2)\sinh(N\sigma_a D/\cos\theta_t + \alpha_{Bd}/2) + \exp(-\alpha_{Bd}/2)\exp(-N\sigma_a D/\cos\theta_t)\sinh(\alpha_{Td}/2)\right]}{\sinh(N\sigma_a D/\cos\theta_t + \alpha_{TdBd})}. \quad (19)$$

The intensities comprising I_C within the slab (see Fig. 2) are calculated as outlined above by determining the chemical potential, $\mu(x, y, z)$, over a mesh of positions within the slab by Newton–Raphson iteration. This chemical potential distribution best satisfies the detailed balance condition (Eq. (6)) at each point in the slab and is then used to calculate the position-dependent fluxes exiting the surfaces. In this calculation, the Newton–Raphson equation below is solved iteratively for μ at each point in the mesh:

$$\mu_s = \mu_{s-1} - \frac{F(\mu_{s-1})}{F'(\mu_{s-1})}, \quad (20)$$

where we ignore the dependence of I_C on μ, so that

$$F'(\mu) \approx \int d\nu \frac{\sigma_e(\nu)}{Q_e}\frac{8\pi n^2 \nu^2}{c^2}\frac{\beta\exp[(h\nu-\mu)\beta]}{\{\exp[(h\nu-\mu)\beta]-1\}^2}. \quad (21)$$

5. RESULTS

This section is divided into three parts. The first details experimental absorption and luminescence measurements, and the latter are shown to compare favorably with predictions from the model. The second section concerns modeling results and discusses the importance of the QD size distribution, the predicted fluxes exiting the surfaces of a slab and the photon chemical potential. In the third part, predicted short-circuit currents resulting from the fluxes exiting the surfaces of sample slabs uniformly illuminated on their top surfaces are compared with experiment. These measurements show that the 3D flux model agrees with experiment, providing a tool for optimization of the QDC.

5.1. Absorption and Luminescence

Both the sample absorption and luminescence are measured on a wavelength calibrated double monochromator system, composed of two 30-cm Bentham monochromators. The source monochromator has a current stabilized 100-W tungsten filament lamp attached to a variable entrance slit. It is also equipped with order sorting filters, a 1800-lines/mm grating and an exit pinhole aperture of 200 μm. The wavelength resolution varies with entrance slit width, but excitation wavelengths <1 nm can be achieved. The spectrometer monochromator also has a pair of variable slits, a 1200-lines/mm grating and a wavelength resolution of 2 nm. A calibrated Newport 818-UV silicon detector was used for all absorption and luminescence measurements as shown in Figs. 3 and 4.

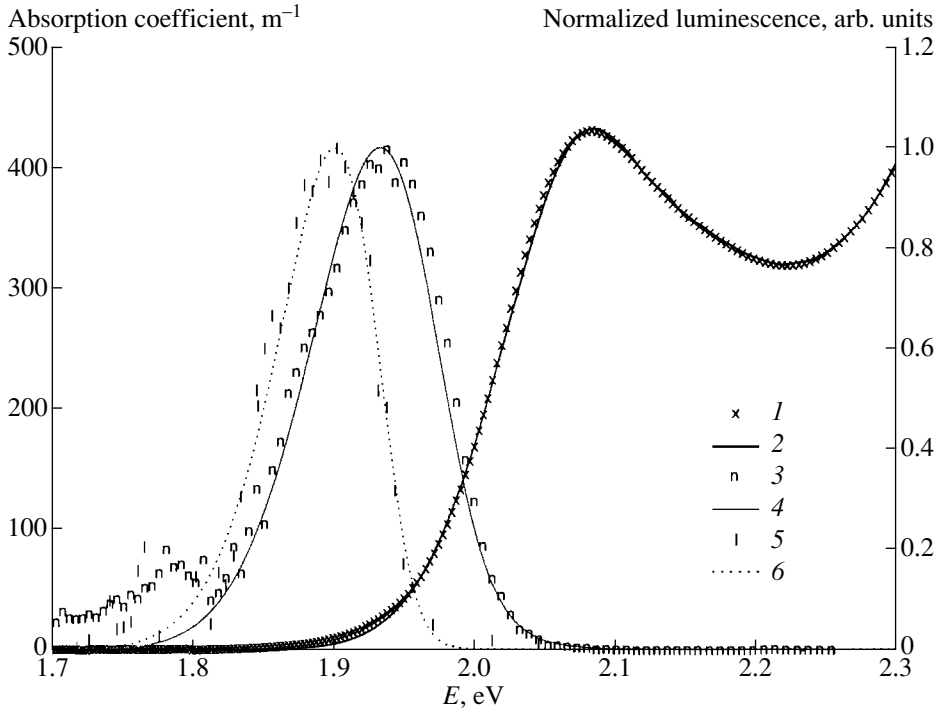

Fig. 5. Measured absorption coefficient (*1*) and Gaussian fit (*2*) to the absorption threshold together with the normalized predicted and observed luminescence for the L × W × D = 42 × 10 × 5 mm^3 test slab of CdSe/CdS QDs in acrylic. For laser illumination on the near surface, (*3*) indicates the predicted and (*4*) the observed luminescence. For laser illumination on the left surface, (*5*) indicates the predicted and (*6*) the observed luminescence.

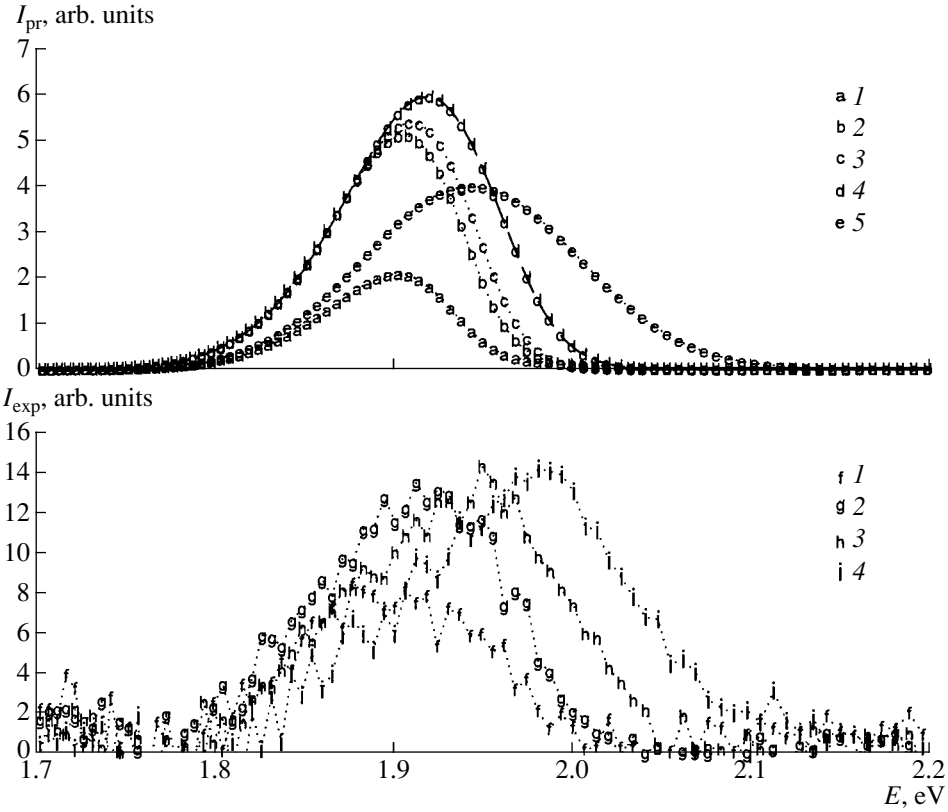

Fig. 6. Variation of the predicted (I_{pr}) and observed (I_{exp}) luminescence escaping the right surface with the position of laser illumination on the top surface for the test slab of CdSe/CdS QDs in acrylic. In the calculations of the predicted luminescence (top chart), it was assumed that Q_e = 0.5 as determined from the photocurrent measurements. Simulations were carried out at laser positions x/L = (*1*) 0, (*2*) 0.25, (*3*) 0.5, (*4*) 0.75, (*5*) 1. The bottom chart shows the experimental luminescence measured with the laser at positions x/L = (*1*) 0.55, (*2*) 0.76, (*3*) 0.86, (*4*) 0.95.

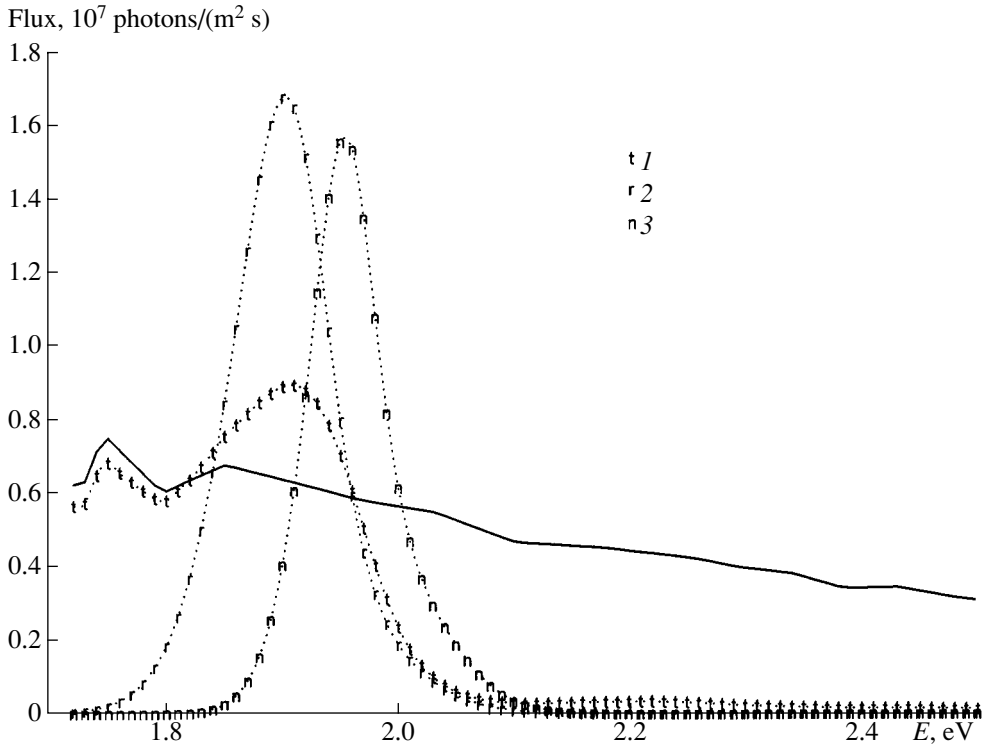

Fig. 7. Predicted average fluxes escaping the top and right surfaces of the test slab of CdSe/CdS QDs in acrylic again assuming the best fit value of $Q_e = 0.5$. The slab has perfect mirrors at $x = 0$, $y = (0, W)$, and $z = D$, and is illuminated by AM1.5 at normal incidence. The solid curve indicates the incident flux. Curves (*1*) and (*2*) represent the average fluxes escaping from the top and right-hand surfaces, respectively; these fluxes were calculated using the Gaussian fit to the experimental absorption threshold with a half-width of 0.07 eV. Curve *3* is the average flux escaping the right surface for a narrower QD size distribution modeled by a Gaussian fit of half-width 0.05 eV.

Absorption measurements were performed in a parallel-beam configuration (see Fig. 3) by acquiring a transmission measurement on the sample and a reference measurement. The absorption coefficient, $N\sigma_a$, corrected for multiple reflections using Eq. (18) is extracted from the data. Scans were generally carried out over the wavelength range 400 to 800 nm under computer control with the output of the silicon detector amplified by a Stanford research systems SR510 lock-in amplifier and the monochromator driven by a Bentham PM C3B/IEEE controller. For absorption measurements, light from the lamp was chopped before it entered the monochromator with a Bentham 218 variable frequency chopper at a frequency of approximately 188 Hz, which was suitably far away from the mains frequency of 50 Hz to produce good results.

Luminescence measurements were often performed with the straight-through configuration (see Fig. 4), and the light escaping the surface of the sample opposite the laser illumination was focused onto the entrance slit of the spectrometer monochromator and detected at the exit slit by the silicon detector. The luminescence scans were carried out over the relevant wavelength range, again under computer control, using a second chopper and monochromator controller. The luminescence signal was corrected for the throughput of the spectrometer by performing two additional scans, firstly, with the beam from the source monochromator focused into the spectrometer and, secondly, a reference scan as for the absorption measurements.

We assume that the frequency dependence of $\sigma_e(\nu)$ at threshold is Gaussian as expected for dots with δ-function density of states and Gaussian distributed diameters [3]. A Gaussian fits the experimental absorption very well down to threshold [6, 7], as illustrated in Fig. 5 together with the predicted and observed luminescence escaping a test slab of CdSe/CdS core-shell QDs in acrylic illuminated by a 530-nm laser in the x and y coordinate directions. The laser spot (diameter 3 mm) was positioned in the center of the face of the slab of material, and the luminescence was collected from the opposite surface. The slab was rotated such that the laser illuminated the left surface at $x = 0$ and the near surface at $y = 0$.

Figure 5 shows the excellent agreement between the shape and position (redshift) of the predicted and observed luminescence for the two directions of laser illumination, although a small laser feature interferes with the experiment between 1.7 and 1.8 eV.

With laser illumination of a slab, the intensity and redshift of the flux escaping the right surface, I_R, is very dependent on the position of laser excitation on the top

surface. In an additional experiment, the luminescence escaping the right surface of the sample slab of CdSe/CdS QDs in acrylic was measured as the laser spot was moved along the center of the top surface. The same equipment as shown in Fig. 4 was used, but the laser was positioned such that the beam was perpendicular to the collection optics. Figure 6 shows both the variation of the predicted and observed luminescence escaping the right surface of the slab with laser illumination position x/L. Unfortunately, the collected signal was too noisy to detect at laser positions less than $x/L = 0.5$ since the path length of the escaping luminescence is longer than in the straight-through configuration. It is easy to adapt the model to simulate laser excitation, because the incident light term depends only on z and can simply be removed from the model at (x, y) positions where the laser is not illuminating the slab. These measurements show that the model predicts the correct trends for the redshift, the profile of the luminescence, and its intensity as the laser position is varied. Compared to illumination at $x/L = 1$, we would expect the luminescence spectrum for illumination at $x/L = 0.95$ to be narrower owing to reabsorption and of higher intensity because more of the laser light can be absorbed.

5.2. Modeling Results

The profile and redshift of the luminescence peak also depends critically on the shape of the absorption cross section near threshold, which reflects the QD size distribution. A narrower distribution of dot diameters can be modeled by narrowing the Gaussian fit to the absorption edge. The calculated fluxes escaping the surfaces for the test slab of CdSe/CdS core-shell QDs in acrylic assuming perfect mirrors at $x = L$ and $y = (0, W)$ are illustrated in Fig. 7 for the Gaussian fit (half-width 0.07 eV) to the experimental absorption. Figure 7 shows the concentration of radiation into the flux that would be collected by a solar cell at the right surface. Also illustrated in Fig. 7 is the predicted flux escaping the right surface if the distribution of QD sizes were narrower such that the Gaussian fit to the absorption threshold has half-width 0.05 eV.

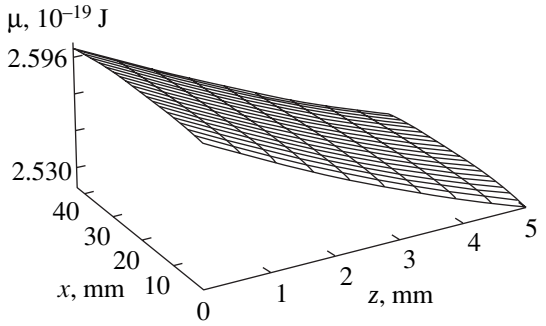

Fig. 8. The position-dependent chemical potential of the test slab of CdSe/CdS QDs in acrylic assuming $Q_e = 1$, perfect mirrors at $y = (0, W)$, and illumination by AM1.5 at normal incidence.

For a narrow distribution of QD sizes characterized by a sharp absorption threshold, there is a smaller redshift and, therefore, greater overlap with the luminescence, leading to larger reabsorption losses [6, 7] and less radiation escaping the right surface. The model allows us to investigate quantitatively the distribution of dot diameters that minimizes these losses. This is particularly important in our experiments, since the luminescence quantum efficiency of the QDs in our test slab was rather low.

The chemical potential determined from the 3D flux analysis as a function of position, (x, z), for the CdSe/CdS QD sample slab with perfect mirrors at $y = (0, W)$ such that there is no variation of μ with y is shown in Fig. 8. With no mirrors on the surfaces in the x direction, the chemical potential is symmetric about $x = L/2$ and decreases with depth z, allowing radiation of low-energy photons near the bottom of the slab.

5.3. Photocurrent Measurements

Short-circuit currents, J_{sc}, resulting from the radiation escaping the bottom, near, and right surfaces of the slab of CdSe/CdS QDs in acrylic and slabs of red and green dyes in perspex were measured and are compared with the predicted values in Tables 1 and 2. The luminescence quantum efficiency, Q_e, of the perylene dyes

Table 1. Measured (top) and predicted (bottom) short-circuit current, J_{sc}, using the 2.65×2.65-mm Si photodetector for the three unmirrored slabs investigated

Luminescent species	Slab size, mm	Q_e	J_{sc}, mA/m^2		
			$z = D$	$y = W$	$x = L$
CdSe/CdS	$42 \times 10 \times 5$	0.50	84.0 ± 2.0	4.6 ± 2.0	11.1 ± 2.0
QDs			78.3 ± 1.9	3.6 ± 0.8	10.0 ± 1.4
Red dye	$40 \times 15 \times 3$	0.95	88.4 ± 2.0	10.4 ± 2.0	20.1 ± 2.0
			85.4 ± 2.0	11.1 ± 1.1	22.0 ± 1.7
Green dye	$40 \times 15 \times 3$	0.95	93.2 ± 2.0	3.2 ± 2.0	4.9 ± 2.0
			96.0 ± 2.1	2.1 ± 0.3	4.0 ± 0.9

Table 2. Measured (top) and predicted (bottom) short-circuit current, J_{sc}, using the 3×3-mm GaAs photodetector for the red mirrored slab

Luminescent species	Slab size, mm	Q_e	Blue filter used	J_{sc}, mA/m^2
				$x = L$
Red dye	$40 \times 15 \times 3$	0.95	No	26.0 ± 2.0
				26.0 ± 2.6
Red dye	$40 \times 15 \times 3$	0.95	Yes	12.7 ± 2.0
				15.6 ± 2.1

Note: The reflectivity of the evaporated aluminum mirrors on the surfaces at $x = 0$, $z = D$, and $y = (0, W)$ was assumed to be 0.9. A blue filter could be placed between the lamp and sample to modify the spectrum of the light incident on the top surface of the slab.

is known to be about 0.95, and the unknown Q_e of the QDs was determined by the best fit to the experimental measurements.

The slabs were positioned on a matt black stage with a matt black background to avoid unwanted reflections and were illuminated at normal incidence by a calibrated Oriel fiber lamp. Two calibrated photodetectors that could be positioned against any surface were utilized to obtain J_{sc} values, using a Keithley 236 source measure unit. The uncertainty in the measurements is due to current generated by coupling of the incident light into the edges of the photodetector, and allowance has been made for this by background measurements. The uncertainty in the predictions is mainly due to the 5% uncertainty in the experimental absorption.

The lamp spectrum was measured using the apparatus in Fig. 4 with the lamp focused into the entrance slit of the spectrometer monochromator. For the J_{sc} measurements, the lamp was positioned such that light reaching the sample could only diverge by five degrees and corrections from normal incidence were negligible. The uniformity of the lamp illumination was checked and found to vary by less than 5% over the plane where the top surface of the test slab was positioned.

The quantum efficiencies (QEs) of the 2.65×2.65-mm Si photodetector and the 3×3 mm-GaAs photodetector was determined with the apparatus in Fig. 3 by taking the ratio of a scan with the photodetector and a reference scan with the Newport 818-UV silicon detector corrected for its known QE. In order to calculate the predicted short-circuit currents, it is necessary to correct for the angular dependence of the QE of the photodetector, since the luminescence escapes at all angles over the hemisphere from each surface. The 2.65×2.65-mm Si photodetector was supplied with a correction curve, and it would have been preferable to use this photodetector for all the measurements. However, it was not available at the time of the measurements on the mirrored red slab, and these could not be repeated owing to poor adhesion of the evaporated aluminum mirrors. Therefore, the same angular corrections were applied to the predictions of the short-circuit

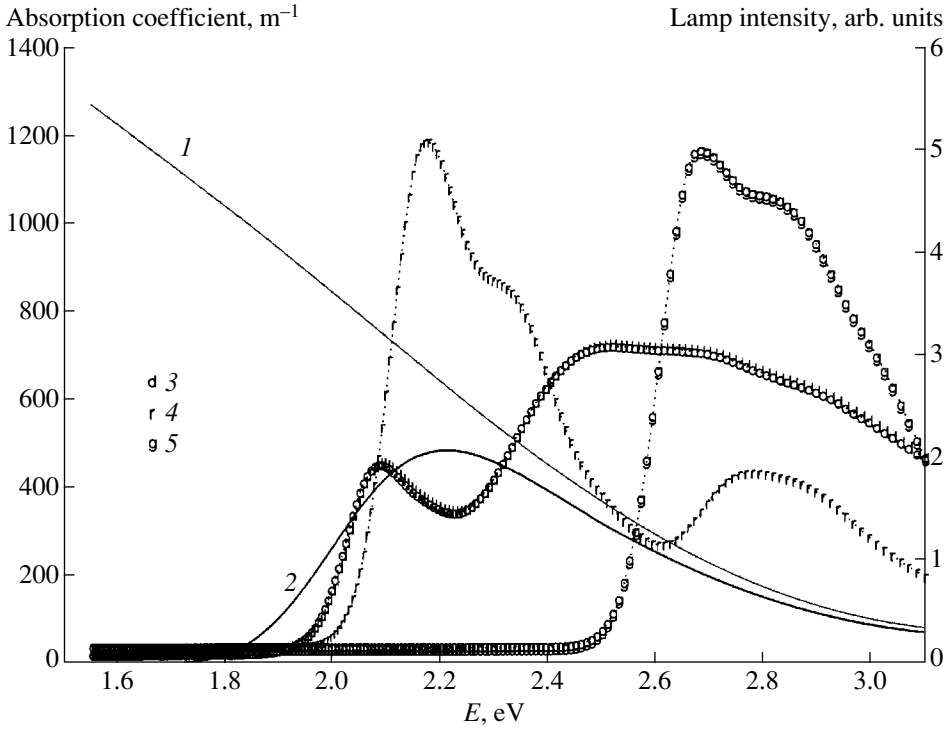

Fig. 9. The Oriel lamp spectrum and effect of the blue filter together with the absorption spectra of the three materials investigated. Curve *1* is the Oriel spectrum, and curve *2* shows how the incident light spectrum is modified when the blue filter is used. Curves with symbols *3*–*5* are the absorption (*3*) of the QDs in acrylic, (*4*) of the red dye in perspex, and (*5*) of the green dye in perspex.

current from the 3×3 mm GaAs photodetector, leading to a greater uncertainty in these predictions.

The Oriel lamp spectrum and effect of the blue filter are illustrated together with the absorption coefficient, $N\sigma_a$, of the three materials in Fig. 9. It is very encouraging that all the measurements agree so well with the predictions, given that the materials absorb strongly in different regions of the lamp spectrum and have very different losses owing to the high Q_e of the dyes and relatively low Q_e of the QDs. Our confidence in the model is also increased by the agreement with experiment for the slab with mirrored surfaces and the continued agreement when the spectrum of the light incident on the test slab is altered by a blue filter.

6. CONCLUSION

We have developed a self-consistent thermodynamic model for planar solar concentrators, which allows for overlap of the incident radiation with the luminescence, for reflections at the surfaces, for reabsorption, and for absorption losses in the "transparent" host material. Our 3D flux model was derived by applying the method of Schwarzschild and Milne to Chandrasekhar's general radiative transfer equation coupled to a detailed balance condition. We can predict the efficiencies of luminescent concentrators using only the absorption properties of the slab, its refractive index, and the quantum efficiency Q_e of the luminescence. The QD size distribution can be chosen to *optimize* the redshift and *minimize* the overlap between absorption and luminescence which is a significant advantage for the QDC compared with the dye concentrator. Our results show that the 3D flux model can predict both the redshift and profile of the luminescence, as well as the total flux escaping each surface of a slab, providing a tool for optimization of the QDC.

ACKNOWLEDGMENTS

We thank BP Solar, Saint-Gobain, the EPSRC, and the European Commission (sixth framework program Integrated Project FULLSPECTRUM contract no. SES6-CT-2003-502620) for financial support. We are grateful to Dave Bushnell for his control software and to Simon Arridge for his helpful participation in discussions concerning the radiative transfer.

REFERENCES

1. A. Goetzberger and W. Greubel, Appl. Phys. **14**, 123 (1977).
2. A. Goetzberger, W. Stahl, and V. Wittwer, in *Proceedings of 6th European Photovoltaic Solar Energy Conference* (Reidel, Dordrecht, 1985), p. 209.
3. K. W. J. Barnham, J. L. Marques, J. Hassard, and P. O'Brien, Appl. Phys. Lett. **76**, 1197 (2000).
4. A. P. Alivisatos, MRS Bull. (February 18, 1998).
5. O. I. Micic, C. J. Curtis, K. M. Jones, *et al.*, J. Phys. Chem. **98**, 4966 (1994).
6. A. J. Chatten, K. W. J. Barnham, B. F. Buxton, *et al.*, in *Proceedings of 17th European Photovoltaic Solar Energy Conference* (Munich, Germany, 2001), p. 200.
7. A. J. Chatten, K. W. J. Barnham, B. F. Buxton, *et al.*, Sol. Energy Mater. Sol. Cells **75**, 363 (2003).
8. E. Yablonovitch, J. Opt. Soc. Am. **70**, 1362 (1980).
9. S. Chandrasekhar, *Radiative Transfer* (Clarendon, Oxford, UK, 1950; Inostrannaya Literatura, Moscow, 1953).
10. E. A. Milne, Mon. Not. R. Astron. Soc. **81**, 361 (1921).

Semiconductors, Vol. 38, No. 8, 2004, pp. 918–922. From Fizika i Tekhnika Poluprovodnikov, Vol. 38, No. 8, 2004, pp. 958–962.

SYMPOSIUM ON THE EFFICIENT USE OF SOLAR RADIATION IN PHOTOVOLTAIC POWER ENGINEERING (St. Petersburg, November 3–4, 2003)

Key Aspects in the Modeling of Concentrator III–V Solar Cells and III–V Thermophotovoltaic Converters[1]

Carlos Algora

Instituto de Energía Solar-Universidad Politécnica de Madrid E.T.S.I. Telecomunicación, 28040 Madrid, Spain

e-mail: algora@ies-def.upm.es

Submitted February 9, 2004; accepted for publication February 11, 2004

Abstract—The development of III–V concentrator solar cells and thermophotovoltaic converters is at a critical point in which both sophisticated technology and an accurate modeling are required. This paper emphasizes the aspects relating to the modeling of multijunction solar cells for the concentration of applications and thermophotovoltaic converters. In the case of solar cells, the key aspects are

—Necessity of three-dimensional modeling,

—Consideration of real conditions of operation,

—Critical review of material parameters.

For TPV converters, the aforementioned aspects are also to be applied. Preliminarily, the material parameters of the less mature thermophotovoltaic semiconductors must be specified or even measured. © *2004 MAIK "Nauka/Interperiodica".*

1. INTRODUCTION

Light concentration together with III–V semiconductor solar cells constitute a strategy that has been proposed as a way to reduce the cost of photovoltaic (PV) electricity to reach levels close or even lower than those of the electricity produced from fossil fuels [1, 2]. Up to now, the highest efficiency for a single junction solar cell at a concentration of 1000 suns has been obtained by a GaAs solar cell with a 26.2% efficiency [3], and there is more room for achieving efficiencies in the range of 28–29% [4]. These practical efficiencies achieved at 1000 suns could lead to a price of 2.5–3.0 €/W_p for a turnkey grid connected PV installation. The corresponding price of the electricity produced would be 0.1 €/kWh for a cumulated production of only 10 MW_p [5].

For an additional reduction of these prices thanks to an increase in efficiency, the use of multijunction cells (where several cells are each used with a different band gap with each one converting a narrow range of photon energies close to its band gap) is necessary. For example, if the current space-cell production were applied in 100-sun concentrator cells and learning were assumed for a cumulated production of 1000 MW_p together with a solar cell efficiency of 40%, the price of the PV electricity would decrease to less than 0.03 €/KWh. The corresponding price for a turnkey PV grid-connected installation would be less than 0.7 €/W_p [5]. This efficiency value of 40% is not extremely optimistic, because in 2003 Spectrolab achieved an efficiency of 36.9% at 309 suns [6].

The path towards these high efficiencies must be guided by an accurate and reliable modeling of the III–V solar cells. This way, the origins of efficiency loss could be determined and consequently avoided. This aspect is very important because concentrator single junction GaAs solar cells have already achieved practical efficiencies of more than 70% of their upper theoretical limit, while in the case of concentrator III–V multijunction cells their practical efficiencies are less than 60% of their ideal limit.

An important challenge in the modeling of III–V concentrator solar cells is the consideration of real operation conditions inside optical concentrators [5]. Among the most important ones are the different illumination spectra as a consequence of the light way through the concentrator optics, the inhomogeneous illumination produced by the optics over the solar cell, the chromatic aberration, the temperature gradients in different parts of the solar cell, etc. Therefore, an accurate and useful model must consider all the aforementioned aspects [7].

In the case of thermophotovoltaic (TPV) converters, their modeling should also consider the particular conditions of each system where they will operate. All the key aspects in the modeling of multijunction solar cells can be applied to TPV devices. But, in addition, there are specific problems because the TPV semiconductor materials are less known and less mature (GaSb, GaInSb, InGaAs, etc.), so there are less reliable material data [8].

[1]This article was submitted by the authors in English.

2. CONCENTRATOR III–V SOLAR CELLS

The Solar Energy Institute of Madrid pioneered several years ago the simultaneous modeling of the whole concentrator solar cell. In the past, the existing models considered only a part of the cell. We proposed to take into account all the parts of the solar cell: the semiconductor structure, ohmic contacts, ARC, external connections like wire bonding, etc. Additional aspects like a given geometry and size of the solar cell were also considered. In this way, we gained wide experience in the two-dimensional (2D) modeling that was applied to GaAs solar cells [9, 10] and GaSb TPV converters [11].

2.1. Necessity of Three-Dimensional Modeling

However, the complexity of concentrator multijunction solar cells requires three-dimensional (3D) modeling. The development of custom tools for 3D modeling is one possibility, whose main advantage is the more familiar implementation of custom-made models, as well as a good control over the whole simulation program. But on the other hand, the development of a very complicated calculation strategy is required and the flexibility for depicting and drawing multiple effects (like variation of voltage, current lines, etc.) is highly limited.

An alternative is the use of commercial programs. Traditionally, the PC-1D has been widely used but mainly for 1-sun silicon solar cells. For III–V solar cells, its use has been very restricted. Lately, the use of very powerful programs that are widely used in microelectronic devices (like Atlas™ from Silvaco, Dessis™ from ISE TCAD, or Taurus-Medici™ from Synopsys) has started in several PV research groups. Although the potential of these simulation tools for multijunction cells has been already applied, their use has been restricted to 2D purposes [12, 13].

A very interesting example of the use of commercial programs not specifically designed for the modeling of semiconductor devices is that of the PSPICE™. The method of 3D simulation requires, firstly, the division of the whole solar cell into elementary subcells. After this, each subcell is modeled by circuit elements composed of diodes, resistors, and current sources. Finally, the resulting nonlinear circuit is solved with the PSPICE™ simulation tool. This approach together with the details of the method and results can be found in [14].

Figure 1 is an example of the great usefulness of this method. The voltage drop in different parts (bus bar, metal fingers, and uncovered regions) of a GaAs solar cell at 1000 suns is shown. Depending on the front contact properties, the voltage drop can be very severe. Thus, a medium or bad quality front metal contact appears as an important origin of resistive losses.

2.2. Consideration of Real Conditions of Operation

An important effect that can be evaluated by this method is the effect of light inhomogeneity on the solar cell when it operates inside a concentrator. Figure 2

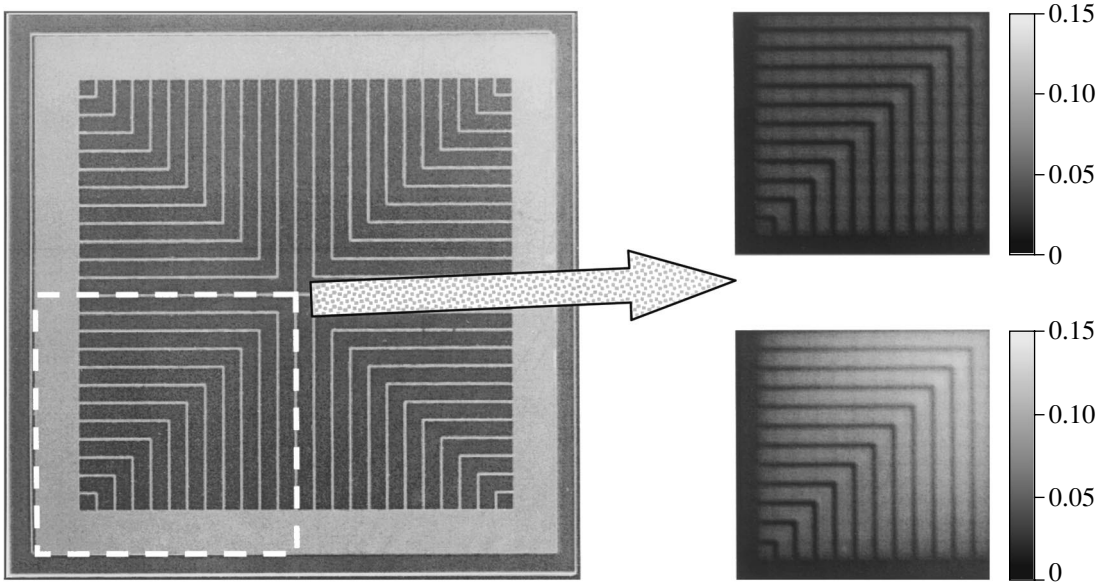

Fig. 1. (Left) Photograph of a *p*-on-*n*-GaAs solar cell manufactured and designed for operation at 1000 suns. Its size inside the bus bar is 1 mm^2. The quarter marked with a dotted line is analyzed by the 3D model of [14], whose results are presented on the right. (Right) Voltage drop in a gray scale from 0.00 to 0.15 volts. The illumination is uniform with an intensity of 1000 suns. Two cases are analyzed: (top) a good front contact characterized by a thickness of 1 micron, a resistivity of 2.2×10^{-6} Ω cm and a specific contact resistance of 5×10^{-5} Ω cm^2; (bottom) a medium quality front contact characterized by a thickness of 1 micron, a resistivity of 2.2×10^{-5} Ω cm and a specific contact resistance of 10^{-4} Ω cm^2.

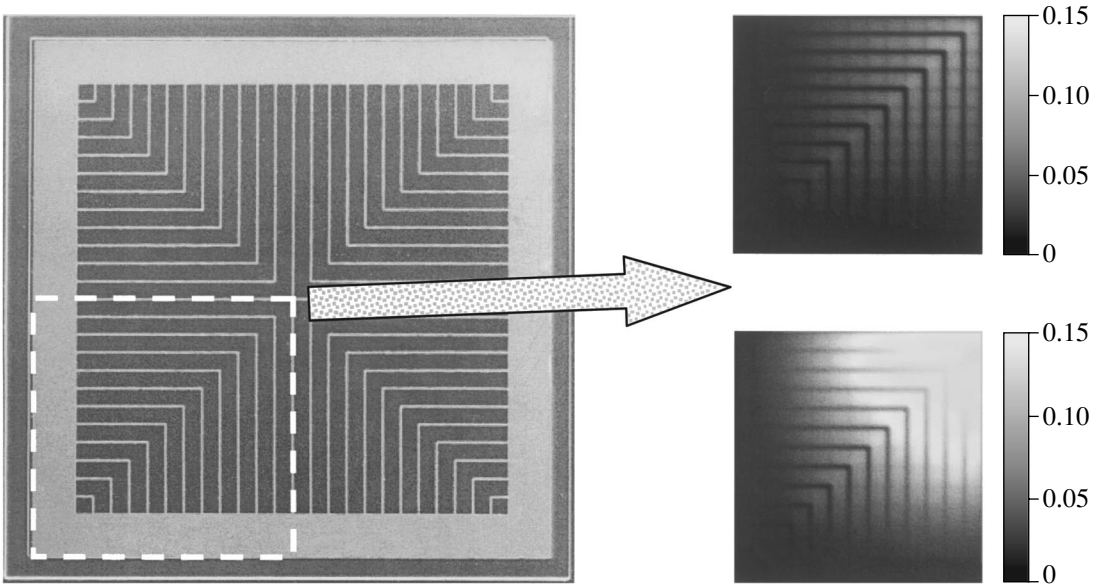

Fig. 2. (Left) Photograph of a *p*-on-*n*-GaAs solar cell manufactured and designed for operation at 1000 suns. Its size inside the bus bar is 1 mm^2. The quarter marked with a dotted line is analyzed by the 3D model of [14] whose results are presented on the right. (Right) Voltage drop in a grey scale from 0.00 to 0.15 volts. The illumination is nonuniform with an average intensity of 1000 suns and a peak of 4000 suns at the center of the solar cell and zero intensity close to the bus bar. Thus, the average light intensity is 1000 suns when the spot is integrated through the whole solar cell. Two cases are analyzed: (top) a good front contact characterized by a thickness of 1 micron, a resistivity of 2.2×10^{-6} Ω cm and a specific contact resistance of 5×10^{-5} Ω cm^2; (bottom) a medium quality front contact characterized by a thickness of 1 micron, a resistivity of 2.2×10^{-5} Ω cm and a specific contact resistance of 10^{-4} Ω cm^2.

shows the same GaAs solar cell but now illuminated by a light spot with a 4000-sun peak at the center of the cell and zero intensity close to the bus bar. Thus, the average light intensity is 1000 suns when the spot is integrated through the whole solar cell. Now, Fig. 2 shows that the voltage drop is more severe than in Fig. 1. There is even a voltage drop of 0.15 V across several metal fingers when the quality of the contact is medium.

Voltage losses of both Figs. 1 and 2 influence the final efficiency in the way presented in Fig. 3. As can be seen, the efficiency losses due to inhomogeneous light on the GaAs solar cell when it operates at an average intensity of 1000 suns is 0.5% (absolute) when the front contact is good, while the losses increase to 1.6% (absolute) for a medium quality contact.

This example of nonuniform illumination introduces the necessity of modeling the concentrator solar cells under real conditions. At present, the characterization of concentrator solar cells is commonly performed by means of the AM1.5D spectrum and by using normal incidence of light onto the solar cell. Obviously, this type of procedure has had such a great influence on the field of simulation and optimization that in fact the majority of simulation results have assumed an AM1.5D spectrum, normal incidence of light, etc. However, a good solar cell at these "standard" concentration conditions could become an average solar cell it when operates inside a real optical concentrator.

Therefore, for concentration applications the efficiency record tables are relatively important because they inform us about the technological level of a laboratory or a company but do not inform us about the real performance of concentrator solar cells. Consequently,

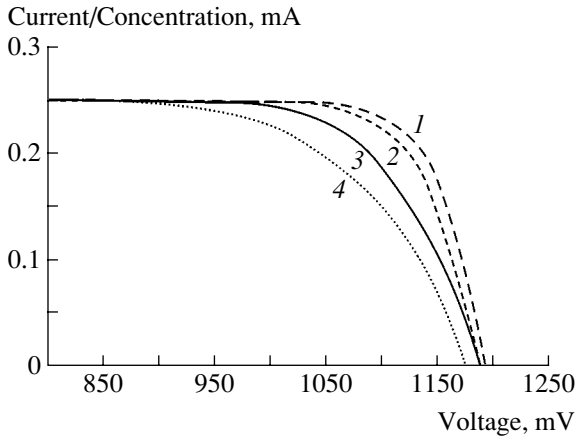

Fig. 3. Illumination *I–V* curves of the concentrator solar cell considering the four cases covered in Figs. 1 and 2, illumination 1000 suns average: (*1*, *2*) good quality front contacts, (*3*, *4*) medium quality front contact, (*1*, *3*) uniform illumination, (*2*, *4*) nonuniform illumination.

concentrator III–V multijunction solar cells should be designed (and of course manufactured) to match a given concentrator (and vice versa).

A kind of real operation appears because of the large area of given concentrator compared to the solar cell size. Light impinges on the solar cell in the shape of an inverted cone, pyramid, etc. (depending on the shape of the optics). So the sine law of concentration forces an increase of the light angle impinging on the cell when concentration increases. Therefore, light impinges on the cell forming a wide-angle cone for high concentrations. The modeling of this situation was stated in [15] and was applied to the practical TIR-R concentrator in [16]. In order to model the wide-angle cone of light, the light power distribution at each angle must be known.

Another example of real conditions is spectrum variation. This has been a recent topic of study but only from the point of view of its variation during the day (more weight of the red or blue part of the solar spectrum) or even during the year. The goal was to maximize the energy produced by the concentrator solar cell [17]. However, it is much more important to consider the change in the spectrum produced by the optical concentrator. Therefore, once the average solar spectrum is determined, its modification by the optical concentrator must be taken into account. Figure 4 shows a clear example where the spectral transmission of the TIR-R concentrator is presented [18]. As can be seen, the weak transmission in the infrared region must be taken into account in a correct design of a multijunction solar cell in order to match the current of the different junctions. The aforementioned examples of real situations presented in this section and the resulting modeling and treatment can be found in [7].

2.3. Critical Review of Physical Parameter Data

On the other hand, one important task to carry out in the modeling is the determination of the optimal semiconductor materials as a function of the number of junctions. The traditional approach has been to use lattice matched materials. In the case of two junctions, the chosen materials were GaInP/GaAs, while for three junctions the chosen materials were GaInP/GaAs/Ge or, more recently, GaInP/GaInAs/Ge [6]. However, there are other options based on mismatched (so-called metamorphic) materials which also produce good efficiencies like $Ga_{0.35}In_{0.65}P/Ga_{0.83}In_{0.17}As/GaAs$ [6, 19].

In all these tasks, the common models of semiconductor devices based on the solution of minority-carrier transport equations need to be fed with accurate physical parameters. Therefore, a critical review of the material parameters of ternary and quaternary alloys must be carried out. Even now, a mature binary material such as GaAs is being reviewed for some of its parameters, like *n*-type band-gap narrowing [20]. The case of GaAs is just the "tip of the iceberg," because the parameters of many materials that are less mature are not well known

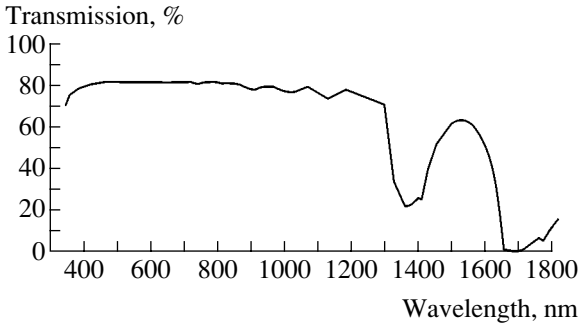

Fig. 4. Spectral transmission of the TIR-R concentrator like the one described in [18].

or are simply unknown. A typical case is that of the "desired 1-eV material" for the 4th junction, for which the most widespread candidate is GaInNAs (so-called "GINA"). In cases like this, there will be a great lack of material physical data, so specific material characterization over semiconductor structures specifically grown for this purpose should be carried out

3. TPV CONVERTERS

There are the following parallelisms and differences between PV and TPV:

—In the case of PV, the source is the sun, while in TPV there are many sources.

—The distance between the source and the converter is fixed in the case of PV (Sun–Earth), while in TPV it can be any distance.

—There are standard spectra for PV (AM1.5D, AM1.5G, etc.), but there are no standard spectra for TPV.

—The efficiency definition is self-consistent for PV, while conditions need to be applied in TPV.

Again, as we concluded for the concentrator multijunction solar cells, the modeling of TPV converters should consider the particular conditions of the system where they will be included, although in TPV the assumption of particular conditions is even more important. Unfortunately, the modeling of TPV devices is still at an early stage in which the inclusion of many real conditions seems rather utopian. First, the following more basic tasks must be undertaken.

The most mature semiconductor material for TPV applications is GaSb. However, its material properties are still under discussion. A good review of the GaSb material properties suitable for TPV devices was carried out in [21] and was complemented and extended in some aspects in [8]. As can be seen in both references, their date of publication is very recent, which shows the scarcity of this type of data. The lack of material parameter models that include their variation with temperature is even more surprising when we consider that TPV devices operate at high temperatures (around 50–100°C). An analysis on this subject has just appeared now in 2004 [22]. Of course, the lack of well-contrasted mate-

rial parameters is more intense in semiconductors that have become more widespread in recent years for TPV devices like GaInAs, InGaSb, InGaAsSb, InAsSbP, etc. Consequently, great effort should be made in the years to come.

Another important aspect is the high doping levels used in GaSb devices when they are manufactured by zinc diffusion. At present, this is the preferred technology for GaSb, with which doping levels of 10^{20}–10^{21} cm^{-3} are achieved (zinc diffusion is also applied to produce TPV devices with other materials like InGaAs, InAs, InAsSbP, etc.). These high doping levels require a specific modeling of the device like the one proposed in [11], which needs material parameters like those presented in [8].

Once all these basic tasks have been overcome, the modeling of TPV devices will take advantage of the modeling carried out previously for III–V concentrator solar cells.

4. CONCLUSION

An accurate modeling of concentrator III–V multijunction solar cells and III–V TPV converters is absolutely necessary in order to guide technology to increase the performance of these devices. The present situation in which concentrator solar cells are beginning to be included in complete concentrator systems for demonstration purposes is unique. Therefore, it is necessary to develop a modeling that is as accurate as possible by considering real conditions of operation.

TPV converters have to some extent lagged behind in this respect. Firstly, intensive work in determining the material parameters of the semiconductors of interest is required. After this, TPV devices will take advantage of the modeling previously developed for solar cells.

ACKNOWLEDGMENTS

The author would like to express his gratitude to Ms. Beatriz Galiana, Mr. Mathieu Baudrit, Mr. Diego Martín, and Prof. Ignacio Rey-Stolle for their close collaboration and involvement in the subjects covered in this paper. The author would also like to thank the rest of the previous and present members of the III–V Semiconductors Group of the Solar Energy Institute of Madrid.

This paper was supported by the European Commission, contract no. SES6-CT-2003-502620 (FULLSPECTRUM project), FEDER funds for scientific infrastructure, and the Spanish Ministry of Science and Technology, project nos. TIC2002-01012 and TIC2002-11391-E.

REFERENCES

1. C. Algora, V. Diaz, J. C. Miñano, and A. Luque, in *Proceedings of 2nd World Conference on Protovoltaic Solar Energy Conversion* (Vienna, 1998), p. 2225.
2. M. Yamaguchi and A. Luque, IEEE Electron Devices **46**, 2139 (1999).
3. C. Algora, E. Ortiz, I. Rey-Stolle, *et al.*, IEEE Electron Devices **48**, 840 (2001).
4. C. Algora, I. Rey-Stolle, and E. Ortiz, in *Proceedings of 17th European Photovoltaic Solar Energy Conference* (Munich, Germany, 2001), p. 88.
5. C. Algora, in *3rd Generation Photovoltaics for High Efficiency through Full Spectrum Utilization*, Ed. by A. Martí and A. Luque (Inst. of Physics, Bristol, 2004), Chap. 6.
6. R. R. King, C. M. Fetzer, C. M. Colter, *et al.*, in *Proceedings of 3rd World Conference on PV Energy Conversion* (Osaka, Japan, 2003).
7. C. Algora, M. Baudrit, I. Rey-Stolle, *et al.*, in *Proceedings of 18th European Photovoltaic Solar Energy Conference* (Paris, 2004).
8. D. Martín and C. Algora, in *Thermophotovoltaic Generation of Electricity*, Ed. by T. J. Coutts, G. Guazzoni, and J. Luther (AIP, 2003), AIP Conf. Proc., Vol. 653, p. 442.
9. C. Algora and V. Díaz, Solid-State Electron. **41**, 1787 (1997).
10. C. Algora and V. Díaz, Prog. Photovoltaics **8**, 211 (2000).
11. C. Algora and D. Martín, in *Thermophotovoltaic Generation of Electricity*, Ed. by T. J. Coutts, G. Guazzoni, and J. Luther (AIP, 2003), AIP Conf. Proc., Vol. 653, p. 452.
12. P. Michalopoulus, Thesis (Naval Postgraduate School, Monterey, California, 2002).
13. G. Létay, Thesis (Fraunhofer Inst., Freiburg, Germany, 2003).
14. B. Galiana, I. Rey-Stolle, C. Algora, and M. Baudrit, in *Proceedings of 18th European Photovoltaic Solar Energy Conference* (Paris, 2004).
15. C. Algora and V. Díaz, Prog. Photovoltaics: Res. Appl. **7**, 379 (1999).
16. C. Algora, V. Díaz, and I. Rey-Stolle, in *Proceedings of 29th IEEE Photovoltaic Specialists Conference, New Orleans, 2002* (IEEE, New York, 2002), p. 848.
17. W. E. MaMahon, S. Kurtz, K. Emery, and M. S. Young, in *Proceedings of National Center for Photovoltaics and Solar Program Review Meeting* (Denver, CO, 2003).
18. M. Hernández, P. Benítez, J. C. Miñano, J. L. Alvarez, V. Diaz, and J. Alonso, *Sunlight Spectrum on Cell through Very High Concentration Optics* (in press).
19. A. Bett, in *3rd Generation Photovoltaics for High Efficiency through Full Spectrum Utilization*, Ed. by A. Martí and A. Luque (Inst. of Physics, Bristol, 2004), Chap. 4.
20. M. Y. Ghannam, G. Flamand, J. Poortmans, and R. P. Mertens, in *Technical Digest of the International PVSEC-14* (Bangkok, Thailand, 2004).
21. G. Stollwerck, O. V. Sulima, and A. W. Bett, IEEE Trans. Electron Devices **47**, 448 (2000).
22. D. Martín and C. Algora, Semicond. Sci. Technol. (2004) (in press).

Semiconductors, Vol. 38, No. 8, 2004, pp. 923–930. Translated from Fizika i Tekhnika Poluprovodnikov, Vol. 38, No. 8, 2004, pp. 963–970.

SYMPOSIUM ON THE EFFICIENT USE OF SOLAR RADIATION IN PHOTOVOLTAIC POWER ENGINEERING (St. Petersburg, November 3–4, 2003)

Quantum Dot Structures: Fabrication Technology and Control of Parameters

V. M. Ustinov

Ioffe Physicotechnical Institute, Russian Academy of Sciences, St. Petersburg, 194021 Russia

e-mail: vmust@beam.ioffe.rssi.ru

Submitted February 9, 2004; accepted for publication February 11, 2004

Abstract—Quantum dot (QD) semiconductor heterostructures for device applications are currently synthesized using the effect of spontaneous transformation of the growth surface at the initial stage of heteroepitaxy of lattice-mismatched layers. When a certain critical layer thickness is reached, the planar growth surface is transformed into an array of nanoscale islands, as was first demonstrated for an InAs/GaAs system. For various device applications, it is desirable to control the shape and size of individual QDs. This is achieved by variation of the effective thickness of the deposited InAs layer, deposition of several QD layers, the use of various matrix materials and a metamorphic buffer layer, and the addition of a small amount of nitrogen into QDs and the matrix material. © *2004 MAIK "Nauka/Interperiodica".*

1. INTRODUCTION

Semiconductor heterostructures with quantum dots (QDs) that demonstrate properties meeting the demands of device applications are currently synthesized using the effect of spontaneous transformation of the growth surface at the initial stage of heteroepitaxy of lattice-mismatched materials. It was established that the growth surface of the strained layer on the lattice-mismatched substrate is initially flat, and the so-called wetting layer (WL) is formed. However, when a certain critical thickness is reached, the planar front of growth is transformed into an array of 3D nanoislands on the WL surface, which was first demonstrated for an InAs/GaAs system [1]. When these InAs islands are overgrown with GaAs, a dense array of coherent nanoinclusions is formed in the GaAs matrix. Since the InAs band gap is much smaller than that of GaAs, an array of InAs QDs is formed [2]. The array of InAs QDs in the GaAs matrix usually demonstrates a wide band of photoluminescence (PL) in the 1.2-eV range at 77 K, which shows a significant red shift compared to the position one would expect based on the effective thickness of the deposited InAs layer (~2 monolayers, ML). Detailed transmission electron microscopy (TEM) studies have shown that the surface density of InAs islands in the array is $(4–5) \times 10^{10}$ cm^{-2}. An island is a square-based pyramid [3] 30–50 Å in height, and the side of the base is 100–150 Å.

However, for various device applications it is necessary to control the parameters of QD arrays and individual islands, such as the surface density, array uniformity, and size and shape of an island. These parameters exert a direct influence on the electron spectrum of QDs. In this study we show that the effective thickness of the deposited InAs layer determines the spectral position of the QD luminescence line; a successive deposition of several QD layers separated by intermediate GaAs layers gives rise to the formation of vertically coupled QDs, characterized by an increased height-to-base ratio. The position of the luminescence line of InAs QDs is strongly affected by the matrix band gap. A significant increase in the surface density of InAs QDs is achieved by using a "seeding" layer of InAlAs QDs with an increased density of islands, with subsequent deposition of InAs QDs. "Submonolayer" QDs, which are formed by successive deposition of InAs and GaAs layers with an effective thickness of less than 1 ML, demonstrate better uniformity, which results in a considerable narrowing of the luminescence line. The increase in the volume of islands with a corresponding increase in the emission wavelength can be reached by overgrowing the InAs QDs with InGaAs or InGaAsN solid solutions. Also, the emission wavelength can be significantly increased if InAs QDs are grown on a metamorphic InGaAs buffer layer.

2. INFLUENCE OF THE EFFECTIVE THICKNESS OF THE DEPOSITED InAs LAYER ON THE LUMINESCENCE SPECTRUM OF InAs QUANTUM DOTS

In this study, the effective thickness of the deposited InAs layer was varied between 1/12 and 6 ML. The transition from the 2D to the 3D mode of InAs growth was determined from the modification of the medium-energy electron diffraction pattern during the epitaxy. The boundary between 2D and island growth modes lay at 1.7 ML [4], which correlates well with the published data. Figure 1a shows PL spectra of QD structures with

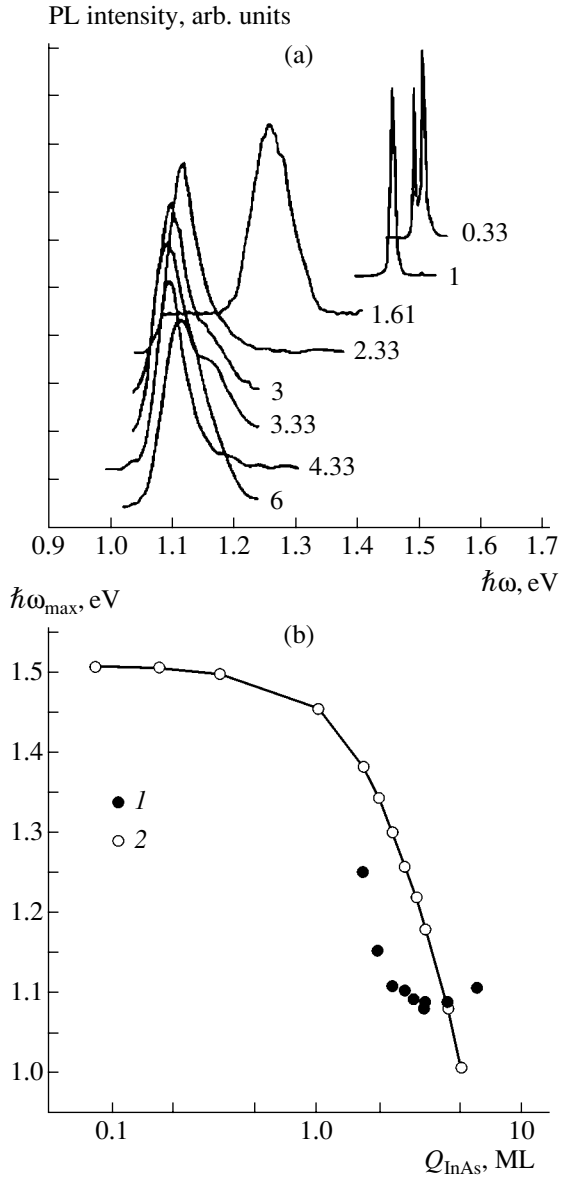

Fig. 1. (a) PL spectra recorded at 77 K from GaAs/InAs/GaAs heterostructures with different effective thicknesses of the deposited InAs layer. Figures by the curves indicate the effective thickness in ML. (b) (*1*) PL peak positions at 77 K as a function of the effective thickness of the deposited InAs layer and (*2*) energies of optical transitions in GaAs/InAs/GaAs heterostructures calculated assuming a 2D distribution of InAs.

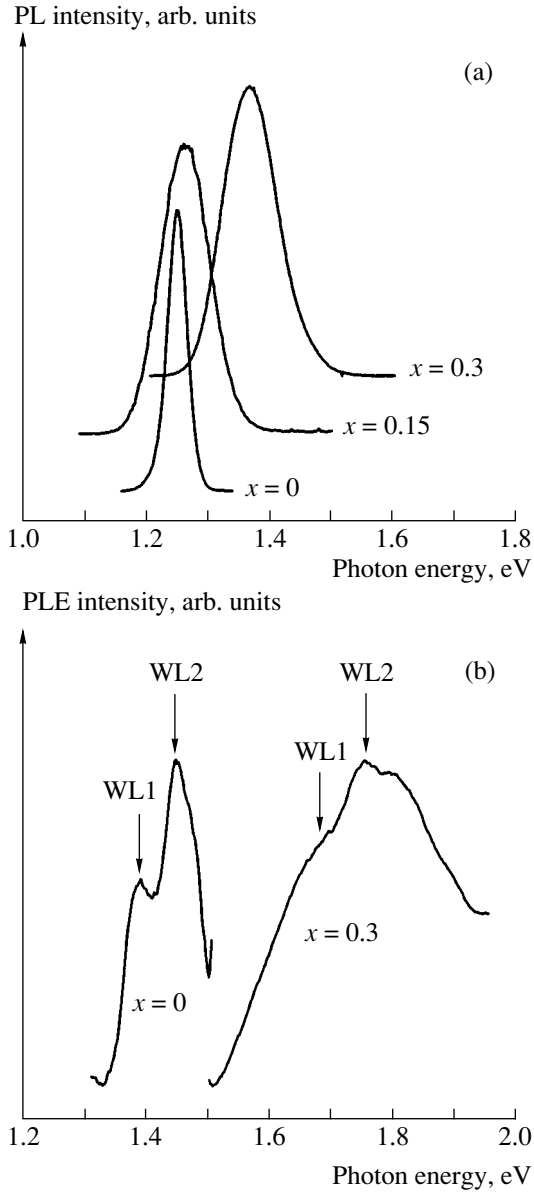

Fig. 2. (a) PL and (b) PL excitation spectra for structures with arrays of InGaAs/AlGaAs QDs; *x* is the mole fraction of AlAs in the matrix material.

different effective thicknesses of the deposited InAs layer, Q_{InAs}, at 77 K. When $Q_{InAs} < 1$ ML, narrow lines are observed, their position is close to that for bulk GaAs. When $Q_{InAs} > 1$ ML, the PL band is broad and it is red-shifted. The typical FWHM is 50 meV. Figure 1b shows the energy position of the PL peak as a function of Q_{InAs}. The experimental data are compared with the energies of optical transitions calculated assuming a 2D distribution of the same amount of InAs [GaAs/InAs/GaAs quantum well (QW)]. It can be seen that the experimental energy of the PL peak becomes significantly smaller than the calculated one when 3D islands are formed. The energy difference is 100 meV at the initial stage of the formation of islands (1.7 ML), and it increases to 200 meV at $Q_{InAs} = 2.3$ ML. As the thickness of the deposited InAs layer increases further, the emission energy decreases to 1.1 eV. A similar dependence was also observed at 300 K. In this case, the maximum emission wavelength of the PL peak was 1.24 μm. The leveling-off of the dependence of the emission wavelength on Q_{InAs} can be accounted for by the scatter in the size of islands and by the relaxation of stresses with the formation of dislocations when the island size exceeds some critical value [4].

3. THE IMPACT OF THE BAND GAP OF THE MATRIX ON THE PARAMETERS OF InAs QUANTUM DOTS

The driving force of island formation is the lattice mismatch between the substrate and the epitaxial layer. Since the difference between the lattice constants of AlGaAs solid solutions and GaAs is small, one may expect the process of QD formation to be similar to that for GaAs. Along with the InAs/GaAs system (lattice mismatch $\Delta a \approx 7\%$), the formation of islands is also observed in the $In_{0.5}Ga_{0.5}As/GaAs$ system ($\Delta a \approx 3.5\%$) [5]. The $InAs/In_{0.53}Ga_{0.47}As$ system is characterized by nearly the same lattice mismatch, thus the island formation at the initial stage of InAs deposition onto the surface of an $In_{0.53}Ga_{0.47}As/InP$ heterostructure can be expected. Below, we discuss the characteristics of QDs in AlGaAs and $In_{0.53}Ga_{0.47}As/InP$ matrices.

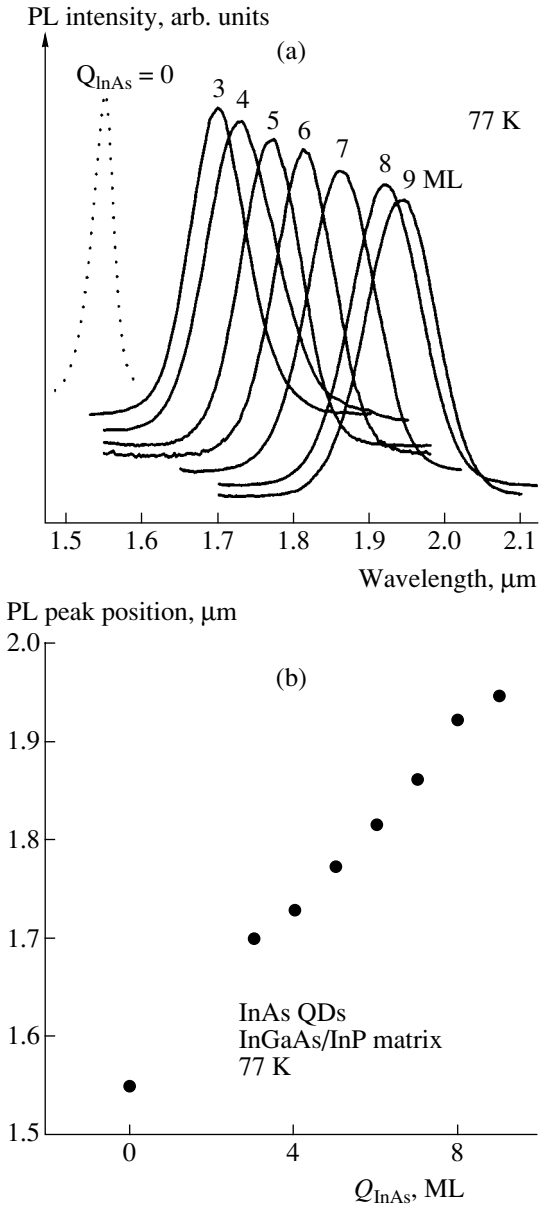

Fig. 3. (a) PL spectra at 77 K and (b) positions of the PL peak in structures with InAs QDs in an $In_{0.53}Ga_{0.47}As/InP$ matrix as functions of the effective thickness of the deposited InAs layer.

3.1. InGaAs QDs in an AlGaAs Matrix

The formation of QDs in an AlGaAs matrix [6] is similar to the case of a GaAs matrix. The critical thickness for the island mode of $In_{0.5}Ga_{0.5}As$ growth is 1 nm, regardless of the value of x in $Al_xGa_{1-x}As$. Figures 2a and 2b show, respectively, the PL spectra of structures containing arrays of InGaAs QDs in an $Al_xGa_{1-x}As$ ($x = 0$, 0.15, and 0.3) matrix and PL excitation spectra at energies above the energy of QD emission. Earlier, it was shown that this emission is related to recombination via the WL states [7]. It can be seen that raising the AlAs molar fraction in an AlGaAs solid solution results in the blue shift of the PL line. When the matrix band gap increases by 370 meV ($x = 0.3$), the blue shift of the QD emission line is 120 meV, whereas the shift of the WL emission line exceeds 300 meV. Thus, the energy spacing between the states of QDs, the WL, and the matrix increases. This effect is similar to the well-known behavior of energy levels in QWs with a rise in the barrier height. This results in a lower relative population of higher lying states at elevated temperatures.

3.2. InAs QDs in an $In_{0.53}Ga_{0.47}As/InP$ Matrix

It was found that an InAs epitaxial layer is transformed into an array of islands when the critical thickness of 3 ML is reached [8], which correlates well with the data for the $In_{0.5}Ga_{0.5}As/GaAs$ system. However, in our system of materials islands are characterized by a much larger base size, smaller height-to-base ratio, and lower surface density [9]. Figures 3a and 3b show, respectively, PL spectra of structures with QDs formed

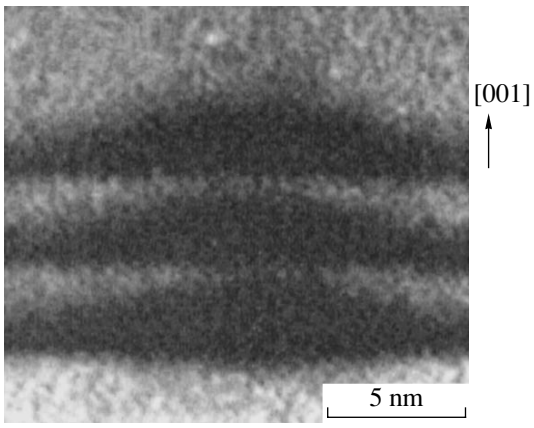

Fig. 4. Cross-sectional TEM image of InAs islands formed by successive deposition of three layers of InAs QDs and 1.5-nm-thick GaAs layers.

by deposition of Q_{InAs} MLs of InAs in an $In_{0.53}Ga_{0.47}As/InP$ matrix and the spectral position of the PL peak as a function of Q_{InAs}. It can be seen that, as soon as islands are formed, the PL peak is strongly red-shifted in respect to the PL peak of the $In_{0.53}Ga_{0.47}As$ matrix. The PL intensity remains nearly constant up to Q_{InAs} = 9 ML and then sharply decreases due to the formation of dislocations.

Thus, the wavelength of emission from InAs QDs can be modified in the range from 0.88 μm (AlGaAs matrix) to 1.7–1.95 μm ($In_{0.53}Ga_{0.47}As/InP$ matrix) by varying the matrix band gap.

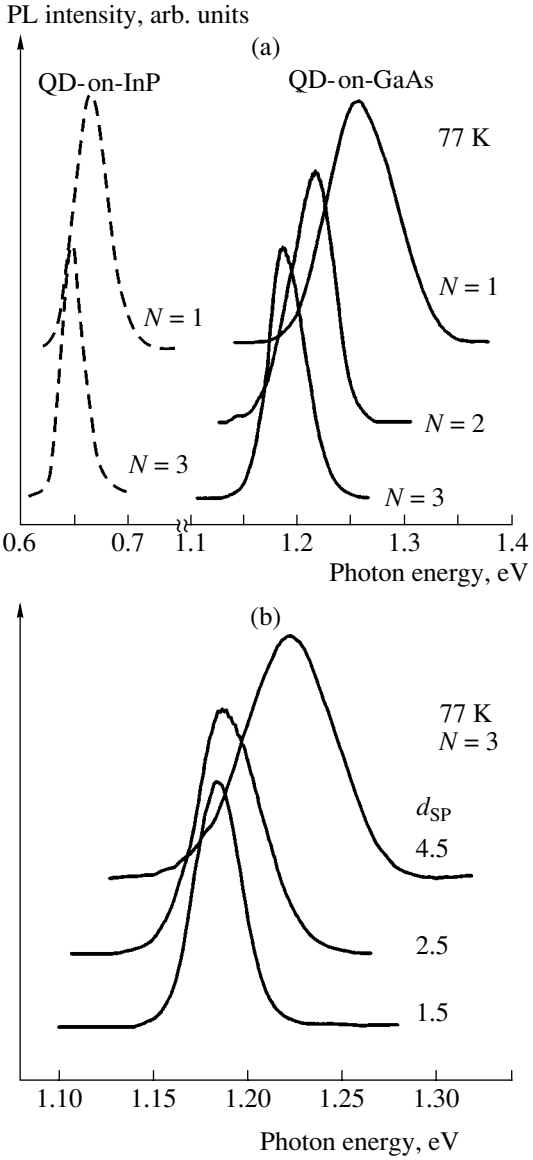

Fig. 5. PL spectra at 77 K for structures containing InGaAs QD layers with GaAs spacers and their dependence on (a) the number of QD layers N and (b) on the spacer thickness d_{SP}. Dashed lines in Fig. 5a show similar spectra for structures with InAs QDs embedded in an $In_{0.53}Ga_{0.47}As/InP$ matrix. The values of d_{SP} (nm) are given by the curves in (b).

4. VERTICALLY COUPLED QDs

It was found that, if the thickness of the GaAs spacer is less than 100 Å, successive deposition of InAs QD layers and thin GaAs spacers results in the formation of islands in a succeeding layer directly above those in the preceding layer [10]. This effect is related to the fact that the formation of the second layer of InAs QDs occurs under the influence of stress fields induced by the first layer. This causes a preferential migration of In atoms to sites located directly above the islands of the preceding layer. If the thickness of the GaAs spacer is less than the height of an island (Fig. 4) [11], then the islands neighboring in the vertical direction will be described by a common system of energy levels. This means that changing the spacer thickness results in a shift of the PL line (Fig. 5). The effect of vertical stacking opens the way to an increase in the surface density of islands with the use of composite InAlAs/InAs QDs.

5. COMPOSITE VERTICALLY COUPLED InAlAs/InAs QDs

The density of QDs is independent of the thickness of the deposited InAs layer. It can be increased by vertically stacking several QD layers. We have shown that an efficient way of raising the surface density of InAs QDs in a plane is the use of InAlAs QDs as nucleation centers for further formation of InAs QDs, since the surface density of InAlAs QDs (~1.5×10^{11} cm^{-2}) is much higher than the density of InGaAs QDs [12]. Figure 6 shows planar and cross-sectional TEM images of structures comprising three layers of stacked InAs QDs (#1), and one layer of InAlAs QDs with subsequent three layers of InAs QDs (#2). It can be seen that vertical alignment occurs in both types of structures. The

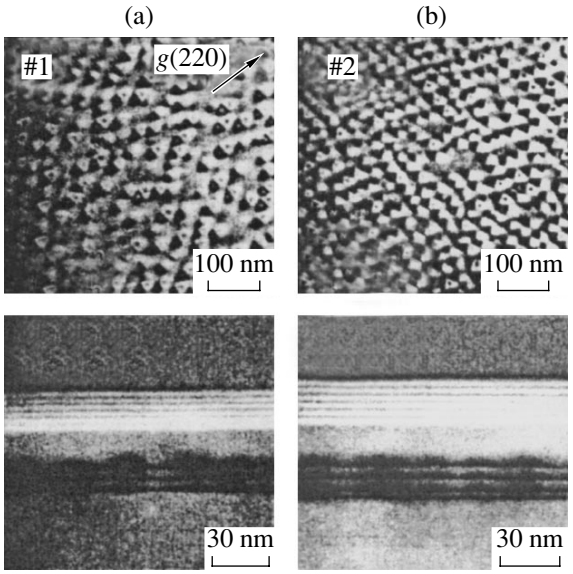

Fig. 6. TEM images of structures with (a) stacked and (b) composite QDs.

surface densities of islands for structures #1 and #2 are, respectively, 5×10^{10} and 10^{11} cm^{-2}, and the PL line positions for these structures differ only slightly, not exceeding the FWHM. Thus, an array of composite vertically coupled InAlAs/InAs QDs exhibits much higher surface density than that in the case of InAs QDs. The density of vertically coupled InAlAs/InAs QDs is defined by the density of InAlAs islands, and the optical transition energy is defined by InAs QDs.

6. SUBMONOLAYER InAs/GaAs QDs

Submonolayer InAs/GaAs QDs (SML QDs) are formed by tenfold deposition of alternating 0.5-ML InAs and 2.5-ML GaAs layers [13]. The sequence of the SML QD formation is shown schematically in Fig. 7. It was shown earlier [2] that, when the effective thickness of the deposited InAs layer is less than 1 ML, a thin InAs film is transformed with optimal technological modes of MBE into an array of islands 1 ML in height, which partially covers the growth surface. Islands in the next InAs layer, which are separated from the preceding layer by a GaAs spacer of several monolayers in thickness, are spatially aligned with the islands in the preceding layer. After several cycles of submonolayer deposition, QD-type In-enriched clusters are formed, which comprise several islands 1 ML in height (Fig. 7e). It is important that the resulting SML QDs are comprised of islands of the same height (1 ML); thus, it can be expected that the SML QD array will be much more uniform than the above-described pyramidal QDs because of the significant scatter of the latter in size. Indeed, a comparison of PL spectra for these two types of QDs has shown that the FWHM for SML QDs is only 19 nm, which is more than three times smaller than that for pyramidal QDs. Thus, submonolayer InAs/GaAs deposition in optimum growth modes allows a considerable improvement in the uniformity of a QD array.

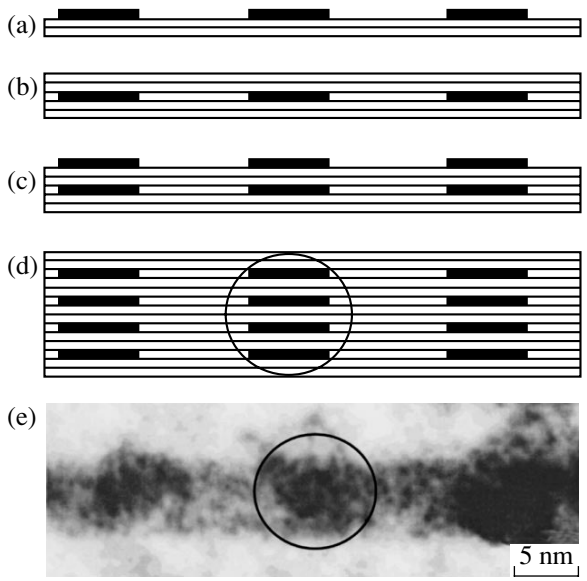

Fig. 7. Successive formation of submonolayer QDs: (a) deposition of InAs (<1 ML) onto GaAs; (b) deposition of several monolayers of GaAs; (c) repeated deposition of InAs, vertical alignment of islands 1 ML in height; (d) InGaAs SML QD; (e) cross-sectional TEM image of SML QD.

7. QUANTUM DOTS IN A QUANTUM WELL

Increasing the effective thickness of the deposited InAs raises the wavelength of the PL peak up to 1.24 μm (see Section 2), but a further increase in Q_{InAs} results in a sharp drop in the PL intensity due to stress relaxation with the formation of mismatch dislocations. An effective method for extending the spectral range of the QD

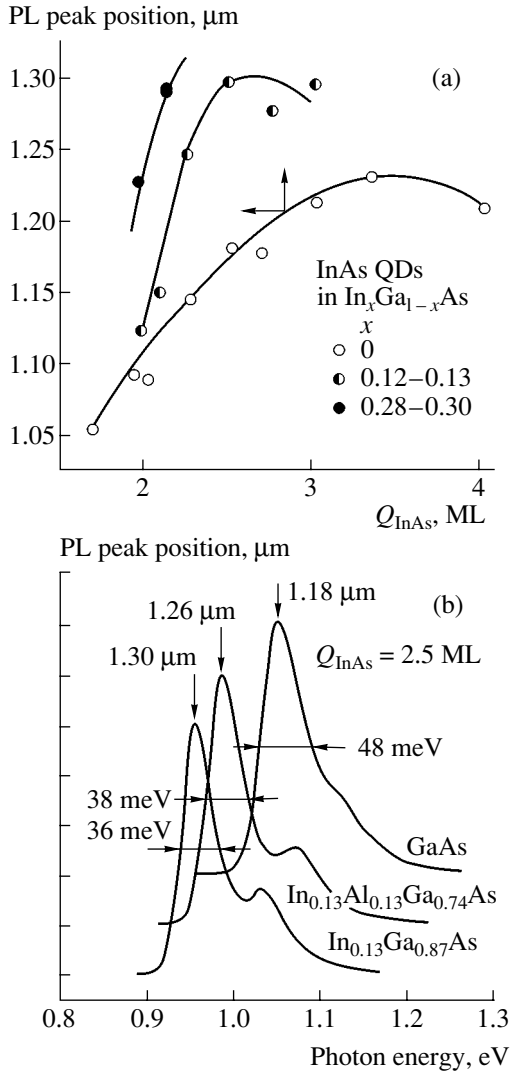

Fig. 8. (a) Positions of the PL peak of InAs QD at 300 K as a function of the effective thickness of the deposited InAs layer, Q_{InAs}, for different QW compositions x. (b) PL spectra at 300 K for InAs QDs overgrown with GaAs or solid solutions of different compositions (indicated in figure).

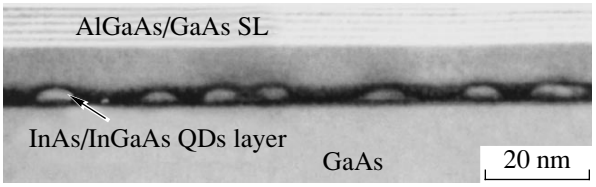

Fig. 9. Cross-sectional TEM image of a sample containing a layer of InAs QDs inserted in InGaAs QW; SL, superlattice.

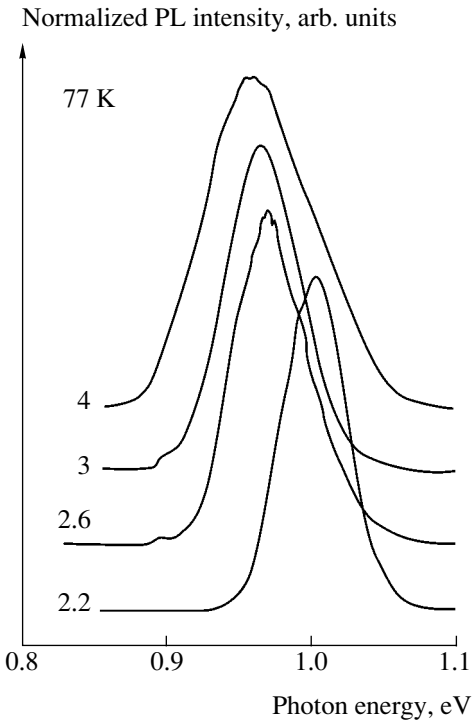

Fig. 10. PL spectra at 77 K for QD structures formed owing to elastic transformation of InAs layers of different thicknesses on the surface of a metamorphic $In_{0.2}Ga_{0.8}As$ layer and overgrown on top with a layer of the same composition. Figures by the curves indicate the InAs layer thickness (ML).

emission is overgrowing the InAs QD layer with a thin layer of $In_xGa_{1-x}As$ solid solution [14]. It turned out that an increase in both Q_{InAs} and x in the solid solution results in a gradual increase in the emission wavelength, which can reach 1.3 μm at certain values of Q_{InAs} and x. Figure 8 shows typical PL spectra of InAs QDs in matrices of different compositions. It is worth noting that the red shift of the PL band is observed also in the case of overgrowing InAs QDs with a quaternary $In_xAl_yGa_{1-x-y}As$ solid solution, whose band gap E_G nearly equals that in GaAs. A cross-sectional TEM study of structures (Fig. 9) has shown that the source of the increase in the emission wavelength is the increase in the volume of QDs, along with the decrease in the matrix band gap.

One should note that InAs/InGaAs QDs are characterized by a high InAs content, which can in principle cause local relaxation of stress with the formation of dislocations. We studied the dependence of PL intensity on the total In content in a structure while maintaining an emission wavelength of 1.3 μm. It turned out that the structures with the minimum In content demonstrate the highest PL intensity, which is indicative of the lowest concentration of defects in this case [15]. Thus, overgrowing InAs QDs with a thin layer of InGaAs alloy allowed us to extend the spectral range of emission of InAs QDs, while retaining a high PL intensity.

8. QUANTUM DOTS ON A METAMORPHIC BUFFER LAYER

A metamorphic buffer layer is an InGaAs epitaxial layer on a GaAs substrate, with a thickness larger than the critical thickness of pseudomorphic growth. Hence, the lattice mismatch between the layer and substrate leads to stress relaxation via the formation of dislocations, and the layer is characterized by its own lattice constant. In this situation, the optimization of the growth parameters makes it possible to reduce the number of dislocations penetrating in the growth direction via generation of dislocations localized along the heterointerface between the layer and substrate [16]. When InAs QDs are grown on the surface of the metamorphic buffer layer, the process of their formation and some of their properties differ from those in the case of a GaAs matrix. It was found that the critical thickness for the formation of InAs 3D islands on an $In_{0.2}Ga_{0.8}As$ surface changed compared with that on a GaAs surface. The critical thickness on GaAs is 1.7 ML, whereas in the case of InAs deposition onto an unstrained $In_{0.2}Ga_{0.8}As$ layer it reaches 2.1 ML, which can be attributed to a decrease in the lattice mismatch between the materials of the matrix and the deposited layer. Figure 10 shows PL spectra at 77 K recorded from InAs QD structures with different effective thicknesses of the deposited InAs layer. It can be seen that the red shift of the PL peak and the increase in the FWHM of spectra (from 50 to 90 meV) are observed with an increase in the thickness of the InAs layer, whose elastic deformation leads to the formation of the QD array. The increase in the FWHM of the spectra indicates that the QD array with the highest size uniformity is formed with the deposition of 2.2 ML of InAs. As the InAs layer thickness increases, the emission wavelength λ_{max} steadily increases; however, at $Q_{InAs} > 2.6$ ML the dependence $\lambda_{max}(Q_{InAs})$ levels off. The largest wavelength of the PL peak reached at room temperature in QD structures was 1372 nm (for a QD structure with an InAs thickness of 4 ML). The highest PL intensity was demonstrated in the structure with QDs formed by deposition of 2.6 ML InAs. A further increase in the thickness of InAs results in a sharp decrease in the PL intensity (by a factor of ~1000), with the red shift ceasing to increase. This effect is caused by the formation of dislocated InAs islands when the thickness of the deposited layer

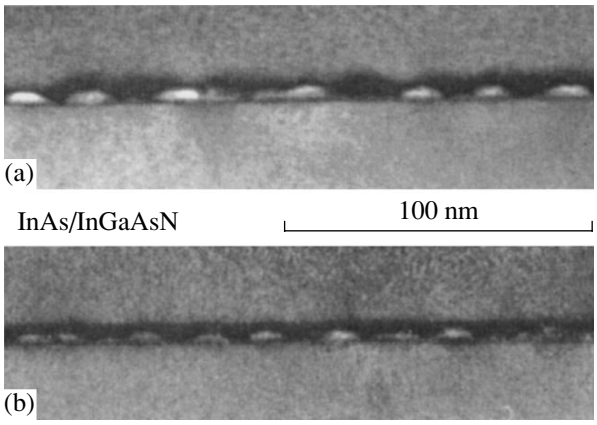

Fig. 11. Cross-sectional TEM images of structures with (a) InAs/InGaAsN and (b) InAs/InGaAs QDs.

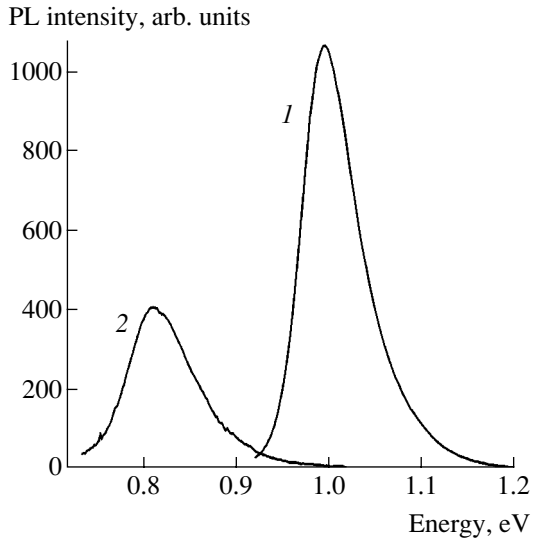

Fig. 12. PL spectra of heterostructures with (*1*) a GaAs/InGaAsN QW and (*2*) InAs/InGaAsN QDs.

exceeds 2.6 ML. To increase the wavelength, a 2.6-ML InAs QD array, which demonstrated the highest PL intensity, was inserted into a 4-nm-thick $In_{0.4}Ga_{0.6}As$ layer. As a result, the PL peak shifted to 1.48 μm without any loss of intensity, which occurred due to the rise of In content in the matrix with the corresponding decrease of its band gap. Thus, the use of a metamorphic buffer layer opens the way to a considerable increase in the wavelength of emission from an array of InAs QDs.

9. HETEROSTRUCTURES WITH NITROGEN-DOPED QUANTUM DOTS EMITTING IN THE LONG-WAVELENGTH RANGE

It is well known that an addition of a small amount (several percent) of nitrogen into GaAs reduces the band gap of the solid solution [17]. We have shown that overgrowing InAs QDs with a quaternary InGaAsN solid solution opens the way to a considerable increase in the emission wavelength compared with InAs/InGaAs QDs [18]. Figure 11 shows cross-sectional TEM images of structures with InAs/InGaAsN and InAs/InGaAs QDs. It can be seen that islands in the InAs/InGaAsN structure are considerably larger than those in InAs/InGaAs. Figure 12 shows PL spectra of a GaAs/InGaAsN QW structure, which emits at 1.3 μm, and an InAs/InGaAsN QD structure. It can be seen that the emission peak of the QD structure lies at about 1.55 μm, and its intensity is only slightly lower than the PL intensity in the QW structure used in the fabrication of a low-threshold-current laser. Thus, the addition of nitrogen to InAs-based QD heterostructures opens the way to a significant increase in the wavelength, while retaining quite a high intensity of emission.

10. CONCLUSION

We have discussed different approaches to the control of parameters of InAs-based QD heterostructures. An increase in the effective thickness of the deposited layer raises the emission wavelength. An increase or decrease in the band gap of the matrix opens the way to an increase or decrease in the energy of photons emitted from QDs, respectively. The successive deposition of several QD layers results in the formation of vertically aligned islands, and the use of high-density QDs in the first layer raises the surface density of islands in the succeeding layers. The deposition of alternating InAs and GaAs layers of submonolayer thickness leads to the formation of new “submonolayer” QDs with an improved array uniformity. Overgrowing InAs QDs with InGaAs or InGaAs solid solutions results in an increase in the island size with the related red shift in the emission spectrum. The growth of InAs QDs on an InGaAs metamorphic buffer layer also increases the wavelength of QD emission. The results obtained are important in the design of new optoelectronic devices.

ACKNOWLEDGMENTS

This study was supported in part by the Russian Foundation for Basic Research; the program of the Ministry of Industry, Science, and Technology of the Russian Federation “Physics of Solid-State Nanostructures”; and joint programs of the Ioffe Physicotechnical Institute and the Industrial Technology Research Institute (Taiwan) and Nanosemiconductor (Germany).

REFERENCES

1. L. Goldstein, F. Glas, J. Y. Marzin, *et al.*, Appl. Phys. Lett. **47**, 1099 (1985).
2. D. Bimberg, M. Grundmann, and N. N. Ledentsov, *Quantum Dot Heterostructures* (Wiley, Chichester, 1999).

3. S. S. Ruvimov, P. Werner, K. Scheerschmidt, *et al.*, Phys. Rev. B **51**, 14766 (1995).
4. A. Yu. Egorov, A. E. Zhukov, P. S. Kop'ev, *et al.*, Fiz. Tekh. Poluprovodn. (St. Petersburg) **30**, 1345 (1996) [Semiconductors **30**, 707 (1996)].
5. D. Leonard, M. Krishnamurthy, C. M. Reaves, *et al.*, Appl. Phys. Lett. **63**, 3203 (1993).
6. A. E. Zhukov, V. M. Ustinov, A. Y. Egorov, *et al.*, J. Electron. Mater. **27**, 106 (1998).
7. A. F. Tsatsul'nikov, N. N. Ledentsov, M. V. Maksimov, *et al.*, Fiz. Tekh. Poluprovodn. (St. Petersburg) **30**, 1793 (1996) [Semiconductors **30**, 938 (1996)].
8. V. M. Ustinov, A. E. Zhukov, A. F. Tsatsul'nikov, *et al.*, Fiz. Tekh. Poluprovodn. (St. Petersburg) **31**, 1256 (1997) [Semiconductors **31**, 1080 (1997)].
9. V. M. Ustinov, E. R. Weber, S. Ruvimov, *et al.*, Appl. Phys. Lett. **72**, 362 (1998).
10. Q. Xie, A. Madhukar, P. Chen, *et al.*, Phys. Rev. Lett. **75**, 2542 (1995).
11. V. M. Ustinov, A. Yu. Egorov, A. E. Zhukov, *et al.*, Mater. Res. Soc. Symp. Proc. **417**, 141 (1996).
12. A. R. Kovsh, A. E. Zhukov, A. Yu. Egorov, *et al.*, Mater. Res. Soc. Symp. Proc. **571**, 109 (1998).
13. S. S. Mikhrin, A. E. Zhukov, A. R. Kovsh, *et al.*, Semicond. Sci. Technol. **15**, 1061 (2000).
14. V. M. Ustinov, N. A. Maleev, A. E. Zhukov, *et al.*, Appl. Phys. Lett. **74**, 2815 (1999).
15. V. M. Ustinov, A. E. Zhukov, A. R. Kovsh, *et al.*, Microelectron. J. **31**, 1 (2000).
16. A. E. Zhukov, A. R. Kovsh, S. S. Mikhrin, *et al.*, Fiz. Tekh. Poluprovodn. (St. Petersburg) **37**, 1143 (2003) [Semiconductors **37**, 1119 (2003)].
17. V. M. Ustinov and A. E. Zhukov, Semicond. Sci. Technol. **15**, R41 (2000).
18. V. A. Odnoblyudov, A. Yu. Egorov, N. V. Kryzhanovskaya, *et al.*, Pis'ma Zh. Tekh. Fiz. **28** (11), 82 (2002) [Tech. Phys. Lett. **28**, 964 (2002)].

Translated by D. Mashovets

Semiconductors, Vol. 38, No. 8, 2004, pp. 931–935. From Fizika i Tekhnika Poluprovodnikov, Vol. 38, No. 8, 2004, pp. 971–974.

SYMPOSIUM ON THE EFFICIENT USE OF SOLAR RADIATION IN PHOTOVOLTAIC POWER ENGINEERING (St. Petersburg, November 3–4, 2003)

Next-Generation Technologies in the USA[1]

R. McConnell

National Center for Photovoltaics, National Renewable Energy Laboratory, Golden, CO 80401-3393, USA
e-mail: robert_mcconnell@nrel.gov

Submitted February 9, 2004; accepted for publication February 11, 2004

Abstract—This presentation describes the highlights of exploratory research into next-generation photovoltaic (PV) technologies funded by the United States Department of Energy (DOE) for the purpose of finding disruptive or "leap frog" technologies that have a chance of leaping ahead, both in terms of vastly higher conversion efficiencies and greater penetration of the PV energy marketplace. Next-generation PV technologies are defined as those not in production or only in limited production because of the need for additional long-term research, development, innovation, and commercialization. Since 1999, DOE and the National Renewable Energy Laboratory have funded 33 universities and companies to explore these concepts, with a total annual budget of about $2 million per year. © *2004 MAIK "Nauka/Interperiodica".*

Next-generation photovoltaic (PV) technologies are defined as those not in production or in limited production of less than 1% of the conventional PV market sales. Exploratory research into these next-generation technologies resulted from the consensus at a 1997 conference often referred to as "The Leap Frog Conference." This conference was convened to review the viability of conventional PV technologies and to present and discuss next-generation PV technologies that might conceivably "leap frog" present-generation solar cells, in terms of higher efficiency, lower cost, or both [1]. The consensus was that the present generation, typically using crystalline silicon, was exhibiting incremental performance increases and cost decreases, with diminishing hope for a dramatic breakthrough that would lead to a much more commercially viable position in the energy marketplace. The next-generation technologies have been called by various terms—Future Generation, Beyond the Horizon PV, PV for the 21st Century, Third-Generation PV, FULLSPECTRUM, etc.—but all these terms allude to dramatically lower cost, higher efficiency energy service from PV. It is important to note that a new crystalline-silicon-based technology can still be a next-generation technology. But rarely will any next-generation technology be discovered unless many exploratory research projects are intentionally conducted by qualified scientists. This situation has been popularized as an optimistic affirmation credited to the Greek poet and playwright Sophocles, who enjoined us all: "Look and you will find it—what is unsought will go undetected."

In 1998, the National Renewable Energy Laboratory (NREL) issued a request for proposals for next-generation PV concepts and conducted a rigorous competition leading to the selection of 18 university groups solely on the basis of the quality of the research proposed and the capabilities of the researchers. Each proposal, funded for three years, was to conduct exploratory research into a next-generation PV topic. This set of projects—called Future-Generation PV—explored many PV ideas, including nanoparticles in polymers, new III–V materials for higher efficiency concentrator cells, porous silicon cells, nanorod solar cells, new transparent conducting oxides, and several studies of the Staebler–Wronski effect in amorphous silicon. Early results from some of the projects appeared at a second conference entitled "Photovoltaics for the 21st Century," along with an identification of exploratory research opportunities in conventional, as well as next-generation, photovoltaic technologies [2]. A second conference in 2001, called "Photovoltaics for the 21st Century II," highlighted presentations of the major results from all of the Future Generation projects [3].

A second request for proposals in 2001—called Beyond the Horizon PV—yielded 15 new three-year projects on technologies such as dye solar cells, liquid-crystal solar cells, multijunction small-molecule cells, polymer cells, nanocrystalline silicon cells, lower cost substrates for III–V concentrator cells, and nonvacuum fabrication processes for polycrystalline thin-film materials. We have published an article containing descriptions of these Beyond the Horizon projects, as well as the earlier Future Generation projects, along with references to published articles from each of the projects [4].

The most recent request for proposals, retaining the earlier title of Future-Generation PV, was completed in 2003 and provided many strong, intriguing proposals for exploratory PV research. However, at the time of writing this manuscript, budget uncertainties delayed the announcement of any new awards.

The mandate for these exploratory projects has been to investigate every plausible technology for generating

[1]This article was submitted by the authors in English.

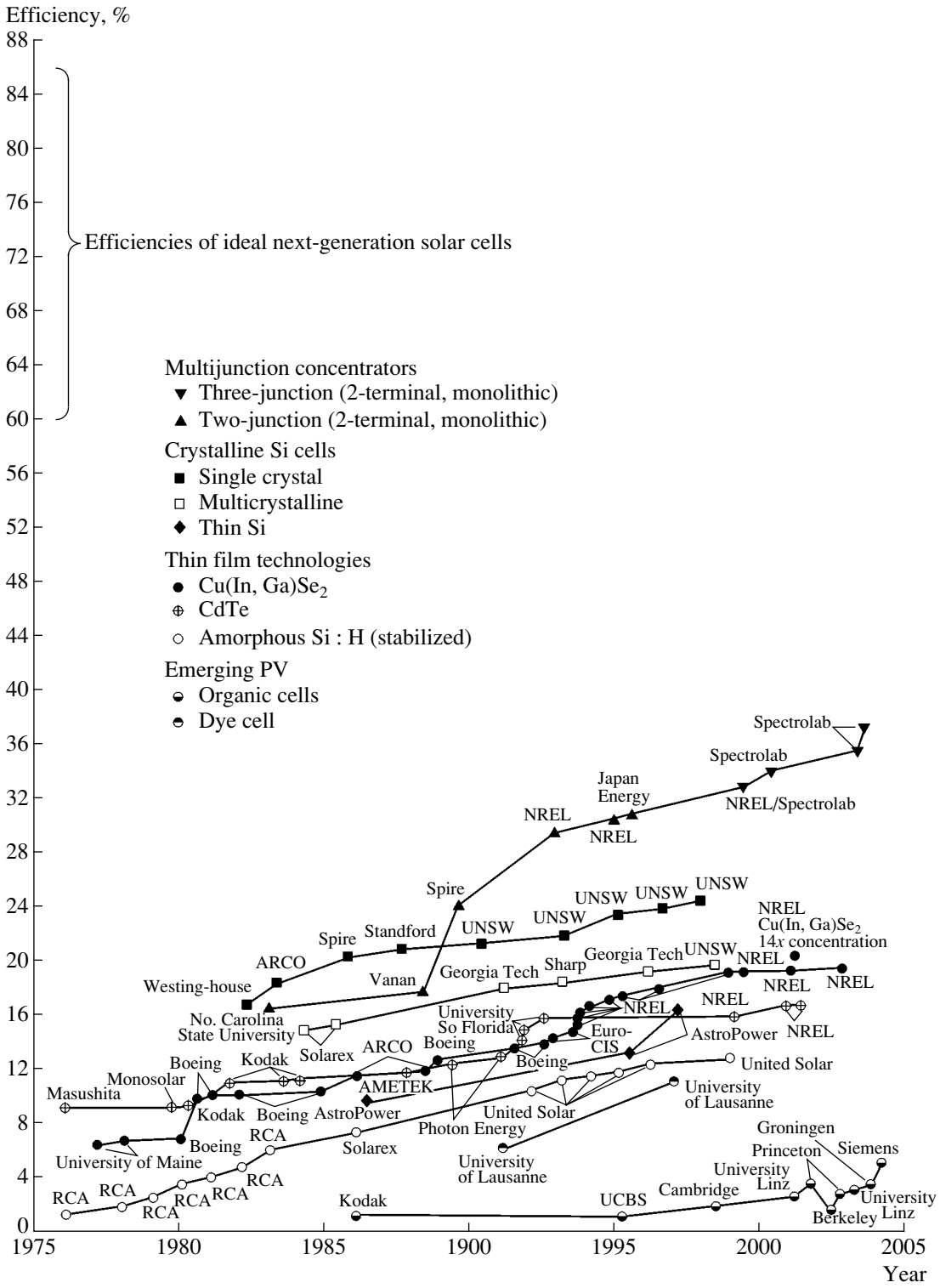

Fig. 1. Highest conversion efficiencies of present and next-generation solar cells measured at NREL. Note that we have a long way to go to reach the desired efficiencies in the 60% to 85% range.

electricity from solar cells, with the goal of identifying "leap frog" possibilities. One of these technologies—high-efficiency III–V solar cells for use in solar electric concentrators—appears likely to become a "leap frog" technology, with the distinct possibility of leaping ahead of existing technologies, rather than taking the more characteristic development time of 10 to 20 years (see Fig. 1). Concentrating sunlight is a technology as

old as Archimedes, and focusing sunlight onto solar cells has been explored since the 1970s, so it is not a new technology. However, as noted in the preface for the "Leap Frog" conference [1], "Indeed, many of these presentations referenced a long history for their ideas. What has changed, perhaps, is the availability of new technologies and discoveries that might make some of these concepts realistic." In the case of solar electric concentrators, the development of high-efficiency crystalline silicon solar cells (now at about 26% efficiency under concentration) in the 1980s and the subsequent development of high-efficiency III–V solar cells (now at about 37% efficiency) in the 1990s have led to an increased possibility that this technology will become a "leap frog" PV technology (see Fig. 1). Both the Future Generation and Beyond the Horizon projects included exploratory research into higher efficiency III–V solar cells and low-cost substrates for them. However, in addition to early funding for in-house research on III–V solar cell at NREL, there was significant early funding from the Department of Energy's Office of Science and later funding provided by other US government agencies (principally the US Air Force within the US Department of Defense) to develop manufacturing facilities for III–V solar cells used for communications satellites. Recently, we have gone further to facilitate the emergence of this technology in the terrestrial energy service market by convening two international solar electric concentrator conferences [5, 6], conducting a system analysis [7] of the cost of future solar electric concentrator technologies, and supporting the development of concentrator test standards to increase the probability that solar electric concentrators will operate reliably when they appear in the marketplace [8].

One of the markets that solar electric concentrators are entering is distributed utility grids, especially those powered by diesel generators. Figure 2 is a photograph of a 220-kW solar concentrator power station that is operating in a diesel grid. This application is cost effective because it saves diesel fuel, which is costly to transport to the generators. Incorporating III–V technology into such a solar station is relatively simple; the receivers are replaced with ones containing the new III–V solar cells. In this case, the power of the same solar station shown in Fig. 2 will increase to about 350 kW.

A second possible "leap frog" PV technology is based on organic materials. These materials absorb sunlight and create charge carriers through a different process than that occurring in almost all the inorganic solar cells, whether conventional or next generation. Photon absorption in almost all inorganic solar cell materials leads to the creation of *independent* electrons and holes that move by means of potential gradients within the solar cells. The photon absorption process in organic materials creates excitons—*bound* pairs of electrons and holes—which diffuse to a nearby internal boundary with another material, where they dissociate into separate charge carriers at the boundary [9]. This fundamentally different photovoltaic process leads to very different length scales: the diffusion lengths for excitons are typically 10 nm, so that the required thicknesses of organic solar cells are measured in 10 s of nanometers, instead of microns or 100 s of microns for crystalline silicon solar cells. Organic solar cells have been demonstrated for a variety of organic materials, including organic dyes, polymers, small molecules, and hybrids of polymers containing inorganic nanoparticles. Inorganic nanoparticles are another breeding ground for exciton creation by photon absorption. The efficiencies of organic solar cells are still quite low, but there is another application having a higher value market than energy service that is spurring research and development. The leveraging of engineering development costs—usually an order of magnitude more expensive than exploratory research efforts—is critical to bringing a new solar technology to market. This scenario has been true with crystalline silicon (the integrated circuit industry), amorphous silicon thin films (thin-film transistors for displays), and III–V solar cells (satellites for defense and commercial applications). Without this leveraging, the time it takes to get to market is measured in decades instead of years. One such organic semiconductor application is the organic light-emitting diode (organic LED), which appears today in high-value display applications such as cellular phones. Equally relevant may be the recent interest of the US Defense Advanced Research Projects Agency in developing portable organic solar cells to replace heavy battery packs for soldiers on reconnaissance missions. These plastic solar cells are expected to weigh considerably less and bend without breaking, and they are showing improving efficiencies. Further, low cost is eventually expected as these organic semiconductors do not use scarce, expensive, or toxic elements and their manufacture involves relatively low process temperatures and, sometimes, no vacuum. Long-term reliability

Fig. 2. To dramatize the impact of the new high-efficiency III–V solar cells on solar concentrator technology, each of these nominal 20-kW dish concentrators developed by Solar Systems Pty Ltd in Australia could be rated at over 30 kW simply by replacing the crystalline silicon solar cells with III–V cells in each receiver of the sun's rays.

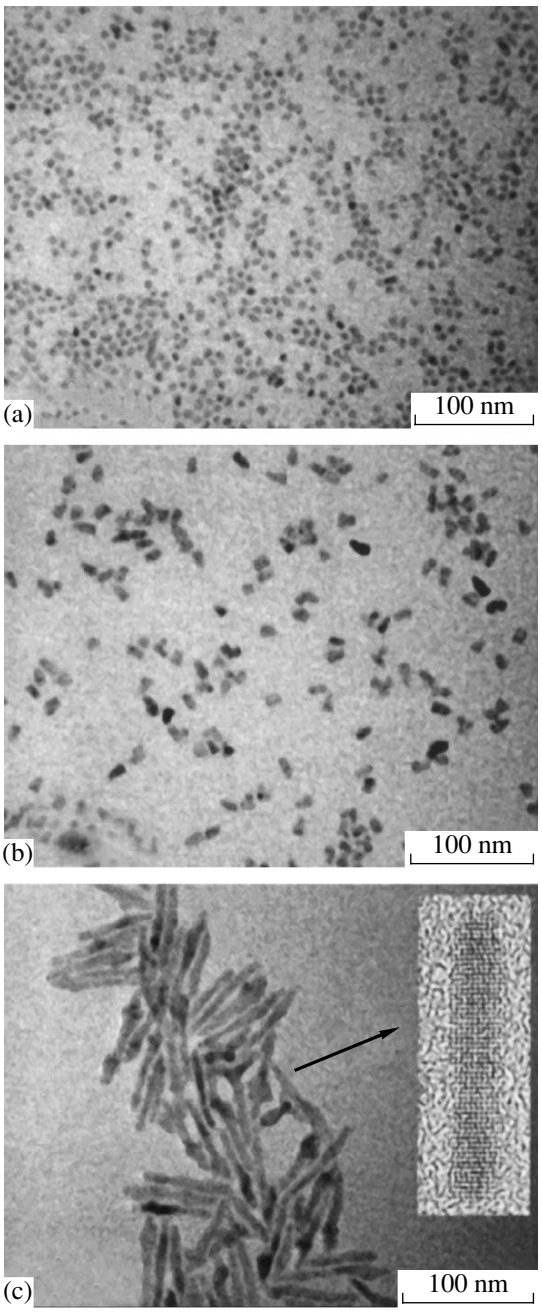

Fig. 3. Innovative growth techniques at University of California (Berkeley) produced these nanospheres (a), short rods (b), and long rods (c) for incorporation into polymer solar cells having improved efficiencies.

is slowly being demonstrated for organic LEDs, but this is certainly an important issue remaining for organic solar cells.

It is our firm conviction that the probability of finding new technologies is increased when high-quality scientific research is conducted. As an example and a highlight of the early Future Generation contracts, Paul Alivisatos at the University of California, Berkeley, has been a pioneer in exploring nanoparticles in polymer solar cells. His group demonstrated how solar cell efficiency could be improved by changing the geometry of nanoparticles. They improved the efficiency of their solar cells by a factor of 2 by incorporating long nanorods in place of nanospheres, and they have ideas for the next nanogeometry that are likely to improve efficiencies further (see Fig. 3). The quality of their scientific achievement in growing different nanostructures was highlighted by the publication of their work in Science [10].

Another example is Steve Forrest at Princeton University, a winner of one of the Beyond the Horizon contracts, who leads the development of another approach to developing organic solar cells. The approach is based on developing an interpenetrating heterojunction between an organic donor and organic materials. Using small molecules instead of polymers, his group discovered the importance of maintaining contact surface morphology during annealing to improve their solar cell efficiency by 50%. Their results recently appeared in Nature [11].

The most recent request for proposals conducted by NREL in 2003 specifically mentioned the Third Generation technologies championed by Martin Green, Hans Queisser, Antonio Luque, Arthur Nozik, and others [12, 13]. These technologies typically have high theoretical efficiencies, between 60% and 85%, and involve radically different photovoltaic processes, such as producing two pairs of electrons and holes with one photon (two excitons per photon in the organic analogue) or minimizing phonon creation in hot-carrier solar cells. These technologies are all deserving of continued exploration as the search for next-generation PV technologies continues throughout the world.

It is important to acknowledge that this work has been carried out with the support of the US Department of Energy through its Solar Energy Technologies Program in its Energy Efficiency and Renewable Energy Office. I also wish to acknowledge the contributions of all the principal investigators selected for funding under the Future Generation and Beyond the Horizon PV projects. Finally, it is a pleasure to acknowledge Lawrence Kazmerski, director of NREL's National Center for Photovoltaics, who has always been a supporter of these efforts, and Richard Matson, a long-time scientist at NREL who became intrigued and later enthusiastic in championing next-generation PV technologies.

REFERENCES

1. *Future Generation Photovoltaic Technologies*, Ed. by R. D. McConnell (Woodbury, New York, 1997), AIP Conf. Proc., Vol. 404.
2. *Photovoltaics for the 21st Century*, Ed. by V. Kapur, R. D. McConnell, D. Carlson, G. P. Ceasar, and A. Rohatgi (ECS, Pennington, N.J., 1999), ECS Proc., Vol. 99-11.

3. *Photovoltaics for the 21st Century II*, Ed. by R. D. McConnell and V. Kapur (ECS, Pennington, N.J., 2001), ECS Proc., Vol. 2001-10.

4. R. Matson and R. McConnell, in *Proceedings of 29th IEEE Photovoltaic Specialists Conference, New Orlean, 2002* (IEEE, New York, 2002), p. 1343.

5. R. D. McConnell, in *Proceedings of First International Conference on Solar Electric Concentrators* (Golden, Colorado, 2002), NREL/EL-590-32461.

6. R. D. McConnell, in *Proceedings of International Solar Electric Concentrator Conference for the Generation of Electricity or Hydrogen* (Golden, Colorado, 2004), NREL/EL-520-35349.

7. R. D. McConnell, in *Renewable Energy Technology Characterizations* (Pleasant Hill, California, 1997), EPRI TR-109496, p. 4.

8. R. McConnell, in *Proceedings of 16th European Photovoltaic Solar Energy Conference* (James and James, London, 2000), p. 2237.

9. B. A. Gregg, J. Phys. Chem. B **107**, 4688 (2003).

10. W. U. Huynh, J. J. Dittmer, and A. P. Alivisatos, Science **295**, 2425 (2002).

11. P. Peumans, S. Uchida, and S. R. Forrest, Nature **425**, 158 (2003).

12. M. Green, *Third Generation Photovoltaics* (Springer, Berlin, 2003).

13. *Next Generation Photovoltaics*, Ed. by A. Marti and A. Luque (Inst. of Physics, London, 2004).

Semiconductors, Vol. 38, No. 8, 2004, pp. 936–940. From Fizika i Tekhnika Poluprovodnikov, Vol. 38, No. 8, 2004, pp. 975–979.

SYMPOSIUM ON THE EFFICIENT USE OF SOLAR RADIATION IN PHOTOVOLTAIC POWER ENGINEERING (St. Petersburg, November 3–4, 2003)

FULLSPECTRUM: A New PV Wave of More Efficient Use of the Solar Spectrum[1]

A. Luque and A. Martí

Instituto de Energía Solar, Universidad Politécnica de Madrid, Spain

e-mail: luque@ies-def.upm.es

Submitted February 9, 2004; accepted for publication February 11, 2004

Abstract—The purpose of this paper is to present to the Russian scientific community a research program that, with the cooperation of one of its institutional members, the Ioffe Physicotechnical Institute, has been presented and sponsored by the European Commission (EC) in order to provide a long-term basis for the development of the photovoltaic conversion of solar energy. This program constitutes what in the EC is known as an integrated project: it is called FULLSPECTRUM for short, as in the title of this paper, and involves 19 research centers in eight different countries with a grant of 8.4 million euros for five years. © *2004 MAIK "Nauka/Interperiodica".*

Photovoltaic (PV) electricity is today a fast-growing business. The explosive growth of the PV module market is presented in Fig. 1 [1]. However, the cost of PV electricity is several times higher than that of the prevalent electricity. The future of PV electricity has been forecasted by several authors [2–4]. It is concluded that, most probably, the present technology, based on silicon, will support an important growth but will not be able to lead to the low prices necessary for a mass utilization of the Sun as a source of electricity.

The reason for this is that, although the Sun provides a tremendous amount of energy every year, much more than the energy used by humankind, its flux is relatively weak. This is the ultimate reason why its exploitation today is expensive. Mass utilization of solar energy will require the best exploitation of this disperse resource.

Present PV technology is based on the following principle. A solar cell is formed from a semiconductor and contacts that are preferential to the conduction band and the valence band. Usually, they are *n* and *p* doped semiconductors, respectively. That is why a solar cell is usually formed from a semiconductor with a *p–n* junction.

Photons pump electrons from the valence band to the conduction band. The electrons are collected by the selective contact to the conduction band (the contact to the *n* region) at high energy and are returned at low energy, after performing some work, to the valence band through the other selective contact (the contact to the *p* region).

Only photons of energy not much higher than the band gap of the semiconductor are effectively converted; the energy of the photons of higher energy is recovered at less than the band-gap energy; the energy of the photons with less energy is lost. This is the motivation of FULLSPECTRUM, which aims at this better exploitation of the resource by a good utilization of the whole solar spectrum.

The specific objectives of FULLSPECTRUM are the development of

(a) III–V multijunction cells (MJC);

(b) solar thermophotovoltaic (TPV) converters;

(c) intermediate band (IB) materials and cells (IBC);

(d) molecular-based concepts (MBC) for full spectrum utilization; and

(e) manufacturing technologies (MFT) for novel concepts including assembling.

Nineteen centers are involved in FULLSPECTRUM. They are listed in the table.

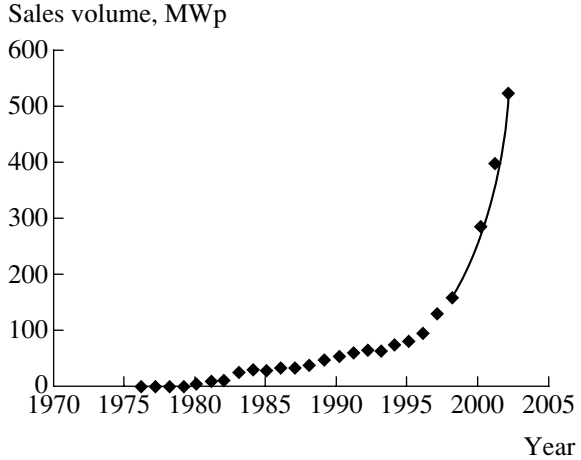

Fig. 1. Evolution of the annual sales of PV modules according to P. Maycock (several publications). The line is the result of the model by A. Luque [2].

[1]This article was submitted by the authors in English.

Participant research centers in the FULLSPECTRUM Integrated Project

Participant number	Participant name	Participant short name	Country
1	Instituto de Energía Solar—Universidad Politécnica de Madrid	IES–UPM	Spain
2	Projektgesellschaft Solare Energiesysteme mbH	PSE	Germany
3	Fraunhofer Institute for Solar Energy Systems(1)	FhG–ISE	Germany
4	Ioffe Physicotechnical Institute	IOFFE	Russia
5	CEA–Départment pour les Technologies des Energies Nouvelles	CEA–DTEN	France
6	RWE–SSP	RWE–SSP	Germany
7	Philipps University of Marburg	PUM	Germany
8	Paul Scherrer Institute	PSI	Switzerland
9	University of Glasgow	UG	United Kingdom
10	Instituto de Catálisis y Petroleoquímica. Consejo Superior de Investigaciones Científicas	CSIC	Spain
11	Energy Research Centre of the Netherlands	ECN	The Netherlands
12	University of Utrecht	UU–Sch	The Netherlands
13	Imperial College of Science, Medicine, and Technology	ICSTM	United Kingdom
14	Fraunhofer-Institut fuer Angewandte Polymerforschung(1)	FhG–IAP	Germany
15	Solaronix	Solaronix	Switzerland
16	ISOFOTON S.A.	ISOFOTON	Spain
17	INSPIRA	INSPIRA	Spain
18	Joint Research Centre—Institute for Environment and Sustainability	EC–DG JRC	Italy
19	University of Cyprus	UCY	Cyprus

The MJC technology is based on depositing a stack of solar cells of different band gaps, so that the photons that are not absorbed by the top semiconductors are absorbed by the successive ones lying underneath. The different solar cells may be interconnected by several means, of which the most widely used today is a tunnel junction through which the conduction and the valence bands of successive semiconductors are interconnected. Such a stack is schematically drawn in Fig. 2. The voltage developed in the stack is the sum of the voltages in each individual cell. Besides the monolithic stack described above, some researchers are developing mechanically stuck stacks, where the different cells can be connected to independent circuits.

Shockley and Queisser presented in 1961 a detailed balance analysis [5] that led to the highest efficiency a solar cell can theoretically have. A single solar cell may have under full concentration (that is, illuminated by an isotropic radiation at 6000 K, approximately the Sun's photosphere temperature) efficiency of 40% and 86% for an MJC stack of an infinite number of cells [6]. The enhancing-efficiency potential of this approach is clear.

The challenge for a monolithic MJC stack is to select the proper band gaps that produce a similar current in all the series-connected cells, because the total stack current will be limited by the cell generating less current. But, for this purpose, both the band gap and the layer thickness are the parameters to adjust. Ternary alloys allow for band gap adjustment. But, in general, lattice mismatch is to be avoided in the whole stack, so removing one degree of freedom and suggesting the need to search for solutions among the quaternary alloys (possibly of lower mobility). However, good results have also been obtained with mismatched stacks.

So far the best results, 36.5% at 100 suns (i.e., at an irradiance of 10 W/cm^2) has been obtained with an InGaP/InGaAs/Ge 3-junction solar cell by Sharp, NASDA, and the Toyota Technological Institute in Japan [7], but this consortium is closely followed by American and European ones, and there is a frantic search for a proper 1-eV band-gap cell that would use Ge cells better (today they illuminated with too many photons) and would open the way to an efficiency of 40%.

In the TPV conversion [8], a radiator is heated to high temperature by the Sun or by a fuel, and this radiation is converted into electricity by solar cells. The efficiency potential of this device is high, because it can recycle the photons that are not well converted by the solar cell. This means that the photons not absorbed by the cell or even those that have an energy well above the cell band gap are returned to the radiator, keeping it hot, by reflection in a filter that lets only the desired photons

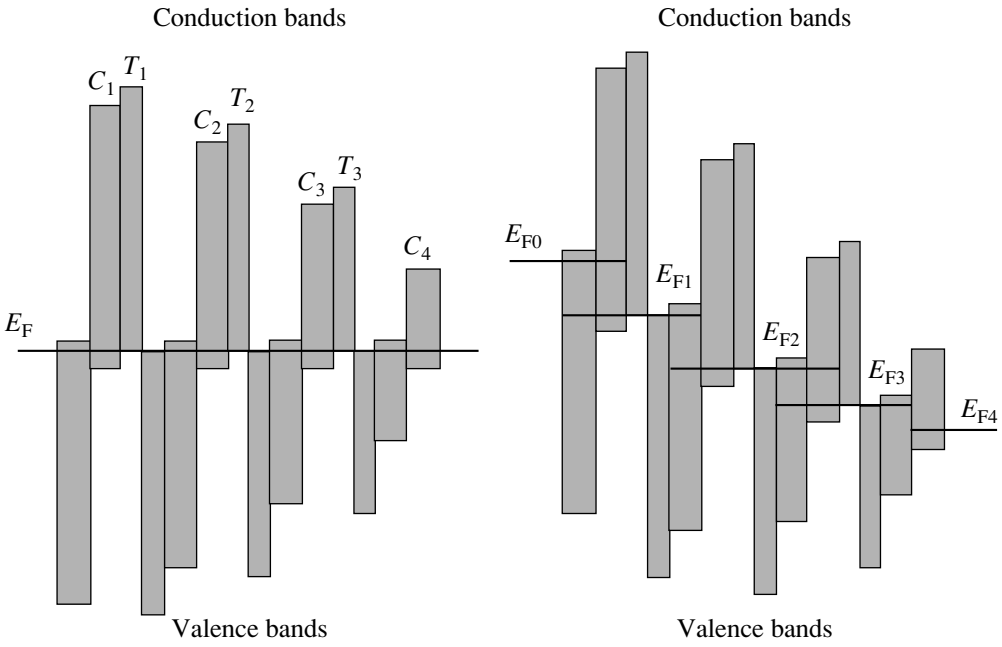

Fig. 2. Band diagram of a monolithic stack of four solar cells (C_1–C_4) interconnected with three tunnel junctions (T_1–T_3): (left) thermal equilibrium, (right) under illumination. The Fermi level E_{F0} splits into four quasi-Fermi levels E_{F1}–E_{F4}.

pass. An alternative way is the use of selective emission radiators that emit photons mainly in the desired range of energies.

The theoretical potential of this concept is 85% [6], almost as high as the one in the MJC. However, most of the technological effort in TPV has been devoted to fuel heated converters, and much less attention has been paid to solar heated converters. One of the challenges here today is probably the achievement of a good photon-recycling scheme with low losses or alternatively a good selective radiator, but much work still needs to be done on this concept.

In the IBC approach, subband-gap photons are exploited by means of an intermediate band (IB). Subband-gap photons pump electrons from the valence band to the IB and, then, from this band to the conduction band. In this way, two low-energy photons pump to the conduction band one electron, as represented in Fig. 3. For proper operation, the Fermi level must split into three quasi-Fermi levels as represented in the same figure. The potential efficiency of this concept is 63.2% [9].

The formation of a material exhibiting an intermediate band can be achieved by means of quantum dots [10]. They present a level in the band gap of the barrier material that can become the origin of the intermediate band. Solar cells based on quantum dots have been initially fabricated by a consortium formed by the Instituto de Energía Solar, the University of Glasgow, and Compound Semiconductor Technologies, and, although the cells do not reach the efficiency of the same structure without quantum dots, there is evidence of subband-gap absorption [11]. At this moment, we are involved in measuring the possible separation of quasi-Fermi levels in our quantum dot IB solar cells. IB materials based on alloys have been sought by theoretical band calculation [12] and have been recently found experimentally [13].

In the case of molecular-based concepts, the research aims, on the one hand, to search for mechanisms where molecules adsorbed to a wide band gap semiconductor (TiO_2) pump electrons from an electrolyte to the conduction band of the semiconductor by using two photons instead of only one, as is the case in the dye solar cells existing today [14].

On the other hand, a new type of purely static concentrator will be investigated (Fig. 4). Concentrators are of interest to reduce the area of the expensive solar converter, thereby separating the functions of energy collector, which is left to the concentrator, and energy converter, which is left to the solar cell. But high concentration concentrators today need mobile elements to focus the sunlight into the solar cells.

Static concentrators are made of a transparent matrix in which some luminescent molecules are diluted. These molecules absorb the light incident on the plate and emit luminescent quasimonochromatic radiation at some lower energy. This radiation is partly transmitted to the edge of the plate due to the total internal reflection experienced by the light when trying to leave the optically dense transparent plate [15].

In the work planned for the future, further investigation will be devoted to the process described and to the utilization of photonic crystals [16] to prevent the escape of luminescent monochromatic light at any inci-

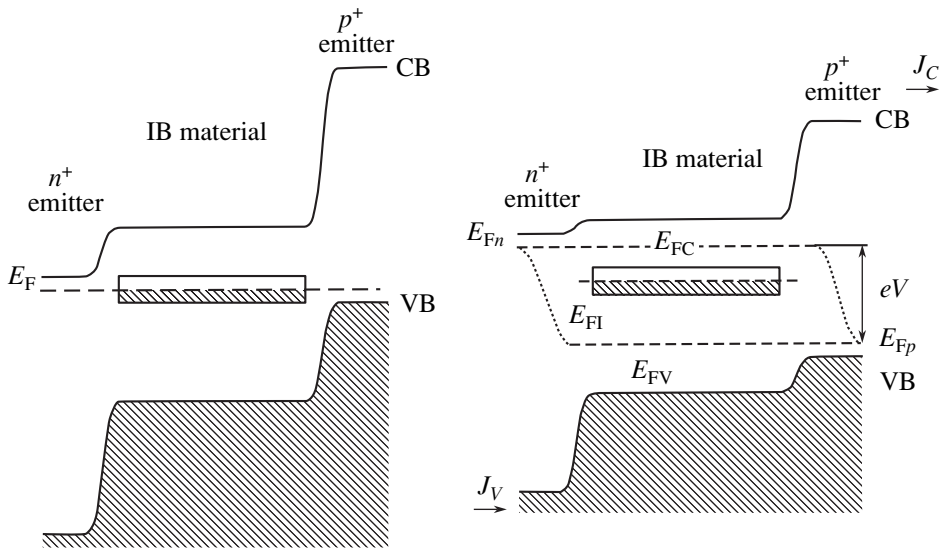

Fig. 3. Band diagram of an intermediate band solar cell (IBC). There is a mid-region of intermediate band material sandwiched between two *p* and *n* ordinary semiconductors: (left) thermal equilibrium, (right) under illumination. The Fermi level E_F splits into three quasi-Fermi levels E_{FC}, E_{FI}, and E_{FV}.

dence direction. This would greatly increase the efficiency of the light transfer to the plate edge [17].

Most of the concepts indicated above involve long or very long-term research, but, in the case of MJC, the concept is already ripe for industrialization. Therefore, FULLSPECTRUM also involves manufacturing concepts. In particular, concentrators are very important, because MJC cells are very expensive. Concentration levels of 1000 suns, that is, up to irradiance fluxes of 100 W/cm^2, are contemplated in this project. One important requirement to reduce prices is the use of wide angular acceptance. This means that the sunrays must stay focused into the cell even if the structure swings a little due to the wind or is somewhat misaligned due to manufacturing errors. The principles of design are in [18]. A multitude of devices have been designed in our institute in recent years based on the principles therein. Furthermore, at the high concentration envisaged, the illumination must be as homogeneous as possible, and this is difficult to conjugate with the angle acceptance requirement. Figure 5 shows an optical system designed for this purpose.

In addition to the optical design, manufacturing the lenses at low cost and assembling the whole system taking into account the cost requirements for heat removal is also a challenge that is being undertaken by the consortium in FULLSPECTRUM.

In summary, the mass exploitation of solar electricity is highly desirable for several reasons. Mass production of the present PV technology alone will probably not be enough to reduce PV electricity costs to reach the levels of prevalent electricity. A better exploitation of the solar spectrum is necessary.

Today, there are scientific bases, for instance, MJC or TPV, for this better utilization, but they are not yet

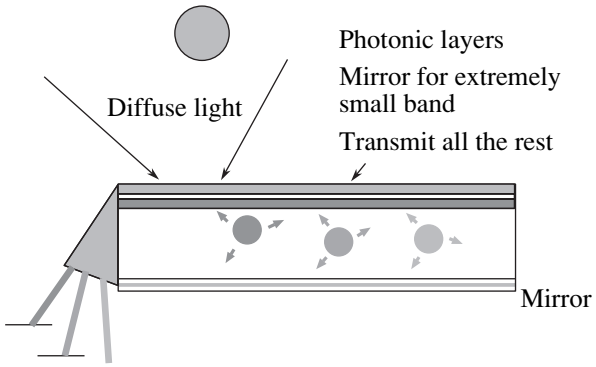

Fig. 4. Schematic of a stationary luminescent concentrator.

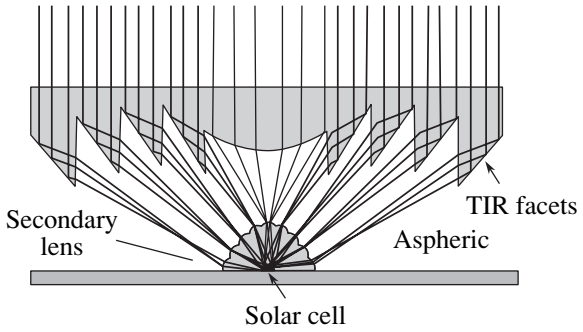

Fig. 5. Schematic of the Hamlet concentrator formed from an aspheric total internal reflection primary lens and a combined secondary. It exhibits a high acceptance angle and high light homogeneity on the solar cell. Joint development of ISOFOTON and the Instituto de Energía Solar.

developed for practical utilization. Our first goal is to develop them. It is necessary that a product with better potential than the present technology be developed as soon as possible. Otherwise, it will be forced to compete with products that are cheaper due to extensive market-associated development.

Furthermore, there are other technologies based on novel concepts that deserve to be developed, although this will take more time. They may hold the key to cheaper and more modular exploitation of solar energy than the solutions envisaged today, much less modular than present PV. It should be borne in mind that modularity has been that key to the present success of the PV market.

FULLSPECTRUM aims to make substantial contributions to all these issues.

ACKNOWLEDGMENTS

This study was carried out with the support of the European Commission (contract no. FP6 502620 FULLSPECTRUM).

REFERENCES

1. PV News (Paul Maycock), February issue of successive years.
2. A. Luque, Prog. Photovoltaics **9**, 303 (2001).
3. *Energy Needs, Choices and Possibilities Scenarios to 2050* (Shell International, 2001), www2.shell.com/home/media-en/downloads/51852.pdf.
4. A. Luque and A. Martí, in *Next Generation Photovoltaics*, Ed. by A. Martí and A. Luque (IOP, Bristol, 2003), Chap. 1.
5. W. Shockley and H. Queisser, J. Appl. Phys. **32**, 510 (1961).
6. A. Luque and A. Martí, in *Handbook of Photovoltaic Science and Engineering*, Ed. by A. Luque and S. Hegedus (Wiley, Chichester, 2003), Chap. 4.
7. T. Takamoto *et al.*, in *Proceedings of 3rd World Photovoltaics Energy Conversion Conference* (Osaka, 2003), ISBN 4-9901816-3-8.
8. V. M. Andreev, V. A. Grilikhes, and V. D. Rumyantsev, *Photovoltaic Conversion of Concentrated Sunlight* (Nauka, Leningrad, 1989; Wiley, Chichester, 1997).
9. A. Luque and A. Martí, Phys. Rev. Lett. **78**, 5014 (1997).
10. A. Martí, L. Cuadra, and A. Luque, in *Proceedings of 28th Photovoltaic Specialists Conference, Anchorage, Alaska, 2000* (IEEE, New York, 2000), p. 940.
11. N. López, D. Zhou, L. Cuadra, *et al.*, in *Proceedings of III Congreso Nacional de Dispositivos Electrónicos* (Barcelona, 2003), CD III 15, p. 15.
12. P. Wahnón and C. Tablero, Phys. Rev. B **65**, 165115 (2002).
13. G. Yu, W. Walukiewicz, J. Wu, *et al.*, Phys. Rev. Lett. **91**, 246403 (2003).
14. M. Späth, J. M. Kroon, P. M. Sommeling, *et al.*, in *Proceedings of 26th IEEE Photovoltaic Specialists Conference* (IEEE, New York, 1997), p. 503.
15. A. Goetzberger and W. Greubel, Appl. Phys. **14**, 123 (1977).
16. K. P. Velikov, C. G. Christova, R. P. A. Dullens, and A. van Blaaderen, Science **296**, 106 (2002).
17. K. Barnham, J. L. Marques, J. Hassard, and P. O'Brien, Appl. Phys. Lett. **76**, 1197 (2000).
18. J. C. Miñano, J. C. González, and P. Benítez, Appl. Opt. **34**, 7850 (1995).

Semiconductors, Vol. 38, No. 8, 2004, pp. 941–945. From Fizika i Tekhnika Poluprovodnikov, Vol. 38, No. 8, 2004, pp. 980–984.

SYMPOSIUM ON THE EFFICIENT USE OF SOLAR RADIATION IN PHOTOVOLTAIC POWER ENGINEERING (St. Petersburg, November 3–4, 2003)

Practical Thermophotovoltaic Generators[1]

S. Bitnar[1]*, W. Durisch[1], G. Palfinger[1], F. von Roth[1], U. Vogt[2], A. Brönstrup[2], and D. Seiler[3]

[1]*Paul Scherrer Institut, CH-5232 Villigen PSI, Switzerland*

**e-mail: bernd.bitnar@psi.ch*

[2]*EMPA, CH-8600 Dübendorf, Switzerland*

[3]*NTB Interstate University for Applied Sciences of Technology, CH-9471 Buchs, Switzerland*

Submitted February 9, 2004; accepted for publication February 11, 2004

Abstract—For use in gas-fired thermophotovoltaic systems, a selective emitter made from Yb_2O_3 foam ceramic has been developed. This foam ceramic is mechanically stable, and FTIR spectroscopy showed that 10% of the radiation power emitted by the foam can be converted by Si photocells. The thermal and thermal-shock stability of Yb_2O_3 foam ceramic was analyzed. The foam passed 200 heating/cooling cycles without major damage. Tubes were manufactured from this material and tested in a thermophotovoltaic demonstration system. An electrical power of 86 W was achieved at a thermal power of 16 kW. Using a simulation model, the potential efficiency of a thermophotovoltaic system based on our technology applied for the conversion of concentrated solar radiation was estimated. © *2004 MAIK "Nauka/Interperiodica".*

1. INTRODUCTION

In thermophotovoltaics thermal energy is used to heat a radiation emitter, which in its turn illuminates photocells that convert the radiation into electricity. In this publication two heat sources will be considered: a combustion flame and concentrated solar radiation.

In case of a combustion flame, thermophotovoltaics is a technology of cogeneration of heat and electricity without the need for any moving parts. The system efficiency η_{sys}, which is defined as electrical power divided by thermal input power, is relatively small: until now, the highest experimentally achieved system efficiency is about 5% [1].

In case of solar thermophotovoltaics, the possible match between the emission spectrum of the radiator and the band gap of the photocell material is the advantage compared to direct solar irradiation to the photocell. If a photocell is illuminated by selective radiation with a narrow emission band closely above the band gap of its material, losses due to thermalization or sub-band-gap transmission arc avoided. The efficiency of a solar cell can be strongly increased compared to direct solar irradiation. Therefore, solar thermophotovoltaics is possibly a way to beat the efficiency limit of existing solar cell technology.

2. FOAM CERAMIC EMITTERS

A novel selective emitter to be used in thermophotovoltaic (TPV) systems has been developed. The following requirements for the TPV emitter were defined:

—The selective emission spectrum should be matched to the band gap of Si.

—The structure should be porous, so that the combustion gas can flow through and combustion can take place in the emitter structure.

—The emitter must be mechanically stable.

—The emitter must be thermally stable up to operating temperatures of 1800 K.

—The thermal-shock resistance must be high, because the material must withstand numerous heating/cooling cycles without any damage.

A selective emissivity that is well matched to the band gap of Si can be achieved by using Yb_2O_3 as the emitter material. Yb_2O_3 mantle emitters have been investigated for applications in TPV systems in the past [2, 3]. High TPV system efficiencies could be achieved with mantle emitters, but they suffered from very poor mechanical stability. The thermal-shock resistivity of Yb_2O_3 mantles was sufficient for laboratory TPV systems.

A solution that avoids these drawbacks and fulfills all of the requirements listed above is a Yb_2O_3-coated foam ceramic emitter.

Foam ceramics were produced for this work using the polymer-sponge method [4]:

—A polymer sponge with the desired shape and pore size is first fabricated. Sponges in the shape of tubes were used for the current work.

—The sponge is infiltrated with a water-based ceramic slurry. In order to remove excess slurry and avoid pores filled with slurry, the sponge is subsequently passed through a mangle.

—The sponge is then carefully dried, resulting in so-called "green ceramic." Several samples of such green ceramic foams and emitter tubes are shown in Fig. 1.

[1]This article was submitted by the authors in English.

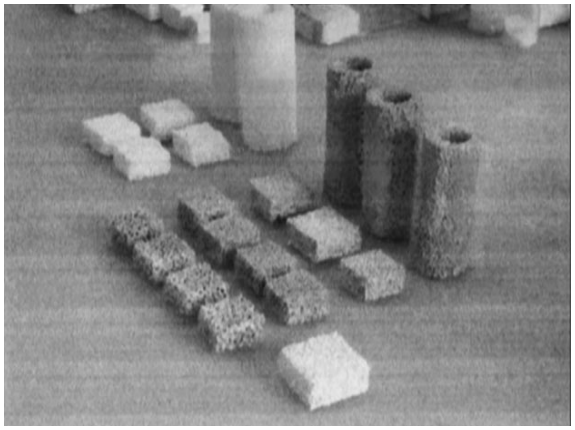

Fig. 1. Examples of foam ceramics and foam ceramic emitter tubes. The gray samples are green bodies after infiltration and drying. After sintering the ceramic appears white.

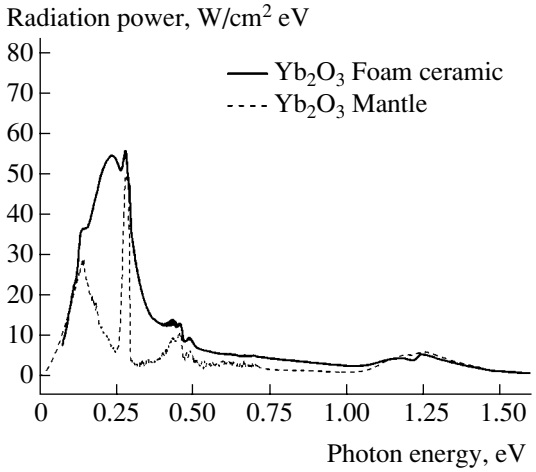

Fig. 2. Radiation spectra of a Yb_2O_3 foam ceramic and a Yb_2O_3 mantle emitter. Both emitters were heated by a 2-kW butane burner. The temperature of the mantle emitter was 1735 K.

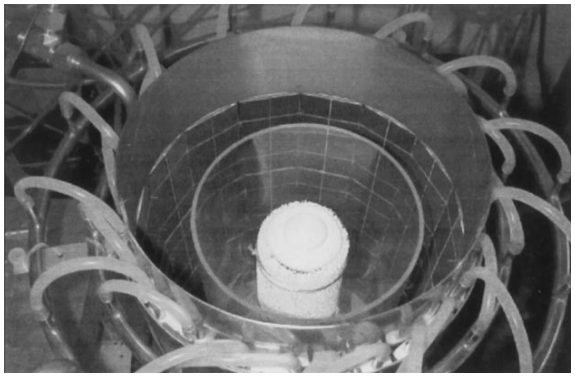

Fig. 3. TPV prototype system: in the center the foam ceramic emitter tube is visible. A quartz tube is placed between the emitter and Si photocells.

—In a subsequent sintering step at temperatures in excess of 1000°C, the polymer sponge vaporizes and the ceramic densifies.

In order to measure the radiation spectrum of these emitter structures, foam ceramic tubes with a diameter of 40 mm and a wall thickness of 10 mm were fabricated that could be heated with a 2-kW butane burner. The emitted radiation was coupled into a Bruker 113 FTIR spectrometer [3, 4]. Figure 2 shows the emission spectrum of the Yb_2O_3 foam ceramic in comparison to the spectrum of a Yb_2O_3 mantle [3]. Both spectra show the selective emission peak at a photon energy of 1.25 eV, which can be converted by Si photocells. While the height of this maximum is comparable for the two spectra, the foam ceramic emitter shows a significantly stronger emission at photon energies below 0.5 eV. The selectivity, which is defined as radiation power at photon energies larger than the Si band gap divided by the total emitted radiation power, is consequently only 10% for the foam ceramic, compared to 20% for the mantle.

The foam ceramic emitters are mechanically stable. They can easily be handled for mounting in a gas burner, so they seem to be suitable for application in TPV systems.

The emitter tubes were heated up to temperatures of 1750 K with gas burners to study the thermal stability of the structures. No thermal instabilities were observed. The surfaces of the surrounding quartz tube and the gold reflector placed above the heated emitter remained clean, indicating that no material evaporated from the samples.

A timer-controlled butane burner was built, with which the thermal-shock stability of the foam ceramics was studied. This device permitted the automatic operation of the emitters over many heating/cooling cycles. With this method the thermal-shock stability of the foam ceramics over at least 200 cycles has been demonstrated.

3. TPV PROTOTYPE SYSTEM

The Yb_2O_3 foam ceramic emitter was tested in a TPV prototype system [5], which is shown in Fig. 3. In this system the emitter is heated by a 10 to 20-kW methane burner. Monocrystalline Si solar cells from RWE Solar (Germany) were glued onto water-cooled heatsinks, and the front side was laminated with a special EVA foil. A quartz tube was placed between emitter and photocells to protect the cell surface from contact with the hot combustion gas. The lower end of the cylindrical TPV system was optically closed with a gold reflector. Figure 3 shows the foam ceramic emitter built into the TPV system.

Table 1 gives the experimental results achieved with this TPV system. The electrical power P_{el} and the system efficiency η_{sys} are given for several values of thermal power P_{th} and air number λ. The air number gives

the amount of combustion air divided by the amount of air for stoichiometric combustion. Our experiments demonstrate the feasibility of the novel Yb_2O_3 foam ceramic emitter. In earlier experiments, by using Yb_2O_3 mantle emitters instead of the foam ceramics, a significantly higher electrical power was achieved [5]. In future, we hope to enhance the selectivity of the foam ceramic emitters by improving the fabrication process.

An increased system efficiency with the existing Yb_2O_3 foam ceramic emitter was achieved with a small TPV system by the following optimizations:

—Special TPV optimized Si photocells were manufactured that have a highly reflective rear side Al mirror and a nontextured front side to reflect sub-band-gap radiation, for which the cell is transparent, directly back to the emitter. This back-reflected radiation is used for an additional heating of the emitter, resulting in a higher emitter temperature for a given thermal power of the burner.

—The ZnS/MgF_2 antireflection coating was optimized for low reflectivity for the Yb_2O_3 emission spectrum.

—The photocell has a low resistant front metallization to reduce the series resistance loss at an illumination level of five to ten times the irradiation of the sun, which occurs in our TPV system.

—The cylindrical photocell generator is mostly optically closed by three gold reflectors, leaving only a slit for the escape of the exhaust gas.

A methane burner with a thermal power of 1.2–2.4 kW was used as a heat source for the emitter. Figure 4 gives the system efficiency that was achieved with the small TPV system as a function of the thermal power. The experiments with a foam ceramic emitter resulted in a system efficiency of more than 1.0% between 1.6 and 2.4 kW. This is twice the efficiency achieved by the larger prototype system. With a mantle emitter, up to 1.8% system efficiency could be obtained.

We plan to build a larger prototype with a similar design allowing a significantly higher system efficiency than the existing demonstration system.

4. SIMULATION OF A SOLAR-POWERED TPV SYSTEM

It was suggested that TPV be applied in solar concentrator systems to exceed the efficiency limit of one-sun single junction solar cells [7]. Below, the expected efficiency of the above-described TPV system, if the emitter is heated by concentrated sunlight, is estimated. For this estimate a simulation model representing the small TPV system was used, which was described in detail elsewhere [2]. The model calculates the electrical power of a TPV system using the geometry, the optical transmittance and reflectance of the inner system surfaces, and the spectral efficiency of the photocells. The total radiation power of the emitter P_{em} is obtained from a combustion model in the case of a fuel fired system [2]. For a solar-heated TPV system P_{em} is calculated from

$$P_{em} = P_{sun} c A_{foc} (1 - R_{em}) \quad (1)$$

with the direct solar irradiation power P_{sun}, the concentration factor c, the area of the focused sunlight on the emitter surface A_{foc}, and the reflectivity of the emitter R_{em}.

The model uses the net radiation method [6], which calculates the radiation balance between all surfaces and the total energy balance of the system [2].

A drawing of the simulated solar TPV system is shown in Fig. 5. Concentrated sunlight is coupled into the system to heat the emitter through a hole in the top reflector. The emitter radiation illuminates the cylindrical photocell module built around it.

For discussion of the results, the assumptions of the simulation model have to be considered:

—A uniform temperature over the whole emitter surface was assumed. This assumption seems to be approximately fulfilled, because the brightness of the visible radiation is uniform over the whole gas porous region of the emitter in gas-fired TPV experiments.

—The spacing between the single photocells was taken into account by using a view factor, and average

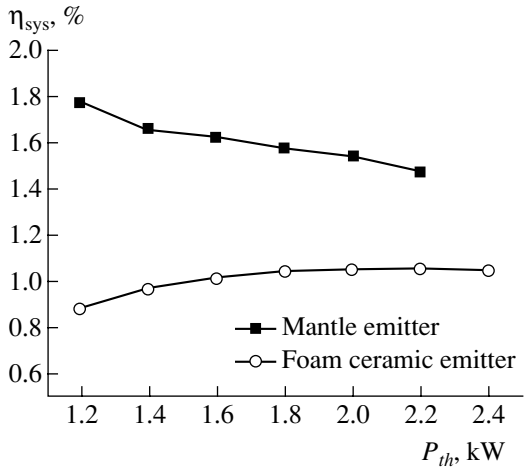

Fig. 4. Experimental results achieved with a small TPV prototype system. The system efficiency η_{sys} is given as a function of the thermal power P_{th} for experiments using an Yb_2O_3 mantle emitter (squares) and a Yb_2O_3 foam ceramic emitter (open circles).

Table 1. Electrical power P_{el} and system efficiency η_{sys} achieved with a TPV prototype system with foam ceramic emitter as a function of the thermal power P_{th} and the air number λ

P_{th}, kW	λ	P_{el}, W	η_{sys}, %
12	1.03	60	0.50
12	1.12	54	0.49
16	1.02	86	0.54

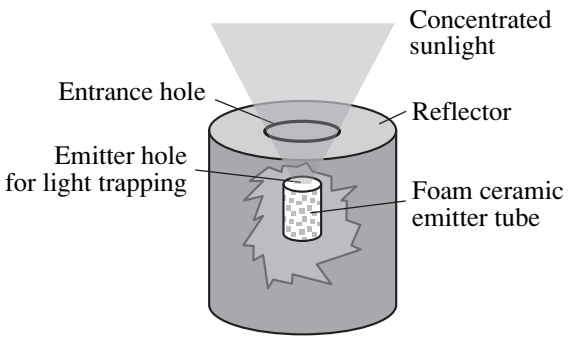

Fig. 5. Draft of a cylindrical solar TPV system.

values of the photocell efficiency and front surface reflectivity were calculated. In the experimental system slits occur between the cells, which were not considered exactly by this simplification.

—The escape of the exhaust gas in the experimental system was effected by a hole in the top reflector, which can be covered with a concave reflector leaving a slit for the exhaust gas flow. In the solar-heated system, a hole in the top reflector is needed through which the concentrated sunlight enters the system. These openings, which are a relevant difficulty for achieving an optical cavity, are considered in the model by using an average reflectivity of the top reflector. For an exact calculation of this relatively complicated geometry, a ray tracing calculation would be necessary.

—The emitter reflectivity R_{em}, which is used for the calculation of a solar TPV system, was assumed to be independent of the photon energy. An efficient light trapping due to the porous surface of the foam ceramic is expected, which depends on the exact geometry of the emitter. The spectral reflectance of such an emitter has not yet been measured.

Simulations of the small gas-fired TPV system with different photocells, reflectors, filters, and emitters show an agreement with the experimentally achieved system efficiencies of better than 90%. It is therefore expected that the assumptions listed above will not cause any major uncertainties in the simulation results. This justifies the application of our model to estimate the efficiency of the TPV system heated with concentrated solar radiation. The simulation model conveniently allows one to study losses that occur in a specific component of the TPV system and their effect on the system efficiency.

Table 2. Simulation result of a solar-heated TPV system. *PSI-TPV* is an existing TPV optimized Si photocell with rear surface reflector, *c* means the concentration factor of the sun radiation, and T_{em} is the resulting emitter temperature

Photocell	Filter	*c*	T_{em}, K	P_{el}, W	η_{sys}, %
PSI-TPV	Quartz	1000	1750	17	4.0
PSI-TPV no FC absorption	Quartz	1000	1850	25	5.9
PSI-TPV no FC absorption	Ideal	2000	2000	44	10
Optimized	Ideal	2000	1960	67	16
Optimized	Ideal	5000	2340	120	29

Table 2 gives the result of these simulations. In the first line the existing small TPV system was modeled: *PSI-TPV* is the photocell manufactured at the Paul Scherrer Institut with a rear surface reflector. A sun radiation concentration factor of 1000 was assumed. The area of the concentrator was 5000 cm^2 for all simulations. The resulting opening in the top reflector, which is needed to illuminate the emitter, had an area of 6.6 cm^2. The reflectivity of the emitter was assumed to be 10%. A system efficiency η_{sys} of 4.0% was obtained for this case.

In subsequent simulations several optimizations were studied to reduce losses in the system and to increase η_{sys}. Using lower doped Si for the fabrication of the photocell to avoid free carrier (FC) absorption of sub-band-gap radiation increases η_{sys} to 5.9%. Further losses are absorption in the quartz tube and radiation loss through the opening in the top reflector. In the following simulations, this opening was made smaller by enlarging the concentration factor *c*, i.e., reducing the focus spot of the concentrated sunlight. The quartz tube was replaced by an idealized filter with an assumed transmittance of 99% for convertible radiation and a reflectance of 99% for sub-band-gap radiation. The resulting η_{sys} was 10%. To estimate an upper limit for η_{sys} of a solar TPV system with Si photocells and Yb_2O_3 emitter based on our technology, an optimized photocell with a monochromatic efficiency of 46% at 1.25 eV was assumed, resulting in a η_{sys} of 16% for a concentration factor of 2000 and 29% for 5000, respectively.

5. CONCLUSION

A Yb_2O_3 foam ceramic emitter has been developed that fulfils the requirements for use in TPV systems. Mechanical and thermal stability up to temperatures of 1800 K were achieved with these emitters. The selectivity of the emitter radiation with respect to the band gap of Si is currently 10%. Thermal-shock stability tests during up to 200 ignition cycles in the laboratory showed that the emitters possess a satisfactory thermal-cycling resistance. Long-term cycle tests are planned in the near future to verify the thermal-shock resistance over a larger number of cycles. The foam ceramic emitters were successfully tested in two prototype TPV systems. A η_{sys} of 1% was achieved with the small prototype. In the larger prototype the η_{sys} was about half of this required value, but it is expected that the η_{sys} will increase once the selectivity of the foam ceramics is improved or the design of the smaller prototype TPV system is adapted to that of the large one.

The use of thermophotovoltaics for the conversion of concentrated sunlight would be attractive, if a η_{sys} value higher than that of high-quality single junction solar cells under concentration, which is 28% at present, could be achieved. Simulations show that, in principle, an efficiency on the order of 30% is achievable with a TPV system using Si photocells and a Yb_2O_3 emitter. However, several simplifying assumptions were made for this calculation, including optimized photocells, an ideal selective filter, and a very high concentration factor of 5000. Experiments with the TPV system discussed here under concentrated sunlight are planned for the future to confirm the calculated values of η_{sys} from the simulations.

ACKNOWLEDGMENTS

This work was funded by the Swiss Commission of Technology and Innovation (CTI), contract no. 5692.2 EBS.

REFERENCES

1. W. E. Horne, M. D. Morgan, V. S. Sundaram, and T. Butcher, in *Proceedings of Fifth Conference on Thermophotovoltic Generation of Electricity,* Ed. by T. J. Coutts, G. E. Guazzoni, and J. Luther (2003), AIP Conf. Proc., Vol. 653, p. 91.
2. B. Bitnar, J.-C. Mayor, W. Durisch, *et al.*, in *Proceedings of Fifth Conference on Thermophotovoltic Generation of Electricity,* Ed. by T. J. Coutts, G. E. Guazzoni, and J. Luther (2003), AIP Conf. Proc., Vol. 653, p. 18.
3. B. Bitnar, W. Durisch, J.-C. Mayor, *et al.*, Sol. Energy Mater. Sol. Cells **73** (3), 221 (2002).
4. B. Bitnar, W. Durisch, F. von Roth, *et al.*, in *Next Generation Photovoltaics: High Efficiency through Full Spectrum Utilization,* Ed. by A. Martí and A. Luque (Inst. of Physics, Bristol, 2004), p. 223.
5. B. Bitnar, W. Durisch, A. Meyer, and G. Palfinger, in *Proceedings of Fifth Conference on Thermophotovoltic Generation of Electricity,* Ed. by T. J. Coutts, G. E. Guazzoni, and J. Luther (2003), AIP Conf. Proc., Vol. 653, p. 465.
6. R. Siegel and J. R. Howell, *Thermal Radiation Heat Transfer,* 2nd ed. (Hemisphere, New York, 1981).
7. K. W. Stone, D. L. Chubb, D. M. Wilt, and M. W. Wanlass, in *Proceedings of Second NREL Conference on Thermophotovoltaic Generation of Electricity,* Ed. by J. P. Benner, T. J. Coutts, and D. S. Ginley (1996), AIP Conf. Proc., Vol. 358, p. 199.
8. Zh. I. Alferov and V. D. Rumyantsev, in *Next Generation Photovoltaics: High Efficiency through Full Spectrum Utilization*, Ed. by A. Marti and A. Luque (Inst. of Physics, Bristol, 2004), p. 19.

Semiconductors, Vol. 38, No. 8, 2004, pp. 946–949. From Fizika i Tekhnika Poluprovodnikov, Vol. 38, No. 8, 2004, pp. 985–987.

SYMPOSIUM ON THE EFFICIENT USE OF SOLAR RADIATION IN PHOTOVOLTAIC POWER ENGINEERING (St. Petersburg, November 3–4, 2003)

Intermediate Band Solar Cells: Comparison with Shockley–Read–Hall Recombination[1]

A. Martí*, L. Cuadra, N. López, and A. Luque

Instituto de Energía Solar, ETSIT de Madrid, Universidad Politécnica de Madrid, 28040 Madrid, Spain

**e-mail: amarti@etsit.upm.es*

Submitted February 9, 2004; accepted for publication February 11, 2004

Abstract—Intermediate band solar cells are characterized by the existence of a collection of energy levels in the middle of the otherwise conventional semiconductor band gap. According to the standard Shockley–Read–Hall recombination theory, the states corresponding to these energy levels behave as nonradiative recombination centers and, therefore, are detrimental to solar cell performance. Nevertheless, the theory of the intermediate band solar cells predicts an enhancement of the solar cell efficiency well above the limiting efficiency of single gap solar cells (63.2% vs. 40.7%) when these levels exist. This paper clarifies the reasons. © *2004 MAIK "Nauka/Interperiodica".*

The basic theory of intermediate band solar cells (IBSCs) has been by now widely disseminated. In this paper, we will assume the reader is familiar with this theory and we will describe here again only those topics that are convenient for the self-consistency of the paper. If the reader is not familiar with the theory and would wish to be so, we suggest he starts with reference [1], to find the original description of the model, and continue with [2] to [3–6]. There he will find a range of subjects from refinements to the theory, such as the discussion of the influence of the impact-ionization and Auger recombination mechanism on the performance of the cell, to thermodynamic analysis, discussion of the implementation of the IBSC with quantum dot technology, and analyses of the influence of the overlap between absorption coefficients on the performance of a cell.

Figure 1 represents the simplified band diagram of an IBSC. The basic structure of this cell consists of an intermediate band material sandwiched between two ordinary semiconductors. The intermediate band material is a semiconductor-like material but characterized by the existence of an intermediate band (IB) located within the otherwise conventional gap defined by the edges of the conduction band (CB) and valence band (VB). Theoretical efficiency improvement of IBSCs over conventional single and even tandems of two solar cells (63.2% vs. 40.7% of single gap and 55.4% of a tandem) comes from two facts. First, the current in the IBSC is enhanced because sub-band-gap photons can contribute to the photocurrent. This is because, thanks to the IB, sub-band-gap photons, such as those labeled *1* and *2* in Fig. 1, can now be absorbed to create one electron–hole pair. Second, the production of this extra current is made out without voltage degradation, that is, without the voltage being limited by any of the lowest subgaps, neither E_L nor E_H. Ultimately, this is due to the fact that the carrier concentration in each band is described by its own quasi-Fermi level (ε_{FC}, ε_{FV}, and ε_{FI} for the CB, VB, and IB respectively), the output voltage being limited by the difference between the CB and VB quasi-Fermi levels. It is the voltage issue that must be emphasized the most, because the solution to increase the photogenerated current of a solar cell could be, for example, just the use of a low band gap energy semi-

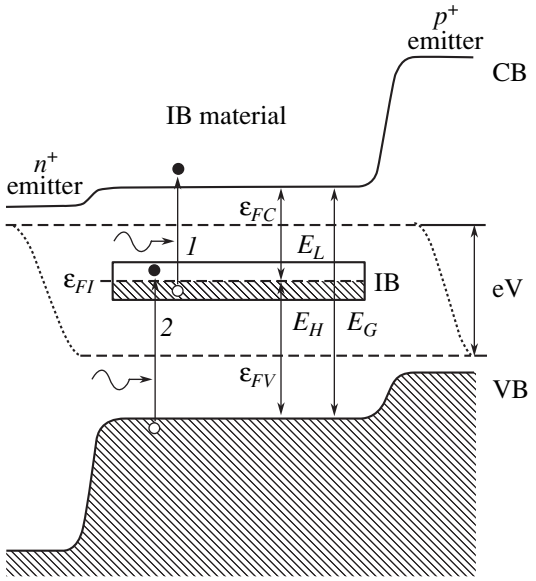

Fig. 1. Simplified band gap diagram of an intermediate band solar cell [5].

[1]This article was submitted by the authors in English.

conductor to manufacture it. In addition, to approach the IBSC limiting efficiency, electronic transitions to and from the IB must be of radiative nature (emitting one photon), the absorption coefficients governing these processes should not overlap when considered as a function of the photon energy, the IB must be half-filled with electrons (metallic), and ε_{FI} must remain clamped to its equilibrium position when the cell becomes excited.

However, the existence of energy levels within the semiconductor band gap is traditionally considered a source of nonradiative recombination, the so-called Shockley–Read–Hall (SRH) recombination, after the authors who first described the governing statistics [7, 8]. Since the existence of nonradiative recombination degrades the performance of the cells, from this perspective, the existence of intermediate levels should be considered an undesirable feature. On the contrary, the basic theory of the IBSC pursues the existence of these levels and moreover, as mentioned, requires that the recombination processes to and from this band be of radiative nature.

Before explaining the reasons why the presence of intermediate energy levels within the semiconductor band gap can lead to such a different behavior from the perspective of recombination (radiative vs. nonradiative), we would like to point out that both frameworks (SRH and IBSC) assume that the existence of three quasi-Fermi levels rules the occupation probability out of the equilibrium in each of the existing group of states (conduction, intermediate, and valence) in the semiconductor.

The existence of its own quasi-Fermi level to describe the occupation probability of the intermediate states is not usually sufficiently emphasized, but it is true since, at some point in the development of the SRH theory, it is stated that the number of intermediate states (often also called *traps* or *defects* in the framework) being occupied by an electron, n_T, compared to the total number of states, N_T, is given by [9]

$$\frac{n_T}{N_T} = \frac{1}{1+\exp\left(\frac{E_T-\varepsilon_{FI}}{kT}\right)} = \frac{c_n N_T n + c_p N_T p_1}{c_n\left[n + n_i\exp\left(\frac{E_T-E_i}{kT}\right)\right] + c_p\left[p + n_i\exp\left(\frac{E_i-E_T}{kT}\right)\right]} \quad (1)$$

where no degeneracy has been assumed for the trap, E_T is the energy of the intermediate state, ε_{FI} is the trap quasi-Fermi level, k is the Boltzmann constant, T is the temperature, n and p are the electron and hole concentrations respectively, c_n and c_p are the electron and hole capture cross sections, n_i is the semiconductor intrinsic concentration, and E_i is the semiconductor intrinsic level.

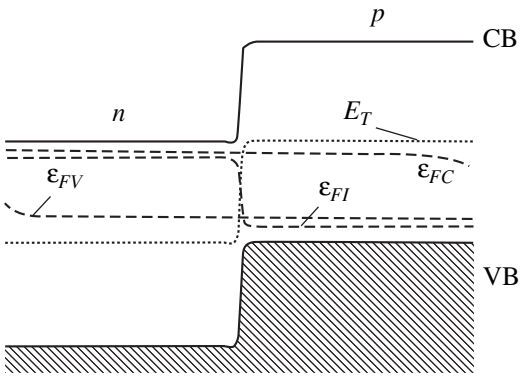

Fig. 2. Band gap diagram of a *p–n* junction forward biased showing the electron, hole, and trap quasi-Fermi levels (ε_{FC}, ε_{FV}, and ε_{FI} respectively).

This fact is also illustrated by the example in Fig. 2. It shows the band gap diagram of a forward biased *p–n* junction and its corresponding quasi-Fermi levels, including the one related to the traps, ε_{FI}. The trap density, N_T, is assumed to be uniform over the whole *p–n* structure and *much lower* than the doping density involved. The trap energy level, E_T, is assumed to be located at the center of the band gap. To emphasize further the need for a specific quasi-Fermi level associated with the occupation of the traps, one can realize that neither the electron quasi-Fermi level, ε_{FC}, nor the hole quasi-Fermi level, ε_{FV}, can rule the trap occupation ratio because the choice of any of them leads to opposite asseverations: the electron quasi-Fermi level, being located well above the trap energy level leads to complete electron occupation of the traps, while the hole quasi-Fermi level, being located well below, leads to its complete emptiness. Therefore, the existence of three different quasi-Fermi levels to explain the operation of the IBSC should not be regarded as an awkward hypothesis of the IBSC theory: it has always been there, even in conventional semiconductor theory.

A couple of aspects of these *traps* are specific in the classic IBSC context. To explain them, it is convenient to define first what we understand by acceptor- and donor-like *traps*. Acceptor-like traps become negatively charged when they capture an electron (its quasi-Fermi level is located then a few kT above E_T), remaining electrically neutral if they do not (its quasi-Fermi level is then located below E_T). Donor-like traps become positively charged when they give away an electron (quasi-Fermi level located below E_T), remaining neutral if they do not (quasi-Fermi level located above E_T). Besides, whatever the type is, its density in conventional devices in which their appearance is unin-

tentional is small and has a negligible contribution to the charge density when compared to the intentional doping contribution (usually characterized by concentrations well above 10^{16} cm^{-3}).

Hence, the two specific aspects regarding these *traps* (which below we will prefer call a *band*) if they had to play the role specified by the basic IBSC theory are, on the one hand, that they should have both an acceptor and a donor character. This means that they become negatively charged when they capture an electron and positively charged when they release one (in other words, they become negatively charged when their quasi-Fermi level lays above E_T and positively charged when it lays below). On the other hand, their concentration should be at least on the order of magnitude of the CB and VB density of states [10]. The reason is the need for the IB to provide both a positive and a negative charge without significant displacement of the IB quasi-Fermi level, so it can remain clamped to its equilibrium position as plotted in Fig. 1.

However, increasing the *trap* concentration, if they still behave nonradiatively, would only worsen things. This point is the point where we prefer to call this collection of intermediate levels a *band* rather than *traps*. The term *band* is used to indicate that the intermediate quantum states have quantum properties no different from those of the CB and VB and, in particular, that they are of delocalized nature; that is, their wave function extends over the whole crystal lattice. This is a necessary condition for the transitions from and to the intermediate band to be of radiative nature [2].

To achieve this delocalization, it is likely that the impurities should not be placed randomly within the crystal lattice but ordered with a periodical pattern [11] or, even better, that the intermediate band arises naturally from a given atomic crystal arrangement [12].

An intriguing question when discussing SRH recombination is where the energy lost by an electron carrying out a transition goes. If it went easily to a photon, we would not be discussing anything here: radiative recombination would already be acknowledged.

To say the energy of the electron in the recombination process goes to phonons needs some comment. Phonons, the quantized vibrations of *lattice atoms*, have an energy in the range of a few tenths of one millielectronvolt [13]. Since the gaps E_L or E_H are in the range of several hundred millielectronvolt, the nonradiative transition of say one electron from the CB to the intermediate levels would require simultaneous interaction with tens (at least) of phonons. This simultaneous concurrence of such a number of phonons is considered extremely unlikely in a perfect crystal. Instead, the preferred figure is that in which the presence of the *trap* not only introduces strictly one energy level *in the middle* of the gap but also some *excited* electronic states and its *own vibration modes*, different from those of the lattice. Hence, in a first step, a CB electron is captured by the *trap*; that is, it carries out a transition to one of the impurity excited electronic states (cascade model [9]). This state is usually localized. The impurity then captures the electron energy and momentum and vibrates. It can do so in one step because its vibration modes are not those of the lattice. Then, this energy is released to the lattice (lattice relaxation) through the emission (not simultaneous!) of the necessary number of phonons (multiphonon model [9]).

Hence, the solution to retake the unlikeness of an electron releasing its energy nonradiatively to the phonons passes through the *blockade* of the two mechanisms just mentioned. And this solution again goes through the allocation of the impurities in a periodical pattern or, what is equivalent, makes them part of the crystal lattice itself. In this way they cannot vibrate freely any more, but their vibrational modes should become those typical of a crystal lattice; that is, those whose energy is in the phonon energy range, a few tenths of one millielectronvolt. So, on the one hand, they would again not be able to capture the energy of the electron in the first instance, while on the other, as mentioned above, their energy spectra would be grouped into bands.

In the case where the IBSC is engineered by means of quantum dots (QDs), this *blockade* of the capability of an electron to release its energy through phonons, although controversial [14], is known as the phonon-bottleneck effect. Physically, in the QD case, the intermediate band arises from the energy of the confined electrons in the dot. Remarkably, the dots are groups of thousands of atoms that again certainly do not have the vibrational properties of single impurity atoms but probably the vibrational properties of a lattice, which again takes us to the case where only phonons with energy of a few tenths of millielectronvolts are available for electron energy release.

In summary, the frameworks of the IBSC and the SRH theories share the introduction of three quasi-Fermi levels to describe carrier occupation of the energy levels, although in the case of the latter, this feature has not commonly be made explicit in the literature. In addition, the IBSC theory assumes that the recombination processes between bands are of predominantly radiative nature. There is nothing in the SRH theory against these processes being of radiative nature, although to make them dominant, it will be required to blockade the possibility of energy transfer from the electrons to the phonons. This could be achieved either by allocating the impurities periodically in the crystal lattice and thereby making them all constitute a new crystal or possibly by using quantum dots to fabricate the intermediate band material.

REFERENCES

1. A. Luque and A. Martí, Phys. Rev. Lett. **78**, 5014 (1997).
2. A. Martí, L. Cuadra, and A. Luque, in *Next Generation Photovoltaics: High Efficiency through Full Spectrum Utilization*, Ed. by A. Martí and A. Luque (IOP, Bristol, 2003).
3. L. Cuadra, A. Martí, and A. Luque, IEEE Trans. Electron Devices **51** (2004) (in press).
4. A. Luque, A. Martí, and L. Cuadra, IEEE Trans. Electron Devices **50**, 447 (2003).
5. A. Luque and A. Martí, Prog. Photovoltaics **9** (2), 73 (2001).
6. A. Luque, A. Martí, and L. Cuadra, IEEE Trans. Electron Devices **48**, 2118 (2001).
7. W. Shockley and W. T. Read, Phys. Rev. **87**, 835 (1952).
8. R. N. Hall, Phys. Rev. **87**, 387 (1952).
9. R. Pierret, in *Modular Series on Solid State Devices*, Vol. 4: *Advanced Semiconductor Fundamentals*, Ed. by R. F. Pierret and G. W. Neudeck (Addison-Wesley, Reading, 1989).
10. A. Martí, L. Cuadra, and A. Luque, in *Proceedings of 199th Electrochemical Society Meeting* (The Electrochemical Society, Pennington, 2001), p. 46.
11. B. K. Ridley, *Quantum Processes in Semiconductors*, 4th ed. (Oxford Univ. Press, Oxford, 1999), Chap. 2.
12. P. Wahnón and C. Tablero, Phys. Rev. B **65**, 165115 (2002).
13. *Handbook Series on Semiconductor Parameters*, Ed. by M. Levinshtein, S. Rumyantsev, and M. Shur (World Sci., Singapore, 1996 and 1999), Vols. 1 and 2.
14. A. J. Nozik, in *Next Generation Photovoltaics: High Efficiency through Full Spectrum Utilization*, Ed. by A. Martí and A. Luque (IOP, Bristol, 2003).

Semiconductors, Vol. 38, No. 8, 2004, pp. 950–955. Translated from Fizika i Tekhnika Poluprovodnikov, Vol. 38, No. 8, 2004, pp. 988–993.

SYMPOSIUM ON THE EFFICIENT USE OF SOLAR RADIATION IN PHOTOVOLTAIC POWER ENGINEERING (St. Petersburg, November 3–4, 2003)

Thermophotovoltaic Cells for Conversion of Thermal Radiation and Concentrated Sunlight to Electricity

V. P. Khvostikov*^, O. A. Khvostikova*, P. Yu. Gazaryan, M. Z. Shvarts*, V. D. Rumyantsev*, and V. M. Andreev***

**Ioffe Physicotechnical Institute, Russian Academy of Sciences, Politekhnicheskaya ul. 26, St. Petersburg, 194021 Russia*
^e-mail: vlkhv@scell.ioffe.ru
***Volgodonsk Institute of the South-Russia State Technical University, Volgodonsk, 347340 Russia*
Submitted February 9, 2004; accepted for publication February 11, 2004

Abstract—The potential of the thermophotovoltaic conversion of thermal and solar energy to electricity using narrow-gap semiconductor photoconverters is shown. Liquid-phase epitaxy, metal-organic chemical vapor deposition, and Zn diffusion from the vapor phase are used to fabricate thermophotovoltaic converters based on GaSb and GaAs/Ge structures and characterized by increased values of both photocurrent and open-circuit voltage. This circumstance made it possible to obtain thermophotovoltaic cells that were based on the aforementioned structures and had efficiencies of 25% (GaSb) and 16% (GaAs/Ge) at a blackbody-radiation temperature of T = 1473 K under the condition of 100% return of low-energy photons to the emitter. © *2004 MAIK "Nauka/Interperiodica".*

1. INTRODUCTION

The development of technologies for the fabrication of high-efficiency photovoltaic converters based on narrow-gap semiconductors has inspired renewed interest in thermophotovoltaic (TPV) generators, which were suggested more than 30 years ago. In TPV systems, thermal radiation is converted into electrical energy using photovoltaic cells based on narrow-gap semiconductors that are photosensitive to the infrared (IR) region of the spectrum.

A TPV generator generally consists of four main components: a source of thermal radiation, an emitter, a spectral filter, and photovoltaic cells (Fig. 1). Radiation generated as a result of heating the material of the emitter to a high temperature (using concentrated solar radiation, natural gas, propane, gasoline, hydrogen, and so on) is converted into electricity by a photovoltaic cell. It is important that the radiation spectrum of the emitter should be matched to the photosensitivity spectral region of the photovoltaic cell.

In order to satisfy the condition for matching, one can employ one of two methods [1]:

(i) the use of a selective emitter as the radiation source or

(ii) the use of an emitter combined with an optical filter.

In this case, the long-wavelength component of radiation, which does not contribute to the electricity generation, is reflected back to the emitter.

In Fig. 1, we illustrate the thermophotoelectric principles of operation of two feasible TPV systems: (I) with a selective emitter and (II) with an optical filter that reflects the unused component of the radiation.

The question of the ultimate efficiency of a TPV generator is of particular importance. The majority of published data are concerned with estimates of the highest efficiency for photovoltaic conversion of thermal radiation absorbed in a semiconductor (i.e., for the "photon–electron" conversion). The attained values of the efficiency of this conversion in a TPV generator

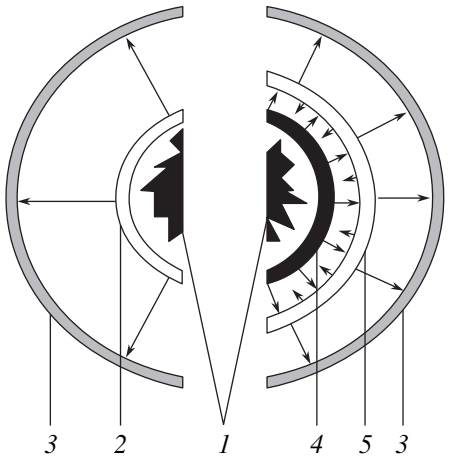

Fig. 1. Schematic representation of a thermophotovoltaic generator of electricity (view from above). A system with a selective emitter is shown on the left, and a system with an emitter and an optical filter is shown on the right. The systems include (*1*) a high-temperature source, (*2*) a selective emitter, (*3*) a photovoltaic cell, (*4*) a nonselective emitter, and (*5*) an optical filter.

with selective emitters are 20–25% at an operating temperature of the emitter of 1300–1500°C. Further improvement and optimization of both the system as a whole and its separate components can be accomplished using cascade heterostructures and a rear reflector and by developing new types of emitters and filters. All these methods together make it possible to increase the efficiency of photovoltaic conversion to 35–40% [2].

As was mentioned above, one of the ways of reducing the losses in a TPV generator is related to the use of the energy of inefficient radiation ($\lambda > \lambda_g$) to maintain the temperature of the emitter that emits in a wide spectral range. To this end, an optical filter is introduced into a TPV system; this filter reflects the long-wavelength radiation that is not used in the photoconversion to the emitter, prevents the overheating of the photovoltaic cell, and reduces the expenditure of fuel spent on maintaining the high temperature of the emitter [1].

The recirculation of low-energy photons can also be attained by placing a "reflector" at the rear side of the photovoltaic cell, for example, by depositing a dielectric coating or a metal film onto the rear surface of the substrate [3].

TPV generators exhibit a number of advantages over other types of self-sustained sources of electrical power. For example, TPV generators have the following merits compared to electromechanical generators:

(i) a long service life due to the lack of moving parts;

(ii) a decrease in the level of pollution of the surrounding medium as a result of more complete and continuous burning of fuel;

(iii) noiseless operation; and

(iv) the possibility of operating with almost any types of fuel.

Compared to solar cells, TPV generators offer the prospect of round-the-clock operation (if combustible fuel is available), whereas earth-based solar cells typically operate for 40% of the time.

At the same time, solar radiation is an ecologically clean and easily available source of energy and has a high energy potential. The use of concentrated solar radiation in a TPV system as a source of heat (instead of combustible fuel) is a promising way to increase the TPV conversion efficiency while preserving all the advantages of solar-radiation converters. The use of hybrid solar–fuel systems makes it possible to employ TPV generators around the clock: the fuel-based TPV generator is used during the night and the solar TPV system is used during daytime.

Owing to the fact that the radiation source can be very close to the photovoltaic cell in the case of TPV conversion, it becomes possible to attain an electrical-power density in the range 2–10 W/cm^2 [4]. Thus, the actually attainable specific energy output from the photoconverter surface in a TPV generator is in the range 20–100 (kW h)/cm^2 per year, which exceeds the average specific energy output from the surface of ground-based solar cells.

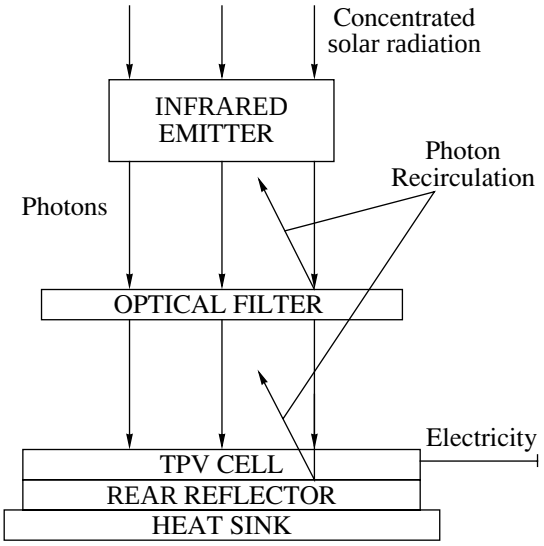

Fig. 2. Main components and processes in a solar thermophotovoltaic cell system.

2. SOLAR THERMOPHOTOVOLTAIC CONVERSION SYSTEMS

The efficiency of photovoltaic cells that convert solar energy into electricity is controlled by two factors that cannot be changed: the solar spectrum and the remoteness of the photovoltaic cell from the energy source. As a consequence of the latter factor, feedback between the photovoltaic converter and the sun is rendered impossible. In this situation, the only variable parameter is the degree of concentration of solar radiation incident on the photovoltaic cell (i.e., the density of operating current through the *p–n* junction). In a TPV system, there is a much larger number of degrees of freedom (Fig. 2): the choice of the IR-radiation source, the material of the photovoltaic cell, and the possibilities of using an optical filter and a rear reflector for recirculation of photons with energies lower than the band gap of the photovoltaic cell material.

There are a number of features common to photovoltaic and thermophotovoltaic systems [6–12]. One of the main similarities is the fact that the energy source has a wide spectrum in both systems. Consequently, the most widespread method for increasing the efficiency of photovoltaic solar cells (the use of cascade photoconverters with several *p–n* junctions) can also be employed to increase the efficiency of solar TPV generators. Narrow-gap materials with E_g = 0.4–0.8 eV are most suitable for fabricating a tandem (cascade) of TPV cells. This range of band gaps may be covered by photovoltaic cells based on GaSb (E_g = 0.7 eV), InGaAs (E_g = 0.75 eV), Ge (E_g = 0.66 eV), and quaternary solid solutions InGaAsSb (E_g = 0.5–0.6 eV).

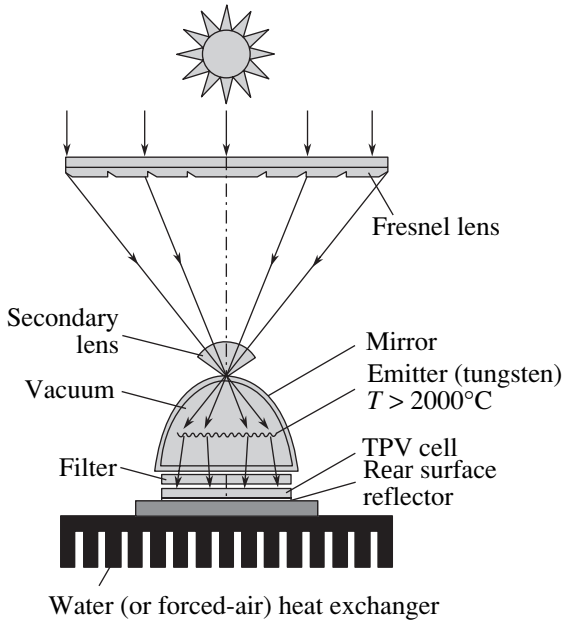

Fig. 3. Schematic representation of a solar thermophotovoltaic system with a high-temperature ($T > 2000$°C) vacuum emitter.

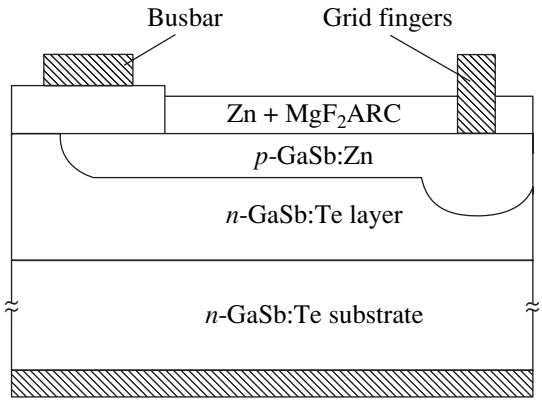

Fig. 4. Cross section of a GaSb epitaxial thermophotovoltaic cell fabricated using two-stage diffusion of zinc. ARC stands for antireflecton coating.

One of the ways of further increasing the efficiency of a solar TPV converter is related to the development of selective emitters matched to the band gap of the photovoltaic cell. A selective emitter must have an emission peak at $h\nu > E_g$ and feature a relatively low emission intensity at longer wavelengths.

The similar problem of matching the emission spectra of emitters to the photosensitivity spectra of photovoltaic cells can be solved using a selective filter installed between the photon emitter and the photovoltaic cell (or on the surface of the photovoltaic cell) in order to reflect the long-wavelength radiation back to the emitter. The photovoltaic cell itself can play the part of this filter if there is a mirror that reflects the radiation that is unabsorbed in the cell material and is formed on the rear surface of the photovoltaic cell. Finally, a selective high-temperature multilayer coating that reflects the long-wavelength radiation can be deposited directly onto the surface of the photon emitter.

We can identify three types of feasible design of solar TPV converters:

(i) converters with a solar high-temperature (1500–2000°C) "vacuum lamp" that plays the part of the emitter (Fig. 3);

(ii) a hybrid solar–fuel system; and

(iii) hybrid systems in which the solar photovoltaic cell converts the visible component of the solar radiation, while the TPV system converts the IR spectral component.

One of the possible structures of the solar TPV system shown in Fig. 3 includes a solar-radiation concentrator (a Fresnel lens and a secondary lens) and an emitter made of tungsten. Calculations show that a decrease in the optical losses to 10% makes it possible to increase the efficiency of a TPV system to at least 30%.

3. THERMOPHOTOVOLTAIC CONVERTERS BASED ON GaSb

The structures of photovoltaic cells based on gallium antimonide were formed using low-temperature diffusion of zinc from the gas phase in a quasi-closed volume. Zinc is a shallow-level acceptor and is often used to dope III–V semiconductors because it is fairly volatile and highly soluble in the solid phase. In addition to high-purity zinc as the diffusion source, we also used high-purity antimony in order to provide an excess pressure that suppressed the surface dissociation of gallium antimonide. Single-crystal *n*-GaSb wafers oriented in the (100) plane and doped with Te to a concentration of $(2–4) \times 10^{17}$ cm^{-3} were used as substrates.

The output characteristics of photoconverters depend to a great extent on the quality of the starting material. Epitaxial layers have undoubtedly a higher purity and a higher morphological quality compared to the material of the substrate onto which the layers are deposited. Introduction of an epitaxial *n*-GaSb layer into the structure of the photovoltaic cell makes it possible to improve the reproducibility of the device parameters, reduce the concentration of background residual impurities, and reduce the effect of intrinsic point defects in the structure.

The photovoltaic cells were fabricated using two-stage diffusion (Fig. 4). A photoactive region with a thickness of 0.3–0.5 μm was formed as a result of the first diffusion for $t = 25–30$ min at $T = 450–470$°C. The second independent diffusion of Zn for $t = 40–45$ min at $T = 480–520$°C made it possible to increase the *p*–*n*-junction depth to 0.8–1.0 μm beneath the contacts to be formed in order to reduce the leakage currents after the operation of fusing the metallic contacts.

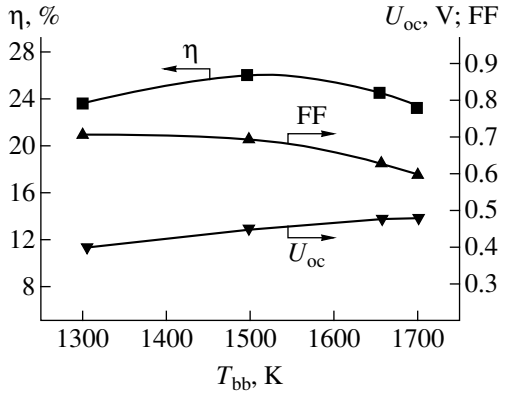

Fig. 5. Dependences of the efficiency (η), the filling factor for the *I–V* characteristic (FF), and the open-circuit voltage (U_{oc}) for the thermophotovoltaic cells based on GaSb on the emitter temperature for the blackbody spectrum cut off in the region λ > 1820 nm under the condition that 100% of the photons with energies $h\nu < E_g$ are reflected back to the emitter from the rear mirror of the cell.

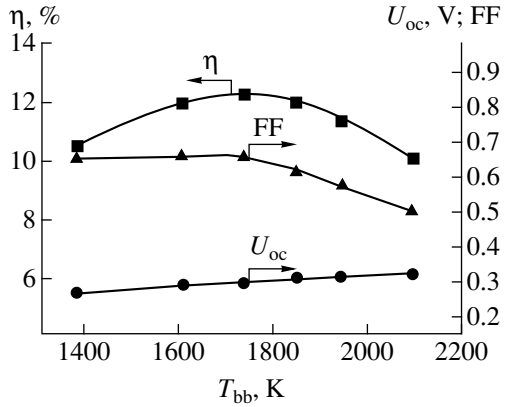

Fig. 6. Dependences of the efficiency (η), the filling factor for the *I–V* characteristic (FF), and the open-circuit voltage (U_{oc}) for the thermophotovoltaic cells based on Ge on the emitter temperature for the blackbody spectrum cut off in the region λ > 1820 nm under the condition that 100% of the photons with energies $h\nu < E_g$ are returned to the emitter as a result of reflection from the rear-surface mirror of the cell.

We studied the effect of the buffer epitaxial layer on the external quantum yield for photovoltaic cells fabricated using the Ga, Pb, and Sb solution–melts [13, 14]. The largest values of the external quantum yield were attained in the cells with an epitaxial layer formed from a Ga melt at growth temperatures of 450–400°C. The values of the external quantum efficiency were as large as 0.94–0.97 in the wavelength range λ = 1.3–1.7 μm and were equal to 0.9–0.93 for λ = 0.9–1.3 μm [15]. The photocurrent density was as high as 54 mA/cm^2 for the AM0 spectrum cut off at a wavelength λ < 900 nm.

The area of the cells varied from 1 to 2 cm^2. The cells with an area of 1 cm^2 had the following characteristics at the short-circuit current I_{sc} = 1 A: U_{oc} = 0.42–0.45 V and the filling factor of the current–voltage (*I–V*) characteristic FF = 0.7–0.72.

In Fig. 5, we show the values of FF, U_{oc}, and the efficiency of the fabricated TPV cells based on gallium antimonide in relation to the emitter temperature (absolute blackbody whose spectrum is cut off in the region λ > 1820 nm) in the case of 100% return of photons with $h\nu < E_g$ from the rear surface of the cells to the emitter.

We fabricated a TPV generator on the basis of 15 cells that each had an area of 1 × 2 cm^2. The output power of the generator was 7 W (at a photocurrent of 2 A); the generator included a metallic emitter heated to *T* = 1250°C using a gaseous (propane-based) torch.

4. THERMOPHOTOVOLTAIC CONVERTERS BASED ON Ge AND GaAs/Ge

The technology of fabrication of a narrow-gap converter based on Ge included zinc diffusion from the gaseous phase. Taking into account the published data on the zinc diffusion coefficient in germanium, we ascertained the conditions for obtaining the optimal depth of the *p–n* junction for a narrow-gap TPV converter based on germanium. The photocurrent density was 56.5 mA/cm^2 in the wavelength range 500–1820 nm for the best photovoltaic cell and was as high as 33.2 mA/cm^2 in the range 900–1820 nm when recalculated in terms of the active surface area exposed to unconcentrated solar radiation with the AM0 spectrum.

In Fig. 6, we show the values of FF, the open-circuit voltage U_{oc}, and the efficiency for the germanium-based TPV cell in relation to the emitter temperature (absolute blackbody whose spectrum is cut off at λ > 1820 nm) under the condition that 100% of the low-energy photons are reflected back to the emitter from the rear surface of the cells.

Further attempts to optimize the above TPV converters based on Ge rely on studies of the effect of the wide-gap GaAs window at the surface of Ge cells on the open-circuit voltage. We developed low-temperature liquid-phase epitaxy of a thin (~0.1 μm) layer of a GaAs window on a Ge substrate [3, 16]. The epitaxy was carried out at a temperature of 380°C from a supercooled liquid phase with a relatively low cooling rate of 2 K/s. Lead was chosen as the metallic solvent, which ensured a low solubility of germanium.

In Fig. 7, we show the dependences of the filling factor FF of the *I–V* characteristic, the open-circuit voltage U_{oc}, and the efficiency for TPV cells based on a GaAs/Ge heterostructure on the emitter temperature (an absolute blackbody whose spectrum is cut off at λ > 1820 nm) under the condition that 100% of photons with $h\nu < E_g$ are reflected from the rear surface of the cell to the emitter.

Recently, interest has grown considerably in GaAs crystallization on Ge substrates employing metal-organic chemical vapor deposition (MOCVD) to fabricate the cascade solar cells. A number of studies have been concerned with fabrication of two-cascade

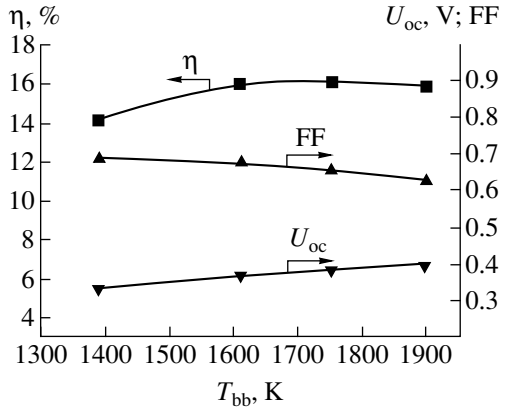

Fig. 7. Dependences of the efficiency (η), the filling factor for an *I–V* characteristic (FF), and the open-circuit voltage (U_{oc}) for the GaAs/Ge cells obtained by liquid-phase epitaxy on the emitter temperature for the blackbody-radiation spectrum cut off in the region $\lambda > 1820$ nm under the condition that 100% of the photons with energies $h\nu < E_g$ are returned back to the emitter as a result of reflection from the rear-surface mirror of the cell.

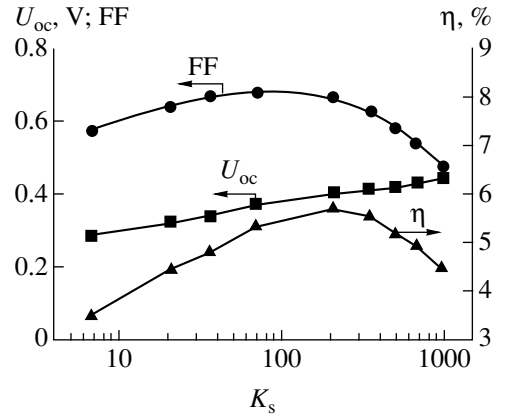

Fig. 8. Dependences of the filling factor for the *I–V* characteristic (FF), the open-circuit voltage (U_{oc}), and the calculated efficiency (η) on the degree of the solar-radiation concentration K_s (for illumination through a GaAs filter and for the AM0 spectrum) for a photovoltaic converter based on GaAs/Ge heterostructures grown using MOCVD.

GaAs/Ge and three-cascade GaInP/GaAs/Ge solar cells on Ge. Although the main characteristics of both the entire cascade solar cell and the lower Ge layer have been improved significantly, the potential of Ge has not yet been realized in full, since the parameters of the *p–n* junction formed in Ge owing to the diffusion of Ga and As from the gaseous phase are rather difficult to stabilize in the course of MOCVD. For example, the open-circuit voltage and the *p–n* junction depth depend heavily on the starting growth temperature. Therefore, a more dependable method for forming a *p–n* junction in germanium is the intentional diffusion of acceptor atoms (for example, those of Zn) into the *n*-Ge substrate. Such a diffusion ensures both the formation of a rather deep *p–n* junction required for efficient conversion of infrared radiation in a TPV cell and the suppression of a "parasitic" junction formed owing to the Ga diffusion.

According to the published data [17], the diffusion depth of As in Ge is equal to several micrometers, whereas the diffusion depth of Ga in Ge is equal to tenths of a micrometer. In connection with the fact that the rate of diffusion of arsenic and gallium decreases with decreasing growth temperature, the temperature of GaAs growth was successively decreased in this study from 680 to 550°C, which ensured a decrease in the coefficient of diffusion from the growing layer by approximately two orders of magnitude [18].

In Fig. 8, we show the dependences of the filling factor (FF) for the *I–V* characteristic, the open-circuit voltage U_{oc}, and the efficiency of a photovoltaic cell based on a GaAs/Ge heterostructure grown by MOCVD at a temperature of 590°C on the degree of concentration K_s of solar radiation [19]. The efficiency of the photovoltaic cell attains its largest value (5.5–5.7% at $K_s = 200$), which exceeds the previously reported values by a factor of almost 2.

5. CONCLUSION

We showed that solar thermophotovoltaic (TPV) systems offer a number of advantages over other self-contained sources of electric power. The external quantum yield of TPV cells based on GaSb was equal to 90–95%. At the blackbody-radiation temperature $T_{bb} = 1473$ K, the following parameters are attained for the above cells: open-circuit voltage $U_{oc} = 0.52$ V and FF = 0.68 at $I_{sc} = 4.5$ A/cm^2. These parameters ensured that the quantum efficiency was equal to 25% for GaSb on the assumption that 100% of the photons with $h\nu < E_g$ ($\lambda > 1.82$ μm) are reflected back to the emitter.

The efficiency $\eta = 16\%$ was attained in Ge-based cells with $U_{oc} = 0.36$ V, FF = 0.6, and a photocurrent density of 3.8 A/cm^2 ($T_{bb} = 1500$ K) under the condition that 100% of the photons with $h\nu < E_g$ were reflected back to the emitter.

REFERENCES

1. A. W. Bett, S. Keser, G. Stollwerck, and O. V. Sulima, in *Proceedings of 14th European Photovoltaic Solar Energy Conference* (Barcelona, Spain, 1997).
2. K. W. Stone, N. S. Fatemi, L. M. Garverick, *et al.*, in *Proceedings of 25th IEEE Photovoltaic Specialists Conference, Washington, 1996* (IEEE, New York, 1996), p. 1421.
3. V. M. Andreev, V. P. Khvostikov, O. A. Khvostikova, *et al.*, in *Proceedings of 17th European Photovoltaic Solar Energy Conference* (Munich, Germany, 2001), p. 219.
4. T. J. Coutts, M. W. Wanlass, J. S. Ward, and S. Johnson, in *Proceedings of 25th IEEE Photovoltaic Specialists Conference, Washington, 1996* (IEEE, New York, 1996), p. 25.

5. J. L. Gray and A. El-Husseini, in *Proceedings of 2nd NREL Conference on Thermophotovoltaic Generation of Electricity* (Colorado Springs, USA, 1995), p. 3.
6. H. Yugami, H. Sai, K. Nakamura, *et al.*, in *Proceedings of 28th IEEE Photovoltaic Specialists Conference, Anchorage, Alaska, 2000* (IEEE, New York, 2000), p. 1214.
7. N.-P. Harder and P. Wufel, Semicond. Sci. Technol. **18** (5), S151 (2003), Special Issue on Thermophotovoltaics, Ed. by K. Barnham, J. Connoly, and C. Rohr.
8. I. Tobias and A. Luque, IEEE Trans. Electron Devices **49**, 2024 (2002).
9. T. J. Coutts, M. W. Wanlass, J. S. Ward, and S. Johnson, in *Proceedings of 25th IEEE Photovoltaic Specialists Conference, Washington, 1996* (IEEE, New York, 1996), p. 25.
10. J. Aschaber, C. Herbling, and J. Luther, Semicond. Sci. Technol. **18** (5), S158 (2003), Special Issue on Thermophotovoltaics, Ed. by K. Barnham, J. Connoly, and C. Rohr.
11. L. M. Fraas, J. E. Avery, H. X. Huang, and R. V. Martinelli, Semicond. Sci. Technol. **18** (5), S165 (2003), Special Issue on Thermophotovoltaics, Ed. by K. Barnham, J. Connoly, and C. Rohr.
12. V. D. Rumyantsev, in *Proceedings of 2nd Workshop on the Path to Ultra-High Efficient Photovoltaics* (JRC Ispra, Italy, 2002), p. 133.
13. V. D. Rumyantsev, V. P. Khvostikov, S. V. Sorokina, *et al.*, in *Proceedings of 4th NREL Conference on Thermophotovoltaic Generation of Electricity,* Ed. by T. J. Coutts, C. S. Allman, and J. P. Benner (AIP, New York, 1999), AIP Conf. Proc., Vol. 460, p. 384.
14. V. M. Andreev, V. P. Khvostikov, V. D. Rumyantsev, *et al.*, in *Proceedings of 28th IEEE Photovoltaic Specialists Conference, Anchorage, Alaska, 2000* (IEEE, New York, 2000), p. 1265.
15. V. M. Andreev, V. P. Khvostikov, V. R. Larionov, *et al.*, in *Proceedings of 2nd World Conference and Exhibition on Photovoltaic Solar Energy Conversion* (Vienna, 1998), p. 330.
16. V. M. Andreev, V. P. Khvostikov, O. A. Khvostikova, and E. V. Oliva, in *Proceedings of 5th Conference on Thermophotovoltaic Generation of Electricity,* Ed. by T. J. Coutts, G. Guazzoni, and J. Luther (AIP, New York, 2003), AIP Conf. Proc., Vol. 653, p. 383.
17. S. P. Tobin, S. M. Vernon, C. Bajgar, *et al.*, IEEE Electron Device Lett. **9**, 405 (1988).
18. B. I. Boltaks, *Diffusion in Semiconductors* (Fizmatgiz, Moscow, 1961; Academic, New York, 1963).
19. V. M. Andreev, V. P. Khvostikov, N. A. Kalyuzhnyĭ, *et al.*, Fiz. Tekh. Poluprovodn. (St. Petersburg) **38**, 369 (2004) [Semiconductors **38**, 355 (2004)].

Translated by A. Spitsyn

Semiconductors, Vol. 38, No. 8, 2004, pp. 956–961. From Fizika i Tekhnika Poluprovodnikov, Vol. 38, No. 8, 2004, pp. 994–999.

SYMPOSIUM ON THE EFFICIENT USE OF SOLAR RADIATION IN PHOTOVOLTAIC POWER ENGINEERING (St. Petersburg, November 3–4, 2003)

Japanese Programs on Novel Concepts in PV[1]

M. Yamaguchi[1], T. Takamoto[2], K. Araki[3], and M. Imaizumi[4]

[1]*Toyota Technological Institute, 2-12 Hisakata, Tempaku, Nagoya 468-8511, Japan*
e-mail: masafumi@toyota-ti.ac.jp
[2]*Sharp Corporation, Hajikami, Shinjo, Nara 639-2198, Japan*
[3]*Daido Steel Corporation, Daido-cho, Minami, Nagoya 457-8545, Japan*
[4]*NASDA, Sengen, Tsukuba, Ibaraki 305-8505, Japan*

Submitted February 9, 2004; accepted for publication February 11, 2004

Abstract—Japanese R&D activities in photovoltaics (PV) and our R&D activities with III–V compound multijunction (MJ) solar cells are presented. We have realized high-efficiency InGaP/InGaAs triple-junction solar cells with an efficiency of 36.5–37% (AM1.5G, 200 suns) and concentrator triple-junction solar cell modules with an outdoor efficiency of 27% as a result of designing a grid structure, developing low optical loss Fresnel lens and homogenizers, and designing low thermal conductivity modules. Our challenge now is to develop low-cost and high output power concentrator MJ solar cell modules with an output power of 400 W/m^2 for terrestrial applications. © *2004 MAIK "Nauka/Interperiodica".*

1. PV R&D PROGRAMS IN JAPAN

Table 1 shows the photovoltaics (PV) roadmap until 2030 (long-term targets for developing large-scale PV power generation technology in Japan). The target by 2039 is to develop PV technology for realizing an electricity cost of 5–6 Japanese yen/kWh, which corresponds to the electricity generation cost of the present nuclear and fossil fuel power generation systems in Japan. Recently, METI (Ministry of Economics, International Trade, and Industry in Japan) revised the New Energy Supply Outlook based on an interim report by the New Energy Subcommittee for the Advisory Committee for Energy. The latest target for PV installation in FY (fiscal year) 2010 is 4.82 GW. To accomplish the target, greater efforts in PV technology to realize about one order higher PV module production and PV system installation are necessary.

To achieve these long-term targets, a new five-year PV R&D program was started in FY 2001 aimed at achieving these targets. The new PV R&D program consists of four projects, namely, "Development of Advanced Manufacturing Technology" (budget in FY 2003 is 7.9 million euro), "Development of Advanced Solar Cells and Modules" (21.7 million euro), "Investigation for Innovative PV Technology" (11.1 million euro), and "Technology Development for Future Mass Deployment" (8.5 million euro).

The project "Development of Advanced Solar Cell Modules" consists of three R&D themes: (1) "Si-based Thin Film Solar Cell Modules," (2) "CIS-based Thin Film Solar Cell Modules," and (3) "Superhigh Efficiency Compound Solar Cells." The target of this project is to develop advanced solar cell module technologies to reduce mass production costs of PV modules to less than 100 yen/W. The target of R&D for "Si-based Thin Film Solar Cell Modules" is to realize 12% efficiency with a 3600 cm^2 module by the end of FY 2005. Kaneka and Mitsubishi Heavy Industries are taking part in this R&D. The target of R&D for "CIS-based Thin Film Solar Cell Modules" is to realize 13% efficiency with a 3600 cm^2 module. Showa Shell Sekiyu and Matsushita Electric are taking part in this R&D. The target of R&D for "Superhigh Efficiency Compound Solar Cells and Modules" is to realize 40% efficiency under concentrator operation. Sharp, Daido Steel, and Daido Metal are taking part in this R&D.

The aim of the project "Investigation for Innovative PV Technology" is to develop innovative PV technologies to realize a drastic reduction in the manufacturing cost of solar cell modules to as low as 15 yen/kWh. This project seeds investigations consisting of (1) novel materials, (2) novel structures, and (3) novel manufacturing processes, and about 20 themes are being investigated. For novel materials, SiGe, $FeSi_2$, carbon, organic semiconductor, wide-band-gap chalcopyrite, and new nitride material solar cells are being investigated. As novel structures, nanostructure Si, spherical Si, advanced light-trapping thin film, wide-band-gap microcrystalline SiC, and dye-sensitized solar cells are also being studied. In addition, Si cell technology with CAT-CVD, a CIS thin film cell by electroplating, and Si thin film cells by lateral growth are being investigated for novel manufacturing processes.

2. R&D BACKGROUND OF MULTIJUNCTION SOLAR CELLS

Multijunction (tandem) solar cells have the potential to achieve high conversion efficiencies of over 40% and

[1]This article was submitted by the authors in English.

are promising for space and terrestrial applications. One of the authors started his research on AlGaAs/GaAs double-junction solar cells in 1982, and his group demonstrated 20.2% efficiency by proposing a double heterostructure tunnel junction as a subcell interconnection in 1987 [1]. In Japan, based on such an activity, an R&D project for "Superhigh Efficiency MJ Solar Cells" has been conducted with the support of NEDO since FY 1990 [2] as a long-term target for the early 21st century. In this project, challenges and efforts are being made in the development of superhigh efficiency solar cell technology that aims to dramatically increase conversion efficiency to over 40% and to develop innovational technologies. We have proposed an AlInP–InGaP double heterostructure (DH) top cell, a wide-band-gap InGaP DH tunnel junction for subcell interconnection, and a lattice-matched InGaAs middle cell. As a result of the above technological developments, mechanically stacked InGaP/GaAs/InGaAs triple-junction cells (1 cm^2) have reached the highest (1-sun world-record) efficiency of 33.3% at 1-sun AM1.5G following joint work by Japan Energy Co., Sumitomo Electric Co., and Toyota Technical Institute [3]. Since FY 2001, this R&D project has been shifted to the project for "Concentrator MJ Solar Cells and Modules."

In this paper, more recent results for high-efficiency III–V compound multijunction (MJ) solar cells and concentrator MJ solar cells and modules conducted under the New Sunshine Project in Japan are presented. The future prospects for superhigh-efficiency and low-cost MJ and concentrator cells and modules are also presented.

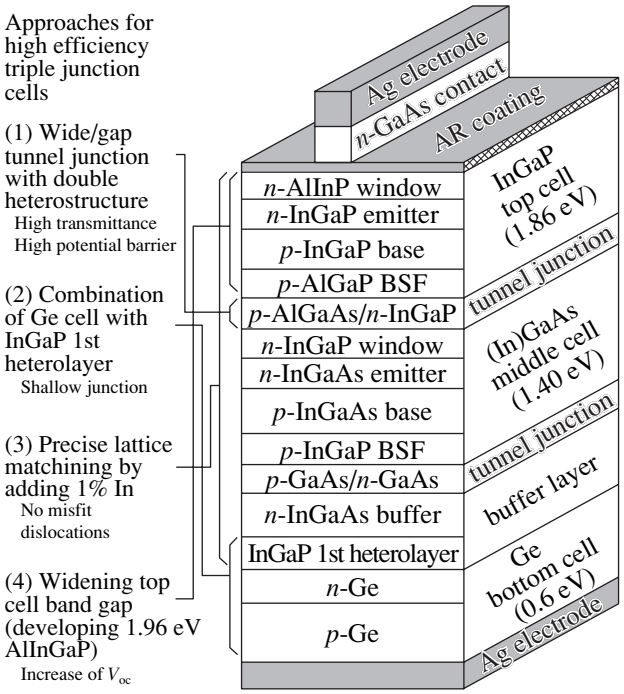

Fig. 1. Schematic illustration of a triple-junction cell and approaches for improving the efficiency of the cell. BSF is back surface field.

3. HIGH-EFFICIENCY MULTIJUNCTION SOLAR CELLS

The conversion efficiency of InGaP/GaAs-based multijunction solar cells has been improved by the following technologies. A schematic illustration of the InGaP(In)GaAs/Ge triple-junction solar cell and key technologies for improving conversion efficiency is shown in Fig. 1.

3.1. Wide-Band-Gap Tunnel Junction

A wide-band-gap tunnel junction which consists of a *p*-Al(Ga)InP/*p*-AlGaAs/*n*-(Al)InGaP/*n*-Al(Ga)InP double heterostructure increases incident light into the (In)GaAs middle cell and produces effective potential barriers for both minority carriers generated in the top and middle cells. The wide band-gap tunnel junction without absorption and recombination losses improves both V_{oc} and I_{sc} of the cells. It is difficult to obtain a high tunneling peak current with a wide gap tunnel junction, so thinning depletion layer width formation of a highly doped junction is quite necessary. Since impurity diffusion occurs during growth of the top cell [4], carbon and silicon, which have a low diffusion coefficient, are used for *p*-type AlGaAs and *n*-type (Al)InGaP, respectively. Furthermore, the double heterostructure is assumed to suppress impurity diffusion from the highly doped tunnel junction [5]. The second tunnel junction between middle and bottom cells consists of *p*-InGaP/*p*-(In)GaAs/*n*-(In)GaAs/*n*-InGaP, which have a wider band-gap than the middle cell materials.

3.2. InGaP/Ge Heteroface Structure Bottom Cell

InGaP/GaAs cell layers are grown from a *p*-type Ge substrate. A *p–n* junction is formed automatically dur-

Table 1. Japanese PV roadmap until 2030

	2000	2005	2010	2020	2030
Manufacturing cost of modules, yen/W	140	100	75	50	30
Technology development (assuming 100 MW/year production)	–	140	100	75	50
Generation cost of electricity, yen/kWh	70	30	25	10–15	5–10
PV systems installed (cumulative), GW	–	–	4.82	23–35	52–82

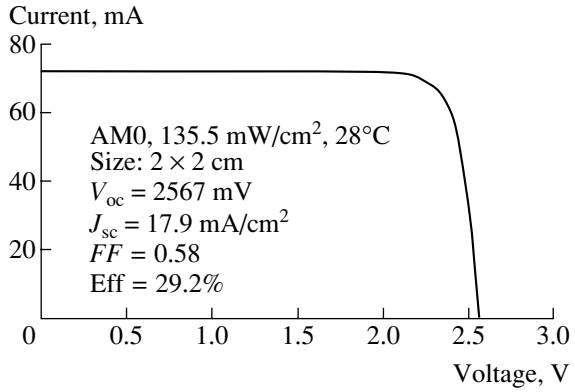

Fig. 2. AM0 *I–V* curve of an InGaP/InGaAs/Ge triple-junction solar cell.

ing MOCVD growth by the diffusion of a V group atom from the first layer grown on the Ge substrate. So the material of the first heterolayer is important for the performance of the Ge bottom cell. An InGaP layer is thought to be a suitable material for the first heterolayer, because phosphor has a lower diffusion coefficient in Ge than arsenic and indium has a lower solubility in Ge than gallium. The quantum efficiency of the Ge bottom cell was improved by the InGaP heterogrowth layer. In the case of a GaAs heterogrowth layer, junction depth was measured as around 1 μm. On the other hand, the thickness of *n*-type layer produced by phosphor from the InGaP layer was 0.1 μm. An increase in Ge quantum efficiency was confirmed to be due to a reduction in junction depth.

It was found that the absorption edge of the InGaP top cell shifted to the longer wavelength region by using the InGaP first heterolayer. The band gap of the InGaP top cell reduced from 1.86 to 1.81 eV by changing the heterogrowth layer from GaAs to InGaP. The fact that the band gap increased as the growth temperature increased indicated this phenomenon was due to the ordering effect in the InGaP material [6]. Since the band-gap narrowing of the top cell decreases V_{oc} of the triple-junction cell, an approach for growth of ordering InGaP less should be necessary. As a matter of a fact, the conversion efficiency has been improved up to 30% (AM0) by increasing the top cell band gap up to 1.89 eV [7].

Table 2. Characteristics and predicted efficiencies (Eff) of the triple-junction cells

InGaP (E_g = 1.82 eV)				
V_{oc} (mV)	J_{sc} (mA/cm^2)	*FF*	Eff (%)	Condition
2567	14.1	0.87	31.5	AM1.5G, 25°C
2568	17.9	0.86	29.2	AM0, 28°C
AlInGaP (E_g = 1.96 eV)				
V_{oc} (mV)	J_{sc} (mA/cm^2)	FF	Eff (%)	Condition
2720	14.1	0.87	33.3	AM1.5G, 25°C
2721	17.9	0.86	31	AM0, 28°C

3.3. Precise Lattice Matching to a Ge Substrate

Although the 0.08% lattice mismatch between GaAs and Ge was thought to be negligibly small, misfit dislocations were generated in thick GaAs layers and deteriorated cell performance. By adding about 1% indium to the InGaP/GaAs cell layers, all cell layers are lattice-matched precisely to the Ge substrate. As a result, the crosshatch pattern caused by misfit dislocation due to lattice mismatch disappeared in the surface morphology of the cell with 1% indium. The misfit dislocations were found to influence not I_{sc} but V_{oc} of the cell. V_{oc} was improved by eliminating misfit dislocations for the cell with 1% indium. In addition, the wavelength of the absorption edge became longer and I_{sc} of both top and middle cells increased, by adding 1% indium.

3.4. Widening of Top Cell Band Gap by AlInGaP

Now, we are developing AlInGaP top cells in order to improve V_{oc} of the triple-junction cells. Current matching between top and middle cells should be done by controlling the top cell band gap instead of thinning the top cell. In this case, V_{oc} of the cell can be increased while maintaining the maximum current. An AlInGaP cell with a 1.96-eV band gap and 2.5-μm thickness was found to attain a high V_{oc} of 1.5 V while keeping the same I_{sc} as the conventional InGaP top cells under condition AM1.5G. For condition AM0, a further increase in the band gap to about 2.0–2.03 eV is required for the AlInGaP cells, although that is dependent on the current matching requirement from the beginning of life (BOL) to the end of life (EOL).

The best data on the triple-junction cells in our laboratory are summarized in Table 2. The technologies described above (Sections 3.1–3.3) were applied to the fabrication of the triple-junction cells. A band gap of the InGaP top cell of about 1.82 eV is still low. By using an AlInGaP top cell with 1.96 eV, a higher V_{oc} close to 2.72 V is predicted. Figure 2 shows an AM0 *I–V* curve of an InGaP/InGaAs/Ge fabricated solar cell. We have demonstrated 31.5–32% at 1-sun AM1.5G and 29.2–30% at 1-sun AM0 with InGaP/InGaAs/Ge triple-junction solar cells [8]. Conversion efficiencies over 33% (AM1.5G) and close to 31% (AM0) are expected for the (Al)InGaP/InGaAs/Ge triple-junction cells.

For approaches to the next generation of multijunction cells, one way is to optimize band gaps to utilize solar energy with a wide energy range above the Ge band gap. A lattice-mismatched AlInGaP(1.8 eV)/InGaAs(1.2 eV)/Ge(0.65 eV) triple-junction cell and a lattice-matched AlGaInP(2.0 eV)/GaAs(1.4 eV)/GaInNAs(1 eV)/Ge(0.65 eV) quadruple-junction cell are challenging structures. Another way is to increase junctions to utilize the high-energy range. Many thin junctions with contiguous band gaps can reduce energy

loss due to the difference between photon energy and band-gap energy. AlInGaP and InGaAsP lattice-matched to GaAs provide various band gaps and might establish high-efficiency cells.

4. HIGH-EFFICIENCY CONCENTRATOR MULTIJUNCTION SOLAR CELLS

The previous R&D project for high-efficiency MJ solar cells has now been taken over by Sharp Co., Daido Steel Co., and Daido Metal Co. and targeted to concentration application, also supported by NEDO. The new target is 40% efficiency with 500-sun concentration by the end of March 2006.

In order to apply a high-efficiency multijunction cell developed for 1-sun conditions to a concentrator cell operating under ~500-sun conditions, reduction in energy loss due to series resistance is the most important issue. Cell size was determined to be 7×7 mm taking into account the total current flow. Grid electrode pitching, height, and width were designed in order to reduce series resistance. Figure 3 shows *FF* of the cell with various grid pitching for 250 suns. A grid electrode with a 5-μm height and a 5-μm width was made of Ag. Grid pitching influences lateral resistance between two grids (R_L) and total electrode resistance (R_E). The series resistance of the cell (R_S), R_E, and R_L are also shown in Fig. 3. R_E was measured directly after removing the electrode from the cell by chemical etching. R_L was calculated by using the sheet resistance of the window and emitter layers. Based on the data in Fig. 3, the grid pitching is determined to be 0.12 mm at this time. In order to reduce the series resistance to 0.01 Ω and obtain high *FF* at 500 suns, the grid height should be increased twofold. The high efficiency at <500 suns is thought to be obtained by the optimal grid design without modification of the cell layer structure, such as emitter thickness and tunnel junction thickness, of the cell developed for 1-sun conditions.

Figure 4 shows the efficiency of a concentrator cell as a function of the concentration ratio. The concentration ratio is defined by the increase in I_{sc}, the I_{sc}/I_{sc}(1-sun) ratio. High conversion efficiency over 36% is measured under concentrated light with a concentration ratio ranging from 100 to 500 suns. At a concentration ratio of 200 suns, the conversion efficiency was measured as 36.5%. The decrease in efficiency is due to a decrease in *FF*, so a reduction in the series resistance is necessary to obtain high *FF* with a high-concentration ratio. A little decrease in V_{oc} under concentrated light over 100 suns is caused by an increase in the cell temperature during irradiation of the light.

5. HIGH-EFFICIENCY AND LOW-COST CONCENTRATOR MULTIJUNCTION CELL MODULES

R&D in Japan on III–V concentrator cells is now done mainly with triple-junction monolithic modules. Besides the cells, extensive studies are done in (1) non-imaging Fresnel concentrators, (2) homogenizers, and (3) new and simple module design [9].

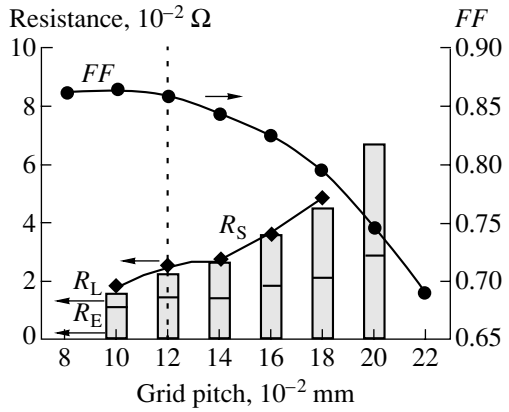

Fig. 3. *FF* of the concentrator cells with various grid pitching under 250-sun light. Series resistance (R_S), lateral resistance (R_L), and total electrode resistance (R_E) are also shown.

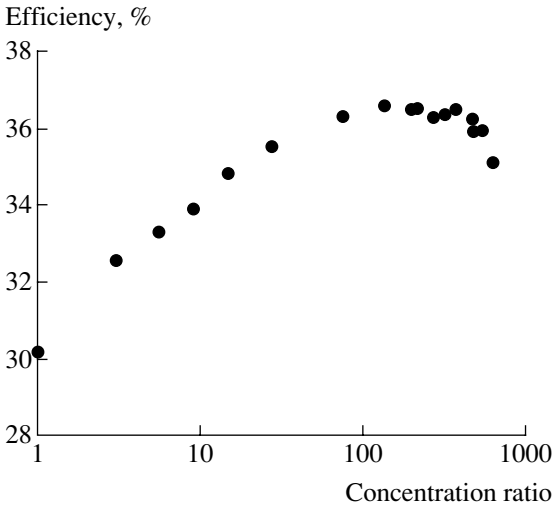

Fig. 4. Efficiency of an InGaP/InGaAs/Ge concentrator triple-junction cell as a function of concentration ratio.

A 400× and 7000 cm^2 concentrator module was fabricated with 36 pieces of the randomly selected receivers connected in series and the same number of the newly developed dome-shaped Fresnel lens. The module wall and not heat sinks dissipated the heat, and no external cooling utilities were used.

The efficiency on a hot summer day (35°C of ambient temperature) was 27.0% [10]. This value was well above the record efficiency of 22.7% established by the Fraunhofer Institute (Germany) in October 2002 with one order less area (768 cm^2). This achievement resulted from several new technologies:

(1) High-pressure and vacuum-free lamination of the solar cell that suppresses temperature rise only to 8°C with 400× geometrical concentration illumination of the sunbeam.

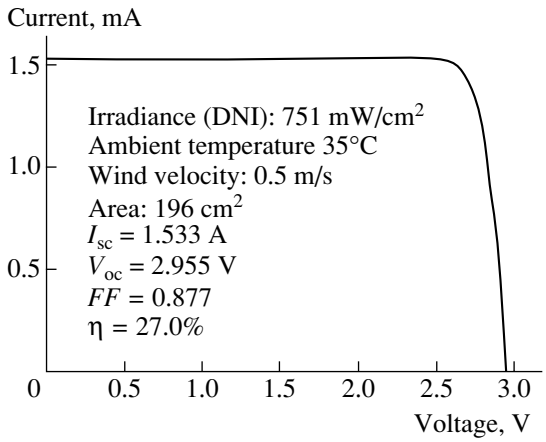

Fig. 5. Outdoor evaluation of *I–V* with a plastic Fresnel lens (including loss in concentrator optics and temperature rise).

(2) Direct and voids-free soldering technologies of a fat metal ribbon to solar cells that suppress hot spots and resistance by an output current that is 300 times higher than normal nonconcentration operation.

(3) A new encapsulating polymer that survives exposure to high-concentration UV light and heat cycles.

(4) Beam-shaping technologies that illuminate the square aperture of the solar cells from a round concentration spot.

(5) Homogenizer technologies that give uniform flux and prevent the conversion loss that stems from chromatic aberrations and surface voltage variation.

(6) Allowing as large as 1.75 mm assembly tolerance. There is no need for special optical alignment. Even local mechanical industries can assemble the main body.

(7) A shaped Fresnel lens designed by nonimaging optics theory and made by a low-cost injection mold that gives tight variation of optical efficiency as narrow as 0.5% (see Fig. 5).

The technological roadmap toward a 31% efficient module is shown in Table 3 [10]. Since we have identified detailed technological problems and how to solve them, the target will be achieved well in advance.

6. FUTURE PROSPECTS

Multijunction (MJ) solar cells will be widely used in space because of their high conversion efficiency and better radiation resistance. In order to apply superhigh-efficiency cells widely, it is necessary to improve their conversion efficiency and reduce their cost. Concentrator triple-junction and quadruple-junction solar cells have great potential for realizing a superhigh efficiency of over 40% [11]. As a triple-junction combination, an InGaP/InGaAs/Ge cell on a Ge substrate will be widely used because this system has already been developed. The quadruple-junction combination of an E_g = 2.0 eV top cell, a GaAs second-layer cell, a material third-layer cell with an E_g of 1.05 eV, and a Ge bottom cell is lattice matched to Ge substrates and has a theoretical 1-sun AM0 efficiency of about 42%. This system also has a potential of over 45% under 500-sun AM1.5 conditions.

Our challenge now is to develop low-cost high output power concentrator MJ solar cell modules with an output power of 400 W/m^2 for terrestrial applications.

Concentrator operation of the MJ cells is essential for their terrestrial applications. Since the concentrator PV systems have potential for cost reduction, R&D on concentrator technologies including MJ cells has started in Japan. Therefore, concentrator MJ and Si-crystal solar cells are expected to contribute to electricity cost reduction for widespread PV applications, as shown in Fig. 6 [12].

Figure 7 shows the correlation between AM0 and AM1.5 efficiencies for various solar cells. Therefore, high-efficiency MJ solar cells developed for terrestrial use can be applied in space solar cells. Another chal-

Table 3. Roadmap table for a module of more than 31% efficiency

	Technologies				
	in Nov. 2002	in Aug. 2003	in Mar. 2004	in Mar. 2005	in Mar. 2006
Cell efficiency (1 sun), %	30.1	30.3	32	–	–
Concentrator cell efficiency, %	34.4	35.3	37	–	40
Lens efficiency, %	72.4	85.4	85.8	–	91
Homogenizer efficiency, %	94.4	96.3	97.5	97.5	97.5
Ohmic loss in circuit, %	0.1	0.1	0.1	0.1	0.1
Spectrum mismatching loss, %	5.3	5.1	3	–	–
Current mismatching loss, %	3.7	3.7	2	2	2
Loss by temperature rise, %	1.2	1.3	1.3	–	1
Total efficiency, %	21.7	27.0	29	>29	>31

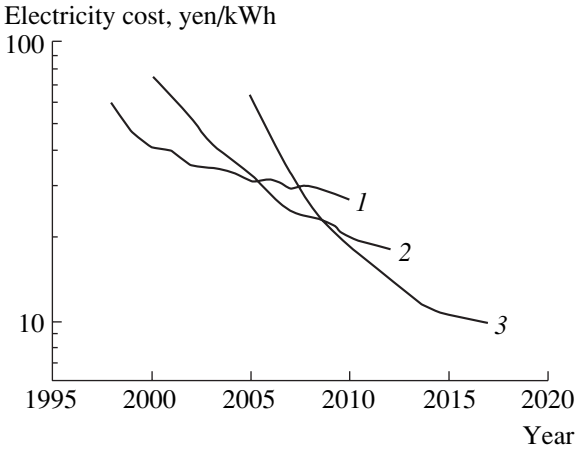

Fig. 6. Scenario of electricity cost reduction by developing concentrator solar cells; type of solar cell: (*1*) Si-crystal, (*2*) thin film, and (*3*) concentrator.

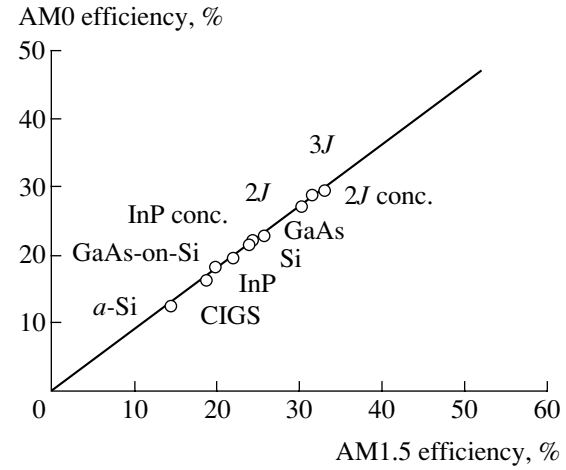

Fig. 7. Correlation between AM0 and AM1.5 efficiencies for various solar cells.

lenge we face is to develop high-efficiency, lightweight, and low-cost MJ solar cells for space applications.

7. SUMMARY

The conversion efficiency of InGaP/InGaAs/Ge cells has been improved up to 31–32% (AM1.5) and 29–30% (AM0) as a result of the development of technologies such as double wide band-gap tunnel heterojunctions, InGaP–Ge heterostructure bottom cells, and precise lattice-matching of the InGaAs middle cell to the Ge substrate by adding indium to a conventional GaAs layer. For concentrator applications, the grid structure has been designed in order to reduce the energy loss due to series resistance, and a 36.5–37% (AM1.5G, 200 suns) efficiency has been demonstrated. In addition, we have realized high-efficiency concentrator InGaP/InGaAs/Ge triple-junction solar cell modules with an outdoor efficiency of 27% as a result of developing high-efficiency InGaP/InGaAs/Ge triple-junction cells, designing a grid contact with low series resistance, developing nonimaging Fresnel lens and second optics (homogenizers) with low optical loss, and designing modules with low series resistance and low thermal conductivity.

Future prospects are also presented. We have proposed concentrator III–V compound MJ solar cells as the third-generation solar cells, in addition to first-generation Si-crystal solar cells and second-generation thin-film solar cells. Our challenge now is to develop low-cost and high output power concentrator MJ solar cell modules with an output power of 400 W/m^2 for terrestrial applications and high-efficiency, lightweight, and low-cost MJ solar cells for space applications.

ACKNOWLEDGMENTS

This work was partially supported by the New Energy and Industrial Technology Development Organization as part of the New Sunshine Program of the Ministry of International Trade and Industry, Japan. This work was also partially supported by the Japanese Ministry of Education, Culture, Sports, Science, and Technology as a part of the Private University Academic Frontier Center Program “Superhigh Efficiency Photovoltaic Research Center.”

REFERENCES

1. M. Yamaguchi, C. Amano, H. Sugiura, and A. Yamamoto, in *Proceedings of 19th IEEE Photovoltaic Specialists Conference* (IEEE, New York, 1987), p. 1484.
2. M. Yamaguchi and S. Wakamatsu, in *Proceedings of 25th IEEE Photovoltaic Specialists Conference, Washington, 1996* (IEEE, New York, 1996), p. 167.
3. T. Takamoto, E. Ikeda, T. Agui, *et al.*, in *Proceedings of 26th IEEE Photovoltaic Specialists Conference* (IEEE, New York, 1997), p. 1031.
4. H. Sugiura, C. Amano, A. Yamamoto, and M. Yamaguchi, Jpn. J. Appl. Phys. **27**, 269 (1988).
5. T. Takamoto, M. Yamaguchi, E. Ikeda, *et al.*, J. Appl. Phys. **85**, 1481 (1998).
6. A. Gomyo, T. Suzuki, K. Kobayashi, *et al.*, Appl. Phys. Lett. **50**, 673 (1987).
7. R. King, C. Fetzer, P. Colter, *et al.*, in *Proceedings of 29th IEEE Photovoltaic Specialists Conference, New Orleans, 2002* (IEEE, New York, 2002), p. 776.
8. T. Takamoto, T. Agui, K. Kamiura, *et al.*, in *Proceedings of 3rd World Conference on Photovoltaic Energy Conversion* (2003) (in press).
9. K. Araki, M. Kondo, H. Uozumi, and M. Yamaguchi, in *Proceedings of 3rd World Conference on Photovoltaic Energy Conversion* (2003) (in press).
10. K. Araki, M. Kondo, H. Uozumi, *et al.*, in *Proceedings of 14th International Photovoltaic Science and Engineering Conference* (in press).
11. M. Yamaguchi, in *Proceedings of 17th European Photovoltaic Solar Energy Conference* (WIP, Munich, Germany, 2002), p. 2144.
12. K. Araki and M. Yamaguchi (in press).

Semiconductors, Vol. 38, No. 8, 2004, pp. 962–969. From Fizika i Tekhnika Poluprovodnikov, Vol. 38, No. 8, 2004, pp. 1000–1006.

SYMPOSIUM ON THE EFFICIENT USE OF SOLAR RADIATION IN PHOTOVOLTAIC POWER ENGINEERING (St. Petersburg, November 3–4, 2003)

Modeling Improvement of Spectral Response of Solar Cells by Deployment of Spectral Converters Containing Semiconductor Nanocrystals[1]

W. G. J. H. M. van Sark[1], A. Meijerink[2], R. E. I. Schropp[2], J. A. M. van Roosmalen[3], and E. H. Lysen[4]

[1]*Copernicus Institute, Utrecht University, 3584 CH Utrecht, The Netherlands*
e-mail: w.g.j.h.m.vansark@chem.uu.nl
[2]*Debye Institute, Utrecht University, 3584 CC Utrecht, The Netherlands*
[3]*ECN Solar Energy, 1755 ZG Petten, The Netherlands*
[4]*Utrecht Centre for Energy Research (UCE), Utrecht University, 3584 CH Utrecht, The Netherlands*
Submitted February 16, 2004; accepted for publication February 16, 2004

Abstract—A planar converter containing quantum dots as wavelength-shifting moieties on top of a solar cell was studied. The highly efficient quantum dots are to shift the wavelengths where the spectral response of the solar cell is low to wavelengths where the spectral response is high in order to improve the conversion efficiency of the solar cell. It was calculated that quantum dots with an emission at 603 nm increase the multicrystalline solar cell short-circuit current by nearly 10%. Simulation results for planar converters on hydrogenated amorphous silicon solar cells show no beneficial effects, due to the high spectral response at low wavelength. © *2004 MAIK "Nauka/Interperiodica".*

1. INTRODUCTION

The fundamental spectral losses in a single-junction solar cell made of a semiconductor material such as silicon can be as large as 50%. This is a result of the mismatch between the incident solar spectrum and the spectral absorption properties of the material [1]. Large parts of the solar spectrum are not absorbed because of the existence of a band gap E_g of the material. Photons with energy E_{ph} larger than the band gap are absorbed, but the excess energy $E_{ph} - E_g$ is not used effectively due to thermalization of the electrons. Photons with $E_{ph} < E_g$ are not absorbed. Several routes have been proposed to overcome this intrinsic property of semiconductor solar cells and thereby increase the power output of solar cells. All these methods or concepts concentrate on a much better use of the solar spectrum and are in general referred to as third-generation photovoltaics [2].

Single-junction solar cells optimally perform under monochromatic light of a wavelength $\lambda_{opt} \simeq 1240/E_g$. For (multi)crystalline silicon (mc-Si) solar cells, λ_{opt} = 1100 nm (with E_g = 1.1 eV); for hydrogenated amorphous silicon (a-Si:H), the optimum wavelength is λ_{opt} = 700 nm (with E_g = 1.77 eV). As amorphous silicon solar cells only contain a thin absorber layer, the optimum spectrum response occurs at about 550 nm [3, 4]. The conversion efficiency of these types of cells measured at incident monochromatic light of 550 nm can be as high as 20%, in contrast to the observed AM1.5G efficiency of 10% [5]. In organic dye cells, the iodine in the electrolyte absorbs a part of the blue incident light, resulting in a decreased blue response [6].

Conversion of the incident solar spectrum to monochromatic light would greatly increase the observed efficiency. To this end, one needs to modify the energy of incident photons such that E_{ph} equals E_g or is slightly larger. To distinguish any modification of photon energy from the distinct terms down and up conversion, we will use the term spectral down conversion (SDC) or spectral up conversion (SUC) throughout this paper. Down conversion strictly is used for the conversion of exactly one high-energy photon to exactly two lower-energy photons, whereas up conversion is the conversion of exactly two low-energy photons to exactly one higher-energy photon.

Spectral down conversion was suggested in the 1970s to be used in so-called luminescent concentrators that were attached onto a solar cell [7–10]. In these concentrators, organic dye molecules absorb incident light and reemit this at a red-shifted wavelength. Internal reflection ensures collection of all the reemitted light in the underlying solar cells. It was suggested that a number of different organic dye molecules be used of which the reemitted light was matched for optimal conversion by different solar cells. This is similar to using a stack of multiple solar cells, each sensitive to a different part of the solar spectrum. The expected high efficiency in practice was not reached as a result of not being able to

[1]This article was submitted by the authors in English.

meet the stringent requirements for the organic dye molecules, such as high quantum efficiency and stability, and the transparency of collector materials in which the dye molecules were dispersed [7–10].

Recently, quantum dots (QDs) were proposed for use in luminescent concentrators instead of organic dye molecules [11–13]. Quantum dots are nanometer-sized semiconductor crystals of which the emission wavelength can be tuned by their size as a result of quantum confinement [14, 15]. The advantages of QDs with respect to organic dye molecules are their high brightness, stability, and quantum efficiency [16]. In addition, QDs absorb all the light of a wavelength smaller than the absorption maximum, in contrast to the small-band absorption of dye molecules. As an example, CdSe/ZnS core-shell QDs of 4 nm diameter have an emission maximum around 550 nm [17–19], which would be ideally suited for amorphous silicon solar cells.

A simple and potentially cheap way of employing the principle of SDC is to coat a solar cell with a transparent layer that contains a spectrum-shifting moiety. Such a planar spectral down converter can be applied to existing solar cells without modifications to the solar cell design. Hence, optimization of the converter can be done independently of the solar cell. Optimization of the converter should lead to an increase in the conversion efficiency of the solar cell. An 8% relative increase in conversion efficiency was reported in the case of a CdS/CdTe solar cell, where the coating in which a fluorescent coloring agent was introduced increased the sensitivity in the blue [20]. Recent results on coating a multicrystalline silicon solar cell indicate a 6% relative increase in conversion efficiency [21]. This species has an absorption band around 400 nm and a broad emission between 450 and 550 nm. As QDs have a much broader absorption, it is expected that in potential the deployment of QDs in planar converters could lead to relative efficiency increases of 20–30%. Besides QDs, other materials have been suggested such as rare-earth ions [22] and dendrimers [23]. A maximum increase of 22.8% was calculated for a thin film coating of $KMgF_3$ doped with Sm on top of a CdS/CdTe solar cell, while experimental results show an increase of 5% [24]. Spectral down conversion employing QDs in a polymer composite has been demonstrated in a light-emitting diode (LED) where a GaN LED was used as an excitation source (λ_{em} = 425 nm) for QDs emitting at 590 nm [25].

In this paper, we will explore the feasibility of QD use in planar converters on top of solar cells. First, a quick method is used to assess the effects of varying emission wavelength on solar cell performance using small-band QD emission spectra. Second, a more detailed method is used, where the effect of the incorporation of QDs in a plastic layer on the incident solar spectrum is determined. This includes different QD sizes (i.e., absorption/emission maxima) and concentrations. The modified spectrum is then used as input in solar cell simulation programs suited for either crystalline or amorphous silicon. We will study the effects of QD size (spectral properties) and concentration of the conversion efficiency and will determine the optimum for both the mc-Si and a-Si:H solar cell. As the spectral response of these types of cells differs, we expect that

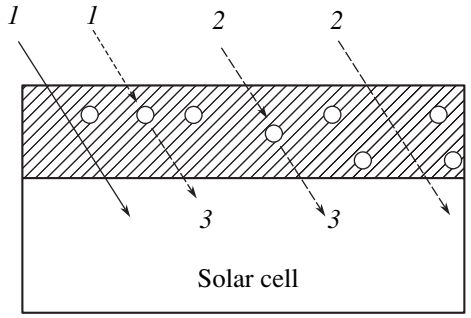

Fig. 1. Schematic drawing of the studied configuration. A plastic layer containing quantum dots is applied on top of a solar cell. Both blue (*1*) and green (*2*) light are absorbed by the quantum dot and reemitted in the red (*3*), which is subsequently absorbed in the solar cell. Also, unabsorbed blue and green light enters the solar cell as well.

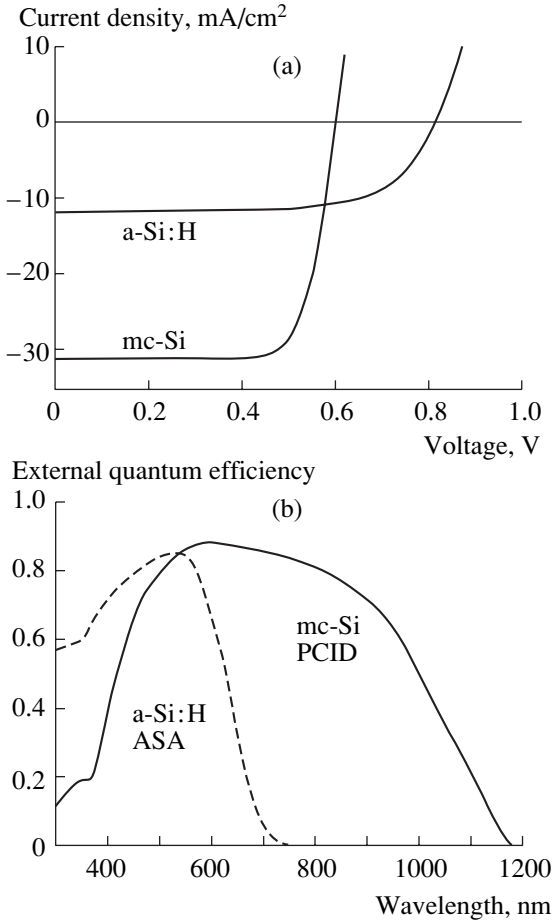

Fig. 2. Performance of the two solar cells, mc-Si and a-Si:H: (a) current–voltage characteristics, (b) spectral response.

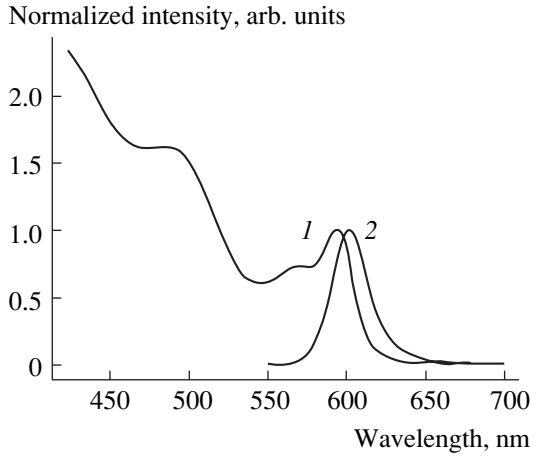

Fig. 3. Normalized absorption (*1*) and emission (*2*) spectrum of CdSe nanocrystals 4.3 nm in diameter, capped with TOPO/TOP/HDA (data from S.F. Wuister (2003); see also [30]).

the optimum combination of QD size and concentration will also differ.

2. METHODOLOGY

The configuration that is studied is depicted in Fig. 1. A plastic layer containing quantum dots is applied on top of a solar cell. The size of the quantum dots is chosen such that their emission maximum is in the red part of the spectrum; thus, they will absorb both blue and green incident light. We implicitly assume that the solar cell has an optimum spectral response in the red. Depending on the concentration of QDs, unabsorbed blue and green light also enters the solar cell. Of course, highly transparent plastics are to be used.

The effects of QDs in planar converters will be assessed on standard baseline solar cells that are reproducibly manufactured at ECN and Utrecht University. We will first describe the two types of solar cells under investigation, i.e., multicrystalline silicon and hydrogenated amorphous silicon. Their performance will be simulated under standard AM1.5G spectral conditions using software specifically designed for either material.

Inclusion of QDs in a planar converter on top of a solar cell leads to spectral changes. We will first study the effect of small-band emission spectra of QDs on the solar cell performance parameters. This will quickly show the potential benefits of QD use. Finally, a more thorough analysis will be carried out that includes the modifications of the AM1.5G spectrum due to QD absorption and emission.

Solar cell performance parameters calculated with PC1D (mc-Si) and ASA (a-Si:H)

	mc-Si	a-Si:H
I_{sc}, mA/cm^2	31.19	11.92
V_{oc}, V	0.6028	0.8135
FF	0.7707	0.6753
η, %	14.49	6.548

2.1. Solar Cell Configurations

The standard baseline n–p–p^+ mc-Si cell has parameters that are typical of low-cost commercial products, including series resistance, shunt conductance, and a second diode [26]. It measures 10×10 cm^2 in area and has a shallow diffused emitter of 50 Ω/sq. The thickness of the cell is 300 μm. The front broadband reflectance is 9% across the solar spectrum. The front surface is coated with a 71 nm thick silicon nitride antireflection coating with a refractive index $n = 2.1$. The thickness of the back-surface field (BSF) is 9 μm and has a p^+ doping level of 4×10^{18} cm^{-3}. The performance of the solar cell is simulated with the simulation program PC1D (version 5.8) [27, 28]. The calculated performance parameters (short-circuit current I_{sc}, open-circuit voltage V_{oc}, fill factor *FF*, efficiency η) are given in the table; the current–voltage characteristics and spectral response are shown in Fig. 2.

The standard baseline a-Si:H cell has the usual layer configuration glass/TCO/*p*-a-SiC:H/*i*-a-Si:H/*n*-a-Si:H/Ag, with layer thicknesses of 1 mm, 1 μm, and 8, 500, 20, and 200 nm, respectively [3]. TCO is a transparent conductive coating, such as SnO_2. Activation energies for the *n* and *p* layers are 0.24 and 0.46 eV, respectively. Solar cell performance is simulated with the program ASA (version 3.3), which includes specific features of amorphous semiconductors, such as sloped band edges and midgap dangling bond density models [3, 29]. The calculated performance is compared to the performance of the mc-Si cell in the table and Fig. 2.

2.2. Small-Band Spectrum

A simple approach that allows the selection of the most appropriate QD size entails simulation of solar cell performance employing small-band QD emission spectra alone. To this end, we used normalized emission spectra and scaled them such that the integrated spectral density was 500 W/m^2. A typical normalized emission spectrum is shown in Fig. 3 [30]. These scaled spectra were then used as input for the simulation programs PC1D and ASA. We varied the center emission wavelengths in 50 nm steps in the range 400–1000 nm and simulated solar cell performance.

2.3. Modified AM1.5G Spectrum

In the configuration shown in Fig. 1, the incident AM1.5G spectrum converted to an amount of photons per wavelength $\Phi_s(\lambda)$ will be modified by absorption of photons. First, the amount of absorbed photons $\Phi_a(\lambda)$ is determined from the QD absorption spectrum, which

depends on the QD size, their concentration in the converter layer, and the thickness of this layer. This absorbed amount is subtracted from the AM1.5G spectrum:

$$\Phi_{sa}(\lambda) = \Phi_s(\lambda) - \Phi_a(\lambda). \quad (1)$$

As the QDs reemit light at a red-shifted wavelength, the amount of emitted photons $\Phi_e(\lambda)$ is calculated from the QD emission spectrum. To this end, data for quantum efficiency is assumed, as well as the assumption that 3/4 of the emitted photons is directed towards the underlying solar cell due to internal reflection in the converter layer [13].

The amount of emitted photons is then added to the already modified AM1.5G spectrum:

$$\Phi_{sae}(\lambda) = \Phi_{sa}(\lambda) + \Phi_e(\lambda). \quad (2)$$

Finally, the resulting spectrum serves as input for the solar cell simulation models.

The most common approach to calculate absorption of photons is by using the Lambert–Beer equation: the photon flux density $\Phi(x, \lambda)$ after passing a distance x in a film with absorption coefficient $\alpha(\lambda)$ is reduced with a factor $\exp[-\alpha(\lambda)x]$, which can be written as

$$\Phi(x, \lambda) = \Phi^0(\lambda)\exp[-\alpha(\lambda)x], \quad (3)$$

where $\Phi^0(\lambda)$ is the incident photon flux density. The exponential term equals $\alpha(\lambda)x = \varepsilon_\lambda CD$, where ε_λ is the molar extinction coefficient (M^{-1} cm^{-1}), C is the chromophore concentration (M), and D is the thickness of the film (cm). The molar extinction coefficient can be measured directly or determined from measurement of the absorption spectrum (see below). The chromophore or QD concentration can be varied at will, from the nanomolar to the millimolar range. The thickness of the film (converter) will typically vary between about one micrometer and a few millimeters. In the following, we will describe in detail the followed procedure for QDs emitting at 603 nm.

Quantum dots of high quantum yield ($\eta_{em} = 0.8$) are routinely synthesized in our laboratory following a single-step route using trioctylphosphine oxide (TOPO) and hexadecylamine (HDA) [30]. The resulting typical (normalized) absorption $A_n(\lambda)$ and emission $E_n(\lambda)$ spectra are shown in Fig. 3. These spectra have been normalized with respect to the absorption and emission maximum occurring at 594 and 603 nm, respectively. The normalized absorption spectrum can be converted to a wavelength-dependent molar extinction coefficient but requires the determination of the QD concentration, which is cumbersome and time-consuming. Instead, we used the reported cubic relationship between the molar extinction coefficient and particle size as reported by Leatherdale *et al.* [31] (radius) and Schmelz *et al.* [32] (diameter). The particle diameter is determined from the absorption maximum at 594 nm using the relation between the absorption maximum and particle diameter reported in the literature [33–35], i.e., 4.24 nm in diameter. Thus, the QD radius a determined from experimental data is 2.12 nm. The absorption spectrum $A(\lambda)$ is scaled such that the molar extinction coefficient ε_λ at 350 nm equals $\varepsilon_\lambda(M^{-1}\ cm^{-1}) = (1.438 \times 10^{26})a^3$, as reported by Leatherdale *et al.* [31]. The calculated ε_λ at 350 nm is $\varepsilon_{350} = 1.37 \times 10^6\ M^{-1}\ cm^{-1}$. The data reported for the molar extinction coefficient by Schmelz *et al.* [32] give $\varepsilon_{602} = 2.65 \times 10^5\ M^{-1}\ cm^{-1}$ for their 4.5 nm diameter CdSe particle. From their data, one can infer that $\varepsilon_{602}/\varepsilon_{350} \approx 4.3$, so there is reasonable agreement with the data from Leatherdale *et al.* with only a difference of about 15% in ε_{350}.

The amount of absorbed photons $\Phi_{a,\,603}(D, \lambda)$ in the converter of thickness D and containing QDs of emission wavelength 603 nm is now

$$\Phi_{a,\,603}(D, \lambda) = \Phi_s(\lambda)\exp(-\varepsilon_\lambda CD), \quad (4)$$

and the modified amount $\Phi_{sa,\,603}(D, \lambda)$ is calculated with Eq. (1):

$$\begin{aligned}\Phi_{sa,\,603}(D, \lambda) &= \Phi_s(\lambda) - \Phi_{a,\,603}(D, \lambda)\\ &= \Phi_s(\lambda)[1 - \exp(-\varepsilon_\lambda CD)].\end{aligned} \quad (5)$$

Now, photons will be emitted at quantum efficiency $\eta_{em} = 0.8$. Further assuming isotropic emission and internal reflection, 75% of the emitted photons will reach the solar cell: $\eta_t = 0.75$. Therefore, the integrated amount of emitted photons equals $\eta_t\eta_{em}$ times the integrated amount of absorbed photons,

$$\eta_t\eta_{em}\int\Phi_{a,\,603}(D, \lambda)d\lambda = \int\Phi_{e,\,603}(D, \lambda)d\lambda = k, \quad (6)$$

where $\Phi_{e,\,603}(D, \lambda)$ is scaled to $\Phi_{e,\,603}(\lambda)$ such that

$$k = \frac{\int\Phi_{e,\,603}(D, \lambda)d\lambda}{\int\Phi_{e,\,603}(\lambda)d\lambda}. \quad (7)$$

The normalized amount of emitted photons as a function of wavelength $\Phi_{e,\,603}(\lambda)$ is calculated from the normalized emission spectrum $E_n(\lambda)$.

The amount of emitted photons $\Phi_{e,\,603}(D, \lambda)$ is then added to the already modified AM1.5G spectrum $\Phi_{sa,\,603}(D, \lambda)$ with Eq. (2) to yield

$$\Phi_{sae,\,603}(D, \lambda) = \Phi_{sa,\,603}(D, \lambda) + \Phi_{e,\,603}(D, \lambda). \quad (8)$$

The modified spectrum $\Phi_{sae,\,603}(D, \lambda)$ serves as input for the solar cell simulation models.

As an example, Fig. 4 shows the result of this procedure for a QD with $\lambda_{em} = 603$ nm, which also illustrates the effect of QD concentration. For a converter thickness $D = 1$ mm, we have varied the QD concentrations from 1 μM to 1 mM. At a concentration of 1 μM, an

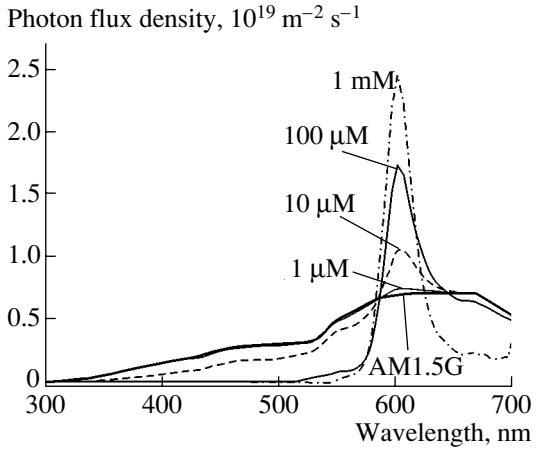

Fig. 4. Calculated modified spectra for various molar QD concentrations that notably influence the AM1.5G spectrum, i.e., 1, 10, and 100 μM and 1 mM.

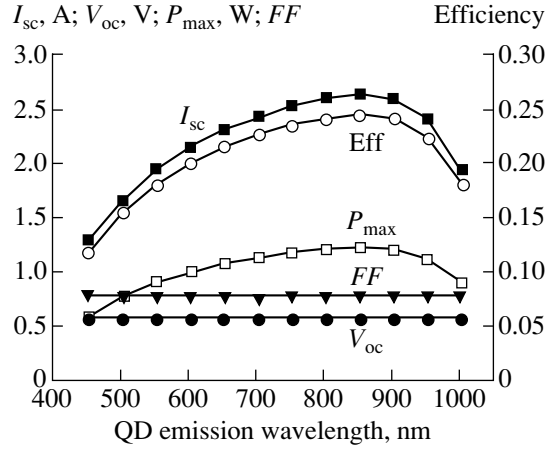

Fig. 5. Effect of small-band QD emission (500 W/m^2) on the parameters I_{sc}, V_{oc}, *FF*, P_{max}, and efficiency (Eff) of the mc-Si solar cell as a function of center emission wavelength. Left-hand scale: I_{sc}, V_{oc}, P_{max}, and *FF*; right-hand scale: efficiency.

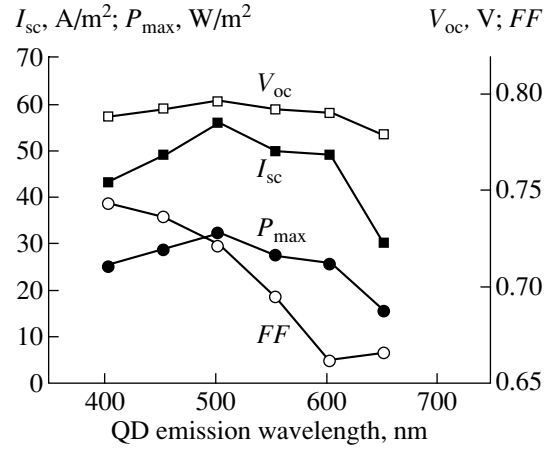

Fig. 6. Effect of small-band QD emission (500 W/m^2) on the parameters I_{sc}, V_{oc}, *FF*, and P_{max} of the a-Si:H solar cell as a function of center emission wavelength. Left-hand scale: I_{sc} and P_{max}, right-hand scale: V_{oc} and *FF*.

appreciable amount of photons is absorbed in the blue part of the AM1.5G spectrum, while the modified spectrum is increased at the QD emission wavelength. For higher concentrations, this effect is clearly much stronger. Note that the product *CD* determines the amount of spectral change. Optimum values for QD concentration are related to the thickness of the converter.

In order to study the effect of different QD size, we shifted the emission spectra in the emission wavelength range 300–700 nm with 50 nm steps. We assumed that the form of spectra remains identical, which is reasonable, as seen in reported absorption/emission spectra as a function of QD size [30–35]. The particle diameters are again determined from the absorption maxima using the relation between the absorption maximum and particle diameter reported in the literature [33–35]. The extinction coefficients are then calculated with the equation from Leatherdale *et al.* [31]. The modified spectra $\Phi_{sa,\lambda_{em}}(D, \lambda)$ are calculated following the procedure described above.

3. RESULTS AND DISCUSSION

3.1. Small-Band Spectrum

The effect of incident small-band spectra on solar cell performance can be easily simulated. We varied the center emission wavelengths of the QDs in 50-nm steps in the range 400–1000 nm, scaled to 500 W/m^2. The results obtained with PC1D for the mc-Si cell are shown in Fig. 5. A clear increase in short-circuit current from 1.3 A at a QD emission wavelength of 453 nm to an optimum of 2.6 A at 853 nm is observed, with a concomitant increase in conversion efficiency from 12 to 24%. Both the fill factor and the open-circuit voltage hardly change. The optimum wavelength of 853 nm does not coincide with the wavelength where the spectral response is at its maximum (see Fig. 2b). At this optimum of about 600 nm, the spectral response is 11% larger than the one at 850 nm. At present, we cannot explain this. The performance parameters compare most favorably to the ones obtained from simulation with an AM1.5G spectrum at 500 W/m^2 spectral density, i.e., short-circuit current I_{sc} = 1.559 A, open-circuit voltage V_{oc} = 0.5851 V, fill factor *FF* = 0.7937, and efficiency η = 14.48%. Clearly, if the complete AM1.5G spectrum could be converted to only one small-banded wavelength region, the optimum center wavelength should be around 850 nm, which leads to a near doubling of conversion efficiency.

The effects on hydrogenated amorphous silicon solar cells are much less spectacular. The simulation results with ASA are shown in Fig. 6. Clearly, an optimum in short-circuit current exists at a QD emission wavelength of 500 nm, i.e., I_{sc} = 55.63 A/m^2. This optimum coincides with the optimum in the spectral response curve (Fig. 2b). However, the optimum is lower than the short-circuit current calculated using the AM1.5G spectrum at 500 W/m^2 spectral density: I_{sc} =

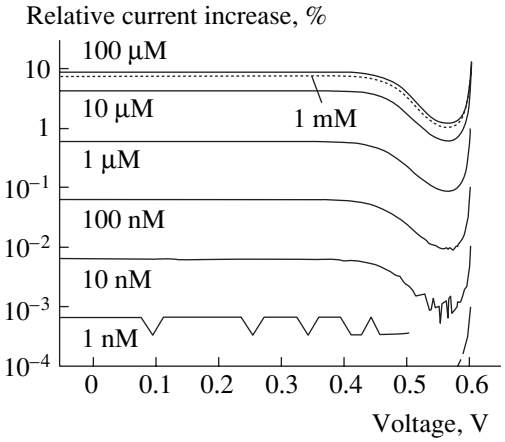

Fig. 7. The effect of QD concentration on the current of the mc-Si solar cell as a function of cell voltage, shown as the current increase relative to the base case (AM1.5G).

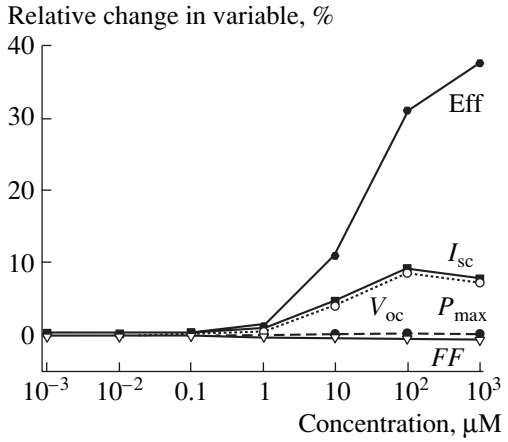

Fig. 8. The absolute change of the variables I_{sc}, V_{oc}, *FF*, P_{max}, and efficiency (Eff) of the mc-Si solar cell as a function of QD concentration.

59.53 A/m^2. This is most probably caused by the small-banded spectral response of the a-Si:H cell.

3.2. Modified AM1.5G Spectrum

As the optimum center emission wavelength of QDs in the planar converter on top of an mc-Si solar cell appears to be around 600 nm, we simulated the solar cell performance changes for the QDs with λ_{em} = 603 nm for a concentration range from 1 nM to 1 mM. The effects on the AM1.5G spectrum were already shown in Fig. 4 for a concentration range from 1 μM to 1 mM.

Figure 7 shows the relative current increase of the mc-Si solar cell as a function of cell voltage for the concentration range from 1 nM to 1 mM. A clear constant increase in short-circuit current of about 6×10^5%/M is observed up to a concentration of 1 μM. For higher concentrations, the effect levels off and even decreases at a concentration of 1 mM. Here, the beneficial effect is counteracted by the increased absorption due to this high concentration. The effect on all solar cell performance parameters is shown in Fig. 8. Clearly, the effects start to occur at 1 μM. While both short-circuit current and maximum generated power P_{max} follow similar behavior, the open-circuit voltage and fill factor only slightly decrease. The efficiency depicted in this figure does not equal $FFI_{sc}V_{oc}$. As the QD concentration increases, the spectral density incident on the solar cell decreases. We calculated the efficiency based on this decreasing intensity and not based on 1000 W/m^2. Therefore, the effect on efficiency is most spectacular: an increase of 30–40% is calculated.

It should be noted that, in practice, the results for the highest concentrations (0.1–1 mM) will not be as high as those presented here, because reabsorption is not taken into account in our simulations. This will lower the amount of emitted photons that enter the solar cell, which will be apparent in a lower peak in the modified spectrum at the QD emission center wavelength. Nevertheless, a relative increase of nearly 10% is in our opinion realizable. In addition, as the product of QD concentration and converter thickness *CD* determines the amount of spectral change, high concentrations can be avoided in converters of larger thickness, as long as *CD* remains constant.

For the simulation of QDs in the planar converter on top of *a*-Si:H cells, we used QDs of center emission wavelength of 503 nm, as at this wavelength the strongest effects are expected (Fig. 6). The results for the short-circuit current are shown in Fig. 9 for a concentration range from 0.1 μM to 10 mM. At about a concentration of 10 μM, the effects on short-circuit current start to be noticeable. This concentration is one order of magnitude higher than in the case of mc-Si. Also, in

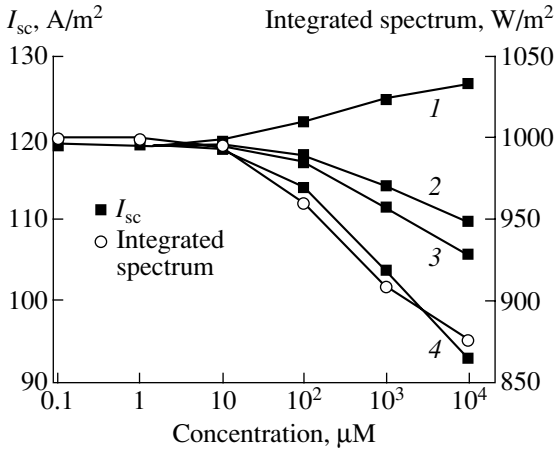

Fig. 9. The relative change of the short-circuit current I_{sc} of the a-Si:H solar cell as a function of QD concentration for combinations of the quantum efficiency η_e and capture efficiency η_t: (*1*) $\eta_e = 1$, $\eta_t = 1$; (*2*) $\eta_e = 0.8$, $\eta_t = 1$; (*3*) $\eta_e = 1$, $\eta_t = 0.75$; and (*4*) $\eta_e = 0.8$, $\eta_t = 0.75$. The integrated spectrum is shown on the right-hand scale for $\eta_e = 0.8$, $\eta_t = 0.75$.

contrast to mc-Si, here, the short-circuit current decreases by about 10% for a concentration of 1 mM, in close correspondence to the decrease in spectral intensity (Fig. 9). This has clearly to do with the amount of absorbed photons balanced with the emitted photons in relation to the spectral response. The aim of applying QDs as wavelength shifters is only sensible when an appreciable difference exists in spectral response between the QD center emission wavelength and the lower wavelengths. As the spectral response of the a-Si:H solar cell is already high at low wavelengths, the beneficial effects, if any, will be small. As a demonstration, when the QD quantum efficiency equals unity, and when in addition all the emitted photons enter the solar cell, an increase in short-circuit current is observed of about 4% for a concentration of 1 mM, as shown in Fig. 9. Increasing either η_{em} or η_t to unity still leads to a decreasing short-circuit current.

4. CONCLUSION

The inclusion of a planar converter that contains wavelength-shifting moieties such as quantum dots allows for a better use of the solar spectrum. However, the most beneficial effects will be accomplished if the spectral response of solar cells has a specific form such that the spectral response is low at low wavelengths and high at high wavelengths. The wavelength-shifting moieties should shift the wavelengths where the spectral response is low to wavelengths where the spectral response is high. Further, losses associated with low quantum efficiency and isotropic emission should be avoided, i.e., the quantum efficiency should be as high as possible (unity preferred) and internal reflection conditions should be optimized.

Here, we demonstrated that QDs with a center emission wavelength of 603 nm included in a planar converter on top of a multicrystalline solar cell are capable of increasing the short-circuit current by nearly 10%. The concomitant increase in efficiency, calculated with the amount of photons incident on the solar cell, can be as high as 30–40%. Simulation results for planar converters on hydrogenated amorphous silicon solar cells show no beneficial effects due to the high spectral response at low wavelength.

Experimental verification of the above results is in progress. To this end, CdSe/ZnS core/shell QDs will be dispersed in a polymer at varying concentrations. The QD/polymer solution will be subsequently spin coated on solar cells. The best polymer candidate is a polylaurylmethacrylate (PLMA) matrix, of which it is reported that the quantum efficiency of QDs is retained after dispersion in PLMA [25].

ACKNOWLEDGMENTS

We gratefully acknowledge the fruitful discussions on QDs with S. Wuister and C. de Mello Donegá (Utrecht University). Furthermore, we would like to thank the Netherlands Organization for Energy and the Environment (NOVEM) for financial support through their NEO program (contract no. 0268-02-03-04-002) and the European Commission for financial support as part of the Framework 6 integrated project FULLSPECTRUM (contract no. SES6-CT-2003-502620). Finally, we would like to thank Zh.I. Alferov, T. d'Estaintot, and A. Luque for organizing the EU–Russian Workshop "Efficient Use of Solar Spectrum in Photovoltaics," November 2–5, 2003, in St. Petersburg, Russia, where this work was discussed, and V.M. Andreev for kindly hosting this conference at the Ioffe Physicotechnical Institute, St. Petersburg (Russia).

REFERENCES

1. M. A. Green, *Solar Cells: Operating Principles, Technology and Systems Application* (Prentice Hall, Englewood Cliffs, N.J., 1982).
2. M. A. Green, *Third Generation Photovoltaics. Advanced Solar Energy Conversion* (Springer, Berlin, 2003).
3. R. E. I. Schropp and M. Zeman, *Amorphous and Microcrystalline Silicon Solar Cells: Modeling, Materials, and Device Technology* (Kluwer Academic, Boston, 1998).
4. W. G. J. H. M. Van Sark, in *Thin Films and Nanostructures*, Ed. by M. H. Francombe (Academic, San Diego, 2002), Vol. 30, p. 1.
5. R. E. I. Schropp, unpublished results.
6. P. M. Sommeling, H. C. Rieffe, J. A. M. van Roosmalen, *et al.*, Sol. Energy Mater. Sol. Cells **62**, 399 (2000).
7. R. L. Garwin, Rev. Sci. Instrum. **31**, 1010 (1960).
8. W. H. Weber and J. Lambe, Appl. Opt. **15**, 2299 (1976).
9. A. Goetzberger and W. Greubel, Appl. Phys. **14**, 123 (1977).
10. C. F. Rapp and N. L. Boling, in *Proceedings of 13th Photovoltaic Specialists Conference* (Washington, DC, 1978), p. 690.
11. K. Barnham, J. L. Marques, J. Hassard, and P. O'Brien, Appl. Phys. Lett. **76**, 1197 (2000).
12. A. J. Chatten, K. W. J. Barnham, B. F. Buxton, *et al.*, Sol. Energy Mater. Sol. Cells **75**, 363 (2003).
13. A. J. Chatten, K. W. J. Barnham, B. F. Buxton, *et al.*, in *Proceedings of 3rd World Congress on Photovoltaic Energy Conversion (WPEC-3), Osaka, Japan, 2003* (in press).
14. A. P. Alivisatos, J. Phys. Chem. **100**, 13226 (1996).
15. S. V. Gaponenko, *Optical Properties of Semiconductor Nanocrystals* (Cambridge Univ. Press, Cambridge, 1998).
16. M. Bruchez, Jr., M. Moronne, P. Gin, *et al.*, Science **281**, 2013 (1998).
17. B. O. Dabbousi, J. Rodriguez-Viejo, F. V. Mikulec, *et al.*, J. Phys. Chem. B **101**, 9463 (1997).
18. F. V. Mikulec, M. Kuno, M. Bennati, *et al.*, J. Am. Chem. Soc. **122**, 2532 (2000).
19. W. G. J. H. M. Van Sark, P. L. T. M. Frederix, A. A. Bol, *et al.*, Chem. Phys. Chem. **3**, 871 (2002).
20. T. Maruyama and R. Kitamura, Sol. Energy Mater. Sol. Cells **69**, 61 (2000).

21. T. Maruyama and J. Bandai, J. Electrochem. Soc. **146**, 4406 (1999).
22. R. T. Wegh, H. Donker, K. D. Oskam, and A. Meijerink, Science **283**, 663 (1999).
23. J. M. Serin, D. W. Brousmiche, and J. M. J. Frechet, J. Am. Chem. Soc. **124**, 11848 (2002).
24. B.-C. Hong and K. Kawano, Sol. Energy Mater. Sol. Cells **80**, 417 (2003).
25. J. Lee, V. C. Sundar, J. R. Heine, *et al.*, Adv. Mater. **12**, 1102 (2000).
26. A. Polman, W. G. J. H. M. Van Sark, W. C. Sinke, and F. W. Saris, Sol. Cells **17**, 241 (1986).
27. P. A. Basore and D. A. Clugston, in *Proceedings of 25th IEEE Photovoltaic Specialists Conference, Washington, 1996* (IEEE, New York, 1996), p. 377.
28. P. A. Basore and D. A. Clugston, *PC1D, User's Manual, Version 5.8* (Univ. of New South Wales, Sydney, Australia, 2002).
29. M. Zeman, J. van den Heuvel, M. Kroon, and J. Willemen, *Amorphous Semiconductor Analysis (ASA), User's Manual, Version 3.3* (Delft Univ. of Technology, Delft, the Netherlands, 2000).
30. C. De Mello Donegá, S. G. Hickey, S. F. Wuister, *et al.*, J. Phys. Chem. B **107**, 489 (2003).
31. C. A. Leatherdale, W.-K. Woo, F. V. Mikulec, and M. G. Bawendi, J. Phys. Chem. B **106**, 7619 (2002).
32. O. Schmelz, A. Mews, T. Basché, *et al.*, Langmuir **17**, 2861 (2001).
33. C. B. Murray, D. J. Norris, and M. G. Bawendi, J. Am. Chem. Soc. **115**, 8706 (1993).
34. J. E. Bowen Katari, V. L. Colvin, and A. P. Alivisatos, J. Phys. Chem. **98**, 4109 (1994).
35. M. Jacobsohn and U. Banin, J. Phys. Chem. B **104**, 1 (2000).

Semiconductors, Vol. 38, No. 8, 2004, pp. 970–975. From Fizika i Tekhnika Poluprovodnikov, Vol. 38, No. 8, 2004, pp. 1007–1012.

SYMPOSIUM ON THE EFFICIENT USE OF SOLAR RADIATION IN PHOTOVOLTAIC POWER ENGINEERING (St. Petersburg, November 3–4, 2003)

Molecular-Based Concepts in PV towards Full Spectrum Utilization[1]

J. A. M. van Roosmalen

Energy Research Centre of the Netherlands (ECN), ECN Solar Energy, 1755 ZG Petten, The Netherlands

e-mail: vanroosmalen@ecn.nl

Submitted February 16, 2004; accepted for publication February 16, 2004

Abstract—Molecular-based concepts offer the potential of low materials and processing costs in photovoltaics (PV), which is especially interesting if high efficiencies can be obtained. To accomplish high efficiencies, a better utilization of the solar spectrum is of high importance. The concept of two-photon absorption in dye-sensitized solar cells and full spectrum aspects of luminescent flat plates concentrators are discussed in this paper. The two-photon dye cell can be compared to a tandem solar cell on the molecular level. The luminescent concentrator offers the potential to employ full spectrum utilization in combination with static concentration of both direct and diffuse light. © *2004 MAIK "Nauka/Interperiodica".*

1. INTRODUCTION

Molecular-based concepts are one of the five activities of the European integrated project "FULLSPECTRUM: A New Photovoltaics (PV) Wave Making More Efficient Use of the Solar Spectrum" [1]. The five activities will focus on enhancement of the performance of solar cells by making more efficient use of the solar spectrum. The work will be based on further developing proven concepts and by identifying new principles:

III–V multijunction solar cells,

Thermophotovoltaics,

Intermediate band materials and cells,

Molecular-based concepts and

Manufacturing technologies.

The area of molecular photovoltaics is not yet characterized by high conversion efficiencies. Nevertheless, ongoing scientific developments in this field continually lead to further progress in material quality with respect to their use in electronic components and the discovery of new properties. In general, molecular materials are interesting for use in photovoltaics if compared to bulk semiconductors because of their distinct light absorption properties and distinct energy levels. Molecular-based PV is believed to be compatible with low cost, large area, high throughput manufacturing technologies. In this respect, not only species chemically seen as molecules and polymers are included, but also quantum dots with discrete energy levels and absorption behavior due to their size confinement. Also crystal lattices can be considered where the properties of the materials involved are dominated by the atomic levels, as for instance often is the case for rare earth ions in crystal lattices.

Molecular-based photovoltaics has started with flat, two-component systems, where one molecular layer acts as an electron donor and the other molecular layer acts as an electron acceptor. Due to limitations in exciton and charge carrier mobilities, a typical thickness of useful material is limited to approximately 10 m. Significant efficiencies have not been reached for flat (bilayer) systems so far. This has led to the development of three-dimensional structures to circumvent the problem of limited charge carrier mobilities. R&D efforts are directed in the field of engineering of molecular devices on the nanometer scale. Both bulk heterojunction solar cells and dye-sensitized solar cell are examples of such nanostructures.

Besides the development in molecular photovoltaics towards engineering the nanometer scale, several scientific developments have led to a renewed interest in the molecular concept of the luminescent concentrator. Due to the ability to collect diffuse light in a flat plate, nonstatic geometry, the flat-plate luminescent concentrator seems to be especially interesting for areas where diffuse light represents a large fraction of the solar energy flux, e.g., large parts of Europe, the United States, and Japan. The dye cell and the luminescent concentrator show interesting features for better use of the solar spectrum, and these specific features will be under investigation in FULLSPECTRUM. The general concepts of the full spectrum aspects of a two-photon dye solar cell and luminescent flat plate concentrator are discussed in this paper.

2. DYE-SENSITIZED SOLAR CELLS

The dye-sensitized solar cell, or dye cell for short (or Grätzel cell, after the inventors Brian O'Regan and Michael Grätzel [2]), is an interesting molecular-based concept with respect to the potential of lowering the

[1]This article was submitted by the authors in English.

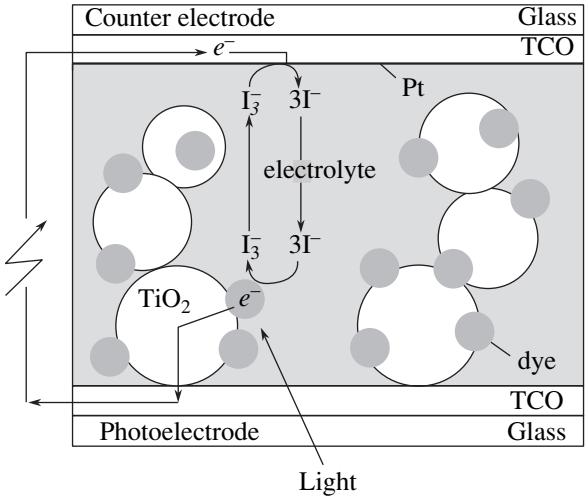

Fig. 1. Schematic representation of the basic processes of the dye-sensitized solar cell. Light is absorbed by a dye molecule. From the excited state of the dye, electron and energy are injected into a nanocrystalline (TiO_2) photoelectrode film of about 10 μm thickness. After transport through the TiO_2 film and lateral conduction through a thin (typically 1 μm) transparent conductive oxide (TCO) on glass, the energy is available for work in the outer circuit. From the outer circuit the electrons are transferred to the iodine/⟨iodide redox⟩ couple in the electrolyte via the counter electrode, which is another TCO layer on glass equipped with a miniscule amount of Pt catalyst. Through diffusion the redox ions reach the oxidized dye molecules and reduce them again to their original (ground) state (the actual reaction as shown releases not one but two electrons).

costs of photovoltaics. In a recent review paper, the fundamentals, properties, and technology were reviewed [3]. At present, practical applications are limited due to the relative poor stability under outdoor conditions. For a long time, heat was considered a very important stress factor for dye cells, but recently good results have been achieved demonstrating stability in a 1000-h, 85°C oven test [4]. The maximum efficiency obtained so far for a limited area dye-sensitized solar cell is 11% [5] and 8.2% for a device exceeding 1 cm^2 [6].

The basic process of the dye cell (see Fig. 1) is light absorption by a dye adsorbed as a monolayer onto a semiconductor surface, with subsequent energy and electron transfer to the semiconductor. An electron is returned to the oxidized dye via the electrolyte or hole conductor. Since the absorption by a single layer of dye molecules is limited, the invention by O'Regan and Grätzel provides a nanocrystalline electrode of a wide band gap, transparent semiconductor, most often consisting of titanium dioxide, TiO_2. In this way, a surface enlargement up to 1000× is obtained as compared to flat layer devices. Typically, such a porous TiO_2 layer contains crystalline TiO_2 nanoparticles with a size of 15–20 nm in a layer of about 10 μm thickness. At present, the highest efficiencies are obtained with a ruthenium compound as the dye, an electrolyte employing the iodine/⟨iodide redox⟩ couple, and TiO_2 as the semiconductor.

One strong point of the dye cell is that only majority charge carrier transport takes place (see Fig. 2), in contrast to semiconductor-based solar cells like crystalline silicon. In the dye cell, after absorption, an electron is injected into the TiO_2. Titanium dioxide is a (majority) photoconductor for electrons.

In crystalline silicon, after light absorption, the minority charge carriers (e.g., electrons in *p*-type silicon) have to diffuse to the junction before they can be collected (see Fig. 2). The maximum open circuit voltage (V_{oc}) in silicon is

$$V_{oc}^{max} = h\nu - (\Delta V_1 + \Delta V_2),$$

where the potentials ΔV_1 and ΔV_2 result from doping the silicon *n*- and *p*-type (potential losses), and $h\nu = E_g$ is photovoltage equal to the Si energy gap E_g. High purity silicon is needed for sufficient minority carrier lifetimes, leading to high costs. In dye cells, materials constraints are less severe, allowing the use of relatively inexpensive materials and large-area, low-cost processing techniques such as screen printing.

The maximum theoretical performance of dye cells can be derived from the energy scheme (see Fig. 3). The absorption characteristics of the dye strongly influence voltage and current. The photocurrent is determined by the overlap of the dye absorption with the solar spec-

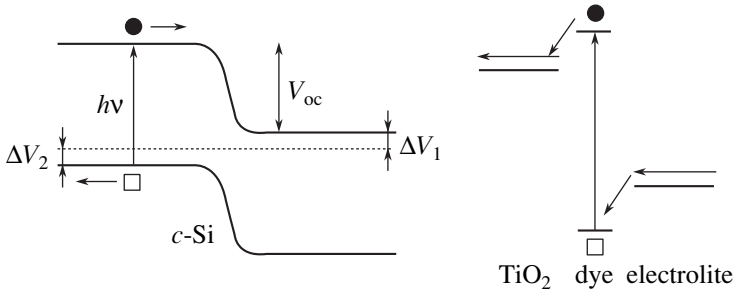

Fig. 2. Representation of carrier transport in crystalline silicon (*c*-Si, left) and dye-sensitized solar cells (right). In *p*-Si, holes (square) are the majority carriers and have normal ohmic transport. Electrons (dot) are the minority carriers and have to diffuse to the junction. In the dye cell the electrons that are injected into TiO_2 are majority carriers and the ions in the electrolyte are majority carriers.

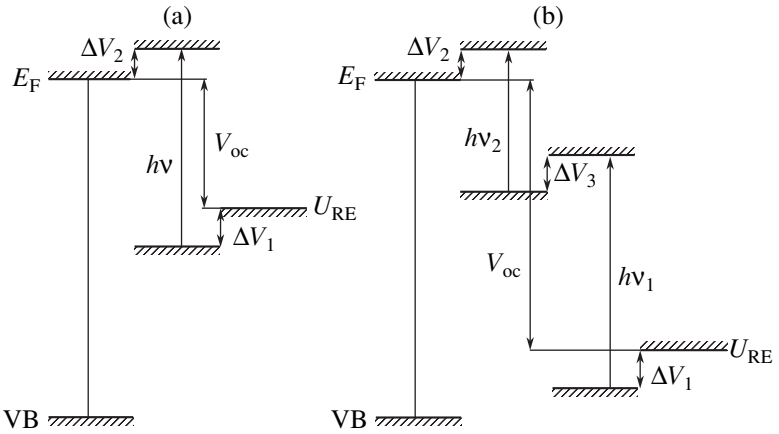

Fig. 3. Energy schemes in which VB is the titanium dioxide valence band, E_F is the Fermi level in TiO_2 (just below the conduction band), and U_{RE} is the redox potential of the electrolyte: (a) representative for the normal dye-sensitized solar cell; photons with minimum energy $h\nu$ are absorbed by the dye; (b) energy scheme for the two-photon dye cell concept.

trum. If $h\nu$ is small, the number of photons absorbed will be high, but the voltage obtained is low, and vice versa. This is typical behavior for a solar cell with a single energy gap (Fig. 3a), as is also the case for crystalline silicon. For a single band gap solar cell with an optimum band gap, the maximum theoretical efficiency is 40.8%, not taking into account fundamental losses [7]. As for silicon, the maximum open circuit voltage V_{oc}^{max} (assuming perfect contacts etc.) of the dye cell is determined by the energy gap (photovoltage $h\nu = E_g$) minus the potential losses. In the dye cell, the maximum open circuit potential V_{oc}^{max} is

$$V_{oc}^{max} = h\nu - (\Delta V_1 + \Delta V_2),$$

where ΔV_1 is the potential losses due to the energy differences between the redox electrolyte potential and the ground state of the dye and ΔV_2 is the loss between the excited state of the dye and the Fermi level of the wide band gap semiconductor TiO_2 (see Fig. 3a).

As can be seen from Fig. 3a, the energy gap of the wide band gap semiconductor (typically > 3 eV) allows for a broader use of the solar spectrum than normally obtained through single photon absorption. A two-photon absorption process has been proposed [8]. In Fig. 3b, potential energy levels for this concept are shown schematically. The proposed mechanism is that a first absorption step ($h\nu_1$) is followed by an electron and energy transfer, after which a second absorption step ($h\nu_2$) should take place. The maximum V_{oc} is

$$V_{oc}^{max} = h\nu_1 + h\nu_2 - (\Delta V_1 + \Delta V_3 + \Delta V_2),$$

where ΔV_1 is the potential loss between the electrolyte redox potential and the ground state of the dye moiety 1; ΔV_3 is the loss between the excited state of the dye moiety 1 and the ground state of the dye moiety 2; ΔV_2 is the loss between the excited state of the dye moiety 2 and the Fermi level in TiO_2. One of the boundary conditions is that the intermediate state has a sufficient lifetime to allow the second absorption step to occur. In two-photon processes where the second absorption is done from the excited state, without energy and electron transfer to an intermediate state, the absorption brass sections are normally extremely low and can only be accomplished by strong lasers. Therefore, the electron and energy transfer to a stable intermediate is a very important part of the model.

In this way a tandemlike approach is accomplished on a molecular scale. As for other tandem-based solar cell devices, both absorption steps have to generate the same current for optimal performance, and the absorbers will have to be tailored to this requirement. If, however, both steps have an identical energy transition, it is also possible to interpret this as an upconversion process, through which it would for instance be possible to add absorption from the infrared to the normal dye absorption (see Fig. 4). In comparison to the single absorption case of the dye cell, the two-photon process does not increase the number of electrons generated and the (maximum) current thus remains unchanged. The efficiency enhancement by two-photon absorption is the result of a fundamental increase in voltage, as is also the case in semiconductor tandems. This cannot be accomplished with the commonly used iodide/⟨iodine redox⟩ couple, since this would result in an unchanged voltage. Other redox couples or hole conductors will be necessary. The theoretical maximum efficiency for a series connected tandem is 55.5%, not taking into account fundamental losses [7].

3. LUMINESCENT CONCENTRATOR

The luminescent concentrator has been under study since the seventies of the last century [9, 10]. The concept is based on incorporating in a transparent matrix

materials that are absorbing (to absorb the sunlight) as well as luminescent. The refractive index of the transparent matrix is chosen larger than the surrounding medium (mostly air). As the luminescent materials emit light in all directions, part of the emitted light will be internally reflected at the matrix/air interface. By designing geometries for which the length and width of the transparent matrix are larger than its thickness (such as for a plate configuration), geometric concentration is accomplished. The emitted light is totally internally reflected and will be concentrated within the matrix, where it can be harvested at the edges of the matrix. There it can be transformed into electricity by solar cells (see Fig. 5).

In the flat plate luminescent concentrator, light from all incoming angles is collected. Because of this property, the luminescent concentrator is a static, nonmoving form for the concentration of solar light. However, it is also an indirect form of photovoltaics, since the sunlight is first absorbed and subsequently emitted by luminescence. Therefore, in order to obtain high overall efficiencies, the luminescence efficiency also has to be high. Since light is collected from all angles, the luminescent concentrator is sensitive to diffuse light. The fact that it is both static and sensitive to diffuse light makes the flat plate concentrator interesting for building integrated applications, especially in areas with a relatively large contribution of diffuse light to the total incoming energy. For instance, in the Netherlands the diffuse part of the incoming solar energy annually is about 50% and therefore quite significant. If it is possible to obtain reasonable overall system efficiencies based on inexpensive materials, flat plate luminescent concentrators can thus be an interesting low-cost photovoltaic option.

In the work that was done some thirty years ago, the overall system efficiencies that were achieved were limited to around 5% only [11]. One of the problems for the organic luminescent materials that were used was probably [12] that the luminescent wavelengths were only slightly higher than the absorption wavelengths. Under those conditions a significant part of the emitted light is lost by reabsorption. For the organic materials that are used in luminescent concentrators, luminescence is based on the Stokes shift. The Gaussian distribution around the absorption maximum is shifted to a higher wavelength (lower energy) where the Gaussian distribution of the luminescence occurs. Since the shift is relatively small, the tails of the Gaussians overlap. For this reason, an important part of the light that is emitted by the luminescence process is reabsorbed, thereby diminishing its performance. Another problem was the relative instability of the luminescent organic materials under operation conditions.

The appealing concept of the luminescent concentrator is now revisited because of several interesting developments in materials science by which the overall system efficiency can be enhanced, e.g., luminescent materials, photonic materials and up- and downconversion, but also in the area of stability, potentially allowing the use of organic and polymeric materials for long term outdoor applications.

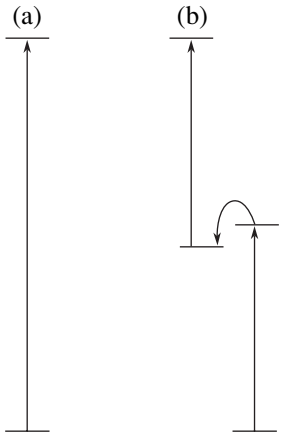

Fig. 4. Schematic representation of how a two-photon dye (b) could be used as an upconverter (e.g., for infrared radiation), together with a normal dye (a). Both could be absorbed on TiO_2, leaving the voltage unchanged.

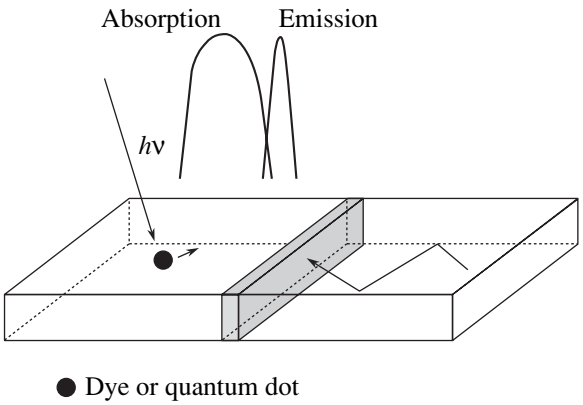

Fig. 5. Schematic representation of a luminescent flat plate concentrator. Direct and diffuse sunlight are absorbed by luminescent materials, e.g., organic dye molecules or quantum dots. The luminescent materials emit light at lower energy in all directions, of which the largest part is reflected at the interface between the plate and air. In this way, it is concentrated and can be collected at the edges. In the graph, a bifacial solar cell is used in between the edges of two luminescent plates.

In recent years, new materials have shown interesting luminescent properties. For use in luminescent concentrators, especially quantum dots are considered [12, 13]. The quantum dots of interest are based on nanocrystalline semiconductor particles. The luminescence process is similar to organic materials, based on the Stokes shift. However, the Stokes shift can be enlarged, as it is influenced by particle size and particle size distribution. The resulting overlap between absorption and luminescent emission can thus be reduced. An additional

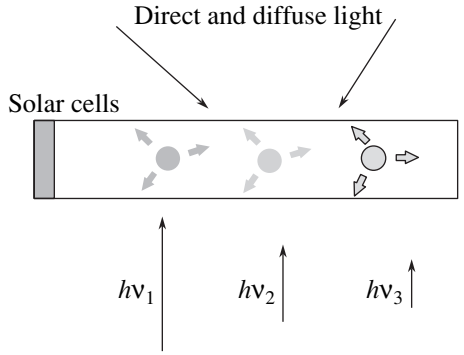

Fig. 6. Schematic representation of a luminescent flat plate concentrator, indicating that different luminescent materials can be integrated to cover different parts of the solar spectrum. In principle, for each emitted wavelength a different solar cell is needed.

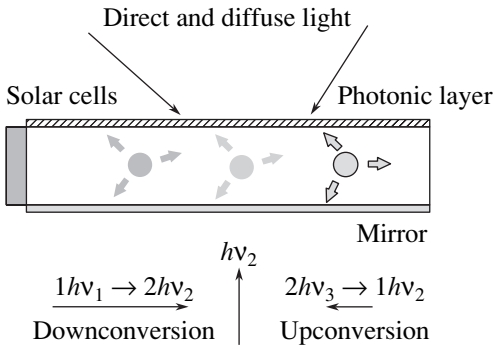

Fig. 7. Representation of an idealized luminescent concentrator. All photons of the solar spectrum are transformed into a single wavelength. By a downconversion process, one high energy photon ($h\nu_1$) is converted into two lower energy photons of energy $h\nu_2$. A second part of the solar spectrum is absorbed by a regular luminescent material and emitted at $h\nu_2$. An upconverter material converts two lower energy photons $h\nu_3$ into one photon with energy $h\nu_2$. A photonic layer on the top acts as a mirror specifically for $h\nu_2$. At the bottom a normal mirror can be used. At the edge a single solar cell can be used.

advantage of quantum dots is that the absorption width is larger as compared to organic materials, so a larger part of the solar spectrum can be absorbed. By varying the size, the absorption wavelength of the quantum dots can be tuned, and by combining various materials, a larger part of the solar spectrum can be covered. Other materials that have shown interesting luminescence properties are rare earth and polymeric materials.

Theoretically, the luminescent concentrator offers very good possibilities for full spectrum utilization. In principle each part of the solar spectrum can be addressed by a different material (see Fig. 6). By using quantum dots and molecular materials almost the complete wavelength regime of the solar spectrum can be covered, from ultraviolet light into deep infrared. In practice, however, this will be limited by the overlap between absorption and emission spectra of the various materials. One way to overcome this is to incorporate each absorber in an individual transparent matrix, separated by air (for instance) to ensure total internal reflection in each to these matrices. Theoretically, in this way the maximum efficiency (unconstrained) for three color centers is 63.8%, not taking into account fundamental losses [7].

To reach the maximum theoretical efficiency is far from trivial. The geometric concentration factors that can be reached are reasonably high. For a hypothetical concentrator plate of, e.g., $100 \times 100 \times 5$ mm, executed in double with a bifacial solar cell of 100×5 mm (Fig. 5), the geometrical concentration is 40×. The system, however, will be strongly limited by the optical efficiency or, in other words, optical losses. An important loss factor, as already mentioned, is the reabsorption of the emitted light [12]. Another optical loss factor is intrinsically determined by the operation principle of the luminescent concentrator, namely, the principle of total internal reflection. The angle under which light is totally internally reflected is dependent on the difference in refractive index between the transparent matrix and the surrounding air. Typical refractive indexes of transparent polymers are on the order of 1.5, and for this reason tens of percent are lost. An aspect that is also of influence on the overall system efficiency is that monochromatic efficiencies for most solar cells (which are used to collect the concentrated light at the edges) are well below 100%.

To improve the total amount of emitted light that is directed towards the solar cells at the edges, recent developments in the area of photonic materials can potentially be used. Photonic crystals are known to act as a mirror for a single wavelength. This property could be used by applying a photonic crystal layer on top of the luminescent concentrator (see Fig. 7). The photonic crystal has to be tuned in such a way that it reflects exactly the emitted, luminescent wavelength. In this way, also the light that would not be reflected by total internal reflection can be reflected and will be concentrated to the edges. The photonic layer will not only reflect the light from within the luminescent concentrator, but will also function as a mirror for that part of the incoming sunlight. This will be a minor loss factor if the wavelength region for the photonic material and the overlap with the absorption of the luminescent materials are small. At the back of the luminescent concentrator, a standard low-cost mirror can be used.

Another principle that can be used to increase the overall system efficiencies is the use of up- and downconversion of photons (see Fig. 7). By the downconversion process, a high energy photon can be transformed into two (or more) lower energy photons. By the upconversion process, two lower energy photons can by "upconverted" to higher energies, e.g., from infrared to visible. If all photons of the solar spectrum can be transformed into a single wavelength, only a single solar cell

is needed to collect the light at the edges, compared to three solar cells if three color centers were used.

A final remark on luminescent concentrators is that it has the interesting feature that it transforms incoming, perpendicular light into reflected, lateral light. This division in perpendicular and lateral light can be used as an interesting engineering tool. For example, if the luminescent concentrator is not equipped with a mirror on the back, in principle it is transparent for all the light that is not absorbed. If for instance only the visible light were absorbed, the infrared could be transmitted (or vice versa) and used for other purposes (e.g., for a thermal collector, room heating, etc.).

4. CONCLUSION

The general concepts of a full spectrum approach with two photon processes in dye cells and a flat plate luminescent concentrator are discussed. For further advancement in these areas, these general concepts need to be refined and elaborated, as is under way in the FULLSPECTRUM project [1].

ACKNOWLEDGMENTS

This paper has been made possible in part by the sixth framework program European Commission integrated project “FULLSPECTRUM: A New PV Wave Making More Efficient Use of The Solar Spectrum,” contract no. SES6-CT-2003-502620.

REFERENCES

1. A. Luque, A. Martí, A. W. Bett, *et al.*, in *Proceedings of 19th European Photovoltaic Specialists Conference* (Paris, 2004) (in press).
2. B. O’Regan and M. Grätzel, Nature **353**, 737 (1991).
3. J. M. Kroon, B. C. O’Regan, J. A. M. van Roosmalen, and W. C. Sinke, in *Handbook of Photochemistry and Photobiology,* Ed. by H. S. Nalwa (Am. Sci., Los Angeles, 2003), Vol. 1, p. 1.
4. P. Wang, S. M. Zakeeruddin, J. E. Moser, *et al.*, Nature Mater. **2**, 402 (2003).
5. M. A. Green, K. Emery, K. Bücher, *et al.*, Prog. Photovoltaics: Res. Appl. **6**, 35 (1999).
6. A. Hinsch, J. Kroon, R. Kern, *et al.*, in *Proceedings of 17th European Photovoltaic Solar Energy Conference* (2001), p. 51.
7. M. A. Green, *Third Generation Photovoltaics. Advanced Solar Energy Conversion* (Springer, Berlin, 2003), p. 61.
8. J. A. M. van Roosmalen, in *Proceedings of First Workshop on the Path to Ultra-High Efficient Solar Cells* (JRC Ispra, Italy, 2001).
9. W. H. Weber and J. Lambe, Appl. Opt. **15**, 2299 (1976).
10. A. Goetzberger and W. Greubel, Appl. Phys. **14**, 123 (1977).
11. V. Wittwer, A. Goetzberger, K. Heidler, and A. Zastrow, J. Lumin. **24–25**, 873 (1981).
12. A. J. Chatten, K. W. J. Barnham, B. F. Buxton, *et al.*, Sol. Energy Mater. Sol. Cells **75**, 363 (2003).
13. K. W. J. Barnham, J. L. Marques, J. Hassard, and P. O’Brien, Appl. Phys. Lett. **76**, 1197 (2000).

Semiconductors, Vol. 38, No. 8, 2004, pp. 976–980. Translated from Fizika i Tekhnika Poluprovodnikov, Vol. 38, No. 8, 2004, pp. 1013–1017.

ELECTRONIC AND OPTICAL PROPERTIES OF SEMICONDUCTORS

Piezoresistance in the Films of *p*-type Polycrystalline Silicon

V. A. Gridchin and V. M. Lyubimsky*

Novosibirsk State Technical University, pr. K. Marksa 20, Novosibirsk, 630092 Russia

**e-mail: lubvlm@ngs.ru*

Submitted December 1, 2003; accepted for publication January 20, 2004

Abstract—The phenomenon of piezoresistance in polycrystalline *p*-type silicon in the case of scattering of holes by intercrystallite potential barriers is described. The values of elastoresistance coefficients for this type of scattering are close to those for scattering by impurity ions and by acoustic lattice vibrations. The difference between the experimental and calculated elastoresistance coefficients may possibly be eliminated if the variation in the effective masses as a result of deformation, the nonsphericity of the valence band, the "small-magnitude effects," and additional scattering mechanisms are taken into account. © *2004 MAIK "Nauka/Interperiodica".*

1. INTRODUCTION

At present, there are several models used to describe the piezoresistive properties of polycrystalline silicon [1–11]. In the majority of publications, the piezoresistive effect in polycrystalline silicon was considered at high impurity concentrations; it was also assumed that the contribution of barriers at the grain boundaries to the effect was insignificant [1–3, 5, 6, 9–11]. A conductivity model according to which the resistivity of polycrystalline silicon is governed by the resistivity of crystallites and the resistance of barriers was used in [4, 7, 8] to determine the piezoresistive coefficients of both crystallites and barriers. However, the results obtained are not convincing according to the opinion of Mosser *et al.* [12].

The objective of this study was to describe the piezoresistive effect in *p*-type polycrystalline silicon in the situation where holes are scattered by intercrystallite potential barriers and to compare the results obtained with experimental data.

We describe the phenomenon of piezoresistance in the following sequence: we consider first the piezoresistive effect in single-crystal silicon in which there are potential barriers that are perpendicular to one of the principal crystal axes and are identified with potential barriers at the crystallite boundaries; we then determine the elastoconductance (M_{ijmn}) and elastoresistance (m_{ijmn}) coefficients for single-crystal silicon. Finally, we calculate the elastoconductance coefficients for polycrystalline silicon ($\langle m_{ijmn}\rangle$) and compare the experimental and calculated values of elastoresistance coefficients.

2. THEORY

The piezoresistive effect is characterized by the elastoconductance, elastoresistance, and piezoresistive coefficients. There is a unique relation between all these coefficients (see, for example, [13]). The piezoresistive and elastoresistance coefficients are determined experimentally, whereas the elastoconductance coefficients are calculated theoretically. The elastoconductance coefficients are defined as

$$\frac{\Delta\sigma_{ij}}{\langle\sigma\rangle} = M_{ijmn}\varepsilon_{mn}, \quad \langle\sigma\rangle = \frac{1}{3}\mathrm{Tr}\,\sigma = \sigma_0, \qquad (1)$$

where $\Delta\sigma_{ij}$ is a variation in conductivity as a result of strain ε_{mn}.

The heavy and light holes make the major contribution to the piezoresistive effect in *p*-Si [13]. If the scattering mechanism is the same for the heavy and light holes, the mean value of the elastoconductance coefficient is then given by [13]

$$M_{ijmn} = M^{(1)}_{ijmn}\left(\frac{\sigma_0^{(1)} - \sigma_0^{(2)}}{\sigma_0^{(1)} + \sigma_0^{(2)}}\right), \qquad (2)$$

where the superscripts (1) and (2) refer to the heavy and light holes, respectively.

As is well known, the piezoresistive effect in semiconductors with degenerate bands is related both to variation in the deformation of the Fermi–Dirac distribution function (f_0) and to variations in the relaxation time (τ) and the group velocity of holes (v) [13].

The electrical conductivity related to each type of holes with the Fermi degeneracy taken into account can be written as

$$\sigma^{t}_{ik} = -\frac{q^2}{4\pi^3}\int \tau^{t}\frac{\partial f_0}{\partial E^{t}} v^{t}_i v^{t}_j d^3k.$$

The variation in the conductivity ($\Delta\sigma^{t}_{ij}$) under the effect of strain (ε_{mn}) is given by [13]

$$\Delta\sigma^{t}_{ij} = \frac{q^2\varepsilon_{mn}}{4\pi^3\hbar^2}\int \frac{\partial}{\partial\varepsilon_{mn}}\left(\tau^{t}\frac{\partial f_0}{\partial E^{t}}\right)\frac{\partial E^{t}}{\partial k_i}\frac{\partial E^{t}}{\partial k_j}d^3k$$

$$+ \frac{2q^2\varepsilon_{mn}}{4\pi^3\hbar^2}\int \tau^{t}\frac{\partial f_0}{\partial E^{t}}\frac{\partial^2 E^{t}}{\partial k_i\partial k_j}\frac{\partial E^{t}}{\partial\varepsilon_{mn}}d^3k,$$

where the superscript t = (1) or (2); E^t, v_i^t, and τ^t are the energy, the velocity component, and the relaxation time for scattering of charge carriers, respectively; and q is the elementary charge.

A variation in the energy under the effect of strain is defined as (the upper sign corresponds to the band of light holes and the lower sign corresponds to the band of heavy holes) [14]

$$\Delta E(k) = \pm\frac{Bb}{2\bar{B}}\left[\frac{3}{k^2}(k_m\varepsilon' k_n) - \varepsilon\right],$$

$$\varepsilon' = \begin{cases}\varepsilon_{mn} & \text{for } m = n\\ \gamma\varepsilon_{mn} & \text{for } m \neq n,\end{cases}$$

$$\gamma = \frac{Dd}{3Bb}, \quad \varepsilon = \varepsilon_{11} + \varepsilon_{22} + \varepsilon_{33},$$

where B, $\bar{B}$, and D are the valence-band parameters in the starting crystal and b and d are the corresponding parameters of strained crystal.

Approximating the constant-energy surfaces with spheres, we obtain

$$\Delta\sigma_{ij}^t = \left(\frac{q^2\hbar^2}{4\pi^3 m^{*2}}\int\frac{\partial}{\partial\varepsilon_{mn}}\left(\tau^t\frac{\partial f_0}{\partial E^t}\right)k_i k_j d^3k + \frac{2q^2}{4\pi^3 m^*}\int\tau^t\frac{\partial f_0}{\partial E^t}\frac{\partial E^t}{\partial\varepsilon_{mn}}d^3k\right)\varepsilon_{mn}. \quad (3)$$

If the relaxation time depends only on the energy and does not exhibit an angular dependence, the second integral in (3) equals zero, as shown in [13, 14].

If the charge carriers are scattered by potential barriers at the crystallite boundaries, the relaxation time τ_b is given by [15]

$$\tau_b = \frac{\hbar^3|k_z|}{2m^*L|U|^2}, \quad U = \frac{1}{L}\int U_0(z)\exp(-i2k_z z)dz, \quad (4)$$

where L is the crystallite size and $U_0(z)$ is the potential energy of the barrier at the crystallite boundary. The axis z lies in the film plane and coincides with the direction of an external electric field (Fig. 1).

As can be seen from formula (4), τ_b exhibits an angular dependence; therefore, the second integral in (3) is nonzero in calculations of M_{1111}^t and M_{1122}^t. In calculating M_{3232}^t, this integral is equal to zero owing to the fact that the relaxation time is independent of the angle ϕ and $\frac{\partial E^t}{\partial\varepsilon_{32}}$ is proportional to $\sin\phi$.

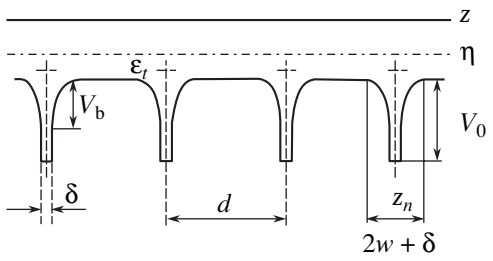

Fig. 1. A model of potential barriers in *p*-type polycrystalline silicon.

When calculating the elastoconductance coefficients, it is convenient to replace the integration with respect to k_x, k_y, and k_z in expression (3) with integration with respect to energy.

The independent components M_{3232}^t, M_{1111}^t, and M_{1122}^t of the elastoconductance tensor are equal to

$$M_{3232}^t = \frac{q^2\sqrt{2m^{t*}}}{\sigma_0^t 2\pi^3\hbar^3}\int_0^\infty\int_0^{2\pi}\int_0^\pi\left[\frac{\partial\tau^t}{\partial\varepsilon_{32}}\frac{\partial f_0}{\partial E^t} \pm \frac{\partial^2 f_0}{\partial(E^t)^2}\frac{Dd}{2\bar{B}}\right.$$
$$\left.\times\cos\theta\sin\theta\sin\phi\right](E^t)^{3/2}\cos\theta\sin^2\theta\sin\phi\, d\theta d\phi dE^t,$$

$$M_{1111}^t = M_{3333}^t = \frac{q^2\sqrt{2m^{t*}}}{\sigma_0^t 2\pi^3\hbar^3}\left\{\int_0^{2\pi}\int_0^\pi\int_0^\infty\left[\frac{\partial\tau^t}{\partial\varepsilon_{33}}\frac{\partial f_0}{\partial E^t}\right.\right.$$
$$\left.\pm\tau^t\frac{\partial^2 f_0}{\partial(E^t)^2}\frac{Bb}{2\bar{B}}(3\cos^2\theta - 1)(E^t)^{3/2}\right]\sin\theta d\theta d\phi dE^t$$
$$\left.\pm\left\{\int_0^\infty\int_0^{2\pi}\int_0^\pi\tau^t\frac{\partial f_0}{\partial E^t}\frac{Bb}{2\bar{B}}(3\cos^2\theta - 1)(E^t)^{1/2}\sin\theta d\theta d\phi dE^t\right\}\right\},$$

$$M_{1122}^t = -\frac{M_{1111}^t}{2}.$$

The elastoresistance coefficients m_{ijmn} that describe the relative variation in the resistivity per unit strain are defined by an expression similar to (1). The following relation exists between these two coefficients in cubic crystals: $m_{ijmn} = -M_{ijmn}$.

The elastoresistance coefficients for polycrystalline silicon ($\langle m_{ijmn}\rangle$) can be derived as a result of averaging the elastoresistance coefficients for single-crystal silicon [11]:

$$\langle m_{ijmn}\rangle = \frac{1}{\Omega}\int_\Omega m'_{ijmn}d\omega = -\left(\frac{\sigma_0^{(1)} - \sigma_0^{(2)}}{\sigma_0^{(1)} + \sigma_0^{(2)}}\right)\frac{1}{\Omega}\int_\Omega M'^{(1)}_{ijmn}d\omega.$$

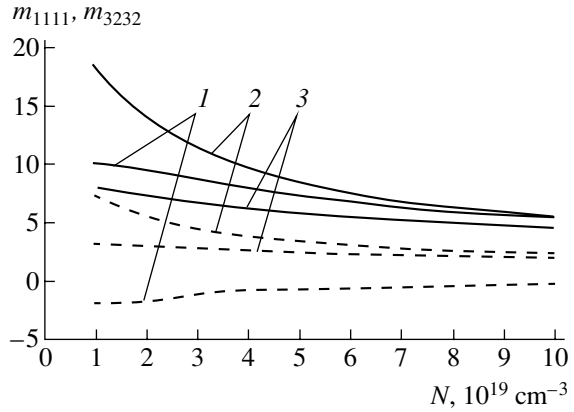

Fig. 2. Dependences of the coefficients m_{1111} and m_{3232} on the impurity concentration for single-crystal *p*-Si. Dashed lines correspond to m_{1111}, and solid lines correspond to m_{3232}. The calculations were carried out for scattering by (*1*) potential barriers, (*2*) acoustic lattice vibrations, and (*3*) impurity ions.

In the case of the most widely used texture ⟨110⟩, we have

$$\langle M_{1111}\rangle = \frac{9}{16}m_{1111} + \frac{7}{16}m_{1122} + \frac{7}{8}M_{3232},$$

$$\langle M_{1122}\rangle = \frac{3}{16}m_{1111} + \frac{13}{16}m_{1122} - \frac{3}{8}M_{3232},$$

$$\langle M_{1133}\rangle = \frac{1}{4}m_{1111} + \frac{3}{4}m_{1122} - \frac{1}{2}M_{3232}.$$

3. DISCUSSION

The model of the charge-carrier scattering by potential barriers is applicable if the free-path length is larger than the potential-barrier width $2w + \delta$. This circumstance imposes restrictions on the impurity concentration. For example, the doping-impurity concentration must be higher than 10^{19} cm^{-3} if the hole mobility is 20–30 cm^2/(V s) and the density of states at the traps is $Q_t = 1.9 \times 10^{12}$–3.7×10^{12} cm^{-2}.

In polycrystalline silicon with an impurity concentration higher than 10^{19} cm^{-3}, the potential at the crystallite boundaries is given by

$$U_0 = \begin{cases} V_b\left(1 + \dfrac{\delta - 2|z|}{2w}\right)^2, & \dfrac{\delta}{2} < |z| < \dfrac{\delta}{2} + w, \\ V_0, & |z| < \dfrac{\delta}{2} \end{cases}$$

and is shown in Fig. 1 [16]. For *p*-type polycrystalline silicon, we have

$$V_b = \frac{q^2 N w^2}{2\varepsilon\varepsilon_0}.$$

In this situation, the half-width of the depletion region w can be estimated from the formula

$$w = \frac{Q_t}{2N},$$

where N is the impurity concentration and Q_t is the density of states at the traps.

In Fig. 2, we show the dependences of the elastoresistance coefficients m_{1111} and m_{3232} on the impurity concentration in single-crystal silicon at 300 K. These dependences were calculated taking into account the scattering of holes by impurity ions, acoustic lattice vibrations, and potential barriers at the grain boundaries. When calculating the elastoresistance coefficients, we assumed that the ratio between the concentrations of the light and heavy holes was controlled by their effective masses and was independent of the strain in the linear approximation. The value of U_0 was calculated assuming that $\delta = 6 \times 10^{-10}$ m, $V_0 = 0.55$ eV, and the density of states at the traps $Q_t = 3.7 \times 10^{16}$ m^{-2}. The crystallite size was assumed to be equal to $L = 0.12$ μm. As can be seen from Fig. 2, the values of the elastoresistance coefficients are of the same order of magnitude for all mechanisms of scattering; however, these values are smaller than those obtained experimentally [17]. This circumstance is caused by the fact that only the main effect related to the variation in the valence-band shape as a result of the violation of symmetry is taken into account in calculations using the above formulas. At the same time, the contribution of the strain-induced variation in the effective masses and the nonsphericity of the valence band to the value of m_{3232} amounts to about 10–20 (due to each of the mechanisms) [13].

The calculated coefficients m_{1111} shown in Fig. 2 are much smaller than m_{3232} for all mechanisms of scattering; the same applies to experimental coefficients. However, experimental values of m_{1111} (in contrast to calculated values) exhibit complex temperature dependences and $m_{1111} \neq m_{1122}$. This circumstance is related to the fact that the strain-induced variation in effective masses is disregarded in the above formulas. If this variation is taken into account, strain-related effects that depend only slightly on temperature are observed. In addition, calculations were performed for a single mechanism of scattering, whereas in fact several mechanisms contribute to the scattering; furthermore, the light and heavy holes make different contributions to both electrical conductivity and piezoresistance [13].

We can estimate the contribution of the variation in effective masses and the valence-band nonsphericity to the value of m_{3232} at (+20)–(+40). In contrast, it is rather difficult to estimate the contribution of "small-magnitude effects," especially if several mechanisms of scattering are taken into account. It is worth noting that the contribution of "small-magnitude effects" to m_{1111} and m_{1122} is quite significant ($|m_{1111} + 2m_{1122}|$ can be as large as 10).

In Figs. 3 and 4, we show the dependences of the elastoresistance coefficients $\langle m_{1111}\rangle$ and $\langle m_{1122}\rangle$ in poly-

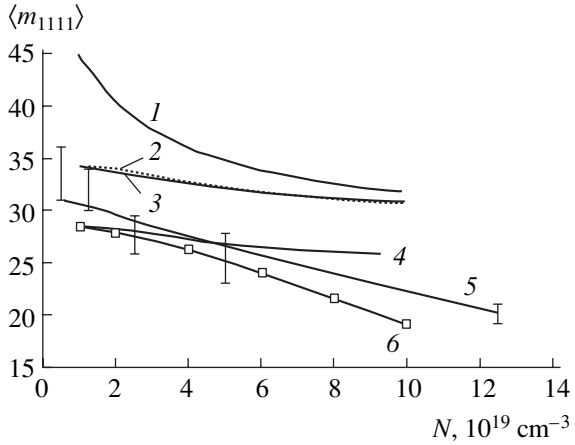

Fig. 3. Dependences of the coefficient $\langle m_{1111}\rangle$ on the impurity concentration N for *p*-type polycrystalline silicon. The calculations were carried out for scattering by (*1*) acoustic lattice vibrations, (*2*) potential barriers, and (*3*) impurity ions. Curve *4* represents the dependence of $\langle m_{1111}\rangle$ on N for corrected values of m_{1111} and m_{3232}. Experimental data from publications [5] and [12] are represented by curves *5* and *6*, respectively.

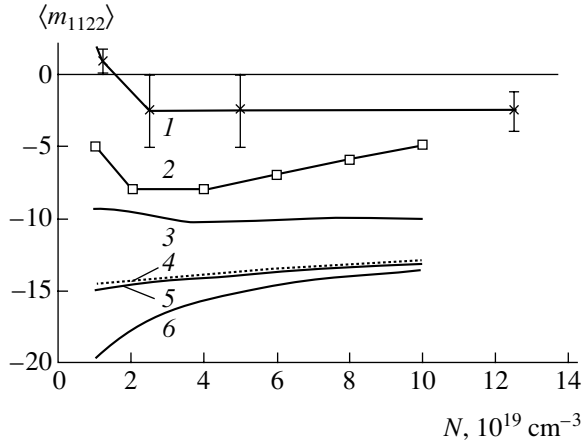

Fig. 4. Dependences of the coefficient $\langle m_{1122}\rangle$ on the impurity concentration N for *p*-type polycrystalline silicon. Curves *1* and *2* represent the experimental data reported in [5] and [12], respectively. Curve *3* represents the results of calculations of $\langle m_{1122}\rangle$ on N with the values of m_{1111} and m_{3232} corrected. Calculated dependences correspond to the scattering by (*4*) potential barriers, (*5*) impurity ions, and (*6*) acoustic lattice vibrations.

crystalline silicon on the impurity concentration for the ⟨110⟩ texture; the dependences were calculated for the mechanisms of scattering under consideration (experimental data [5, 12] are also shown). It can be seen from Figs. 3 and 4 that experimental dependences of the coefficients $\langle m_{1111}\rangle$ and $\langle m_{1122}\rangle$ on N are not similar. This circumstance may be related mainly to the fact that these coefficients are controlled not only by the values of m_{3232} but also by m_{1111} and m_{1122} for single-crystal *p*-Si. The coefficients $\langle m_{1111}\rangle$ and $\langle m_{1122}\rangle$ calculated after increasing m_{3232} by 30 and without correcting the values of m_{1111} and m_{1122} exceed the experimental coefficients in magnitude. The large values of these coefficients may be related for example to the fact that the actual shape of the intercrystallite potential barrier differs from the shape shown in Fig. 1 or that we disregarded some other mechanisms of scattering, e.g., the scattering of holes due to the misorientation of crystallites. The latter mechanism is independent of the impurity concentration and should lead to a decrease in the electrical conductivity and possibly to a decrease in the coefficient m_{3232}.

It can be seen from the data reported in [12] and shown in Fig. 3 that the experimental dependence of $\langle m_{1111}\rangle$ on N levels off as the impurity concentration decreases. This behavior may be attributed to the fact that the scattering by potential barriers becomes more important as the impurity concentration decreases. In addition, the value of m_{3232} in the case of scattering by potential barriers is smaller than that in the case of scattering by acoustic lattice vibrations.

It can be seen from Fig. 4 that experimental values of $\langle m_{1122}\rangle$ decrease in magnitude as the impurity concentration decreases. This behavior is related to the fact that scattering by potential barriers becomes more significant as the impurity concentration decreases; the value of m_{1111} is negative in the case of scattering by potential barriers. However, it is necessary that the coefficient m_{3232} be slightly smaller and $|m_{1111}|$ slightly larger than the calculated values in order to fit the calculated elastoresistance coefficients to experimental data. For example, a decrease in m_{3232} by a factor of 1.2 and an increase in $|m_{1111}|$ by a factor of 2.5 when considering the scattering by potential barriers lead to impurity-concentration dependences of $\langle m_{1111}\rangle$ and $\langle m_{1122}\rangle$ that are in satisfactory agreement with the dependences calculated for the impurity concentrations 10^{19}–4×10^{19} cm^{-3} (Figs. 3, 4). Potential barriers are low at an impurity concentration on the order of 10^{20} cm^{-3}; as a result, the elastoresistance coefficients are controlled by other mechanisms of scattering. A decrease in m_{3232} by a factor of 1.2 and an increase in $|m_{1111}|$ from 2 to 5 is quite possible if the impurity concentration is equal to 10^{19} cm^{-3} and if the scattering by misoriented crystallites and the "small-magnitude effects" are taken into account.

4. CONCLUSION

Thus, we described the piezoresistive effect in *p*-type polycrystalline silicon in the situation where holes were scattered by intercrystallite potential barriers. Quantitative agreement between experimental and calculated elastoresistance coefficients can be attained if strain-induced changes in effective masses, nonsphericity of the valence band, "small-magnitude effects," and the additional mechanism (or mechanisms) of scattering are taken into account.

REFERENCES

1. J. Suski, V. Mosser, and J. Goss, Sens. Actuators **17**, 405 (1989).
2. J. Suski, V. Mosser, and G. Le Roux, in *Proceedings of Electrochemical Society Conference* (San Diego, CA, USA, 1986), p. 331.
3. E. Obermeir, PhD Thesis (Univ. of Munich, 1983).
4. P. H. French and A. G. R. Evans, Sens. Actuators **7**, 135 (1985).
5. D. Schubert, W. Jenschke, T. Uhlig, and F. M. Schmidt, Sens. Actuators **11**, 145 (1987).
6. V. A. Gridchin, V. M. Lubimsky, and M. P. Sarina, Sens. Actuators A **49**, 67 (1995).
7. P. H. French and A. G. R. Evans, Electron. Lett. **24**, 999 (1984).
8. T. Toriyama, Y. Yokoyama, and S. Sugiyama, Sens. Mater. **12**, 473 (2000).
9. P. H. French and A. G. R. Evans, Solid-State Electron. **32**, 1 (1989).
10. M. Le Berre, M. Lemiti, D. Barbier, *et al.*, Sens. Actuators A **46–47**, 166 (1995).
11. V. A. Gridchin and V. M. Lyubimskiĭ, Mikroélektronika **32**, 261 (2003).
12. V. Mosser, J. Suski, J. Goss, and E. Obermeir, Sens. Actuators A **28**, 113 (1991).
13. G. L. Bir and G. E. Pikus, *Symmetry and Stain-Induced Effects in Semiconductors* (Nauka, Moscow, 1972; Wiley, New York, 1975).
14. G. E. Pikus and G. L. Bir, Fiz. Tverd. Tela (Leningrad) **1**, 1828 (1959) [Sov. Phys. Solid State **1**, 1675 (1959)].
15. V. A. Gridchin, V. M. Lyubimskiĭ, and A. G. Moiseev, Fiz. Tekh. Poluprovodn. (St. Petersburg) (in press).
16. N. C. C. Lu, C. Y. Gerberg, C. Y. Lu, and J. D. Meidl, IEEE Trans. Electron. Devices **28**, 818 (1981).
17. M. Granveaud and P. Malsan, Onde Electr. **47**, 392 (1967).

Translated by A. Spitsyn

Semiconductors, Vol. 38, No. 8, 2004, pp. 981–986. Translated from Fizika i Tekhnika Poluprovodnikov, Vol. 38, No. 8, 2004, pp. 1018–1023.

SEMICONDUCTOR STRUCTURES, INTERFACES, AND SURFACES

A Photoelectric Study of Charge-Carrier Collection in CdZnTe-Based Detectors of X-ray and γ Radiation

L. A. Kosyachenko*, E. L. Maslyanchuk, I. M. Rarenko, and V. M. Sklyarchuk

Chernovtsy National University, Chernovtsy, 58012 Ukraine

**e-mail: lakos@chv.ukrpack.net*

Submitted December 10, 2003; accepted for publication December 30, 2003

Abstract—A scheme of photoconductivity excitation in which an external electric field is parallel to the direction of the radiation penetration is considered. Spatial distribution of nonequilibrium electrons and the conditions for separation of electron–hole pairs (for the charge-carrier collection) are analyzed in relation to the value of the voltage applied to the crystal. A method for determining the electron lifetime from measurements of photoconductivity is suggested. © *2004 MAIK "Nauka/Interperiodica".*

1. INTRODUCTION

The efficiency of charge-carrier collection (the ratio between the number of charge carriers involved in the pulse formation in the detector circuit and the total number of electron–hole pairs generated as a result of absorption of a photon) is one of the most important parameters of a semiconductor detector of X-ray and γ radiation. The problem of charge-carrier collection is very important for widely used detectors based on CdTe and $Cd_{1-x}Zn_xTe$ solid solution with a low content of Zn, since the charge-carrier lifetimes in these materials (no larger than several microseconds) are much shorter than those in Ge and Si [1]. It is the charge-collection problem that most complicates the operation of these detectors: a high voltage (100–500 V) has to be applied to the detector if the crystal thickness is 1–5 μm; as a result, one has to select the most pure crystals with the highest structural quality and reduce the operation temperature of the detector using a thermoelectric refrigerator [2]. Since the mobility of holes in CdTe and $Cd_{1-x}Zn_xTe$ is lower by more than an order of magnitude than that of electrons, it is practically impossible to make the drift length of a hole larger than the detector thickness by increasing the supply voltage, even if the lifetimes of holes and electrons are equal ($\mu_p\tau_p \ll \mu_n\tau_n$, where μ_n and μ_p are the mobilities of electrons and holes and τ_n and τ_p are the corresponding lifetimes). The problem is typically solved using a special system for processing the electrical signal in the detector circuit [3, 4] or by employing a complex configuration of electrodes (a system of microstrips) [5]. At the same time, such an important characteristic as the efficiency of collection of excited charge carriers cannot be measured directly; rather, this characteristic manifests itself when the completed device is connected to a detecting system (a multichannel pulse-height analyzer). Below, we report results that indicate that the efficiency of charge collection can be estimated with a fairly high accuracy if we carry out a comparatively simple measurement of photoconductivity of the crystal prepared for installation in the detector.

2. EXPERIMENTAL RESULTS AND PHYSICAL MODEL

In our studies, we used *p*-$Cd_{1-x}Zn_xTe$ single crystals ($x = 0.1$ and band gap $E_g = 1.57$ eV) grown by the modified Bridgman–Stockbarger method and subjected to subsequent annealing for several weeks in Cd vapors. The samples with the highest resistivity (in this case, with a resistivity of 10^{10} Ω cm), i.e., samples suitable for detectors, were chosen among all the grown crystals. The mechanism of annealing-induced partial compensation of $Cd_{1-x}Zn_xTe$ *p*-type conductivity caused mainly by V_{Cd} vacancies (deep acceptor levels) is not quite clear, and we did not aim to clarify this mechanism in this study. Among the possible processes that may occur in the course of annealing, we mention the origination of either interstitial Cd atoms that act as compensating shallow-level donors or complexes that include a Cd vacancy (so-called *A* centers) and act as deep-level donors (filling V_{Cd} vacancies with Cd atoms is usually not considered) [6].

In order to study photoconductivity, we formed contacts on the opposite faces of the crystal that had an area of 4×4 mm^2 and a thickness of 1.3 mm; the front contact was semitransparent (Fig. 1). The contact material Ni was deposited using vacuum evaporation onto the polished and chemically treated crystal surface. The contacts were strictly ohmic in the entire range of applied voltages (1–350 V) irrespective of the voltage polarity. Thus, the scheme we use for charge-carrier excitation is similar to the excitation with the X-ray or γ-ray photons except for the fact that a cascade of electron–hole pairs is generated in the latter case.

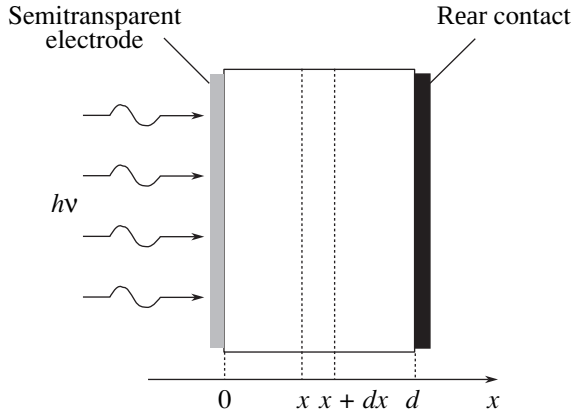

Fig. 1. The photoconductivity-excitation scheme under consideration.

If the optical-absorption coefficient α is fairly large and the diffusion length of electrons L_n is smaller than the crystal thickness d ($1/\alpha \ll d$, $L_n \ll d$), photons are absorbed in a thin layer near the irradiated surface. As a result, electron–hole pairs are not generated in most of the crystal. This situation takes place for high energies of optical photons $h\nu$ and low energies of X-ray or γ-ray photons whose absorption coefficient is proportional to $h\nu^{-7/2}$. If a voltage is applied to the crystal, the pattern of occurring processes changes. If the illuminated surface is charged negatively, excited electrons are repelled from the surface and driven to the bulk; as a result, the resistivity decreases and the photoconductivity of the sample increases as a whole. If the charge of the surface is opposite, electrons are repelled from the crystal by the electric field. As a result, the photoconductivity of the crystal decreases. In the second case, holes are pulled into the crystal bulk; however (as was mentioned above), the mobility of holes in $Cd_{1-x}Zn_xTe$ is more than an order of magnitude lower than that of electrons (the hole mobility is 50–80 $cm^2/(V\ s)$ compared with 1000–1050 $cm^2/(V\ s)$ for electrons). Therefore, the hole component $e\mu_p\Delta p$ in the photoconductivity can be disregarded in comparison with the electron component $e\mu_n\Delta n$ (here, e is the elementary charge and Δp and Δn are excess concentrations of holes and electrons, respectively) even if the lifetimes of electrons and holes are of the same order of magnitude, which is sometimes observed [7].

If the photon-absorption coefficient is so small that $1/\alpha \gg d$, electron–hole pairs are generated almost uniformly throughout the volume. This condition is satisfied for $Cd_{1-x}Zn_xTe$-based detectors in the important photon-energy region with $h\nu >$ ~200 keV [8]. Electrons are repelled from the negatively charged electrode under the effect of an external electric field; i.e., electrons are repelled from either the front or the rear surface, depending on the polarity of the applied voltage. In both cases, the photoconductivity of the sample is expected to decrease to approximately the same extent. These inferences are confirmed by the results of measurements of the photoconductivity spectra shown in Fig. 2.

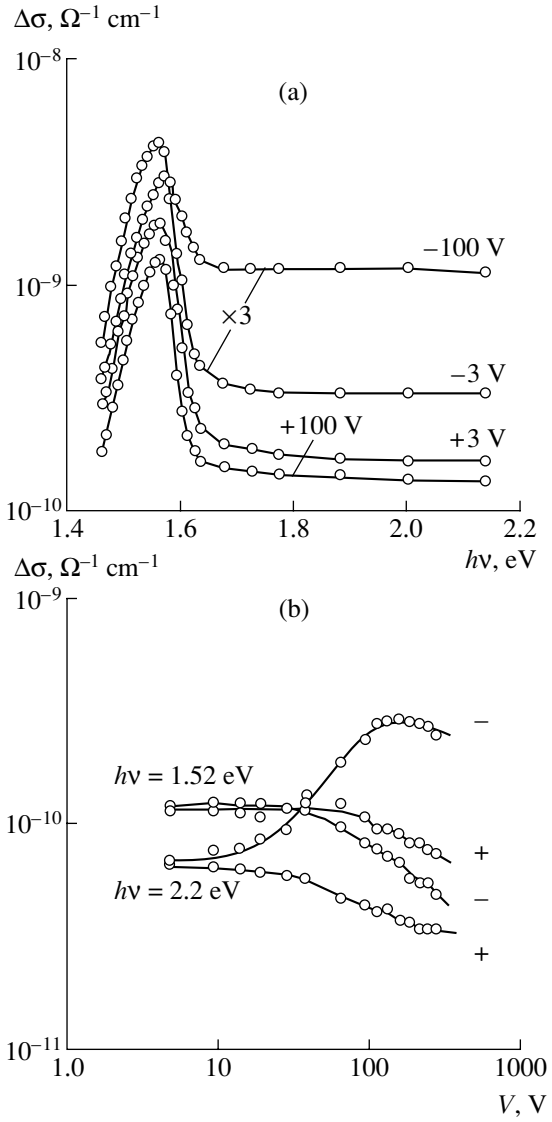

Fig. 2. (a) Spectral distribution of photoconductivity in a $Cd_{1-x}Zn_xTe$ crystal for two polarities of the bias voltage and (b) the dependences of photoconductivity excited with photons with different energies on the bias voltage. The front-electrode polarity is indicated. The curves were measured at room temperature.

The photoconductivity $\Delta\sigma$ was determined from the measured photocurrent I_{ph} at a voltage V as I_{ph}/VS, where S is the contact area. As can be seen from Fig. 2a, the curves corresponding to $V = -3$ and -100 V cross each other; i.e., the photoconductivity in the case of a negatively charged surface increases appreciably as the voltage increases in the region of high photon energies $h\nu$ (large values of α) and decreases in the region of small values of $h\nu$ (small values of α). If the illuminated surface is charged positively, the photoconductivity decreases with increasing voltage in the entire spectral range. The dependence of photoconductivity on the

voltage in the range 3–300 V is shown in Fig. 2b for two values, $h\nu = 2.2$ and 1.52 eV (absorption for $h\nu = 1.52$ eV is possible since the absorption edge for $Cd_{1-x}Zn_xTe$ and for other semiconductors is not abrupt).

3. A MATHEMATICAL DESCRIPTION OF PHOTOCONDUCTIVITY

The photoconductivity is typically calculated for the situation where an electric field is directed perpendicularly to the direction of the optical beam incident on the sample surface (see, for example, [9]). In this case, the photoconductivity spectrum is independent of both the polarity and magnitude of the applied voltage. We describe the photoconductivity for the excitation scheme illustrated in Fig. 1 on the basis of a continuity equation that can be written as (for electrons in the steady state)

$$\frac{1}{e}\frac{dj_n}{dx} - \frac{\Delta n}{\tau_n} + \Phi_0\alpha\exp(-\alpha x) = 0, \quad (1)$$

where j_n is the electron-current density; Δn and τ_n are the excess concentration and lifetime of electrons, respectively; $\Phi_0\alpha\exp(-\alpha x)$ is the photogeneration rate of charge carriers; and Φ_0 is the number of photons incident on the unit surface area per unit time.

Taking into account the drift and diffusion components of the current, we obtain

$$j_n = eF\mu_n n + eD_n\frac{dn}{dx}, \quad (2)$$

where D_n is the diffusion coefficient of electrons and F is the electric-field strength. If the voltage is applied in the plane perpendicular to the optical-beam direction, an electric field is still observed in the direction of the light propagation owing to the difference between the electron and hole mobilities. This field is taken into account by introducing the bipolar-diffusion coefficient $D_{\text{eff}} = D_nD_p(n + p)/(nD_n + pD_p)$, which is nearly equal to the diffusion coefficient of electrons as the minority charge carriers (D_p is the diffusion coefficient of holes) [9]. The introduction of D_{eff} leads to the fact that the term containing the electric-field strength is absent in the continuity equation. It is important to realize that we cannot ignore this term in the scheme of the photoconductivity excitation under consideration since in this scheme the electric-field strength F is related to the applied external voltage as V/d, so that the drift-related term in (2) may become important at large values of V. In the situation where the external voltage is low, a certain error may still appear in the results of calculations if the intrinsic field $F_{\text{int}}(kT/e)[(\mu_n - \mu_p)/(\mu_n + \mu_p)](d\Delta\sigma/dx)/\sigma$ is disregarded ($\Delta\sigma$ is the photoconductivity and σ is the conductivity under illumination) [10]. In order to estimate the intrinsic field, we assume that the main change in the conductivity occurs over a distance equal to the diffusion length for electrons L_n. Since $\mu_n/\mu_p > 10$, we may also set $(\mu_n - \mu_p)/(\mu_n + \mu_p) \approx 1$. As a result, we obtain $F_{\text{int}} \approx (kT/e)(\Delta\sigma/\sigma)/L_n$. The electron diffusion length in $Cd_{1-x}Zn_xTe$ is typically in the range from $(5–50)\times10^{-4}$ cm; the value of $\Delta\sigma/\sigma$ was no larger than 0.3–0.5 in the experiments under consideration. It then follows that $F_{\text{int}} = 2–20$ V/cm, which corresponds to the applied external voltage 0.2–2 V for a crystal thickness of ~1 mm. So low bias voltages are of no practical interest in the operation of the detectors under consideration.

Thus, substituting formula (2) into Eq. (1), we obtain the equation

$$D_n\frac{d^2\Delta n}{dx^2} + \mu_nF\frac{d\Delta n}{dx} - \frac{\Delta n}{\tau_n} + \Phi_0\alpha\exp(-\alpha x) = 0. \quad (3)$$

A particular solution to this equation is given by $\Delta n_{\text{part}} = C\exp(-\alpha x)$, where

$$C = \frac{\alpha\Phi_0\tau}{1 + \alpha L_{\text{dr}} - \alpha^2L_n^2}, \quad (4)$$

and $L_{\text{dr}} = \mu_nF\tau_n$ denotes the drift length, i.e., the average distance traveled by an electron in the direction of the applied field in a time equal to the lifetime.

We will seek the general solution to a homogeneous equation that corresponds to Eq. (3) in the form $\Delta n_{\text{gen}} = A\exp(kx)$, which leads to the characteristic equation

$$k^2 + \frac{L_{\text{dr}}}{L_n^2}k - \frac{1}{L_n^2} = 0. \quad (5)$$

The roots of this equation are equal to

$$k_{1,2} = -\frac{L_{\text{dr}}}{2L_n^2} \pm \sqrt{\left(\frac{L_{\text{dr}}}{2L_n^2}\right)^2 + \frac{1}{L_n^2}}, \quad (6)$$

where $L_n = (D_n\tau_n)^{1/2}$ denotes the electron diffusion length (the roots $k_{1,2}$ become equal to $\pm1/L_n$ if $F \longrightarrow 0$).

Thus, the general solution to inhomogeneous Eq. (3) is given by

$$\Delta n(x, \alpha) = A\exp(k_1x) + B\exp(k_2x) + C\exp(-\alpha x). \quad (7)$$

If the sample is comparatively thick, the condition that Δn tends to zero if $x \longrightarrow \infty$ is most often used; we should then set one of the constants (A or B) equal to zero. In the case under consideration, the sample thickness (0.13 cm) far exceeds the diffusion length for electrons (~0.005 cm even at a long lifetime $\tau_n = 10^{-6}$ s). However, the photoexcited electrons can penetrate deep into the crystal if an external pulling field is applied. Moreover, in order to ensure the efficient operation of the detector, one has to apply a very high bias voltage so that all excited electrons can reach the rear electrode. As a result, the constants A and B should be determined from two boundary conditions:

$$S_f\Delta n(0) = \frac{1}{e}j_n(0), \quad (8)$$

$$S_b\Delta n(d) = -\frac{1}{e}j_n(d), \quad (9)$$

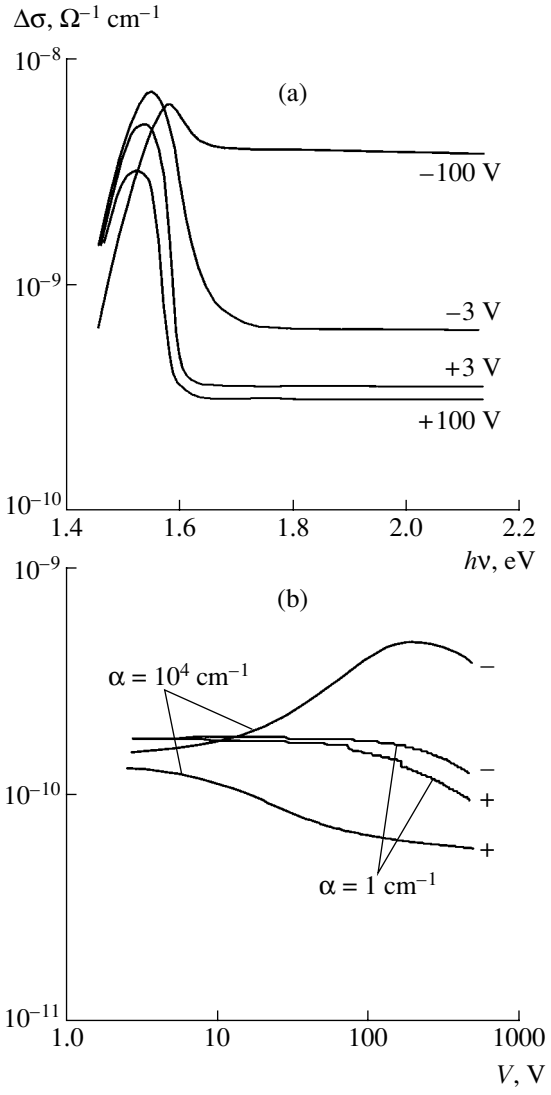

Fig. 3. (a) Photoconductivity spectra calculated using formula (7) for several bias voltages and (b) the voltage dependences of photoconductivity excited with radiation with two different absorption coefficients. The polarity of the front surface is indicated.

where S_f and S_b are the surface-recombination velocities at the front and rear crystal faces, respectively. Using formulas (8) and (9) and performing algebraic transformations, we obtain

$$A = \frac{B(M_2 - S_f) + C(M_3 - S_f)}{S_f - M_1}, \tag{10}$$

$$B = C[(M_3 - S_f)(S_b - M_1)\exp(k_1 d) + (S_b - M_3)(S_f - M_1)\exp(-ad)]/[(M_2 - S_f) \times (S_b - M_1)\exp(k_1 d) + (S_b - M_2)(S_f - M_1)\exp(k_2 d)], \tag{11}$$

$$M_1 = D_n k_1 + \mu_n F, \quad M_2 = D_n k_2 + \mu_n F,$$

$$M_3 = \mu_n F - \alpha D_n. \tag{12}$$

Knowing the distribution of excess electrons over the depth in the sample (7) and the dark semiconductor conductivity $\sigma_0 = 1/\rho$, we can determine the resistance of a layer with the thickness dx as $dx/(e\mu_n\Delta n + \sigma_0)$ (see Fig. 1); integrating then with respect to x from 0 to d, we obtain the following expression for the sample resistance under irradiation:

$$R_{\text{irr}}(\alpha, V)\int_0^d \frac{dx}{e\mu_n\Delta n + \sigma_0}. \tag{13}$$

The photocurrent density at a voltage V is equal to the difference between the currents under irradiation and in the dark; i.e.,

$$I_{\text{ph}} = \frac{V}{R_{\text{irr}}} - \frac{V\sigma_0}{d}. \tag{14}$$

4. DISCUSSION

Formula (14) makes it possible to calculate the photocurrent for specified values of the absorption coefficient α and the bias voltage *V*. In order to obtain the spectral characteristic of photoconductivity, we should know the absorption curve $\alpha(h\nu)$ of the material under consideration in a wide range of variations in α. The absorption edge, which is most affected by the composition inhomogeneity and the conditions of growth of the material, was determined from measurements of optical transmission for 150-μm-thick wafers. The data for $\alpha(h\nu)$ in the region of large values of α were taken from [11].

In Fig. 3a, we show the photoconductivity curves $\Delta\sigma(h\nu) = I_{\text{ph}}/(VS)$ calculated for different polarity and several magnitudes of the bias voltage. As can be seen, the calculated curves reproduce the aforementioned trends in the spectral characteristics (it was assumed that $\tau_n = 2 \times 10^{-8}$ s and $S_f = S_b = 10^5$ cm/s). Indeed, if the irradiated surface is charged negatively and the voltage increases, photoconductivity increases in the region of large values of $h\nu$ and decreases in the region of small values of $h\nu$. The photoconductivity increases in the regions of both large and small values of $h\nu$ with increasing voltage if the irradiated surface is charged positively. Comparison of Figs. 2b and 3b shows that the dependences $\Delta\sigma(V)$ calculated for two fixed values of the absorption coefficient (α = 1 and 10^4 cm^{-1}) are also consistent with experimental data.

Thus, the suggested physical model and the analytical expressions derived on the basis of this model adequately describe the photoelectric processes that occur in a $Cd_{1-x}Zn_xTe$ crystal; i.e., the ideas developed can be used to analyze the process of collection of charge carriers generated during illumination of the crystal. First of all, important information can be obtained by analyzing expression (7) for spatial distribution of electrons excited by radiation with different absorption

coefficients and for different polarity and magnitude of the bias voltage.

In Fig. 4a, we show the calculated distributions $\Delta n(x)$ of electrons generated near the negatively charged front surface of the crystal ($\alpha = 10^4$ cm^{-1}). The lifetime of excess electrons was assumed to be equal to 10^{-6} s, i.e., the value typical of the CdTe and $Cd_{1-x}Zn_xTe$ compounds used in the detectors of the X-ray and γ radiation [1–3]. On the same grounds, we set the crystal thickness equal to 2 mm. As can be seen from Fig. 4a, in the case of $V = 0$, the photogenerated electrons are concentrated near the crystal surface within the diffusion length (50 μm); the distribution falls off steeply at $x \longrightarrow 0$ owing to surface recombination. At $V = -10$ V, the degree of penetration of Δn into the crystal increases severalfold. As the voltage increases further, the number of electrons in the crystal becomes progressively smaller, so that the excess-electron concentration is very low at $|V| > 300$ V. This behavior indicates that all electrons generated by radiation reach the rear electrode.

If electrons are generated by radiation with a small absorption coefficient ($\alpha = 1$ cm^{-1}), the excess electrons are distributed more or less uniformly over the distance from the front electrode (the photogeneration rate does decrease somewhat with increasing x); the distribution falls off in the vicinity of both surfaces owing to surface recombination (Fig. 4b). If a bias voltage is applied, electrons are pushed from the front surface by an electric field; as a result, at $V = -300$ V, they remain in the crystal in an amount comparable to that in the case of $\alpha = 10^4$ cm^{-1}. This behavior is understandable since the longest time for traversing the crystal is needed for the electrons generated near the front surface, i.e., in the region where the excess electrons are generated under irradiation with photons with a large value of α.

The results shown in Fig. 4c illustrate the extent to which the conditions of electron collection vary when the electron lifetime τ_n is changed. As can be seen, even at a voltage of –300 V, a significant portion of the photogenerated electrons does not reach the rear electrode at $\tau_n = 10^{-7}$ s; this is true for the vast majority of electrons if $\tau_n = 10^{-8}$ s. Thus, our calculations confirm the experimentally established requirement: efficient collection of excess electrons at an operating detector voltage of 200–400 V is feasible only in a material with an electron lifetime of $\tau_n = 10^{-6}$ s or longer [2, 3].

Clearly, the above conclusions concerning the collection of electrons are valid only if a hole generated as a result of absorption of a photon reaches the negatively charged electrode simultaneously with the electron that reaches the positively charged electrode. Since the product of the lifetime of holes by their mobility ($\tau_p\mu_p$) in $Cd_{1-x}Zn_xTe$ is much smaller than the corresponding quantity for electrons ($\tau_n\mu_n$), it is completely unrealistic to ensure the collection of holes by increasing the bias voltage. All that remains is to use the developed methods for processing the signal in the detector circuit and employ a special configuration of electrodes [3, 4].

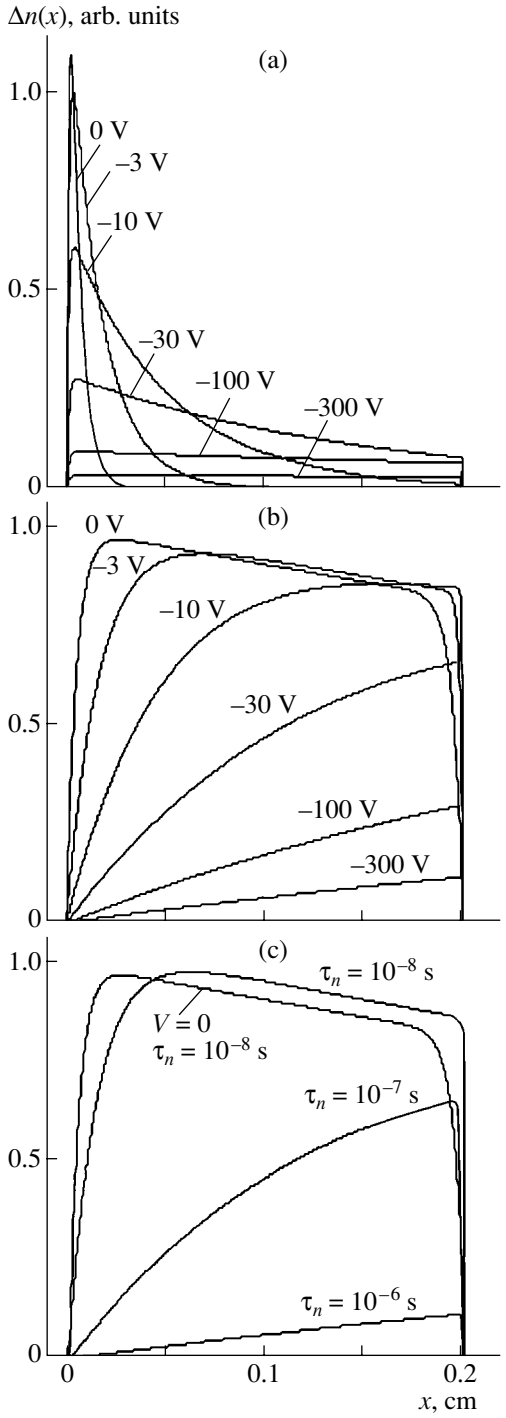

Fig. 4. Spatial distribution of excess electrons: (a) excitation with radiation with absorption coefficient $\alpha = 10^4$ cm^{-1} for various bias voltages; (b) the same for $\alpha = 1$ cm^{-1}; and (c) $\alpha = 1$ cm^{-1}, the bias voltage is –300 V, and several values of the lifetime τ_n (the curve $\Delta n(x)$ for $V = 0$ and $\tau_n = 10^{-8}$ s is shown for comparison).

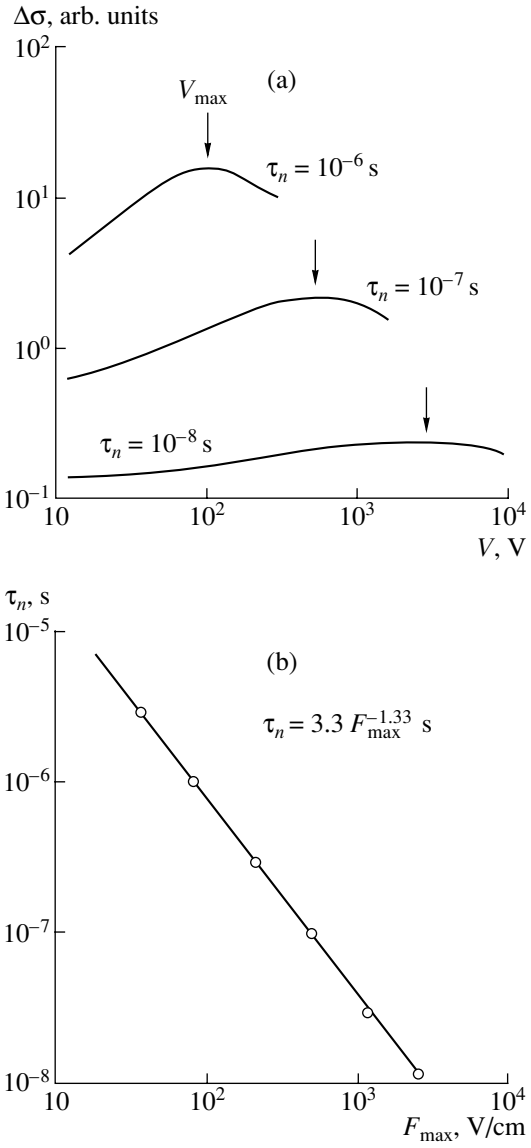

Fig. 5. (a) Dependence of the photoconductivity in the crystal on the bias voltage for several lifetimes of electrons and (b) relation between the electron lifetime and the electric-field strength at which the peak in the photoconductivity curve is observed.

If the front electrode is charged negatively, a peak is observed in both the measured and calculated photoconductivity curves $\Delta\sigma(V)$ (Figs. 2b, 3b); the position of this peak V_{max} is controlled primarily by the electron lifetime τ_n. This circumstance can be used to determine the key parameter τ_n of the detector material. In Fig. 5a, we show the curves $\Delta\sigma(V)$ calculated for several values of τ_n (d = 2 mm); the circles in Fig. 5b represent the dependence of τ_n on the electric-field strength $F_{max} = V_{max}/d$ at which the peak is observed.

As can be seen, the obtained dependence $\tau_n(F_{max})$ plotted on the log–log scale is represented by a straight line; i.e., this dependence can be described by a power-law function. If the electric-field strength is expressed in V/cm and the lifetime is expressed in seconds, the function under consideration can be represented as (the solid line in Fig. 5b)

$$\tau_n = 3.3F_{max}^{-1.33}. \quad (15)$$

We emphasize that the curve $\Delta\sigma(V)$ from which the quantity V_{max} (and, consequently, the quantity $F_{max} = V_{max}/d$ is determined is measured for a crystal used in a detector of X-ray and γ radiation. Clearly, the empirical dependence (15) will change somewhat if the electron mobility deviates from the value (1000 cm^2/(V s)) used in calculation of the curves shown in Fig. 5a.

5. CONCLUSION

We measured the photoconductivity spectra of $Cd_{1-x}Zn_xTe$ crystals for the configuration where an external voltage is applied along the penetration direction of the excitation optical beam, i.e., under conditions when the separation of electron–hole pairs and collection of the charge carriers are similar to those in a detector of X-ray and γ radiation. The value of photoconductivity and the shape of spectral curves obtained in this scheme of excitation depend heavily on the polarity and magnitude of the bias voltage. Analytic expressions derived from the continuity equation adequately describe the observed experimental dependences and their modification induced by changes in the conditions of excitation. We obtained an empirical expression that establishes a relation between the electron lifetime and the electric-field strength corresponding to the crystal photoconductivity at a maximum.

REFERENCES

1. Y. Eisen and A. Shor, J. Cryst. Growth **184–185**, 1302 (1998).
2. R. H. Redus, A. C. Huber, and J. A. Pantazis, Nucl. Instrum. Methods Phys. Res. A **458**, 214 (2001).
3. http:/www.amptek.com/a250ap.html.
4. M. R. Squillante and G. Entine, Nucl. Instrum. Methods Phys. Res. A **380**, 160 (1996).
5. M. A. J. van Pamelen, C. Budtz-Jorgensen, and I. Kuvvetli, Nucl. Instrum. Methods Phys. Res. A **439**, 625 (2000).
6. A. D. M. Hofmann, W. Stadler, P. Chrismann, and B. K. Meyer, Nucl. Instrum. Methods Phys. Res. A **380**, 117 (1996).
7. M. Jung, J. Morel, P. Fougeres, *et al.*, Nucl. Instrum. Methods Phys. Res. A **428**, 45 (1999).
8. S. Kraft, M. Bavdaz, B. Castelletto, *et al.*, Nucl. Instrum. Methods Phys. Res. A **418**, 337 (1998).
9. G. E. Pikus, *Fundamentals of the Theory of Semiconductor Devices* (Nauka, Moscow, 1965) [in Russian].
10. S. M. Ryvkin, *Photoelectric Effects in Semiconductors* (Fizmatgiz, Leningrad, 1963; Consultants Bureau, New York, 1964).
11. T. Toshifumi, S. Adachi, H. Nakanishi, and K. Ohtsuka, Jpn. J. Appl. Phys., Part 1 **32**, 3496 (1993).

Translated by A. Spitsyn